INAUGURAL - DISSERTATION

zur
Erlangung der Doktorwürde
der
Naturwissenschaftlich - Mathematischen
Gesamtfakultät
der Ruprecht - Karls - Universität
Heidelberg

vorgelegt von
Dipl.-Phys. Siri Jetter
aus Heidelberg

Tag der mündlichen Prüfung: 25.10.2011

Development of a Pencil Beam Algorithm for the fast Calculation of Dose applied in keV Imaging Procedures in Image Guided Radiotherapy

Gutachter: Prof. Dr. Uwe Oelfke
Prof. Dr. Wolfgang Schlegel

Entwicklung eines Pencil-Beam-Algorithmus zur schnellen Dosisberechnung für die keV-Bildgebung in der bildgeführten Strahlentherapie

Die Einführung der bildgesteuerten Strahlentherapie in die klinische Routine im Verlauf der letzten Jahre hat zu einer verstärkten Strahlenbelastung der Patienten durch keV-Bildgebung geführt. Eine tägliche Bildgebung, z.B. zur Lagerungskontrolle, kann zu einer signifikanten zusätzlichen Dosisbelastung in Risikoorganen führen. Eine möglichst genaue Abschätzung dieser Dosis bildet die Grundlage für die Integration der Dosis in die Bestrahlungsplanung. Diese Arbeit präsentiert die Entwicklung eines schnellen Algorithmus zur Dosisberechnung für individuelle Patientengeometrien für den Einsatz im keV-Energiebereich. Der vorgestellte Algorithmus basiert auf einem Pencil-Beam-Algorithmus, der für die Einbeziehung von Inhomogenitäten mit empirischen Tiefen- und Dosisskalierungsfaktoren kombiniert wird. Um eine hohe Genauigkeit zu erreichen wird sowohl im Design des Algorithmus, als auch in den Monte-Carlo Simulationen, die als Gold Standard dienen, eine hohe Anzahl unterschiedlicher Gewebetypen berücksichtigt. Die Genauigkeit und die Limitationen des Algorithmus werden für Phantom und Patientengeometrien analysiert. Es wird gezeigt, dass der entwickelte Pencil-Beam-Algorithmus in der Anwendung für Patienten für alle untersuchten Konfigurationen eine genaue Vorhersage der mittleren Dosis in Risikoorganen ermöglicht und für Cone-Beam-CT- Aufnahmen die Möglichkeit zur präzisen Berechnung ganzer Dosisverteilungen im Patienten innerhalb einiger Minuten bietet.

Development of a Pencil Beam Algorithm for the fast Calculation of Dose applied in keV Imaging Procedures in Image Guided Radiotherapy

Over the last years, the introduction of image guided radiotherapy into clinical practice has led to an increased exposure of patients to radiation in keV imaging procedures. Daily imaging can significantly contribute to the dose in the organs at risk. The accurate assessment of this additional dose due to imaging is essential for the inclusion of the dose into the therapy planning process. In this work, the development of a fast patient specific dose calculation algorithm for the keV energy range is presented. The algorithm is based on a pencil beam algorithm combined with semi-empirical factors for the scaling of depth and dose to account for inhomogeneities. To achieve a high accuracy, a high number of different body tissues is included in the design of the algorithm as well as in the Monte Carlo simulation used as the gold standard. The accuracy and limitations of the algorithm are evaluated for different phantom and patient geometries. For the application to patients, the proposed algorithm is shown to accurately calculate the mean dose in organs at risk for all beam geometries and accurate dose distributions for the full patient geometries for cone beam CT acquisitions within a very short timeframe.

Contents

1. Introduction **1**

2. Motivation: Techniques and Doses in Image guided radiation therapy (IGRT) **3**
2.1. Setup errors and organ motion . . . 4
2.2. 2D imaging systems . . . 5
2.2.1. Single projection imaging . . . 5
2.2.2. Perpendicular projections . . . 5
2.2.3. Stereoscopic imaging . . . 5
2.3. 3D imaging systems . . . 7
2.3.1. CT on rails . . . 7
2.3.2. MV Fan Beam CT . . . 7
2.3.3. Linac integrated MV- and kV-imaging . . . 7
2.4. Reported imaging doses . . . 9

3. Basics **11**
3.1. Basic Terms and Definitions . . . 11
3.2. Coordinate systems . . . 12
3.2.1. IEC coordinate system . . . 12
3.2.2. Phantom coordinate system . . . 13
3.2.3. Patient coordinate system . . . 13
3.3. Production, Spectra and Dose Deposition - keV vs. MeV Photons . . . 14
3.3.1. Photon Production . . . 14
3.3.2. Photon Dose Deposition . . . 17
3.4. Pencil Beam Dose Calculation . . . 20

4. Monte Carlo Simulation Model of the X-ray tube **23**
4.1. X-ray tube simulation . . . 23
4.1.1. BEAMnrc . . . 23
4.1.2. Simulation setup . . . 24
4.2. Dose Simulation . . . 25
4.2.1. DOSXYZnrc . . . 25
4.2.2. Phantom Definition . . . 25
4.3. Verification Measurement & First Simulation . . . 25
4.3.1. Measurement . . . 26
4.3.2. Simulation . . . 26
4.3.3. Results and Discussion . . . 27

5. Calculation of the keV Pencil Beam Kernel and the Primary Fluence 31
5.1. Methods . . . 31
5.1.1. Changes in the Kernel Calculation Algorithm . . . 31
5.1.2. Calculation Steps in the Kernel Calculation Algorithm . . . 32
5.1.3. Simulation of the Input Data . . . 34
5.2. Results . . . 36
5.2.1. Phase Space files . . . 36
5.2.2. Obtained Input Data . . . 37
5.2.3. Analysis on the Accuracy of the Calculation Algorithm . . . 38

6. keV Dose Calculation Accuracy for different Water Phantoms 43
6.1. Methods . . . 43
6.1.1. Difference maps for dose cubes . . . 43
6.2. Single Photon Beam for a Large Rectangular Water Phantom . . . 44
6.2.1. MC-Simulations and Pencil Beam Calculations . . . 44
6.2.2. Results . . . 44
6.2.3. Summary . . . 50
6.3. Single Photon Beam for a Small Cylindrical Phantom . . . 50
6.3.1. MC-Simulation and Pencil Beam Calculations . . . 51
6.3.2. Results . . . 52
6.4. Cone Beam CT Acquisition for a Water-filled Patient Outline . . . 54
6.4.1. MC-Simulation and Pencil Beam Calculation . . . 54
6.4.2. Results . . . 55
6.4.3. Discussion . . . 57

7. Inhomogeneities: Scaling factors for depth and dose 59
7.1. Dose to water vs. dose to medium . . . 59
7.2. Methods . . . 60
7.2.1. Conventional Depth Scaling for MeV-Dose Calculation . . . 60
7.2.2. Scaling Algorithm for the keV Energy Range . . . 61
7.2.3. Converting CT-data to material and density maps . . . 62
7.2.4. Material Conversion Tables . . . 63
7.2.5. Estimation of the depth scaling factors α . . . 65
7.2.6. Preliminary Dose Scaling Factors β . . . 66
7.3. Scaling Factor Estimation . . . 68
7.3.1. Simulations . . . 68
7.3.2. Results & Discussion . . . 68

8. The Use of CT Dataset for Monte Carlo Simulations 73
8.1. Methods . . . 73
8.1.1. .egsphant Phantom Files . . . 73
8.1.2. Interface Realization . . . 74
8.2. Simulation Geometry and Settings . . . 75
8.3. Results . . . 75
8.3.1. Material and Density Maps . . . 75
8.3.2. Dose Distributions for a CBCT acquisition . . . 77
8.4. Discussion . . . 79

9. Pencil Beam Dose Calculation for Patient Geometries **81**
9.1. Methods . . . 81
9.1.1. keV Dose Scaling . . . 81
9.1.2. General Remarks on the Measure of Accuracies . . . 83
9.1.3. Dose normalization . . . 84
9.2. MC-simulations and Pencil Beam Calculations . . . 84
9.2.1. Phantom Creation . . . 84
9.2.2. Beam geometry . . . 84
9.2.3. Simulation Settings . . . 85
9.2.4. Pencil Beam Calculations . . . 85
9.3. Head & Neck Patients . . . 85
9.3.1. Patient Description . . . 85
9.3.2. Dose Scaling Factors $\beta(Z)$ . . . 86
9.3.3. Single beam - Dose Comparison . . . 88
9.3.4. CBCT - Dose Comparison . . . 92
9.4. Pelvis Patients . . . 96
9.4.1. Patient Description . . . 97
9.4.2. Dose Scaling Factors $\beta(Z)$ . . . 98
9.4.3. Single Beam - Dose Comparison . . . 98
9.4.4. CBCT - Dose Comparison . . . 102

10. Discussion and Outlook **107**
10.1. Monte Carlo Gold Standard . . . 107
10.2. Pencil Beam Kernel Calculation and Dose in Water . . . 108
10.3. keV Depth- and Dose-Scaling . . . 108
10.3.1. Depth Scaling Factors . . . 108
10.3.2. Dose Scaling Factors . . . 109
10.3.3. Comparison with Existing Algorithms . . . 109
10.4. Calculation Speed . . . 111
10.5. Accuracy of the Developed Algorithm . . . 111
10.5.1. Single Photon Beams . . . 112
10.5.2. CBCT Acquisitions . . . 112

11. Conclusion **115**

A. Summary of Simulation parameters **117**
A.1. Common Settings . . . 117
A.1.1. All simulations . . . 117
A.1.2. X-ray tube simulation . . . 117
A.1.3. Collimator simulation . . . 118
A.1.4. Dose deposition simulation . . . 118
A.2. Individual Parameters . . . 119

B. Simulated vs. pencil beam dose slices **121**
B.1. Single Beam - Head and Neck . . . 123
B.2. Cone beam CT - Head and Neck . . . 137
B.3. Single beam - Pelvis . . . 151
B.4. Cone beam CT - Pelvis . . . 159

List of Figures **167**

List of Tables **171**

Bibliography **173**

1. Introduction

The aim of radiotherapy is to achieve tumor control combined with a low rate of normal tissue complications by applying a high homogeneous radiation dose to the tumor volume, while keeping the dose in the surrounding tissue as low as possible. The technical developments in radiation therapy such as intensity modulated radiation therapy (IMRT), or rotational therapies allow for a very precise shaping of a homogeneous high dose region to the target volume and a good sparing of the organs at risk [1, 2, 3, 4], which leads to high dose gradients at the tumor edges. The planned dose distribution is calculated on a reference computed tomography (CT) dataset, which is acquired several days before the treatment starts. Due to the high gradients the knowledge about the position of the tumor and the organs at risk is the key point to achieve a treatment dose application as planned.

Though it is possible to achieve a certain reproducibility with immobilization devices, imaging of the patient in the treatment position can improve the accuracy and is nowadays an important part of the radiation treatment [5, 6, 7]. This combination of the radiotherapy treatment and imaging is called "image guided radiation therapy" (IGRT). Though other solutions such as a combination of a linear accelerator and magnetic resonance imaging are investigated in research, they are not clinically available yet [8, 9]. The widely used imaging with photon beams in the keV energy range is an attractive imaging option, but also leads to an additional dose to the organs at risk as all imaging modalities utilizing ionizing radiation. The amount of dose applied in keV imaging procedures has been investigated in phantom measurement or Monte Carlo simulations in numerous studies [10, 11, 12, 13, 14, 15, 16, 17, 18]. Other than in a diagnostic situation, the dose due to image guidance is added to a significant dose already applied due to the radiation treatment, which makes an accurate assessment of the organ specific doses even more important. For this an algorithm for the calculation of voxelized dose distribution for individualized geometries, including the patient anatomy and the imaging beam settings, is needed to calculate patient specific keV imaging doses to organ at risk, as they are available for the calculation of dose due to the MeV treatment beam.

The analytic algorithms available to calculate MeV dose can be grouped into two major classes: pencil beam algorithms and superposition algorithms. While pencil beam algorithms provide a fast method of dose calculation, the accuracy of superposition algorithms is generally superior to the pencil beam algorithms especially for the calculation of dose in and close to low density tissue [19].

Due to different physical properties of the photon beam for the lower energy range, the use of MeV dose calculation algorithms without any adaptations does not lead to a satisfactory accuracy of the calculated dose. In the literature, a calculation method based on a superposition method for the calculation of the dose for patient geometries with slight adaptations for the keV energy range has been described and evaluated by Alaei et al. [20, 21, 22]. Despite the fact, that the dose to soft tissue could be calculated with an acceptable accuracy, the algorithm did not yield satisfactory results for the calculation of doses in bony structures. Over the last years, different post processing corrections for dose distributions similar to those calculated with the algorithm

by Alaei et al. without the keV adaption, have been suggested to improve the calculation of dose in bony structures [23, 24, 25].
The aim of this work is the development and evaluation of a fast keV dose calculation algorithm for patient geometries based on the principle of pencil beam algorithms. Over the course of this thesis the reader is taken through the different steps in the development of the algorithm. To make the influence of the respective method on the accuracy of the algorithm as clear as possible, the evaluation results are presented in close proximity to the description of the method. The results for all steps are discussed together in one chapter. This leads to the division of the thesis into the following parts: Chapter 2 gives a short summary on image guided radiation therapy options and the associated imaging doses to present motivation for this work. In the following chapter 3, basic terms and principles are discussed. Before being able to evaluate the accuracy for any kind of dose calculation algorithm, one first has to define a gold standard, which determines the "true" dose distribution, to which the calculation results are compared. This step is described in chapter 4, where the Monte Carlo simulation models, which form the gold standard in this thesis, are introduced and validated in a measurement. Chapter 5 describes and evaluates the first step for the application of the pencil beam algorithm for the keV energy range: the calculation of pencil beam kernels for the imaging beam. This is followed by an analysis of the accuracy of the pencil beam algorithm for the dose calculation in homogeneous water phantoms with different geometries and beam configurations in chapter 6. The next step towards the application on patient geometries is presented in chapter 7, which describes the theory and the introduction of methods for the consideration of inhomogeneities. Before the accuracy of the algorithm can be investigated for real patient geometries, the Monte Carlo gold standard has to be extended to include the use of patient CT datasets for the definition of the simulation geometry. This is described in chapter 8 focusing on the effect of Hounsfield Unit material conversion tables on keV dose distributions. Finally in chapter 9, the accuracy of the new algorithm for the calculation of dose due to keV imaging is evaluated for real patient datasets. All presented results are discussed in chapter 10.

2. Motivation: Techniques and Doses in Image guided radiation therapy (IGRT)

As described in the introduction, the recent technical developments in photon radiation therapy including intensity modulated radiation therapy (IMRT) or rotational therapies, allow the application of highly conformal dose distributions leading to high dose gradients at the tumor edges. This makes the monitoring of the tumor position throughout the radiation treatment an essential part of the radiotherapy process to achieve a safe application of the planned treatment dose, which lead to the introduction of Image guided radiation therapy (IGRT). This term summarizes the combination of radiotherapy treatment with imaging modalities, which includes imaging with ionizing radiation, but also ultrasound or MR-imaging. The first option - imaging with ionizing radiation - is the one most used in clinical practice, such imaging systems are available in combination with treatment machines at different vendors (see also Figures 2.1,2.3 and 2.4). To explain the motivation of this work, but also as an introduction to different imaging geometries, this section gives an overview on the aims of image guidance as well as discussing current image guidance techniques and associated doses.

Figure 2.1.: *Linac integrated IGRT solutions by Elekta and Varian. Both offer a keV imaging system mounted perpendicular to the treatment system. Left: Elekta Synergy®(Detail of Elekta press image [26]). Right: Varian Trilogy® medical linear accelerator (Illustration: Detail of Varian press image [27]). The kV imaging system consisting of an X-ray tube and a flat panel detector is mounted on the linac gantry perpendicular to the treatment system.*

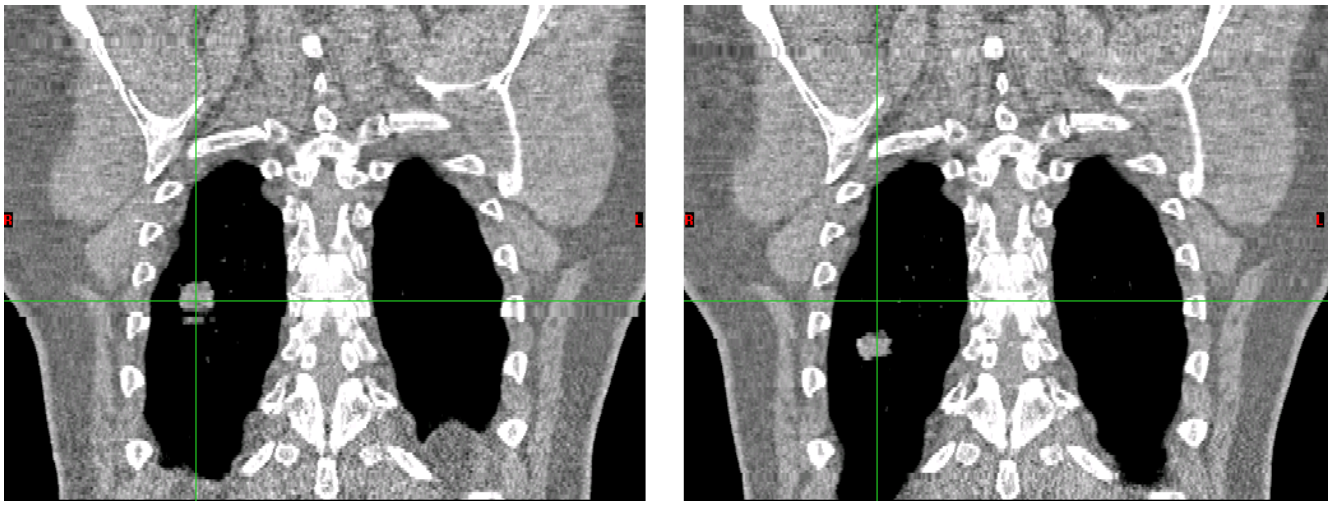

Figure 2.2.: *Extreme case of intrafractional tumor motion of a lung tumor. Frontal slices from a 4D-computed tomography. Left: Tumor position at full expiration. Right: Tumor position at full inspiration. The lung metastasis, which can clearly be seen within the lung, has moved by several cm within several seconds.*

2.1. Setup errors and organ motion

A fractionated radiotherapy treatment extends over up to several weeks including multiple treatment sessions. For each of the fractions, the patient has to be positioned on the treatment couch with the goal of reproducing the exact positioning of the patient (including the positions of the tumor and all organs at risk) as for the acquisition of the planning CT. As the patient is not rigid, neither in the outline nor regarding the position of internal structures relative to each other, this can only be achieved to a certain extend. According to the timescale, on which they occur, one can break down the occurring errors in two groups.
The term "interfractional errors" summarizes errors, that occur due to a wrong positioning of the patient within the immobilization device or due to changes in the patient anatomy on a timescale, that is larger than the time for one treatment fraction. One example for such a change is weight loss of the patient due to the radiation treatment or a change in tumor size and the connected displacement of neighboring organs. Due to the large timescale, the correction of interfractional errors is based on the assumption that no changes in the patient anatomy occur within one treatment fraction and include translation of the patient couch, but in extreme cases also replanning of the treatment. Based on this assumption the acquisition of one single image set before the start of each treatment fraction is sufficient to monitor and correct for interfractional errors, continuous monitoring of the patient is not necessary. The extent of interfractional errors can be significant, e.g. a study by Zeidan et al. showed that the deviation between planned and actual position of the target volume for head and neck patients immobilized with a head mask on average exceeds 3mm in 72% of the fractions and 5mm in 37% of the fractions [28] (study based on daily 3D-images for 24 patients comparing planned and imaged tumor position assuming perfect positioning for daily imaging). The same study showed that imaging at every other treatment fraction with a trend correction decreases the errors to exceed 3mm in only 29% of the fractions and 5mm in 11% of the fractions [28]. A similar analysis for prostate patients was undertaken by Kupelian et al. (based on the position of intraprostatic implanted metallic fiducials for 74 patients also assuming perfect positioning for daily imaging). Depending on the patient the deviation between planned and actual imaged position of the target volume on average exceeds 5mm in 35%-100% of the fractions with imaging at every other treatment fraction and trend correction decreasing the percentage to 5%-50% of the treatment fractions depending on the patient [29].
The second group of errors consists of intrafractional errors, which are due to physiological pro-

cesses or patient motion on a time scale shorter than the duration of one treatment fraction. The most prominent example for intrafractional motion is breathing motion, where the tumor volume often moves more than 1cm within only a few seconds [30, 31, 32]. Figure 2.2 shows slices from a 4D-computed tomography for a patient with a lung metastasis. In this extreme example, the tumor, which is clearly discernible in the lung, moves several cm from full expiration (left image) to full expiration (right image). Even though to a lower extent, intrafractional motion can occur for other tumor sites as well. For instance the timescale for rectal gas movement, rectal filling and bladder filling, which all influence the position of the prostate but also the position of organs at risk, is in the range of minutes. It has been shown, that intrafractional prostate motion regularly exceeds 3mm and can be up to 1cm in extreme cases [33, 34, 35, 36]. The management of intrafractional organ motion involves continuous imaging within each of the treatment fractions with a system capable of a very fast acquisition and evaluation of the patient images, as well as strategies to adapt the treatment to the detected motion, which include methods like tracking or gating.

2.2. 2D imaging systems

2.2.1. Single projection imaging

The most simple kind of image guidance is the acquisition of single projection images. This can be done either using the treatment beam (portal imaging) or if available, also using a keV X-ray tube; the resulting projection images can be either digital (with a flat panel detector) or analog (with a film measurement). Even though the contrast in keV images is higher than in the MeV images (due to the different interaction processes described in chapter 3.3.2), the soft tissue contrast is relatively low, so that the detection of tumor motion or setup errors is only possible based on the bony structure of the patient, implanted radiopaque markers or in high contrast soft tissue regions such as the lung [37]. Of course in a single projection image this is only possible in two dimensions, no information is available on the position of any of the visible structures in the third dimension. As the acquisition of single projection images is very fast, is can also be used to monitor the tumor motion continuously, especially if the motion mainly occurs along an axis that is mounted perpendicular to the imaging direction. This is for example the case for lung tumors, where in many cases, the main axis of tumor motion is the cranio-caudal axis.

2.2.2. Perpendicular projections

With the acquisition of two perpendicular 2-dimensional projection images of the patient, it is possible to detect setup errors or motion in all 3 dimensions. This technique has been used as the standard procedure a long time before image guided radiation therapy has attracted new attention. Again, the projection images can be obtained using the treatment beam (MeV photons), a keV photon beam or even a combination of both, leading to a different contrast in the projection images. Again, only the position of radiopaque markers or the bony anatomy can be extracted from the projection images. The main use of the perpendicular projections is the correction of setup errors, but with the radiopaque markers interfractional motion of the tumor itself can also be accounted for in all 3 dimensions.

2.2.3. Stereoscopic imaging

Stereoscopic imaging is the direct advancement of the perpendicular projection concept. Figure 2.3 shows the Cyberknife Suite by Accuray (Accuray Incorporated, Sunnyvale, CA, USA) with

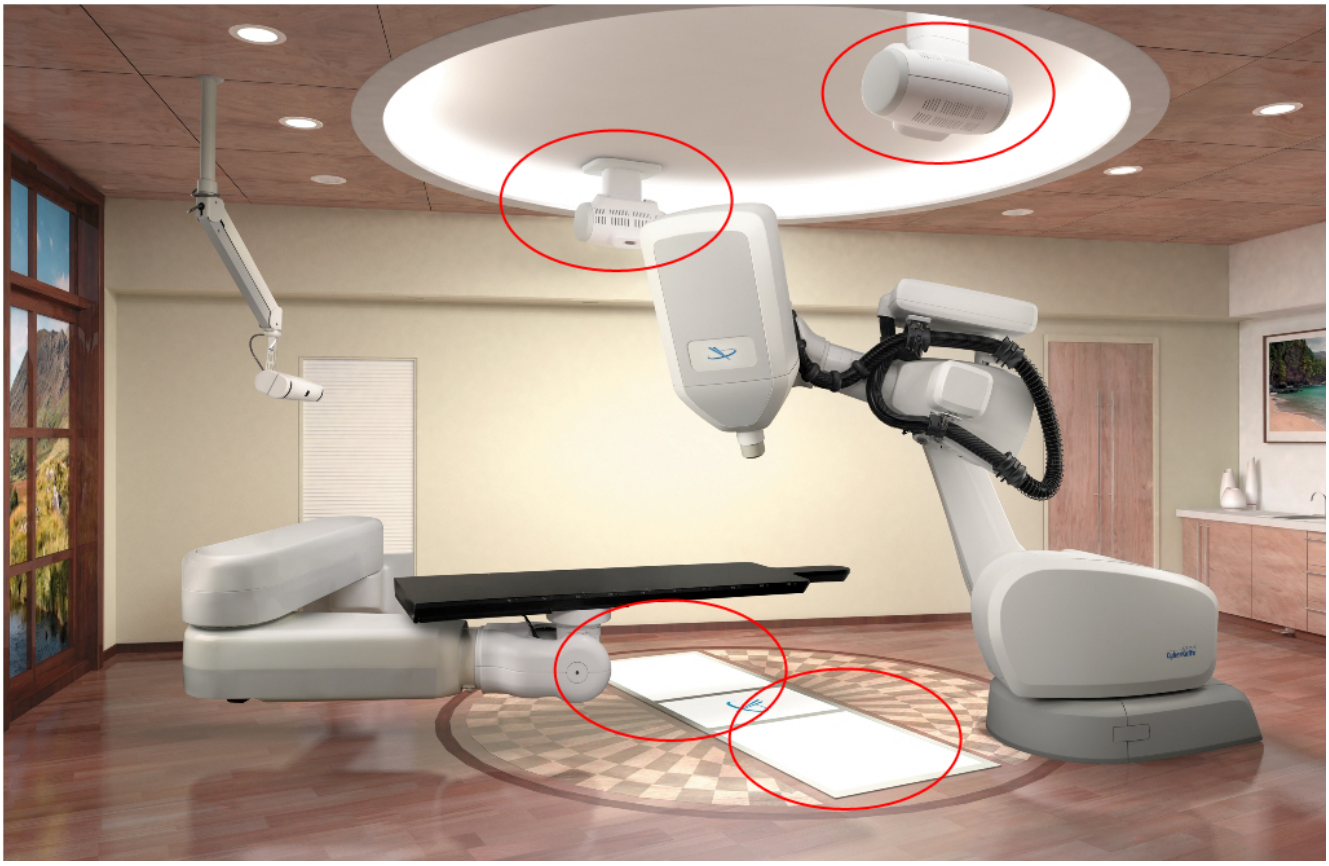

Figure 2.3.: *Stereoscopic imaging in the Accuray Cyberknife Suite (Illustration: Accuray press image [38]). The imaging components are marked with red circles. Two X-ray tubes are mounted at the ceiling of the treatment room combined with flat panel detectors in the floor. Projection images from the two directions can be acquired simultaneously. The position of radiopaque implanted markers in 3 dimensions can be estimated from the projection images.*

stereoscopic imaging. A similar system is used in the ™Novalis Tx setup by Varian (Varian Medical Systems Inc., Palo Alto, CA, USA) and BrainLAB (BrainLAB AG, Feldkirchen, Germany). In the figure, the imaging components are marked by red circles. To avoid the need to rotate the radiation source and detector for the acquisition of two projections, stereoscopic systems use two separate imaging setups. Another advantage of this is that both projections can be acquired at the same time, so that no intrafractional motion can occur between the two acquisitions. X-ray tubes, which are mounted on the ceiling or in the floor, are used as sources of keV-photon beams for the imaging procedure. Two flat panel detectors are installed in floor or at the ceiling respectively, opposite to the imaging sources. As described for the perpendicular case, the soft tissue contrast in the acquired projection images is low, in all areas but the lung, only bony structures or implanted markers are discernible. Other than the perpendicular projections stereoscopic imaging is mainly used in combination with radiopaque markers, the position of the markers in three dimensions can be estimated from the marker positions in the projection images.
Stereoscopic imaging is a very fast imaging modality, so that the positions of implanted markers (as a surrogate for the tumor position) can be determined almost at real-time. This allows to monitor not only interfractional motion (also to correct setup errors) in a single acquisition but also intrafractional motion by repetitive imaging over the whole treatment fraction. In this case the limiting factor is the radiation dose due to the imaging beam, therefore the tumor motion is often monitored by using external markers as surrogates, the imaging system is then used to verify the correlation between the external signal and the tumor motion at certain intervals. As the imaging system is completely separated from the treatment machine, a main advantage of the

stereoscopic imaging system is, that it can be installed in addition to an already existing linear accelerator, to enable the user to use image guidance without installing new therapy equipment.

2.3. 3D imaging systems

2.3.1. CT on rails

One way to obtain 3-dimensional high quality images of the patient in treatment position is to install a standard computed tomography (CT) scanner in the treatment room [39]. The CT gantry is installed on rails to replace the couch movement by gantry movement, the treatment couch is rotated so that the CT can be acquired with the patient already positioned on the treatment table. The image quality in such a system is very high, as a conventional CT scanner is used. Due to the high soft tissue contrast, repositioning based on the tumor position to compensate for setup errors or interfractional motion is possible. The disadvantages of this method are the need to rotate the table which increases not only the total treatment time but also the time between imaging and treatment, which increases the chance for intrafractional motion. In addition a full CT scanner has to be placed within treatment room, which in addition to the cost of the machine itself, requires a certain size of the radiation bunker.

2.3.2. MV Fan Beam CT

The Tomotherapy system, is a treatment system, which uses a rotating MV treatment beam source to apply the treatment dose in a slice wise fashion. Due to the similar beam arrangement to a standard CT scanner, it is also possible to acquire a helical CT using the MV beam. The advantage of this method is the small extension of the imaging beam and the detector in the cranio-caudal direction (fan beam), which leads to a lower number of scattered photons registered in the detector. For the image acquisition, a reduced energy of 3.5 MV is employed instead of using the therapeutic beam. Due to the fan beam geometry, a high image quality can be achieved despite the use of an MV-beam for imaging [40].

2.3.3. Linac integrated MV- and kV-imaging

The last major group of systems for imaging in treatment position is the group of linac integrated imaging. These systems offer a kV imaging system in addition to the MV treatment beam. Even though this group is listed under the 3-dimensional imaging devices, it is also possible to acquire 2-dimensional projection images. Even though 3-dimensional imaging is also possible using the MeV treatment beam, this causes a much higher dose to the patient than using a separate imaging beam [40]. Figures 2.1 and 2.4 show linac integrated imaging solutions from the three major vendors: Elekta Synergy (Elekta Oncology Systems Ltd., Crawley, UK), Varian Trilogy (Varian Medical Systems Inc., Palo Alto, CA, USA) and Siemens ARTISTE (Oncology Care Systems, Siemens Medical Solutions, Concord, CA, USA). There is one major difference between the vendors: In the systems produced by Elekta and Varian, the imaging beam is perpendicular to the treatment beam, while the Siemens system, which is not yet commercially available, uses a so called inline geometry, where the X-ray tube is mounted opposite to the treatment head. The inline geometry has the advantage that motion perpendicular to the beam direction, which is the type of motion deciding whether the therapy beam hits the tumor or not, can be observed in 2D-projection images over the whole treatment fraction [41]. In all of these systems, the projection images are acquired with a flat panel detector and therefore digital images. The main feature which both geometries of the different linac integrated imaging systems offer is the 3D-imaging option: the cone beam

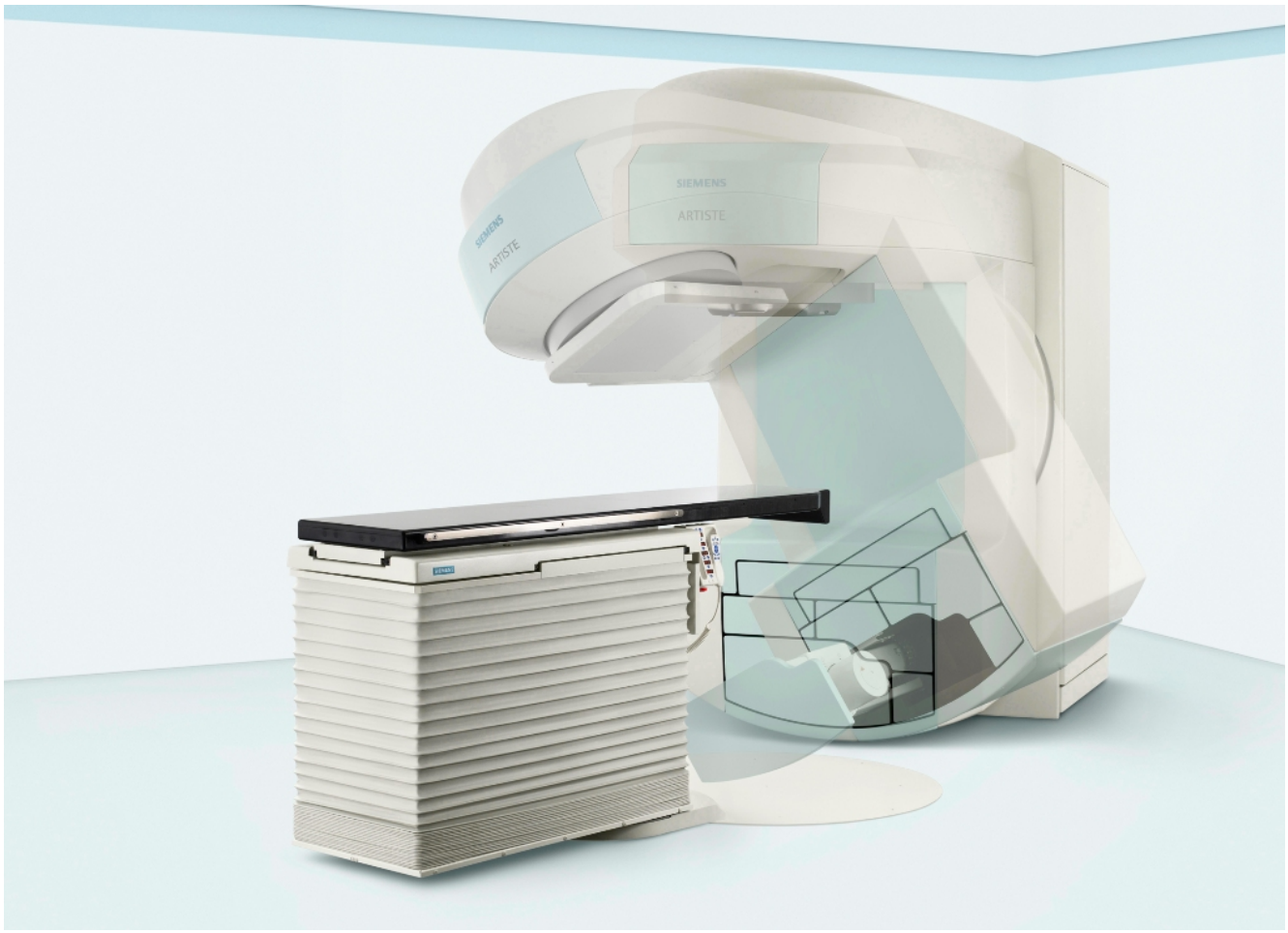

Figure 2.4.: *Linac integrated IGRT solution by Siemens with inline kV imaging system: Siemens ARTISTE^{TM} (Illustration: Press image [42]) (not yet commercially available). An X-ray tube is mounted on the linac gantry opposite to the treatment head, the flat panel detector is placed directly below the treatment head, so that the treatment beam traverses the detector. With implanted markers, the tumor motion perpendicular to the treatment beam direction can be monitored using this setup.*

computed tomography (CBCT). The main difference between a standard CT scan and a CBCT scan is that the imaging beam is not a fan beam but a cone beam so that the whole volume can be imaged in one rotation of the source and detector around the patient compared to the helical acquisition of single slices as in a diagnostic CT. Due to the more challenging scatter situation the contrast in standard CT images is superior to CBCT images, but the soft tissue contrast in CBCT images is sufficient to correct the patient position based on the tumor position without using implanted markers [40]. The acquisition of such a 3D-patient image takes several 10s of seconds, in addition to the time for the computer based comparison between the planning CT and the CBCT for setup correction. For the image acquisition, the linac gantry has to rotate around the patient, so that the 3D-imaging option cannot be used to monitor intrafractional motion but only to detect interfractional errors in the position of the tumor and organs at risk. Different acquisition patterns can be used to acquire a 3D-CBCT. For the reconstruction, it is sufficient to acquire projection images over an angle of app. 200°, depending on the opening angle of the imaging beam. It is also possible to use a full 360°-rotation of the linac gantry. In both cases, the size of the imaging photon beam and therefore the imaged volume is limited by the size of the centered detector and the distances between source, isocenter and detector. To increase the size of the imaged volume, it is also possible to shift the detector laterally, in this case it is always necessary to acquire projection images at 360°.

2.4. Reported imaging doses

All imaging methods described above use ionizing radiation for the image acquisition and therefore apply additional dose to a radiotherapy patient, where the doses to organs at risk due to the therapy are often already close to the tolerance dose. The amount of dose due to imaging highly depends firstly on the chosen method, e.g. single acquisition of a 2D-projection image causes less dose than a full 3D-scan of the patient, secondly on the beam setting like the photon energy, beam intensity, SSD and imaging field size. For a chosen beam energy, mostly the trade off is between a lower image quality and a higher dose. Generally, imaging with a keV photon beam yields better image

Table 2.1.: *Organ absorbed doses and effective doses from CBCT*

	Mean absorbed dose per scan (cGy)		
Tissue/organ	Head scan	Chest scan	Pelvis scan
Gonads (ovary)	0.02 ± 0.008	0.06 ± 0.011	3.75 ± 0.309
Bone marrow (whole body)	0.8 ± 2.91	3.04 ± 3.23	2.03 ± 2.061
Bone marrow (irradiated site)	5.89 ± 0.78	6.89 ± 0.46	4.22 ± 0.33
Spinal cord	4.08 ± 3.62	3.58 ± 3.23	0.11 ± 0.064
Colon	0.05 ± 0.018	0.35 ± 0.067	5.43 ± 0.18
Lung	0.57 ± 0.31	5.34 ± 1.77	0.08 ± 0.024
Stomach	0.07 ± 0.02	4.37 ± 1.61	0.59 ± 0.124
Bladder	0.02 ± 0.006	0.07 ± 0.002	5.29 ± 0.819
Rectum	0.02 ± 0.006	0.05 ± 0.008	3.99 ± 0.274
Breast	0.21 ± 0.048	4.69 ± 0.175	0.12 ± 0.035
Liver	0.07 ± 0.017	3.87 ± 1.76	0.63 ± 0.139
Esophagus	3.81 ± 4.43	3.59 ± 2.57	0.08 ± 0.04
Thyroid	11.08 ± 1.19	0.79 ± 0.07	0.04 ± 0.008
Skin (whole body)	0.92 ± 3.27	2.77 ± 3.1	2.59 ± 2.67
Skin (irradiated site)	6.66 ± 1.19	6.44 ± 0.95	5.43 ± 1.37
Bone surface	0.8 ± 2.91	3.04 ± 3.23	2.03 ± 2.061

Organ absorbed doses from cone beam computed tomography using standard mode for the different treatment sites of a Varian OBI (Varian Medical Systems, Inc., Palo Alto, CA) measured in a female anthropomorphic phantom (the RANDO phantom, The Phanthom Laboratory, Salem, NY) with thermoluminescent dosimeters as measured by Kan et al. [11].

quality at a lower dose compared to MeV imaging [40]. The use of a fan beam CT-geometries yields a better image quality than cone beam CT methods at the same dose.
Reported doses for single projection images are 3-10cGy for imaging with the therapy beam, compared to 0.1-0.3cGy for imaging with a linac mounted X-ray tube [43]. Stereoscopic imaging as well as perpendicular projections requires the acquisition of two projection images, but the dose is applied from different directions, so that the dose cannot simply be doubled. The dose for continuous monitoring of motion during the treatment, e.g. with stereoscopic imaging, highly depends on the number of acquired projection images, which in turn depends on the treatment time and the imaging frequency. While a setup correction at the beginning of a fraction requires only two projection images with a relatively low dose, monitoring intrafractional motion on frequent projections can add up to a significant dose due to imaging. As the orientation of the imaging beam is fixed, especially the dose in organs close to the skin or the skin itself where the beam enters the patient can be significantly increased. The "Report of the AAPM Task Group 75" on "The management of imaging dose during image-guided radiotherapy" states that: "By way of comparison, an IGRT treatment involving a 4D planning CT, 5 min of pretreatment fluoroscopy to assess tumor motion, followed by thirty fractions of fluoroscopically guided radiation therapy

Table 2.2.: *Threshold skin entrance doses for different skin injuries*

Single-Dose Effect	Threshold [Gy] (single irradiation)	Onset
Early transient erythema	2	Hours
Main erythema	6	App. 10 days
Temporary epilation	3	App. 3 wks
Permanent epilation	7	App. 3 wks
Dermal atrophy (1st phase)	10	Greater than 14 wks
Dermal atrophy (2nd phase)	10	Greater than 1 yr
Induration (invasive fibrosis)	10	No estim. available
Telangiectasia	10	Greater than 1 yr
Skin cancer	Not known	Greater than 5 yrs

Threshold skin entrance doses for different skin injuries for single irradiation as reported in [44] (selected injuries with threshold doses below 10Gy).

(2 min per fraction), ending with a follow-up CT can result in a total skin dose exceeding 1500 mGy."
Even though 3D-imaging is usually only employed once per fraction, the number of projection images for the reconstruction one CBCT varies between 100 and 800 depending on the rotation angle and the stepsize. Therefore the dose is much higher than for setup correction with 2D-imaging. Again the use of the keV-photon beam decreases the dose compared to MeV imaging, while offering a superior image quality [40]. The dose applied during a Cone-beam-CT acquisition with a keV-photon beam has been measured or simulated in many studies [10, 11, 12, 13, 14, 15, 16, 17, 18]. Many studies employ water phantoms for their measurement or simulate the dose distribution using Monte Carlo techniques, but measured data for anthropomorphic phantoms is also available. The dose values for the different organs of course depend on the treatment site, but also on the protocol used for the imaging procedure. Predefined protocols for clinical use are available for the Varian and the Elekta machines including settings for the field size, the photon energy, the tube current and irradiation time. It has been shown, that for a CBCT acquisition using the standard protocols for the X-ray Volumetric Imager XVI® of the Elekta Synergy (Elekta Oncology Systems, Norcross, GA) and On-Board Imager OBI® of the Varian Trilogy (Varian Medical Systems,Palo Alto, CA), the organ doses tend to be lower for the Elekta machine [12]. Organ doses can also be reduced using a low dose protocol, which in turn reduces the image quality [11, 45].
Table 2.1 shows selected organ doses from CBCT using standard mode for the different treatment sites of a Varian OBI (Varian Medical Systems, Inc., Palo Alto, CA) measured in a RANDO-phantom (The Phantom Laboratory, Salem, NY) with thermoluminescent dosimeters from a study by Kan et al.[11]. The dose distribution of course highly depends on the treatment site, the organ doses for the typical organs at risk for the respective sites all exceed 3.5cGy. Considering a fractionated treatment with daily image guidance, this number has to be multiplied by the number of fractions. E.g. for 30 fractions this would result (as the most extreme case) in a dose of 3,32Gy in the thyroid, or 1.8Gy in the skin at the irradiated site. This dose has to be added to the dose received due to the radiation treatment, which is often very close to the tolerance doses by itself. To give an example on the effect of the dose, Table 2.2 summarizes threshold skin entrance doses for different skin injuries as reported in [44], which shows, that the dose due to imaging by itself is already close to the threshold dose e.g. for early transient erythema or temporary epilation. The total dose as calculated above provides a rough estimation on the effect of the additional dose due to imaging, with the restriction that the threshold doses are given for a single irradiation only, the expected effect of a fractionated dose deposition (as by daily image guidance) is lower than for a single irradiation.

3. Basics

This chapter summarizes the basic physical principles underlying this work and gives a short introduction to MeV pencil beam dose calculation. In the first part, the most important basic terms and definitions are discussed. The coordinate systems used in this work are presented in the second part. To point out the differences between the photon beam energies used for imaging and those for external beam radiotherapy, the next section comprehends a review on the principles underlying the photon production and the dose deposition. Finally the pencil beam dose calculation algorithm in water for therapeutic MV photon beams, that forms the basis of this work, is described.

3.1. Basic Terms and Definitions

Absorbed Dose The "absorbed dose" (also referred to as "radiation dose" or just "dose") is one of the key measures in radiation therapy. It quantifies the average energy $\bar{\varepsilon}$ deposited in a certain mass element dm [46]:

$$D_m = \frac{\bar{\varepsilon}}{dm}\,[Gy] \tag{3.1}$$

The unit for dose is called Gray (Gy), 1 Gray is equal to 1 Joule per kilogram. In radiation therapy, the distribution of the local dose values is used to predict the clinical effects, that the irradiation has on the patient. These effects can be tumor control, but also unwanted side effects in the healthy organs surrounding the tumor.

Organs at risk (OAR) In radiation therapy planning, upon creation of the irradiation plan, a number of volumes are defined based on the 3-dimensional computed tomography (CT) dataset of the patient, which is also used as the basis for the dose calculation. As it is not possible to limit the application of radiation dose in external beam therapy to the tumor volume itself, the surrounding organs, which could also be affected by the irradiation, are delimited as so called organs at risk (OARs). For the irradiation of a patient, the maximum possible applied dose to the tumor is limited by the dose deposit within the organs at risk.

Percentage Depth Dose (PDD) The Percentage Depth Dose (PDD) for a point P(0,0,d) on the central axis is defined as the ratio in percent between the dose at this point and the dose at a reference point P_{ref} for the same irradiation geometry (field size A, Source-Surface-Distance SSD):

$$PDD(P, SSD, A) = \frac{D(d, SSD, A)}{D(d_{ref}, SSD, A)} * 100[\%] \tag{3.2}$$

The dependence of the Percentage Depth Dose (PDD) on the depth is one of the quantities that can be used to characterize the properties of a photon beam. The PDD as a function of depth is obtained by measuring a dose profile along the beam axis in the center of the photon beam at a fixed Source-Surface-Distance (SSD). The dose values are then normalized to a certain reference point and converted to percentage values yielding PDDs for one SSD and one field size as a function of depth, which can be written as $PDD_{SSD,A}(d)$. In radiotherapy the reference point for the PDD normalization is often placed at a depth of 5 cm in the water phantom or at the depth of the dose maximum. For a fixed beam energy

spectrum and intensity, the PDD depends on the SSD and the fieldsize. Upon the measurement of a PDD, the setup of the water phantom is kept constant, while varying the measurement point within the phantom. Especially for small fields, where large lateral dose gradients are present, the measurement of a PDD requires a perfect alignment between the photon beam direction and the axis at which the profile is measured. Due to the energy dependence of the mass absorption coefficient, which is described in chapter 3.3.2, a PDD curve is steeper for lower photon energies than for higher photon energies.

Tissue Phantom Ratio (TPR) Similar to the PDD, the tissue phantom ratio (TPR) can be measured as a function of the depth in water. The TPR for a field size A (in the plane of the measurement point) is defined as the ratio between the dose measured at that reference point P_{ref} at one Source-Surface-Distance (SSD) and the dose measured in the same point using the reference SSD:

$$TPR(SSD, A) = \frac{D(P_{ref}, SSD, A)}{D(P_{ref}, SSD_{ref}, A)} \tag{3.3}$$

By changing the SSD while keeping a constant point of measurement, the depth in water for the reference point also changes. With a fixed distance between the reference point and the radiation source, the dependence on the SSD can be converted into a dependence only on the depth d in water: $TPR_A(d)$. For the measurement of a TPR, the measurement point is kept constant while varying the setup of the water phantom. Due to this, the measurement of a TPR for small fields is easier than the measurement of a PDD.

Output Factor (OF) The output factor (OF) for a reference SSD is defined as the ratio between the dose at a reference point P_{ref} for a given field size A and SSD and the same irradiation for a reference field size A_{ref}(e.g. 10cm x 10cm) at the same SSD:

$$OF(A) = \frac{D(P_{ref}, SSD_{ref}, A)}{D(P_{ref}, SSD_{ref}, A_{ref})} \tag{3.4}$$

For MeV photon beams, variations in the output factor are mainly due to variations in the field size, the dependence on the SSD is relatively low [46]. To account for a possible dependence of the output factor on the SSD for keV photon beams, in this work a modified output factor $OF_r(SSD)$ is used, which is calculated using the dose value for the reference field size for only one reference SSD as the normalization dose for all other SSDs, so that the inverse square law dependence on the SSD is also reflected in the output factor values.

3.2. Coordinate systems

3.2.1. IEC coordinate system

The main coordinate system is defined according to the International Electrotechnical Commission (IEC) standard 61217 [47]. The orientation of this right-handed cartesian coordinate system is illustrated in Figure 3.1. The z-axis is vertical, pointing to the ceiling, the x-y-plane therefore a horizontal plane. The y-axis is the rotation axis of the gantry of the linear accelerator, pointing towards the accelerator itself. Upon gantry rotation, all central rays of the photon field intersect in one point, the so called isocenter, which is also the origin of the coordinate system. The isocenter also lies on the rotation axis of the treatment table. This definition of the coordinate system implies the following determination of the gantry angle: The rotation angle of the gantry, which is the angle between the central ray of the treatment beam and the z-axis of the coordinate system, is equal to the inclination angle θ in spherical coordinates:

$$\alpha_{gantry,IEC} = \theta_{spherical,IEC} \tag{3.5}$$

To allow for a better comparability for different irradiation geometries despite the dependence of the photon field size on the distance from the radiation source, the field size is often given as the field size in the isocenter plane, which is a plane perpendicular to the central ray and contains the isocenter.

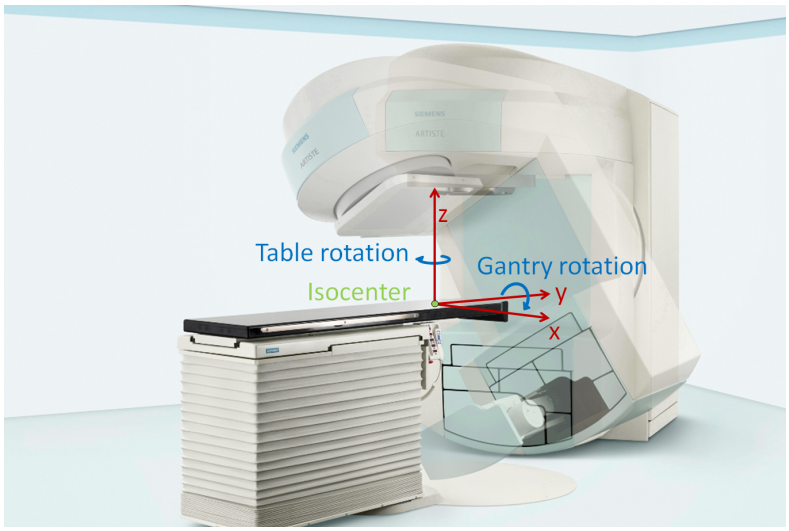

Figure 3.1.: *IEC coordinate system. This coordinate system has a fixed orientation in the treatment room as illustrated. The origin is placed in the isocenter of the linear accelerator. The treatment table rotates around the vertical z-axis, which points towards the ceiling, the linac gantry rotates around the horizontal y-axis, which points towards the gantry. The horizontal x-axis completes the right-handed cartesian coordinate system. (Figure adapted from Siemens Press image [42]*

3.2.2. Phantom coordinate system

In this work, the coordinate system for phantoms is defined independent of the IEC coordinate system. A right-handed cartesian coordinate system was chosen, its orientation is determined by the orientation of the X-ray tube used for irradiation. The x-axis is defined parallel to the axis of the X-ray tube, whose design is explained in further detail in chapter 3.3.1. The orientation of the x-axis is defined as opposing to the electron beam direction in the X-ray tube. The z-axis is also called the central and is the axis of photon beam propagation, it points away from the X-ray tube. As depicted in Figure 3.2, the origin is placed at the surface of the phantom in the center of the photon beam. The depth in water (or other phantom material) is described by the z-value.

3.2.3. Patient coordinate system

The right-handed cartesian patient coordinate system is depicted in Figure 3.3 on the right. The z-axis is parallel to the cranio-caudal direction pointing from the feet towards the head of the patient. The x-axis is antiparallel to the patients left-right (LR) direction, the y-axis parallel to the anterior-posterior (AP) direction. The position of the origin is not predefined, e.g. it can be placed at the corner of the CT-dataset or in the center of the tumor volume and planned to coincide with the isocenter of the treatment room. The patient coordinate system is the coordinate system, which is used by the planning system used in this work. If the patient lies on the treatment table on his back with a table angle of 0° and the origin of the patient system is placed in the isocenter, the x-axis in the patient coordinate system

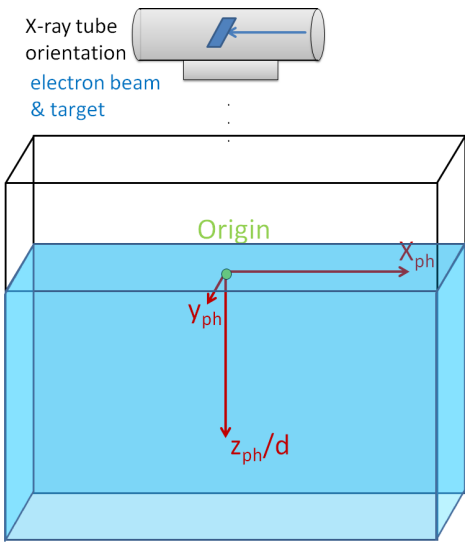

Figure 3.2.: *Phantom coordinate systems. The orientation of the coordinate system is defined depending on the orientation of the X-ray tube. The x-axis is parallel to the tube axis, the z-axis is vertical, pointing from the radiation source into the phantom. The y-axis completes the right-handed cartesian coordinate system, where the origin is in the center of the photon beam at the surface of the phantom.*

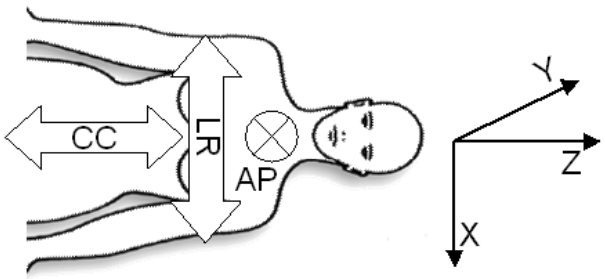

Figure 3.3.: *Patient coordinate system. (Figure from [48]) The x-axis is parallel to the left-right (LR) direction, pointing from the right of the patient to the left, the y-axis in the anterior-posterior (AP) direction, the z-axis is parallel to the cranio-caudal direction. This coordinate system is also used in the planning software.*

coincides with the x-axis in the IEC system. The z-axis in the patient coordinate system coincides with the IEC-y-axis. The patient's y-axis is antiparallel to the IEC-z-axis. In a more general case, where the isocenter (origin) of the IEC system lies at the coordinates (x_0, y_0, z_0) in the patient coordinate system, this results in the following coordinate transformation from the patient system to the IEC system:

$$\vec{x}_{IEC} \begin{pmatrix} x \\ y \\ z \end{pmatrix} = \begin{pmatrix} 1 & 0 & 0 & -x_0 \\ 0 & 0 & 1 & -z_0 \\ 0 & -1 & 0 & y_0 \end{pmatrix} \begin{pmatrix} x_{pat} \\ y_{pat} \\ z_{pat} \\ 1 \end{pmatrix} \tag{3.6}$$

3.3. Production, Spectra and Dose Deposition - keV vs. MeV Photons

3.3.1. Photon Production

This section describes the setup for photon production for imaging and therapeutic applications and gives a short characterization of the photon beams. As the properties of the photon beams, which are of concern in this work, do not result from the setup for the acceleration of the electrons, the main focus of this section lies on the positioning and the geometry of the target, where the photon production takes place.

X-ray tube

Typically photons in the keV-energy range are produced in an X-ray tube. Electrons are emitted from the cathode into the tube vacuum. Due to the high voltage between the emitting cathode and the target anode (app. 30 keV - 200 keV in imaging applications) the electrons are accelerated towards the target. The electron beam hits the target, where the electrons are decelerated causing the emission of bremsstrahlung photons and characteristic X-rays. Most of the photons are absorbed again within the target, which means that only a small fraction of the produced photons leaves the target. About 99% of the incoming energy is released as heat, only app. 1% is emitted as photons [49]. To enhance the cooling of the target, most X-ray tubes use a rotating anode, so that the electron beam does not hit the target in the same point at all times.
The left part of Figure 3.4 shows the geometry of a typical rotating anode X-ray tube. For a tube orientation, where the photon beam is emitted in the vertical direction, the electron beam hits the target app. horizontally. To decrease the spot size for the photon production in the direction of the photon beam, while keeping the same size of the electron beam, the target surface is tilted. The tilt angle depends on the intended application for the X-ray tube. While the spot size decreases, if the angle between target surface and electron beam increases towards 90°, the possible opening angle of the beam at the target side is limited by the same angle. The photons leave the target at the same surface as the electrons enter it. The typical target material is tungsten, but other materials with a high atomic number (e.g.

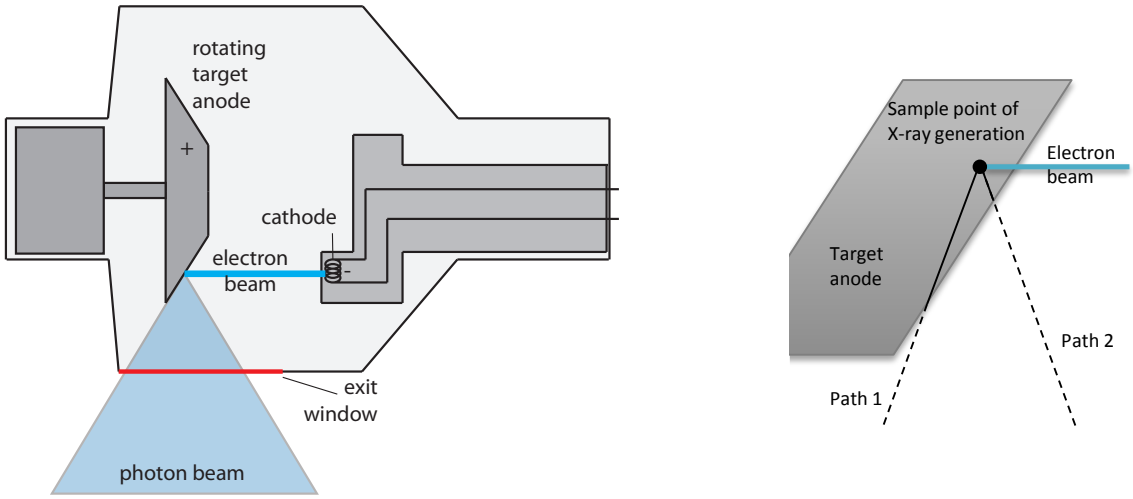

Figure 3.4.: *Left: Rotating anode X-ray tube setup. Electrons are emitted from the cathode and accelerated towards the anode target. Bremsstrahlung photons and characteristic X-rays are emitted from the target. Right: Heel Effect. Bremsstrahlung photons are genetrated in a sample point within the target. Photons travelling along path 1 have to travel a much longer distance within the target material than on path 2 (solid black lines). Due to absorption in the target material, the intensity of the photon beam is higher at the cathode side of the beam (path 2) than on the anode side (path 1).*

molybdenum or rhenium) are also used [49]. Nowadays most if the anode used are compound anodes consisting of compounds of the latter materials. The photon beam leaves the tube vacuum through a beryllium window, which has a very low absorption coefficient. Figure 3.5 shows cross sections of a real X-ray tube from a cone beam CT dataset acquired using the treatment beam of a linear accelerator.
A direct consequence of the tube geometry is the so called Heel Effect, which is illustrated in the right part of Figure 3.4. The photons from a sample interaction point are emitted at different angles within the target. Depending on the emission angle, the photons have to travel through a different amount of material before leaving the target. Due to the absorption in the target material, the intensity of the photon beam is higher at the cathode side of the beam than on the anode side [50]. As the absorption of low energy photons is higher than for higher energies, the absorption in the target also leads to a slight lateral variation of the photon spectrum.

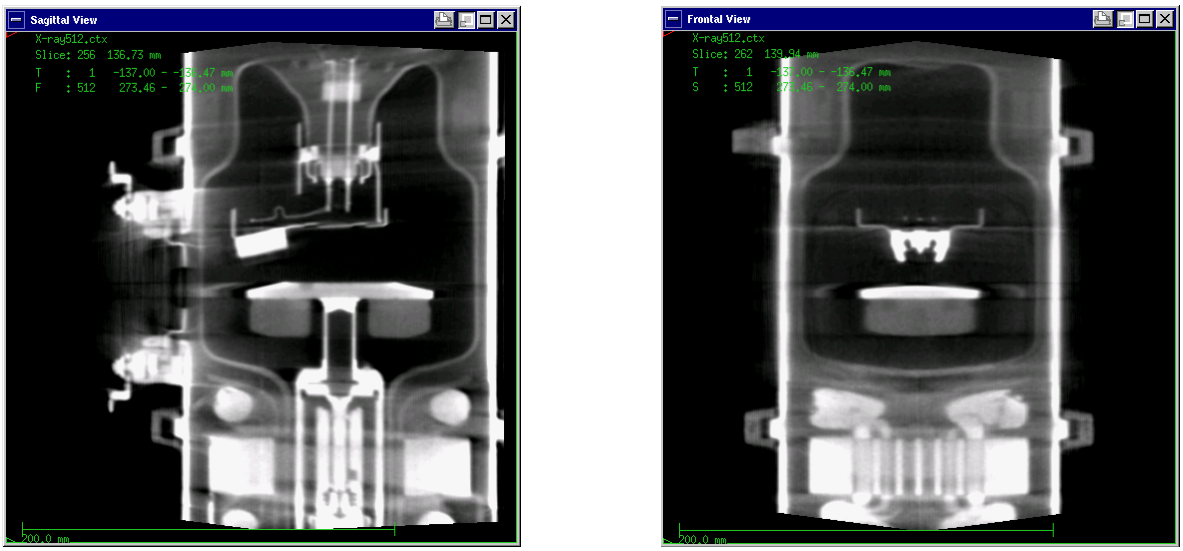

Figure 3.5.: *Sagittal and frontal cross sections of an X-ray tube from a MV cone beam CT without collimator. In the sagittal view, the arrangement of the cathode and anode target is visible. In this view, the photon beam exits the tube towards the left. The frontal view offers a more detailed view on the cathode geometry.*

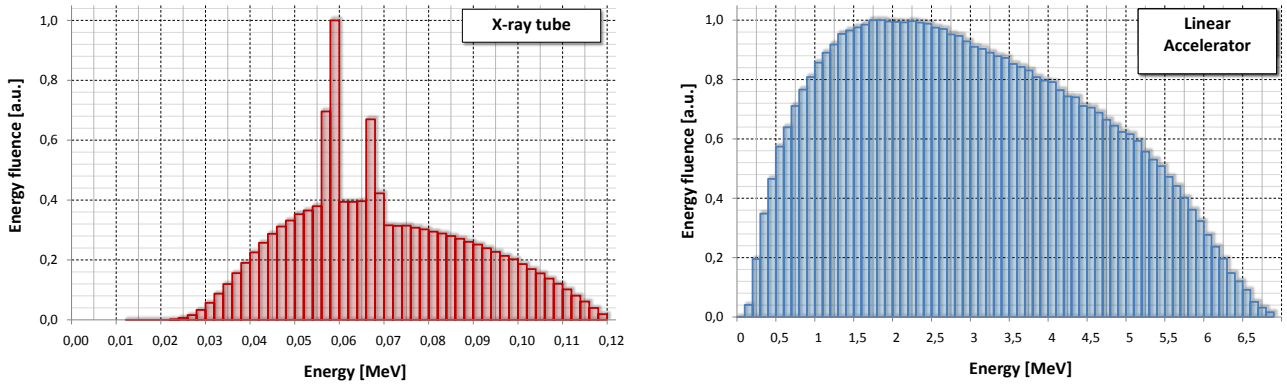

Figure 3.6.: *Left: Simulated X-ray tube spectrum for an accelerating voltage of 121 kV. Right: Photon spectrum of the central area (radius 3cm at a distance of 100cm from the source) of a 6MV photon beam from a Siemens MX2 linear accelerator obtained from a Monte Carlo simulation of the treatment head by Kim et al. (relative photon fluence extracted from [51]).*

The spectrum of the photon beam emitted from an X-ray tube of course depends on the tube voltage but also on the target material. To further influence the spectrum (mainly to reduce the low energy fraction of the beam), filters are inserted into the photon beam. In medical applications a reduction of the low energy fraction is desirable, as low energy photons are absorbed in the skin of the patient, leading to a higher skin dose with no improve in image contrast. Common filter materials are copper or aluminum. The thicknesses of the filters depend on the material and the desired effect and range from submillimeter to several millimeters. The filters also reduce the lateral variation in the spectrum of the photon beam, which was described before.
On the left side Figure 3.6 shows the simulated spectrum of an X-ray tube with a tungsten target, a 2.5mm aluminum filter and a 0.2 mm copper filter (simulated with BEAMnrc). The accelerating voltage in the tube is 121 kV. The K-alpha and K-beta lines for tungsten occur at wavelength of app. 0,021nm and 0,018nm [50]. These lines are clearly discernible in the spectrum at the corresponding energies of app. 59 keV and 69 keV. Due to the filters virtually no photons below an energy of 20 keV leave the X-ray tube, the maximum photon energy equals the maximum electron energy. The average energy is app. 63 keV.

Linear Accelerator

For therapeutic applications electrons are accelerated to an energy of several MeV, typical energies are in the range of 6 MeV or 15 MeV. Electron energies in this range cannot be reached with a simple X-ray tube arrangement, in this case the electrons are accelerated in a waveguide setup. Similar to the keV photons in the X-ray tube, the MeV electrons are then directed to a target where the electrons are decelerated and Bremsstrahlung photons are emitted. Due to the high energy of the electrons, the Bremsstrahlung photons are mainly emitted in forward direction. This leads to a different setup geometry for the target than in the X-ray tube, which is shown in Figure 3.7. The photon beam leaves the target opposite to the electron beam, both beams are directed along the same axis. This setup is symmetric to the beam axis so that the uncollimated beam also shows a rotational symmetry. The intensity of the photon beam behind the target is higher in the middle than on the edges, due to the forward direction of the Bremsstrahlung photons. If needed, the intensity profile of the roughly collimated photon beam can then be flattened in a flattening filter and further collimated.

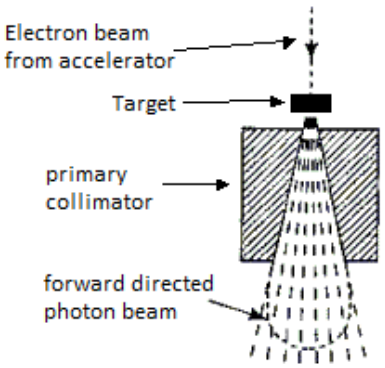

Figure 3.7.: *Photon production in a medical linear accelerator. (Figure shows a detail of a figure from [46])*

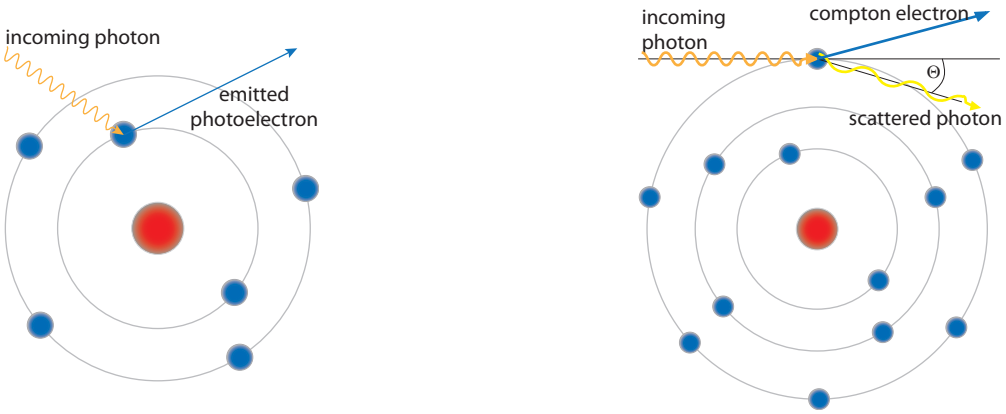

Figure 3.8.: *Left: Photoelectric effect. The incoming photon transfers its energy to an inner shell electron which is then is ejected. Right: Compton effect. The incoming photon is scattered transferring a fraction of its energy to an electron.*

The right side of Figure 3.6 shows a photon spectrum of the central area (radius 3cm at a distance of 100cm from the source) of a photon beam with produced with a electron beam with an average energy of 6.7MeV for a Siemens MX2 linear accelerator obtained from a Monte Carlo simulation of the treatment head (relative photon fluence extracted from [51]). The maximum of the energy fluence is at app. 2 MeV, according to [51], the average energy of the photons is app. 1.93 MeV. The energy fraction of low energy photons (below 300 keV) is app. 0.5%, even for 500 keV it does not exceed 2.5%.

3.3.2. Photon Dose Deposition

This section describes the processes leading to the dose deposition within the patient. As before, a main focus lies on the differences between photon beams used for imaging and radiation therapy.

Photoelectric Effect

In the photoelectric effect, the incoming photon is completely absorbed, transferring its energy to a bound electron mainly from one of the inner shells [52] (see also Fig. 3.8 on the left). The so called photoelectron is ejected with the kinetic Energy $E_{kin} = E_{photon} - E_B$, where E_{photon} is the energy of the incoming photon and E_B is the binding energy of the electron. The photoelectron is also called secondary electron (compared to the primary photon), it deposits its kinetic energy in the absorber material (see also chapter 3.3.2). The photoelectric effect shows a high dependency on the atomic number of the absorber material and the inverse of the photon energy. The dependence of the cross section for the photoeffect on Z and E can be summarized to

$$\begin{aligned} \sigma_{photo} &\propto \frac{Z^n}{E^3} \qquad for\ E \ll 511keV \\ \sigma_{photo} &\propto \frac{Z^n}{E} \qquad for\ E \gg 511keV \end{aligned} \tag{3.7}$$

with $n \approx 3.6$ for low Z materials and $n = 3$ for high atomic numbers (formula derived from [53]). Due to the high dependency on the photon energy, the photoelectric effect plays an important role in the dose deposition of photons in the keV energy range while it is almost negligible in the MeV energy range.

Compton Scattering

The Compton effect is illustrated on the right side of Figure 3.8. During this process the incoming photon transfers a part of its energy to a bound electron of one of the outer shells [52]. A scattered photon is emitted carrying the energy $E'_\gamma = E_\gamma - E_{kin}$, where E_γ is the energy of the incoming photon and E_{kin} is the kinetic energy of the emitted electron. Kinematic considerations result in a formula for the energy of

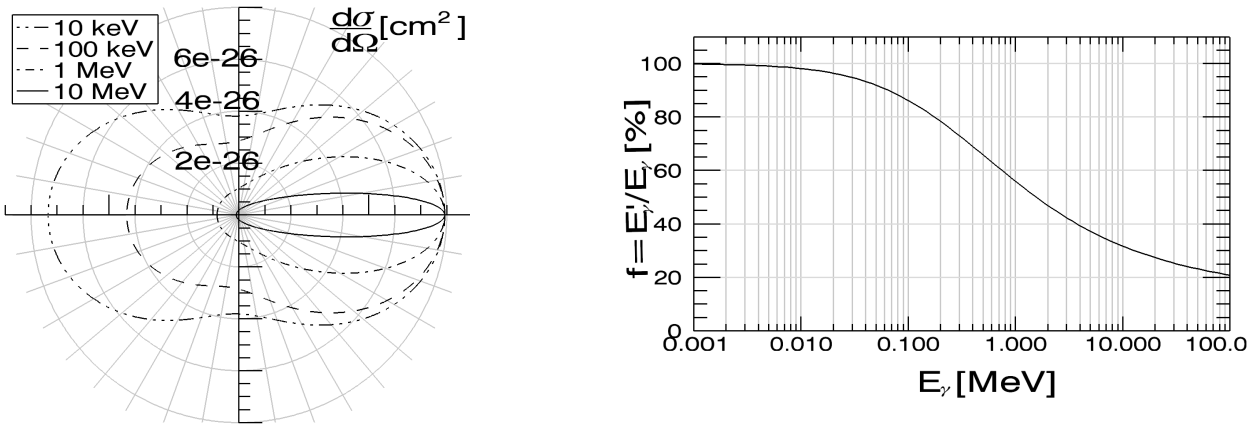

Figure 3.9.: *Compton Effect. Left: Polar plot of the differential cross section of the Compton effect and its dependence on the energy of the incoming photon. The photon enters the geometry along the negative x-axis, the Compton effect takes place at the zero point. Right: Energy dependence of the energy fraction* $\frac{E'_\gamma}{E_\gamma}$ *between the incoming and the scattered photon.*

the scattered photon as a function of the scattering angle θ:

$$E'_\gamma = E_\gamma \frac{1}{1+\alpha(1-cos\theta)} \quad with \quad \alpha = \frac{E_\gamma}{m_e c^2} \tag{3.8}$$

where m_e is the electron radius. The probability for the different scatter angles θ is given by the differential cross section according to Klein and Nishina:

$$\frac{d\sigma_{Compton}}{d\Omega} = \frac{r_e^2}{2}\left(\left(\frac{E'_\gamma}{E_\gamma}\right)^2 + \frac{1}{\frac{E'_\gamma}{E_\gamma}} - sin^2\theta\right), \tag{3.9}$$

where r_e is the classical electron radius [54]. The differential cross section for a number of energies is plotted in Figure 3.9 on the left side. In this polar plot the incoming photon enters the geometry along the x-axis, the Compton effect takes place in the zero point. Scatter in the direction of the positive x-axis therefore equals $\theta = 0°$, while the negative x-axis equals $\theta = 180°$. The plot indicates that for energies in the therapeutic range (larger than 1 MeV) most of the scattered photons are directed in the forward direction while for the imaging range (10keV-150keV) the backscatter situation becomes more likely. For very low energies (below 1keV) the differential cross section is almost symmetric to the y-axis. Using the differential cross section and the dependence of E'_γ on θ one can calculate the average energy fraction between the incoming and the outgoing photon. The dependency of this energy fraction $\frac{E'_\gamma}{E_\gamma}$ is plotted on the right side of Figure 3.9. As the plot shows, the energy fraction decreases rapidly with increasing energy. While the average energy of the scattered photon in the therapeutic energy range is just about 40-60% of the energy of the incoming photon, this fraction is about 80-100% for the imaging energy range with a much higher chance for high scatter angles.
The total cross section for the Compton effect can be calculated by integration of the differential cross section. It shows no dependency on the atomic number Z of the surrounding medium, the dependence of the total absorption coefficient can therefore be reduced to a linear dependency on the electron density (see also the section "Absorption Coefficient", which is part of this chapter).

Pair Production

Pair production can only occur for photon energies $E_\gamma > 1,022 MeV$, which is equal to two times the rest mass of an electron. In the field of a nucleus, the photon can spontaneously change into an electron-positron pair. The energy of the photon is partly used in this reaction, the remaining energy is split between the electron and the positron as kinetic energy $E_{kin,total} = E_\gamma - 2m_e c^2$. As described in the

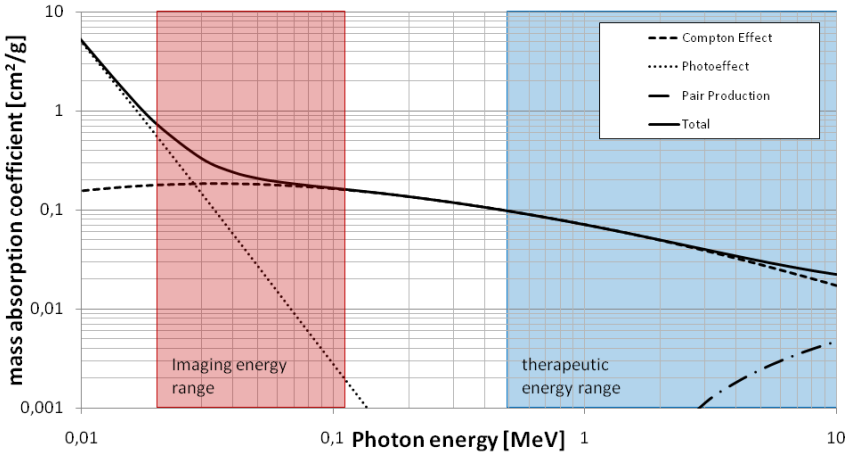

Figure 3.10.: *Mass Absorption Coefficient for Water. The mass absorption coefficients for the interaction processes sum up to the total mass absorption coefficient. While the Compton Effect is the dominant process for the therapeutic energy range, for the imaging energy range the absorption coefficient for photoeffect and Compton effect are in the same range. The pair production only plays a minor role for both 6 MV photon irradiation and imaging but becomes more important for the 15 MV therapy beam (all data for this plot extracted from the NIST XCOM: Photon Cross Sections Database [56])*

section "Secondary Electrons" the electron deposits its kinetic energy in the surrounding medium. The positron also transfers its kinetic energy to the medium and is destroyed in a collision with a random electron. Two photons with an energy of 0,511 MeV are emitted. For pair production, the mass absorption coefficient is proportional to Z. For energies higher than 1,022 MeV it increases rapidly with the photon energy [55].

Absorption Coefficient

To obtain the mass absorption coefficient $\frac{\mu}{\rho_m}(E_\gamma, Z)$ as a function of the photon energy E_γ and the atomic number Z, the cross section $\sigma(E_\gamma, Z)$ for a process has to be multiplied by the density of scattering centers $\rho_e(Z, A)$ divided by the mass density ρ:

$$\frac{\mu}{\rho_m}(E_\gamma, Z) = \sigma(E_\gamma, Z)\frac{\rho_e(Z, A)}{\rho} = \sigma(E_\gamma, Z)\frac{N_A Z}{A}, \tag{3.10}$$

where N_A is the Avogadro constant, Z the atomic number and A the atomic weight of the considered medium. The total mass absorption coefficient $\frac{\mu}{\rho}$ for a material is equal to the sum of the mass absorption coefficients for each of the different interaction processes.

$$\left(\frac{\mu}{\rho_m}\right)_{total} = \left(\frac{\mu}{\rho_m}\right)_{photo} + \left(\frac{\mu}{\rho_m}\right)_{Compton} + \left(\frac{\mu}{\rho_m}\right)_{pair} \tag{3.11}$$

Figure 3.10 shows the energy dependence of the contributions for the described interaction processes and the total mass absorption coefficient in water. As described above, the cross section and therefore the mass absorption coefficient for the photoeffect drops rapidly with increasing energy, while the contribution of the compton effect first increases slightly and then drops slowly. Pair production only takes places above 1,022 MeV. For the therapeutic energy range, the Compton effect is the predominant process, for higher energies the pair production also plays a minor role. Hence the material dependence of the total mass absorption coefficient is also dominated by the material dependency of the Compton effect. This is even the case for higher atomic numbers even though the photoeffect contribution can be higher in this case. In contrast, for the imaging energy range the mass absorption coefficients for photoeffect and Compton effect are in the same range, due to the higher contribution of the photoeffect, the mass absorption coefficient also shows a much higher dependency on the atomic number Z.

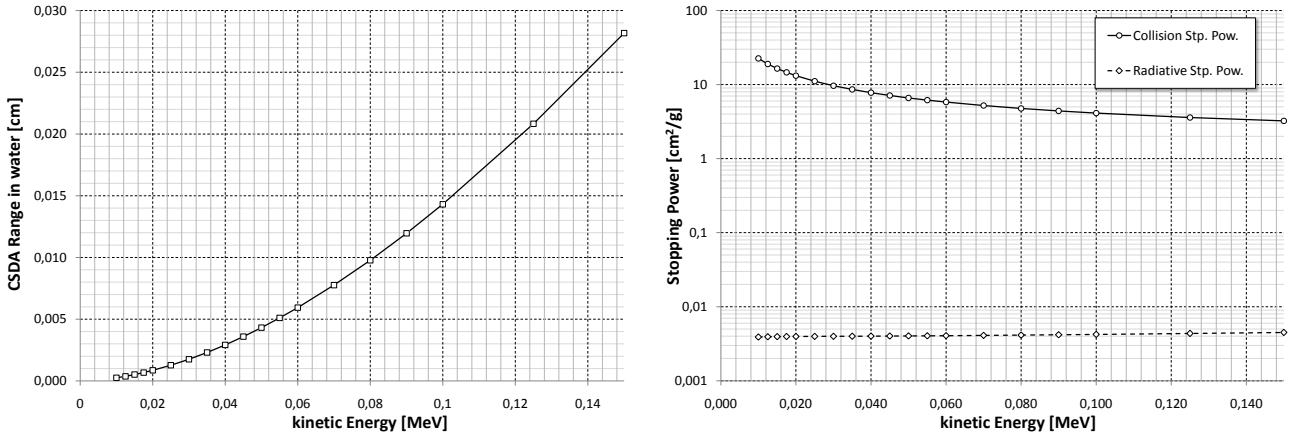

Figure 3.11.: *Left: CSDA-ranges for electrons in water below 150keV. Due to the low range of the electron, it can be assumed, that all kinetic energy of the electron is deposited locally (within the respective voxel) Right: Radiative and collision stopping power for electrons below 150keV in water. The collision stopping power is much higher that the radiative stopping power, meaning that the kinetic energy of the electron is mainly deposited in collisions, only a negligible amount of energy can be further transported through the medium as photons.(All data extracted from the NIST ESTAR: Stopping Powers and Ranges for Electrons database [57])*

Secondary Electrons

In the sections above interaction processes of photons with matter have been described mainly focusing on the basic principles and the secondary photons produced in the processes. As the secondary photons do not deposit their energy directly in the medium, but are subject to the same interaction processes as the primary photons, so far the dose deposition itself has not been discussed. In all of the above interaction processes, secondary electrons are produced, which deposit their kinetic energy in the surrounding medium. The maximum amount of kinetic energy, which can be transferred to a secondary electron, would be in a photoeffect with a photon of maximum energy. Therefore the maximum kinetic of a secondary electron is limited by the kinetic energy of the accelerated electrons for the photon production (neglecting the binding energy of the electron). The average path length of the electrons highly depends on the available kinetic energy. Using the "continuous slowing down approximation" (CSDA), which assumes a microscopically homogeneous media, and a mass density of $\rho_m = 1\frac{g}{cm^3}$, a 60 keV electron has a range in water $R_{CSDA} = 0.059mm$, while for a 2 MeV electron the normalized CSDA range is $R_{CSDA} = 9.785mm$ [57]. CSDA ranges in water for the imaging energy range are shown in Figure 3.11 on the left side. Due to the short range of the electrons at imaging energies compared to the voxel size virtually no energy is transported across voxel boundaries by the electrons, it can be assumed that all energy transferred to electrons is deposited at the point of the primary interaction. On contrast the secondary electrons with a higher kinetic energy (as can be produced by a therapeutic photon beam) transport energy for up to several centimeters in water. The deposition of the electron energy can be either due to collision or bremsstrahlung. While the energy in a collision is directly transferred to the medium, the bremsstrahlung photons could still transport the energy to other voxels. On the right side, Figure 3.11 shows the respective stopping powers for electrons in water. For the investigated energies, the collision stopping powers is more than 100 times the radiative stopping power. In combination with the CSDA-range, this means that almost all of the kinetic energy of the secondary electrons is deposited in the medium in collisions within a very short range. For the Monte Carlo Simulation of dose deposition in phantoms with voxel sizes of several millimeters, this means that the error due to the omission of the simulation of electron transport is negligible.

3.4. Pencil Beam Dose Calculation

In MeV dose calculation, two main types of analytical calculation algorithms are available, where there is usually a tradeoff between the calculation time and the resulting accuracy of the calculated doses.

The fastest type of MeV dose calculation algorithms are pencil beam algorithms, which is based on the breakdown of the photon beam into very narrow pencil beam [58]. The second type of algorithms are superposition algorithms, where point spread kernels describe the dose distribution for a given primary interaction point [58, 59]. Again a convolution method is used to derive the final dose distribution from the kernels [19], in this case the convolution is much more complex than in the pencil beam case, which leads to a much higher computational effort and higher calculation times.
As a low calculation time was desired, the aim of this work is the development of a pencil beam dose calculation algorithm for the use in a typical keV energy range for image guidance in radiotherapy. The basis of this algorithm lies in an existing pencil beam dose calculation algorithm routinely in use for the fast calculation of treatment dose. As described above, the basic idea of a pencil beam dose calculation algorithm is the breakdown of the photon field for irradiation into a high number of extremely thin beams called pencil beams. In this chapter, only the algorithm for the dose calculation in a water phantom is explained as described by Bortfeld et al.[60], the mechanism to account for inhomogeneities is described in chapter 7.2.1.
Assuming that all incoming pencil beams are parallel, the dose on the central axis for an irregular field can be calculated as:

$$D'_{irreg}(d) = \int_{-\infty}^{\infty}\int_{-\infty}^{\infty} \psi'(x,y)F(x,y)K(x,y,d)dx\,dy \tag{3.12}$$

with x, y being coordinates perpendicular to the beam direction, $\psi'(x,y)$ the energy fluence of the uncollimated photon beam, $F(x,y)$ a transmission function for beam shaping objects like the collimator, and the kernel $K(x,y,d)$[60]. As all beams are assumed to be parallel, ψ' and F do not depend on the depth d in the phantom. The kernel K(x,y,d) is the normalized contribution to the dose at a point (0,0,d) from a pencil beam at the position (x,y) or a beam element at the radius r with an infinitesimal extension:

$$K(r,d) = \frac{1}{\psi'_N(r)}\frac{\delta D'_r(d)}{\delta r} \tag{3.13}$$

with the normalization factor

$$\psi'_N(r) = \int_0^{2\pi} \psi'(r,\phi)rd\phi \tag{3.14}$$

The kernel K(x,y,d) is often called the pencil beam kernel, which is equal to the dose distribution of a pencil beam at the central axis. What is not mentioned by Bortfeld et al.[60], this is only the case if the dose contribution of a pencil beam at the central axis (0,0) to a point $R(x_r, y_r, d_r)$ at the distance $r_Q = \sqrt{x_r^2 + y_r^2}$ from the central axis equals the contribution of a pencil beam at (x_r, y_r) to a point Q $(0, 0, d_r)$ at the central axis and the same depth as point R. This condition is fulfilled if the energy spectrum of the photon beam is assumed to not depend on x and y, as by Bortfeld et al.[60]. In this case, the kernel is also laterally invariant and shows an axial symmetry. The dose at any point $P(x_p, y_p, d)$ can then be calculated as:

$$D'_{irreg}(x_p, y_p, d) = \int_{-\infty}^{\infty}\int_{-\infty}^{\infty} \psi'(x,y)F(x,y)K(x-x_p, y-y_p, d)dx\,dy \tag{3.15}$$

The axially symmetric pencil beam kernel $K(r,d)$ and the energy fluence $\psi'(x,y)$ of the unchanged photon beam can be precalculated, the transmission function $F(x,y)$ depends on the field shape so that a 2-dimensional convolution is needed for every depth in the water phantom.
To further decrease the calculation time, Bortfeld et al. suggest the so called "single value decomposition" which includes the decomposition of the pencil beam kernel into a sum of factorized terms [60]:

$$K(r,d) \approx \sum_{i=1}^{N} w_i(r)D'_i(d) \tag{3.16}$$

where $D'_i(d)$ are given functions of the depth and the weights $w_i(r)$. Considering the formula connecting the depth dose curve with the kernel, the weights $w_i(r)$ can be derived using a least square fit of measured

or simulated depth dose curves according to the following formula:

$$D'_r(d) \approx \sum_{i=1}^{N} W_i(r) D'_i(d) \tag{3.17}$$

using the same functions $D'_i(d)$ to get their respective weights $W_i(r)$. As the kernel is the derivative of the depth dose curve divided by the normalization factor $\psi'_N(r)$, the weights $w_i(r)$ can then be derived as

$$w_i(r) = \frac{1}{\psi'_N(r)} \frac{\partial W_i(r)}{\partial r} \tag{3.18}$$

Including the kernel decomposition in the dose calculation at a point P= (x_p, y_p, d), this results in the following formula [60]:

$$D'_{irreg}(x_p, y_p, d) = \sum_{i=1}^{N} W_i(r) D'_i(d) \int_{-\infty}^{\infty} \int_{-\infty}^{\infty} \psi'(x, y) F(x, y) w_i(x - x_p, y - y_p, d) dx\, dy \tag{3.19}$$

The 2-dimensional convolution now no longer depends on the depth in the phantom, to calculate the 3-dimensional dose distribution, it has to be calculated only once for each of the N weight functions. N is usually set to 3 but there are also applications where an N of 4 is used.
The cited formulas from Bortfeld et al.[60] are all based on the assumption that all pencil beams are parallel, which is not the case in a point source situation, as in most irradiation devices. Therefore measured or simulated depth dose data has to be converted to the required coordinate system removing the inverse square dependency on the distance from the source of the dose values. As the collimator of a linear accelerator as well as for X-ray tubes can only collimate the beam to rectangular fields not the circular ones needed for the kernel calculation, the equivalent square field approach is used as described by [60]. In this approach square fields are set equivalent to circular fields with the same field cross section.

4. Monte Carlo Simulation Model of the X-ray tube

To validate any doses calculated with the new pencil beam dose calculation algorithm and to estimate its accuracy, it is necessary to define a gold standard, which determines the "true" dose value. An ideal gold standard would offer the possibility to derive a continuous distribution of dose values in water as well as in inhomogeneities for all investigated geometries (including patient data if necessary), reproducing the "real" dose values with a high accuracy. For dose calculation in therapy planning, different gold standards are common to use including measurements (e.g. film measurements, thermoluminescent dosimeters (TLDs) or ion chambers), already existing dose calculation algorithms with a known high accuracy but also Monte Carlo simulations are often used [16, 61, 17, 62]. The main advantage of Monte Carlo (MC) simulations vs. measurements is that dose values can be obtained for the whole geometry (phantom or patient) compared to a limited number of measurement points. For instance for patients, a dose measurement is only possible at the surface or in existing cavities (e.g. at the skin or inside orifices), which is why Monte Carlo simulations were chosen as the gold standard in this work. For this work, two programs from the EGSnrc coding system were chosen for the Monte-Carlo simulation: BEAMnrc and DOSXYZnrc. Due to the different functionality of the programs, the simulation of the dose distribution was split into two major parts. The photon generation, the filters and the collimation of the X-ray tube were simulated with BEAMnrc, the dose deposition in the different phantom or patient geometries were simulated using DOSXYZnrc. All simulation settings described in the text are summarized in Appendix A.

4.1. X-ray tube simulation

4.1.1. BEAMnrc

As a part of the EGSnrc coding system, BEAMnrc is a widely used tool for the Monte-Carlo simulation of medical radiation sources [62, 63, 64, 65, 66, 67]. It enables the user to create user codes for user defined simulation geometries, while offering the photon and electron transport algorithms and parameters of the EGSnrc system. A graphical user interface (GUI) for BEAMnrc is available, which allows for an easy definition of the simulation geometry [68]. To create a custom geometry, the user can choose from several predefined components, e.g. slabs or jaws, which can be arranged along the z-axis of the simulation geometry. The composition of geometrical components is then codified in an executable file. In the next step the details for each component and the simulation source can be defined in the GUI. The general parameters for the simulation include for instance the number of particles used in the simulation, the energies at which the simulation of electron or photon transport is stopped, a particle source for the simulation or the number and positioning of so called scoring planes. The transport parameters (e.g. charge, weight, location, energy, direction) of all particles crossing the scoring plane are saved to a phase space file, which can be used as a particle source for further simulations. To increase the efficiency of the simulation for the photon beam generation, a directional bremsstrahlungs splitting option can be used to determine where the number of photons emitted in a bremsstrahlung process in directions specified by the user is increased [69]. Geometrical details (like exact measurements or materials) of the geometry components can also be entered in the graphical user interface, which creates an input file for

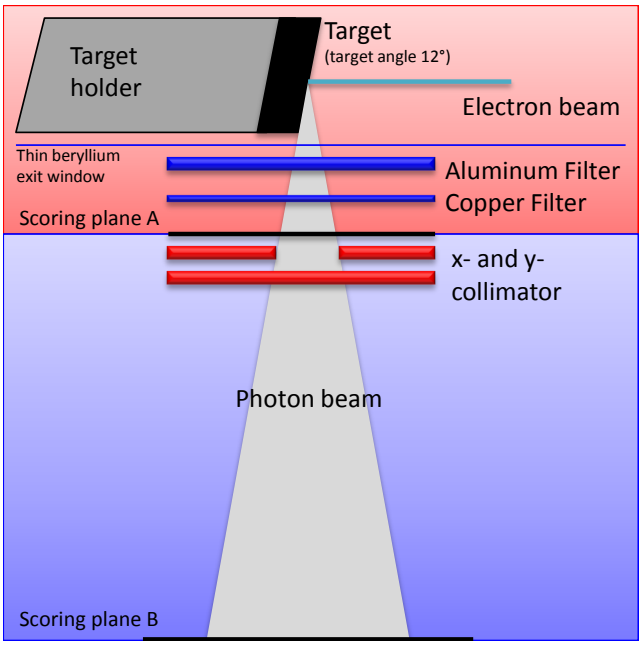

Figure 4.1.: *Simulation geometry for the X-ray tube simulation. The simulation is again split in two, to avoid the full target simulation to generate phase space files for different collimator settings (field sizes).*

the simulation. EGSnrc transport parameters (e.g. specifically specifying the transport processes to be used) are not available in the interface, the user has to put these manually into the input file. The cross sections for the different materials that can be used in the simulation have to be supplied in a file, which can be produced with a modified PEGS4 system [70].

4.1.2. Simulation setup

For the simulation of the X-ray tube a simple model was used as the simulation geometry, which is depicted in Figure 4.1. To avoid the repeated simulation of the photon generation in the target to obtain phase space files for different field sizes, this simulation was also split in two parts.
The first part consists of all components that are common to all field sizes, namely the target and the filters (red background in Figure 4.1). The cathode and the acceleration of the electrons was not simulated explicitly, the BEAMnrc source nr. "13 - Parallel rectangular beam incident from side" was chosen as an electron source. The electrons were assumed to be monoenergetic. For the simulation of the target, the BEAMnrc component "Xtube" was used - the thickness of the tungsten target was set to 1cm to rule out any influences of the copper target holder. The BEAMnrc component "Flatflt" was used for the simulation of the thin beryllium exit window and two filters for the removal of low energy photons from the beam: a 2.5 mm aluminum filter and a 0.2 mm copper filter. All particles that reach the 20cm x 20cm scoring plane A at a 20cm distance from the focal spot on the target, are saved in a phase space file. To increase the number of photons in the phase space file, while keeping the simulation time in an acceptable range, directional bremsstrahlung splitting was used to duplicate all bremsstrahlungsphotons produced in the target, which, according to their emission angle, would cross a circle with a radius of 40 cm positioned at an distance of 70 cm from the source perpendicular to the beam direction. The splitting factor was set to 2000. This part of the simulation only has to be executed once per electron energy, assuming that the tube geometry is constant.
The phase space file obtained in the first part of the simulation is used as the simulation source for the second part. This part mainly simulates the collimator, in addition the photons cross a certain amount of air before reaching the second scoring plane B (blue background in Figure 4.1). Electron transport is simulated above a kinetic energy of 10keV, range rejection was used for electrons below 20keV. The collimator is simulated using the BEAMnrc component jaws. The thicknesses of the x- and y-jaws are set to 0.39 cm. Lead is used as the jaw material. To exclude that the material of the collimator has a major influence on the dose distribution, tungsten was also simulated as a collimator material for a very small field (side length 1cm), which did not show a difference in the dose distribution above the uncertainty of

the Monte Carlo simulation. The collimator opening was set using the GUI, the inner edge of the jaws is tilted depending on the jaw opening and position, so that the upper and the lower edge result in the same fieldsize projected to the scoring plane B. Due to the low energy of the photons, the high absorption in the collimator material and the relatively large fields usually used in imaging, the shape of the jaw edges is not expected to have a big influence on the imaging dose distribution. The remaining geometry is filled with air, the scoring plane B can be positioned perpendicular to the beam at different distances as needed for the dose simulation. To account for the different transport processes for low energy photons and electrons, the following options were enabled for the EGSnrc particle transport simulation matching the settings reported in [18]: spin effects, bound Compton scattering, photoelectron angular sampling, Rayleigh scattering, atomic relaxations, electron impact ionization, angular sampling for bremsstrahlung events according to Koch and Motz. Bremsstrahlung cross sections from the NIST-database were used as well as xcom photon cross sections.

4.2. Dose Simulation

4.2.1. DOSXYZnrc

Like BEAMnrc, DOSXYZnrc is part of the EGSnrc coding system. It is a designated code for the simulation of dose distributions for rectilinear voxel geometries [71]. As for BEAMnrc, a graphical user interface is available to help the user with the creation an input file containing the voxel geometry and the simulation settings [68]. The definition of the voxel geometry is described in further detail in the next section. Within the interface the user can also enter general simulation setting such as the number of particles to be used for the simulation and the source type. For this work, two of the available source types are of special interest. Both offer the possibility to use a phase space file from a BEAMnrc simulation as a particle source, one is irradiating the geometry from a constant position, the other offers the rotation of the phase space file around the zero point of the voxel geometry, so that e.g. the situation of a cone beam computed tomography acquisition can be simulated. To increase the simulation speed for homogenous phantoms, the user can activate the HOWFARLESS option. This causes the EGSnrc system to ignore voxel boundaries within the phantom for the photon transport calculation.

4.2.2. Phantom Definition

Only voxel geometries fulfilling certain requirement can be used for a dose simulation with DOSXYZnrc. Even though voxels of different sizes are allowed, the voxel boundaries in one direction can only be specified for the whole geometry at once so that the voxels are formed by perpendicular planes intersecting each other. Each of the resulting voxels can have a different material and mass density. The graphical user interface for DOSXYZnrc offers a “direct” input of the geometry. For each axis, the user can enter the voxel boundaries either one by one or as groups of voxels of different side length. Materials and mass densities can then be assigned to single voxels or voxel groups. Of course this procedure is not feasible for the definition of a highly inhomogeneous geometry, such as patient data. For this case the voxel data can alternatively be included in the simulation using a predefined phantom definition file. The format and creation of such a file is described in detail in chapter 8.1.1. The same parameters as in the X-ray tube simulation were used for the simulation of particle transport.

4.3. Verification Measurement & First Simulation

To verify the simplified model of the X-ray tube of our Siemens Artiste used in the Monte Carlo simulation, a verification measurement in a water phantom was performed. Several dose profiles under continuous irradiation with the tube were measured and compared to normalized dose profiles from a Monte Carlo simulation. In this chapter all axis denominations refer to the phantom coordinate system described in chapter 3.2.2.

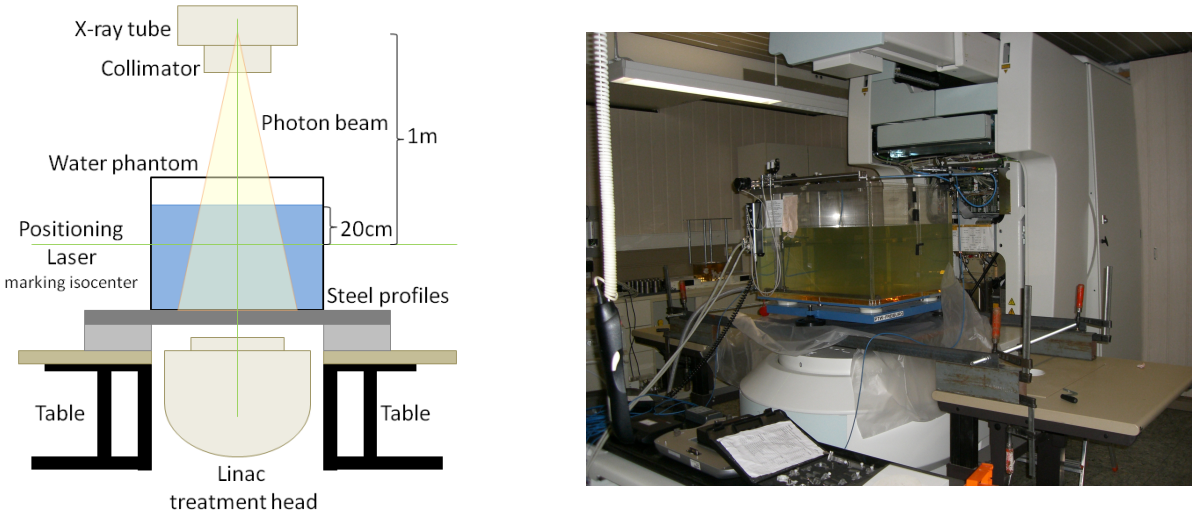

Figure 4.2.: *Measurement setup for the verification of the tube model. The water phantom has to be placed above the treatment head to allow for an irradiation of the phantom with the X-ray tube from above*

4.3.1. Measurement

The setup for the verification of the Monte Carlo tube model is shown in Figure 4.2. Due to the inline concept of the used linear accelerator - a Siemens Artiste (Oncology Care Systems, Siemens Medical Solutions Concord, CA, USA) - the X-ray tube is mounted opposite to the treatment head of the linear accelerator. While this is an advantage in a real treatment situation, as all motion perpendicular to the beam direction can be imaged, it is a challenge for the measurement of imaging dose with a water phantom - the heavy water phantom has to be placed above the treatment head. The final setup used for the measurement is shown in Figure 4.2. Steel profiles were fixated on tables next to the treatment head, the water phantom was placed on a board resting on the profiles. A plastic foil was placed under the phantom to protect the linear accelerator against any water. The water phantom was aligned using the positioning lasers, which mark the isocenter. A ($0.125cm^3$ Semiflex Ion Chamber (31010 - PTW, Freiburg, Germany) was used to measure the applied dose, the origin of the measurement coordinate system was manually set to the surface of the water phantom at the center of the photon field. The measurement time per dose point was varied according to the desired accuracy. Multiple profiles parallel to all three axes were measured for a very large field (app. 35cm x 35cm) using varying step sizes and integration times. As the maximum energy of the X-ray tube for continuous irradiation was 110kV, this energy was used for the measurement instead of the typical 121kV used for imaging. Due to the very small differences in the photon spectrum, the energy setting was assumed to have no influence on the validity of the tube model. The tube current was set to 25mA, the zero point for the measurement was set to the center of the photon beam at the surface of the phantom.

4.3.2. Simulation

For the simulation, the above described simulation parts were used to model the X-ray tube and the dose deposition in the water phantom. As in the measurement, the electron energy was set to 110keV and the collimator opening to an equivalent of 31.8cm in the isocenter plane in each direction. The number of electrons in the first part of the tube simulation was set to $3.5 * 10^9$. Directional bremsstrahlung splitting was activated for a square field with 40 cm half width at a distance of 70cm from the source with a splitting factor of 2000. This part of the simulation resulted in a phase space file containing app. $1.02 * 10^9$ particles, which were all used as source particles for the collimator simulation. In this part of the simulation, the scoring plane was positioned at 60cm distance from the source (the point, were the electrons hit the target and photons are created). For the final dose calculation, all of the app. $2.29 * 10^8$ particles from the resulting phase space file were used as source particles with a recycle factor of 10 for

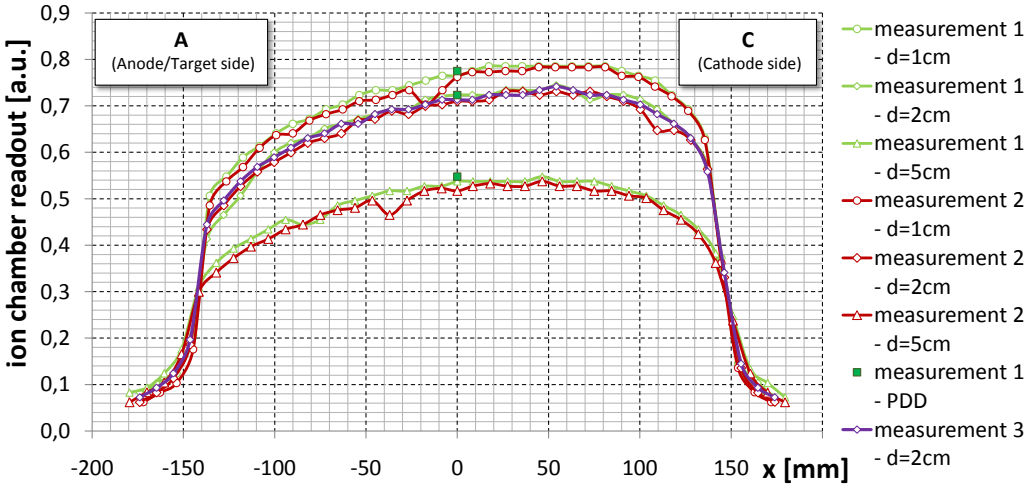

Figure 4.3.: *Measured profiles along the axis parallel to the tube axis. The increase in dose from the anode side (A) towards the cathode side (C), which results from the higher absorption of the beam in the target on the cathode side. The profiles were measured repeatedly in several sets, which result in slightly different dose levels each time. For the comparison, only profiles measured within one set (meaning a measurement within a short time) were considered using the same normalization. Also note the drops in dose, that occur over 2-4 measurement points at a time.*

each particle. The dimensions of the phantom were 60.3cm x 60.3cm x 75.125cm, the voxel resolution in the area of interest 3mm x 3mm x 2.5mm. Matching the measurement conditions of 20cm water depth for the isocenter and 1m distance between source and isocenter, the phantom surface was set to an SSD of 80cm.

4.3.3. Results and Discussion

Measured Profiles

Figure 4.3 shows the comparison of different sets of measured profiles at 1cm, 2cm and 5cm depth parallel to the tube axis (x-axis). One can clearly see the intensity variation due to the Heel effect described in chapter 3.3.1. Due to the lower absorption of the beam in the target and the resulting higher intensity of the photon beam at the cathode side of the tube (C in Figure, positive x-axis) compared to the anode side (A in Figure, negative x-axis), the dose on the cathode side is also higher. The plots of the measured data revealed different limitations of the measured data: Repetitive measurement of the same profiles at different times showed that even though the profile shape was constant, the dose level of the whole profile varied. The profile sets from the two measurements plotted in Figure 4.3 were acquired with a time distance of 1.5h, the third measurement was executed 15 min after the first. Even within this short time, the doses at the central axis changes, throughout the profiles, differences of several percent occur. Also the measured points of the PDD in measurement 1 do not exactly coincide with the measured points from the profiles in the same measurement set. This could be due to a drift in the output of the X-ray tube e.g. due to temperature changes. The accuracy of the dose measurement is therefore assumed to be 3%. As the zero position for the ionization chamber was manually set to the water surface, this is another source of errors. For the lateral profiles, one additional percent is added to account for the uncertainty in the measurement depth, which is app. equal to the average relative change in dose over 1mm. This brings the total measurement error up to 4%. As it can also be seen in several of the profiles for the second measurement shown in Figure 4.3, sudden drops in dose occur over 2-4 measurement points at a time in the measured dose profiles, the reason for these drops could not be identified. They could be either due to a decrease in the photon output of the X-ray tube, or due to problems with the measurement equipment. These values were regarded as measurement uncertainties. To improve the stability of the calibration for the measured data, only profiles measured within a relatively short time were considered using the same normalization.

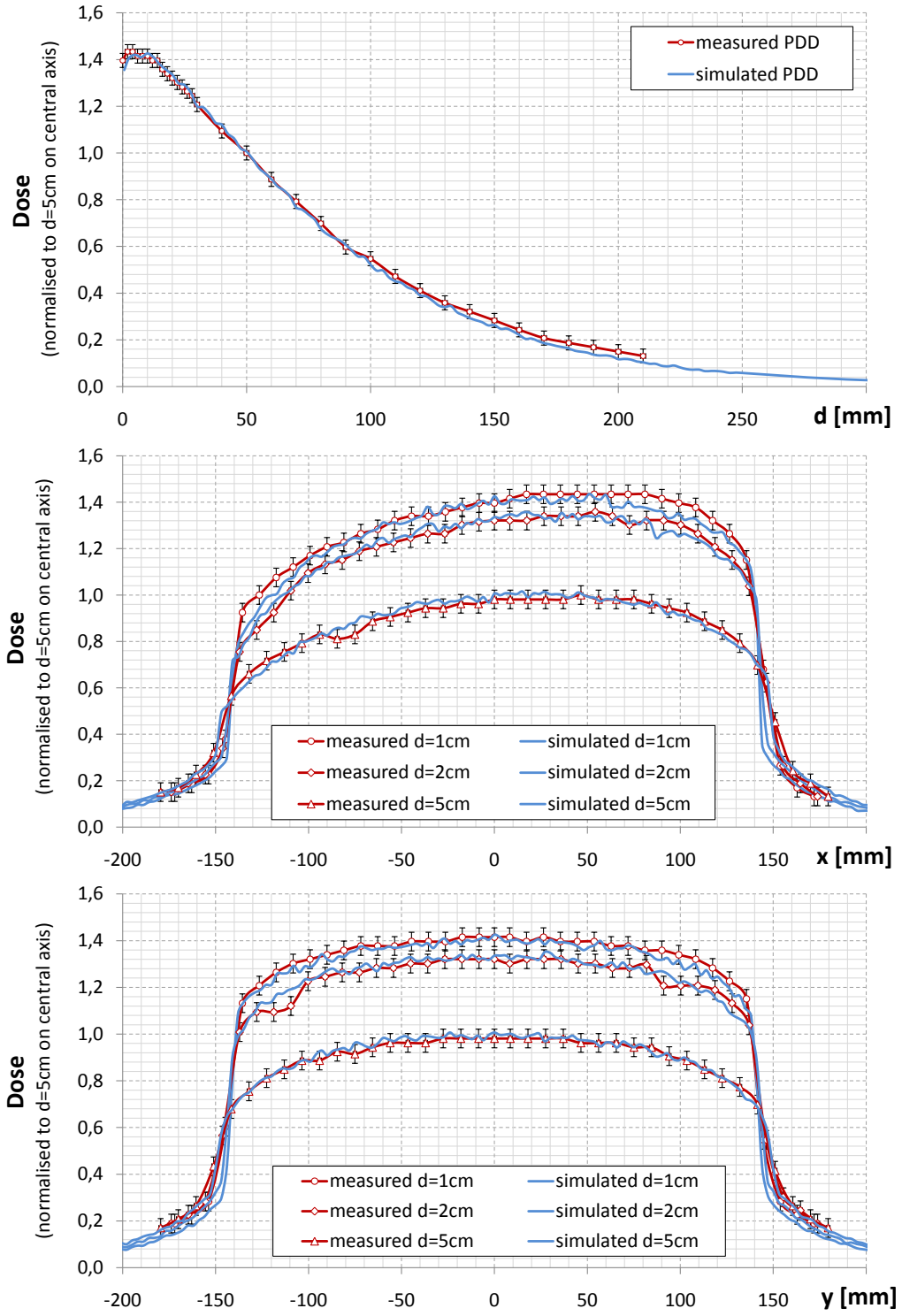

Figure 4.4.: *Comparison between measured and simulated profiles along the x-, y- and z-axis. All profiles are normalized to the measured dose at the reference point, which is placed at a depth of 5cm on the central axis (value taken from the depth dose curve). To also account for the uncertainty in depth, the error bars for the lateral profiles have a fixed absolute length of 4% on the dose and the profile along the z-axis a value of 3% on the dose and 1mm on the depth.*

Comparison Measurement vs. Simulation

For comparison, both, the simulated and the measured dose distribution were normalized to the dose at a reference point P=(0cm,0cm,5cm) on the central axis at a depth of 5cm. Due to the low statistics of the Monte Carlo simulation, in this case, the reference dose was averaged over the neighboring voxels. The profiles along the different axes of the simulated and the measured dose distribution are shown in Figure 4.4. In general the profiles match quite well. In the profile along the x-axis at a depth of 1cm, for very high positive or negative x-values the dose values from the MC simulation are systematically lower than the measured values. The maximum differences in these areas are app. 8%, which about two times the assumed accuracy of the measurement. The field edges are sharper in the simulation than in the measurement, which correlates with the tilted collimator edges in the simulation. The increased difference in the gradient at the field edge at the positive x-axis compared to the one at the negative x-axis could be explained by a variation of the spectrum which is not simulated or a setup error in the measurement (tilt of the z-axis). For very high depth, the dose resulting from the Monte Carlo simulation is slightly lower than the measured dose, which can be explained by the smaller extent of the water phantom in the measurement and the increased amount of backscatter from the supporting table. Even though the comparison between simulation and measurement did show minor differences, the simulations were accepted as accurate enough to use the underlying model of the X-ray tube for all further investigations. As the measurement of dose data is already complicated in a water phantom let alone in inhomogeneous phantoms and even impossible for patients, Monte Carlo simulations were used as the gold standard in this work.

5. Calculation of the keV Pencil Beam Kernel and the Primary Fluence

In a pencil-beam dose calculation algorithm, the total dose distribution is calculated by integrating the dose distributions for very narrow pencil-beams over the whole photon beam area. The dose distribution for one single pencil-beam is called the pencil-beam kernel. As a prerequisite for the pencil-beam dose calculation, one first needs to calculate this pencil-beam kernel for the medium in which the dose is to be calculated. Due to the high water content in most body tissues and its consequential similarity to such but also the convenience of an easily available liquid medium for measurements, water is the most common medium used for dose calculation in homogeneous phantoms. One method for the pencil beam kernel calculation is the single value decomposition described in chapter 3.4, where the pencil-beam kernel is calculated from depth dose curves in a way that also speeds up the dose calculation itself. In this chapter, the changes applied to an already existing kernel calculation algorithm are described, the acquisition of the input data is presented and the accuracy of the algorithm for the new energy range is analyzed.

5.1. Methods

As the pencil-beam algorithm is a well established algorithm in the dose calculation for therapeutic MV beams, a C++ implementation of a calculation algorithm for the pencil beam kernel from measured data, which uses the single value decomposition described in chapter 3.4, already existed prior to this work. Due to the specific properties of the keV-photon beam, the algorithm had to be adapted for the use in this energy range. In addition to the implemented changes, this chapter describes the input data needed for this algorithm and how it was obtained.

5.1.1. Changes in the Kernel Calculation Algorithm

Primary fluence model for the keV photon beam

For the pencil beam dose calculation, a 2-dimensional primary fluence $\psi(x, y)$ is needed (see chapter 3.4), whose calculation is included in the kernel calculation algorithm. Due to the rotational symmetry of the photon production setup in the linear accelerator, the existing MeV kernel calculation algorithm approximates the 2-dimensional fluence by rotating a 1-dimensional profile around the axis of the photon beam. This concept cannot be used for the keV version of the algorithm as the X-ray tube does not offer rotational symmetry. Therefore a model for the primary fluence was developed reconstructing the primary fluence from 2 perpendicular profiles. The shape of lateral profiles of the primary fluence (profiles normalized to the central point) was assumed to be invariant to translation, which leads to the following equations for the normalized profile values $P_{x/y}(x_1/y_1)$:

$$\begin{aligned} x-profile: \quad P_x(x_1) &= \frac{\psi(x_1,0)}{\psi(0,0)} = \frac{\psi(x_1,y_1)}{\psi(0,y_1)} \\ y-profile: \quad P_y(y_1) &= \frac{\psi(0,y_1)}{\psi(0,0)} = \frac{\psi(x_1,y_1)}{\psi(x_1,0)} \end{aligned} \tag{5.1}$$

with $\psi(x, y)$ being the primary fluence at the point (x,y) and x_1 and y_1 are random x- and y-coordinates. Under this assumption, the formula for the calculation of the primary fluence $\psi(x_p, y_p)$ for a point $P(x_P, y_p)$ with given profiles values $P_x(x_p)$ and $P_y(y_p)$ can be derived as following:

$$\begin{aligned}\psi(x_P, y_P) &= \frac{\psi(x_P, y_P)}{\psi(0, y_P)}\psi(0, y_P) \\ &= P_x(x_P)\frac{\psi(0, y_P)}{\psi(0, 0)}\psi(0, 0) \\ &= P_x(x_P)P_y(y_P)\psi(0, 0)\end{aligned} \tag{5.2}$$

Using a normalization of the primary fluence to the central axis, so that $\psi(0, 0) = 1$, this results in the following formula:

$$\psi(x_P, y_P) = P_x(x_P)P_y(y_P) \tag{5.3}$$

If the profile values $P_x(x_P)$ and $P_y(y_P)$ are not available for the required x- and y-values, both values are derived by linear interpolation of the neighboring profile points at the x-coordinates $x_{lt} < x_P$ and $x_{gt} > x_P$ or y-coordinates $y_a < y_P$ and $y_b > y_P$:

$$\begin{aligned}P_x(x_P) =& \frac{P_x(x_b) - P_x(x_a)}{x_b - x_a}(x_P - x_a) + P_x(x_a) \\ P_y(y_P) =& \frac{P_y(y_b) - P_y(y_a)}{y_b - y_a}(y_P - y_a) + P_y(y_a)\end{aligned} \tag{5.4}$$

Analog to the high energy (MeV) case [60], dose profiles in water are employed to determine the profile shapes P_x and P_y of the primary fluence. For this, a reference depth of 1cm and a reference SSD of 90cm were used.

Depth dose curves

All input data for the MeV kernel calculation algorithm can be measured at the linear accelerator to allow for a pencil beam kernel, which is specific for each linac without knowing the geometrical details of the system. In the original kernel calculation algorithm measured TPRs in combination with the measured output factors for different field sizes for a reference source-surface distances (SSD) are used to obtain depth dose curves for multiple SSDs and field sizes in the parallel pencil beam coordinate system (see chapter 3.4). This has been introduced, as especially for small fields, the tissue phantom ratio (TPR) allows for a measurement with a higher geometric accuracy due to the fix measurement point in a changing phantom geometry compared to the varying point of measurement in a fix phantom geometry for the percentage depth dose (PDD). All input data for the keV version of the algorithm is obtained from Monte-Carlo Simulations, where it is much easier to simulate the PDD instead of the TPR with an equal accuracy (due to the constant simulation geometry per SSD and field size). Even though it would be possible to directly simulate a dose distribution for a pencil beam, the single value decomposition algorithm was maintained, to preserve the possibility of measured input data and the speedup of the dose calculation algorithm. The C++ algorithm was therefore adapted to directly accept PDD curves and output factors separately for each SSD instead of TPRs and output factors. To maintain the dependence of the output factors on the SSD, as well as the dose ratios between the different SSDs, the read in for the output factors was also adapted to be separate for each SSD. To achieve an overall normalization of the dose calculation to the point (x,y,d)=(0,0,5)cm for a reference SSD ($SSD_{ref} = 90cm$) and the reference field size 10cm x 10cm, the output factors for every SSD were normalized to the dose simulated for the described reference conditions.

5.1.2. Calculation Steps in the Kernel Calculation Algorithm

The calculation algorithm of the pencil beam kernel consists of a sequence of steps to derive the decomposed pencil beam kernel from the input data (see also chapter 3.4). As a first step, the PDDs from the

input data are converted to a coordinate system, where all pencil beams are parallel, by removing the inverse square dependency on the distance from the radiation source and normalizing the curve.

$$PDD'(d) = PDD(d) * \left(\frac{SSD + d}{SAD}\right)^2 \tag{5.5}$$

,where SAD is the distance between the source and the isocenter. As the PDD is normalized to 1 at the reference depth, the formula implies the following normalization of PDD':

$$PDD'(d_{ref}) = \left(\frac{SSD + d_{ref}}{SAD}\right)^2 \tag{5.6}$$

This step is a simple division by known values, so no inaccuracies are introduced. In the second step, the converted depth dose curves are approximated using a least square fit of factorized terms. Other than described in chapter 3.4, the normalized depth dose curves $PDD'(d)$ are used for this step. To return to absolute depth dose curves the weights are later multiplied with the respective output factor (OF). The linear fit of the PDD curve can be described by

$$PDD'(r, d) \approx \sum_{i=1}^{3} W_i^*(r) D_i'(d) \tag{5.7}$$

, where $W_i^*(r)$ are the weights and $D_i'(d)$ are given fit-functions. These functions $D_i'(d)$ are chosen as

$$D_i'(d) = \frac{\beta_i}{\beta_i - \mu}\left(e^{-\mu d} - e^{-\beta_i d}\right) \tag{5.8}$$

according to Bortfelds publication on pencil beam kernel decomposition [60]. Parameters for the functions $D_i'(d)$ are derived from the depth dose curves as well, one set of functions is then used for all PDDs for one SSD. The parameter μ is set to the slope of a linear fit of the logarithmic PDD curve for the smallest field size. The parameters β_i are not set directly, but calculated from the desired positions of the maxima $z_{i,max}$ of the different fit-functions using an iterative approach to solve the following equation:

$$\beta_i e^{-\beta_i z_{i,max}} - \mu e^{-\mu z_{i,max}} = 0 \tag{5.9}$$

In contrast to the MeV-Version of the algorithm, the position of the first maximum $z_{1,max}$ is not defined depending on the calculated absorption coefficient but set to a constant value of 0.01mm, so that the first fit-function is almost an exponential decrease with the absorption coefficient. This solution was chosen to account for the lack of a build-up region in the depth dose curve for a keV photon beam, compared to a MeV-photon beam, where the dose increases over the first centimeters in a phantom. The position of the maximum of the third fit-function $z_{3,max}$ is set to two times the inverse of the absorption coefficient. The second maximum is assigned a value in between the two other maxima, so that the $z_{i,max}$ can be summarized as

$$\begin{aligned} z_{1,max} &= 0.01 \\ z_{2,max} &= 0.3 * \left(0.01 + \frac{2.0}{\mu}\right) \\ z_{3,max} &= \frac{2.0}{\mu} \end{aligned} \tag{5.10}$$

All fields with a side length a are assigned an equivalent field size radius $r_{equivalent}$, which is the radius of a circular field with the same area as the square field.

$$r_{i,equivalent} = \frac{a_i}{\sqrt{\pi}} \tag{5.11}$$

In the next step, the product of the weights $W_i^*(r)$, which are obtained from the linear fit of the PDD with the derived fit-functions, and the output factors are interpolated using a cubic interpolation. The fourth step is the calculation of the derivative of the interpolated product. The last step is the normalization of the kernel according to the primary fluence in the respective area.

5.1.3. Simulation of the Input Data

All simulations undertaken to obtain the input data for the kernel calculation algorithm are summarized in Figure 5.1. As depicted in chapter 4.1 the dose simulations for obtaining the input data were split in two parts. The first part was the X-ray tube simulation, which also defines the field size, resulting in a phase space file. This file was used as a particle source for the second part, the simulation of dose deposition in a water phantom.

X-ray tube Simulation As described above, the X-ray tube simulation was split into two simulation steps: 1. the simulation of the tube geometry common to all field sizes and 2. the collimator and the air above the phantom. For the first step, the details of the common X-ray tube geometry used in this work are described in detail in chapter 4.1. Two different phase space files were created in this step, one with a smaller diameter for collimator simulations for small fields (r=10cm at z=20cm, simulations connected to this phase space marked with light blue contours in Figure 5.1) and one with a larger diameter for collimator simulations for large fields (r=20cm at z=20cm, simulations marked with orange contours in Figure 5.1). The diameter of the phase space file is defined by the maximum diameter of the geometry components for a simulation. To achieve a sufficiently high number of photons in the resulting phase space file, the number of incoming electrons with an energy of 121kV was set to $3.5 * 10^9$ and $4.0 * 10^9$ respectively. Directional bremsstrahlung splitting was activated for a square field with 40 cm half width (60cm) at a distance of $z_{total} = 70cm$ ($z_{total} = 100cm$) from the source with a splitting factor of 2000. In both cases, the scoring plane was placed below the filters of the tube at a distance of 20cm from the photon source. As the electron transport is an important process in this part of the simulation, the cutoff energies for transport were set to a total energy of 0.512MeV for electrons (which is equal to a kinetic energy of 1keV) and to 1keV for photons. For electrons below an energy of 0.531keV, range rejection was activated.
These phase space files were employed as the particle sources for the second step of the X-ray tube simulations. To use all particles from the file, the number of particles to be simulated was set to the number of particles in the respective source file. As shown in Figure 5.1, the phase space file with the smaller diameter was used to simulate different collimator openings, each resulting in a new separate phase space file for a specific field size. In this case the scoring plane was positioned at a distance of 60cm ($z_{total} = 60cm$) from the source. The medium of the gap between the collimator and the scoring plane was set to air. Within the lead collimator, no electron transport was simulated, within air, the cutoff energy was set to 0.521MeV. As the influence of the collimator shape on the central axis depth dose curve in negligible for very large fields, the simulations in the second step using the large diameter phase space file use an open collimator and therefore only simulate the transport of the particles through a large amount of air. Phase space files with a radius of 50cm were created for two different z-positions, one at $z_{total} = 70cm$ and one at $z_{total} = 90cm$. The main goal of this simulation step was to exclude a big part of the air between the X-ray tube and the phantom from the dose simulations and obtain a phase space file located closer to the phantom.

Dose deposition simulation For the dose simulation the phase space files from the second step of the X-ray tube simulation were used as a phase space source in a constant position (in DOSXYZnrc: isource = 2) [71]. To increase the accuracy of the simulation, several transport histories were simulated per particle from the phase space sources. For field side lengths between 5cm and 35cm this recycle factor was set to 10, while for smaller fields ranging from 2cm to 5cm a factor of 30 was used (due to the lower number of particles in the phase space file). For the 1cm x 1cm field, the factor was increased to 50, as the number of histories simulated with a factor of 30 did not yield satisfactory statistics. For field side lengths up to 35cm, for which a specific phase space file was available, the number of histories to be simulated was adapted accordingly, so that all particles in the phase space files were used. The homogeneous water phantom used for this simulation was created using the graphical user interface for DOSXYZnrc. It has a size of 64.3cm x 64.3cm x 50.25cm, the voxels in the center region of the phantom have a size of 3mm in each direction, only the first voxel in z-direction is reduced to 3mm x 3mm x 2.5mm, so that one plane of voxels had its center at a depth of 1cm, allowing for profile extraction at

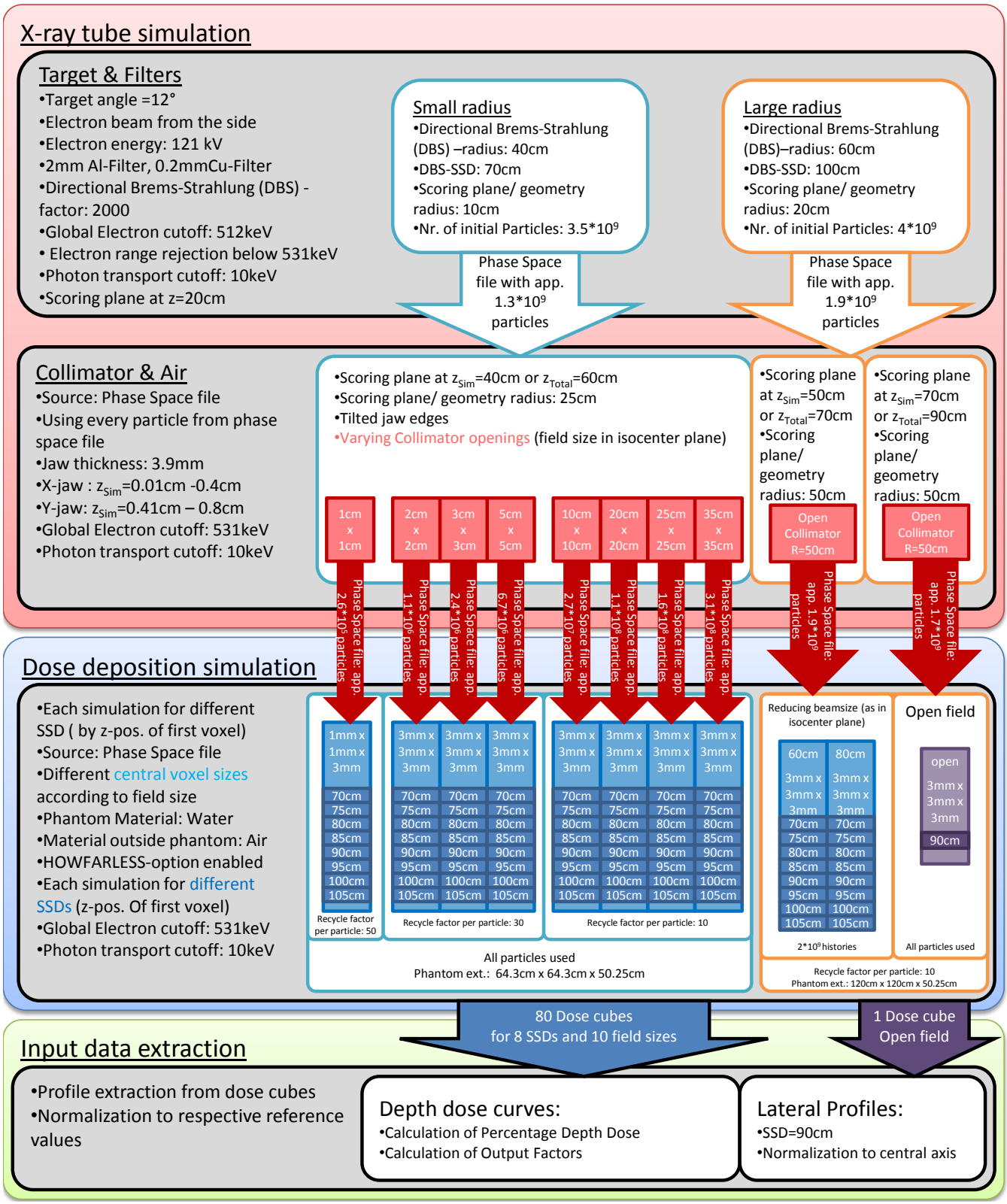

Figure 5.1.: *Summary of simulations to obtain the input data for the kernel calculation algorithm. The simulation is split in two parts: The X-ray tube simulation (red) and the dose deposition simulation (blue). The input data (green) in form of depth dose curves and lateral profiles is extracted from the resulting 65 dose cubes. The red rectangles in the X-ray tube simulations show the field sizes in the isocenter plane for each simulation. In the blue/lilac rectangles, the voxel sizes at the positions of the profiles is given, as well as the field size, if set in the dose simulation. In dark blue/lilac, the simulated SSDs are listed.*

this depth. For the 1cm x 1cm field, the resolution was increased to 1mm x 1mm x 3mm to account for the high lateral variation of the dose distribution. To obtain depth dose curves for a number of SSDs ranging from 70cm to 105cm in steps of 5cm, the distance between the first voxel and the phase space file source was varied accordingly. Due to the higher number of particles to be simulated, the simulation time rapidly increase with the field size. The phase space file with a field radius of 50cm was used to add depth dose curves for larger fields to the input data, as well as lateral profiles from a very large field for the primary fluence estimation. To obtain the dose distributions for a 60cm x 60cm and an 80cm x 80cm field, the beam size was restricted using an option of DOSXYZnrc, where particles from the phase space file outside a square field can be discarded. As the field sizes are much larger, the water phantoms extension was increased to 120cm x 120cm x 50.25cm. As the lateral variation of the dose around the central axis was already very low for the 35cm x 35cm field, the voxel size was increased to 20mm x 20mm x 3mm for all larger fields to decrease the number of simulated histories to $2.0 * 10^9$ with a recycle factor of 10, while maintaining the accuracy of the simulation. Again the simulations were executed for different SSDs by varying the z-position of the first voxel of the phantom. To obtain the lateral profiles for a large field at an SSD of 90cm, which are needed for the primary fluence estimation, the phase space file with a radius of 50cm at $z_{total} = 90cm$ was used as the simulation source. All particles from the phase space file were used, in combination with the recycle factor of 10, $1.7 * 10^{10}$ histories were simulated. The phantom extensions were 112.3cm x 112.3cm x 70.25cm, with voxel sizes of 3mm x 3mm x 3mm in the central area. In all dose deposition simulations no electron transport was simulated due to the short range of electrons in water in the considered energy range. Photon transport was simulated above 1keV. As the simulation geometry is homogenous, the HOWFARLESS option was used to decrease the simulation time.

Input data extraction For the differently sized square fields, depth dose curves at the central axis were extracted for the kernel calculation from each of the 80 simulated dose cubes. The dose values at the point (x,y,d)=(0cm,0cm,5cm) were normalized to the 10cm x 10cm field at the reference SSD=90cm and used as output factors. The depth dose curves were normalized to their respective dose value at (x,y,d)=(0,0,5)cm. For the estimation of the 2-dimensional primary fluence, lateral profiles parallel to the x- and y-axis at a depth of 1cm were extracted for different y/x-positions from the simulated dose distribution for an open field at an SSD of 90cm and were normalized to their respective dose value at the center. To avoid that the fluctuations due to the statistics in the Monte Carlo simulation are inherited by the primary fluence, normalized profiles from several positions were averaged. For the x-profile, profiles at y-values ranging from -20cm to 20cm in steps of 5cm were used, for the y-profile the range of x-values was -10cm to 20cm due to the extremely low dose for smaller x-values. To further decrease the fluctuations in the final profiles P_x and P_y, a sliding average was applied to the averaged curves, where the dose value for each voxel was replaced by the average of the values of the voxel itself and two neighbors in each direction. Due to the normalization of the primary fluence profiles to the central axis and of the output factors to the reference dose at (x,y,d)=(0,0,5)cm for a reference SSD of 90cm and a field size of 10cm x 10cm, the dose calculated with the pencil beam algorithm will also be normalized to this dose. In principle, it would also be possible to multiply one of the profiles for the primary fluence with the reference dose, so that the pencil beam algorithm also calculates the dose per source particle as the Monte Carlo simulation does.

5.2. Results

5.2.1. Phase Space files

A total number of 12 phase space files were created to obtain the input data for the kernel calculation. Two phase space files with different radii from the simulation of target and filters and 10 phase space files after the simulation of collimator and air including 8 different field sizes and 2 open fields phase spaces at different SSDs. The phase space file with a radius of 10cm contains almost $1.3 * 10^9$ particles and has a size of app. 34 Gigabyte, the one with a radius of 20cm app. $1.9 * 10^9$ and a size of 51 Gigabyte. The approximate numbers of particles in the phase space files for the different simulated collimator openings

Table 5.1.: *Number of particles in the phase space files*

Field size (isocenter plane)	Number of particles (rounded)
$z_{total} = 60cm$	
1cm x 1cm	$2.62 * 10^5$
2cm x 2cm	$1.06 * 10^6$
3cm x 3cm	$2.40 * 10^6$
5cm x 5cm	$6.70 * 10^6$
10cm x 10cm	$2.68 * 10^7$
20cm x 20cm	$1.05 * 10^8$
25cm x 25cm	$1.63 * 10^8$
35cm x 35cm	$3.05 * 10^8$
$z_{total} = 70cm$	
r=50cm	$1.93 * 10^9$
$z_{total} = 90cm$	
r=50cm	$1.74 * 10^9$

The number of particles in the phase space files is given for different field sizes projected to the isocenter plane.

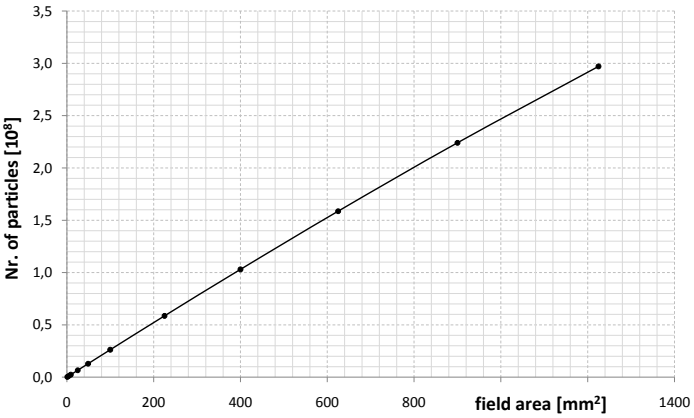

Figure 5.2.: *Nr. of particles in phase space files as a function of field area. The increase is almost linear, though for larger field, the number of particles is lower due to the reduced intensity caused by the Heel effect.*

are listed in Table 5.1 and show an almost linear increase with the area of the photon beam (see also Figure 5.2). The phase space files for a phase space radius of 50cm are also listed in the same table. In all phase space files, the fraction of photons in relation to all particles (electron and photons) exceeds 99.996%.

5.2.2. Obtained Input Data

From the simulation described above, a total of 80 percentage depth dose curves (for 8 source-surface-distances and 10 field sizes), 8 output factor curves (for 8 SSDs) and 2 lateral profiles for the primary fluence estimation were extracted. The reference dose at (x,y,d)=(0,0,5)cm for the 10cm field at an SSD of 90cm was found to be $1.38733 * 10^{-20}$ Gy/source particle and is also used for the normalization of all Monte Carlo dose cubes in chapter 6:

$$d_{norm} = d_{SSD=90cm,10cmx10cm}(0cm, 0cm, 5cm) = 1.38733e^{-20} \frac{Gy}{source\ particle} \tag{5.12}$$

Representative for the large number of PDDs, the curves for an SSD of 80cm are shown in Figure 5.3. The steepness of the curves decreases with increasing field size. This is due to the higher fraction of dose due to scattered photons from the additional primary beam area, whose number increases with depth. Therefore they deposit more dose at higher depth than at smaller depth, which causes a shallowing of

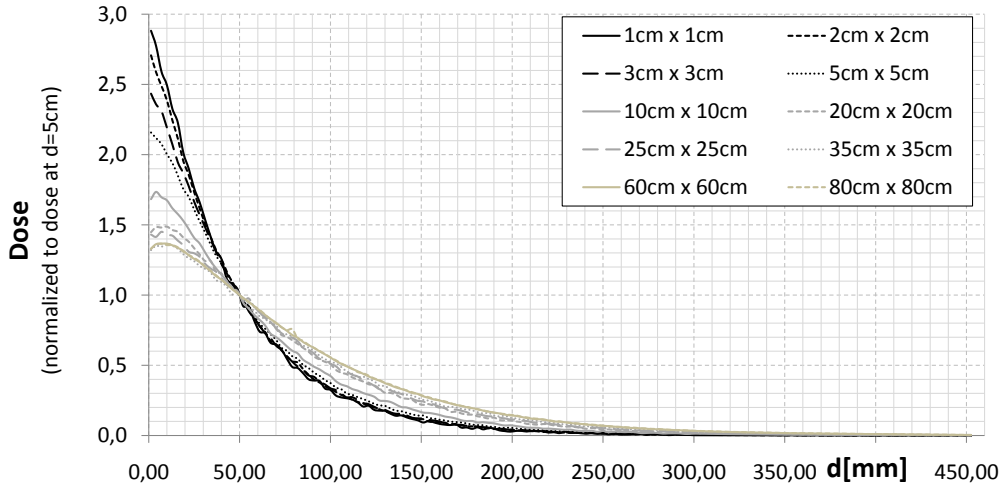

Figure 5.3.: *Input Data. PDDs for an SSD of 80cm. Due to the normalization, all PDD curves intersect at a depth of 5cm. As expected, the curves are steeper for small fields than for larger fields, due to the lower fraction of dose due to scattered photons.*

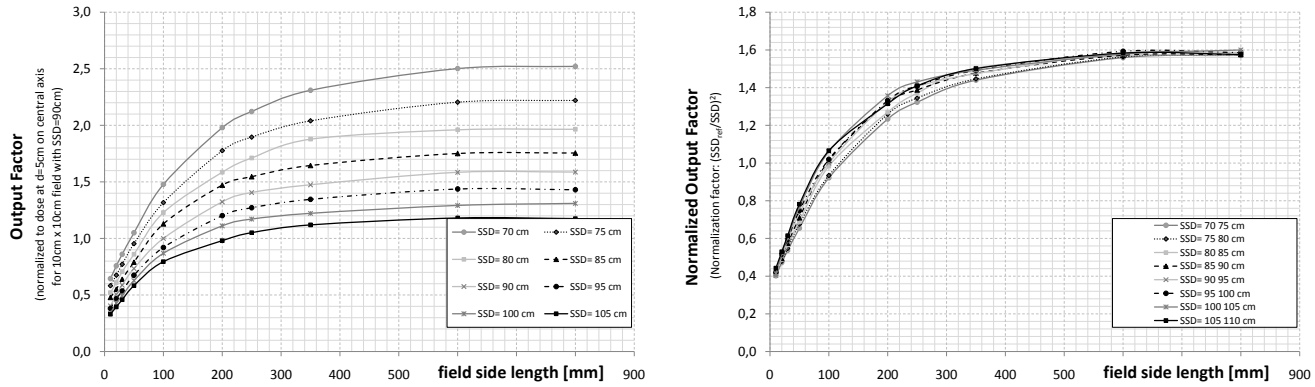

(a) (b)

Figure 5.4.: *Input Data: Output Factors. (a) Output factors for all SSDs. The Output factors increase with the fieldsize and decreasing SSD. (a) Output factors normalized to* $((SSD_{ref} + d_{ref})/(SSD) + d_{ref})^2$. *Clearly, the dependency of the output factors on the SSD is not a pure inverse square dependency, which supports the usage of separate output factor files.*

the depth dose curve. For the smaller field sizes ($< 5cm$), no build-up effect is visible, the dose is highest in the voxel with the lowest depth. For larger field sizes, the dose first increases to a maximum dose at a depth of up to 1cm, though for the considered energies, this is not due to a build-up of secondary electrons but to the photons scattered towards the central axis at higher depth. The described behaviour of the PDD curves can be observed for all SSDs. The plot in Figure 5.4a shows all output factor curves used as input data. As expected, the output factors increase with increasing field size and decreasing SSD. A far more interesting view on the output factors is provided by the plot in Figure 5.4b. Here the output factors are normalized using the normalization factor $((SSD_{ref} + d_{ref})/(SSD) + d_{ref})^2$, meaning that the dependency on the inverse square of the distance to the source is removed. The normalized output factors show a dependency on the SSD, which is highest for medium field sizes. Depending on the SSD the normalized output factor varies by up to app. $\pm 8\%$, which supports the usage of a separate output factor file per SSD.

5.2.3. Analysis on the Accuracy of the Calculation Algorithm

The kernel calculation algorithm undertakes different steps to estimate the pencil beam kernel and the 2D-primary fluence from the input data. Any deviations introduced in one of the steps of the pencil beam

Figure 5.5.: *Comparison of normalized profiles for an open field for different offaxis positions. All profiles show a good agreement with the averaged and smoothed profiles* P_x *and* P_y *used as the input for the primary fluence calculation. The differences of app. 2% are not systematic but random and due to the statistics of the Monte Carlo simulation.*

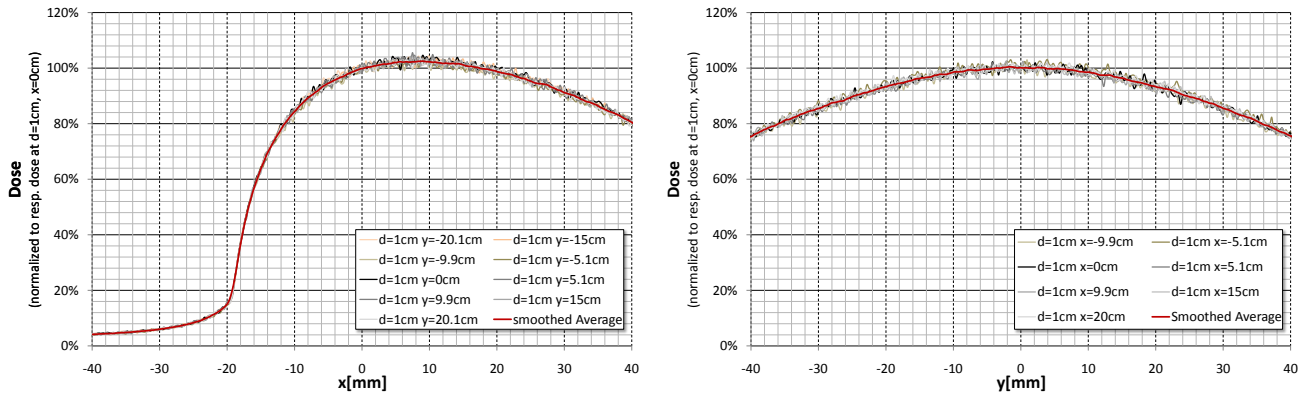

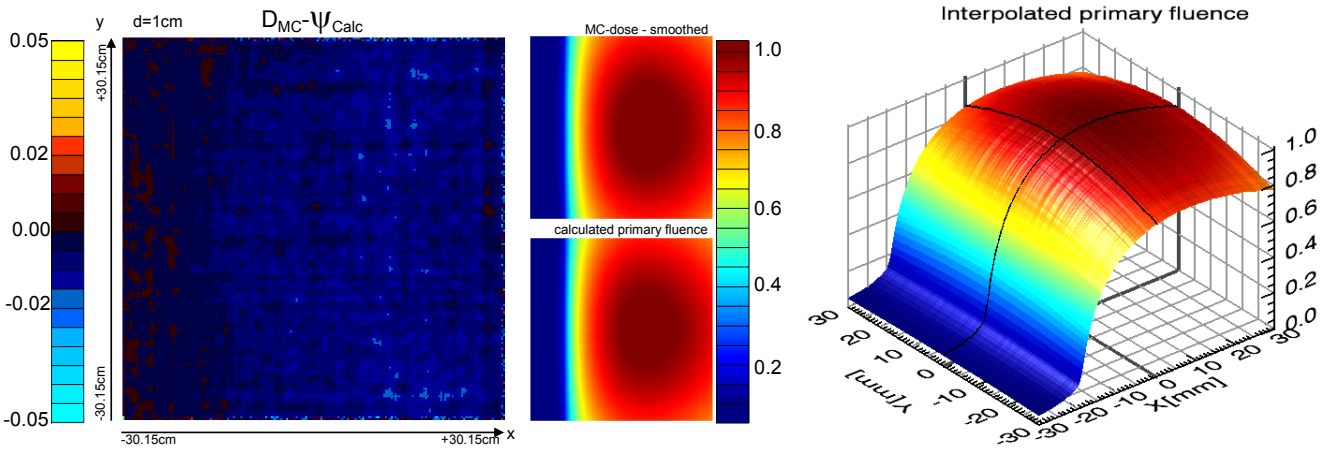

(a) **(b)**

Figure 5.6.: *(a) Comparison between the smoothed MC-simulated dose plane normalized to the average of the center ± 2 voxels and the estimated primary fluence. On the right side the respective dose distributions are shown. The primary fluence as well as the differences are normalized to the central axis. (b) 3-dimensional visualization of the estimated 2-dimensional primary fluence. The black lines are the input profiles used to determine the fluence. (Colorscale as in (a))*

kernel calculation is inherited by the pencil beam kernel, causing inaccuracies in the calculated dose. In this section, different steps from the calculation algorithm are analyzed, evaluating the accuracy of the used algorithm for the imaging energy range.

Primary fluence model

As described above, the 2-dimensional primary fluence is calculated from 2 perpendicular profiles by multiplying linearly interpolated values of the respective neighboring profile points for both profiles. Due to the fluctuations in the profiles from the simulated dose distributions, averaged and smoothed curves are used as the input profiles. The primary assumption of the developed fluence model is, that the shape of the normalized dose profiles is invariant to translation along the perpendicular axis. To validate this assumption, Figure 5.5 shows the lateral profiles parallel to the x- and y-axis of the dose distribution simulated at an SSD of 90cm (shades of grey), which were used to determine the input profiles. For comparison, the averaged and smoothed profiles P_x and P_y used for the primary fluence estimation (red) is also presented. All of the profiles are normalized to their respective dose value at x=0cm or y=0cm. The agreement between the profiles is good, the averaged and smoothed profiles reproduce the shape of all profiles. Due to the statistics of the Monte Carlo simulation, random deviations of up to app. 2% occur for all profiles. No systematic trends can be observed.
A 2D-comparison between the estimated primary fluence and the dose plane from the MC-simulation, that the input profiles are based on is shown in Figure 5.6a. In this case, the MC-dose distribution is normalized to the average of the center ± 2 voxels, for a better visualization, the dose is smoothed averaging over a 3x3 area for each voxel. The vertical red stripe on the difference image lies in the area is caused by the smoothing of the profiles in a high gradient area. In most other areas, the differences are below 2%, the mean difference within the investigated area of 60.3cm x 60.3cm is 0.0058 ± 0.0040 (mean ± standard deviation). This means that not only the mean value is close to 0 but also the standard deviation is very low. Based on the above analysis, the multiplication of linearly interpolated values of the averaged and smoothed profiles is assumed to reproduce the primary fluence well. The 2D-primary fluence calculated according to the formulas used in the kernel calculation algorithm is visualized in a 3D-plot in Figure 5.6b.

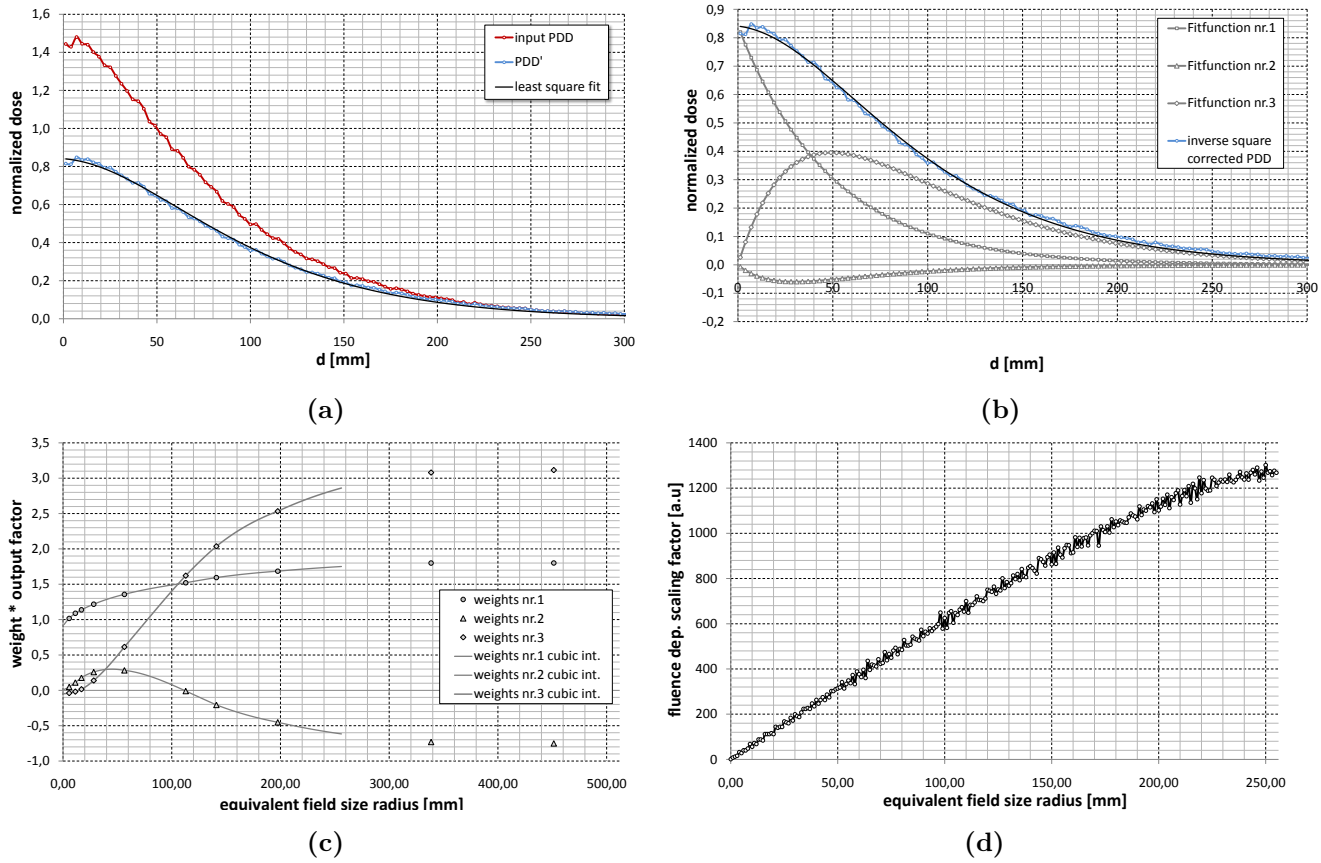

Figure 5.7.: *Different steps in the kernel decomposition algorithm for an SSD of 75cm and a field size of 20cm. (a) Input PDD, PDD' - corrected for the square dependency on the distance from the source - and fitted function from the kernel calculation algorithm. (b) Composition of the summed fitted function and the fraction of the different fit-function. (c) Product of Weights and Ouput Factor vs. equivalent field size radius and their cubic interpolation. For a larger field sizes, the fit-function nr.3 with the maximum at a higher depth becomes more important, for small fields fit-function nr.1 is dominant. where the maximum is very close to the surface. (d) normalization factor* $\psi'_N(r)$.

Kernel calculation steps

In this part, the kernel calculation from PDDs and output factors is considered. As an analysis of the calculation process for every single one of the 80 PDD curves would go beyond the scope of this work, a sample SSD and field size was selected for the detailed analysis. Unless stated otherwise all numbers and graphs given in this section refer to the kernel calculation for an SSD of 75cm and a field size of 25cm x 25cm. The kernel size is 512 x 512 with a resolution of 1mm. The kernel calculation steps themselves are described in section 5.1.2. Figure 5.7a shows the original PDD, the inverse square corrected PDD' and the function resulting from the least square fit. Clearly, the fitted function matches its counterpart quite well, though it does not perfectly model its curvature. For this specific profile the maximum differences between the two curves are app. 3% of the respective dose at a depth of 5cm, which is very close to the uncertainty of the Monte Carlo simulation (max. 2%). Nevertheless, the differences are not purely the random differences due to the simulation but there is also a systematic contribution due to the limitation of the fitting model.
For more field sizes, this is shown in Figure 5.8, where the differences between square corrected PDD and the fitted function are shown for all used field sizes. As the single curves are very noisy, the black curve shows the average curve for all field sizes. While the dose is overestimated in the entrance region (0cm-0.5cm), an area of underestimation (app. d=0.5cm-3cm) by up to 3% on average is followed by a larger area of overestimation (app d=3cm-10cm) of up to app. 2% on average. The dose in depth higher than 10cm tends to be underestimated, this effect is more pronounced for fields of at least 35cm x 35cm (where the dose is higher at these depths), for which the difference exceeds 3%, and very small

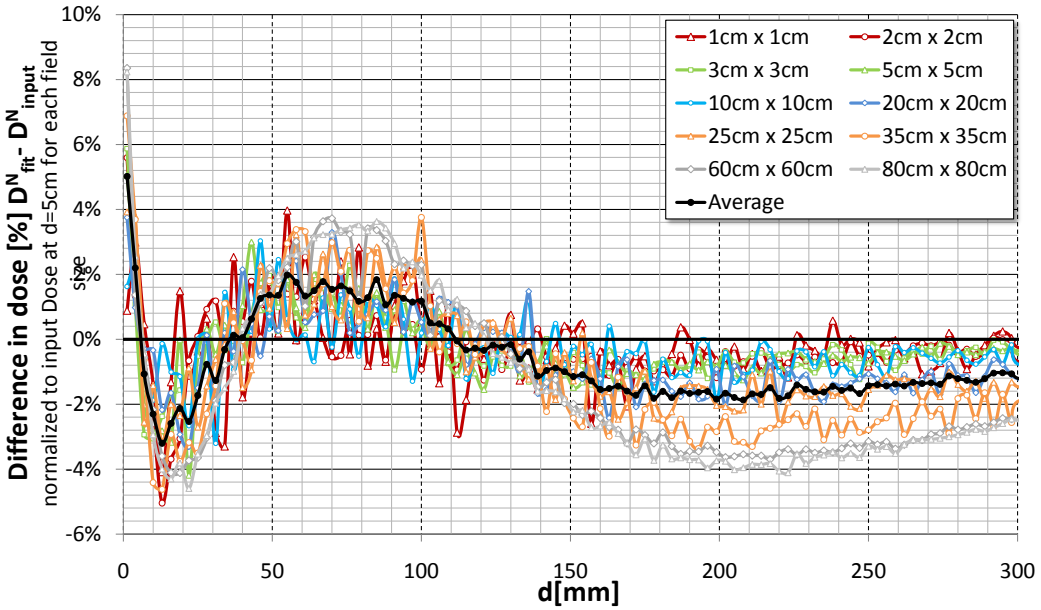

Figure 5.8.: *Differences between square corrected PDD and fitted function for different field sizes normalized to the respective dose at 5cm depth. Note that the areas of over- and underestimation are common to all field sizes. The black line shows the average value for all field sizes.*

for fields smaller than 10cm x 10cm, where it is below 1%. This is due to the lower curvature of the depth dose curves for large fields which cannot be modeled with the fit-functions in combination with the specific derived parameters. The choice of the parameters for the fit-functions influences the accuracy of this step, e.g. an increase of the depth of the maxima of the second and third fit-function increases the accuracy for large fields but decreases the fit quality for small fields. Figure 5.7b shows the shape of the different fit-functions $D_i'(d)$ and their contributions $W_i(r)D_i'(d)$ to the fit of the given profile (SSD=75cm, A=25cm x 25cm). In this special case, the first and the third fit-function have a relatively high positive contribution, while the second fit-function has a negative contribution. In 5.7c, the dependency of the scaled weights $W_i(r) = W_i^*(r) * OF$ on the equivalent field size and their cubic interpolations are shown. This interpolation of the scaled weights is the next source of inaccuracies in the kernel calculation. As the dose distributions are only known for a limited number of field sizes, the error caused by the interpolation again cannot be quantified. This is another possible source of errors, as it is possible, that the interpolated points do not reflect the true values for in between the field sizes already included in the data acquisition. The next step in the algorithm is the calculation of the derivative of the scaled weights $w_i(r)\psi_N'(r) = \partial W_i(r)/\partial r$. In a last step, the kernel is scaled according to the fluence within the respective fields $\psi_N'(r)$, the dependence of scaling factor on the radius is plotted in Figure 5.7d. For small fields its increase is roughly linear, while it increases more slowly for larger fields, were the primary fluence not only decreases generally, but quickly drops to zero on the anode side as the maximum angle for the emittance of photons from the target is determined by the target angle.

6. keV Dose Calculation Accuracy for different Water Phantoms

Using the calculated pencil beam kernels for the medium water, it possible to calculate first dose distributions for the keV imaging range. As the most simple geometry we consider a very large phantom consisting of the medium for which the kernel was calculated in the first place. A dose calculation in a water phantom with extensions much larger than the beam area gives a good estimation of the maximum accuracy achievable with the used algorithm (Figure 6.1a). A more challenging situation is given for smaller phantoms, where pencil beams enter the phantom close to the edge, so that a high number of scattered photons leave the phantom geometry. This is investigated for 2 different beam geometries and phantom shapes: First a single photon beam in combination with a cylindrical phantom (Figure 6.1b) and then to investigate the effect as in a real imaging situation for a 360° rotation of the X-ray tube around a water phantom shaped according to a real patient outline (Figure 6.1c).

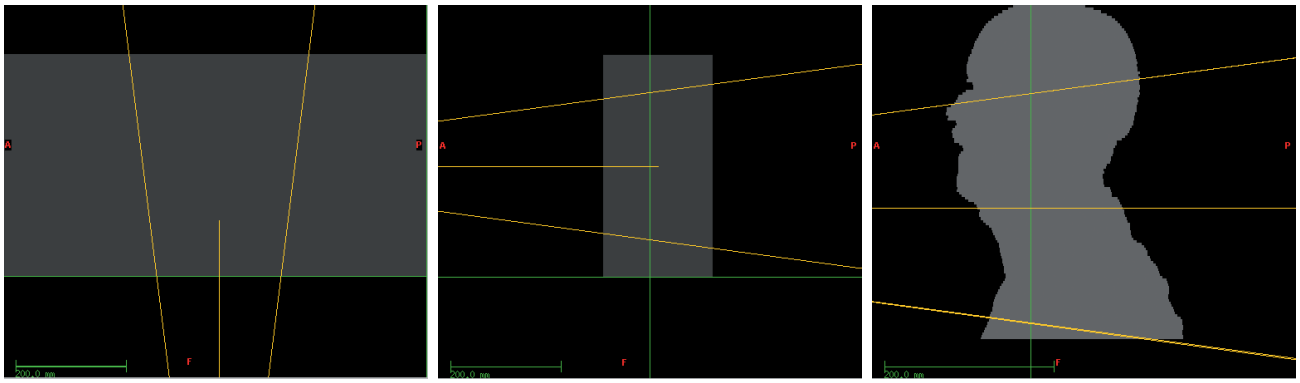

(a) *Large rectangular water phantom* **(b)** *Cylindrical Phantom* **(c)** *Water-filled patient outline*

Figure 6.1.: *Water phantom geometries: Single beam for a large rectangular water phantom, a single beam from the side for a cylindrical phantom. For the water-filled patient outline, the X-ray tube rotates around the cranio-caudal axis of the patient. Depicted in the image is the beam geometry for a sample angle.*

6.1. Methods

6.1.1. Difference maps for dose cubes

Even though the comparison of dose profiles is an important tool to assess the agreement between dose distributions, the quantification of the differences between calculated and simulated doses in profile plots or also in plots of the differences between two profiles themselves is complicated by the statistical variations in the MC-dose. In addition it is limited to a very low number of dose points. To visualize and quantify those differences more efficiently, color-coded 2-dimensional maps of the dose differences were calculated, which offer a much wider overview over the difference distribution within the phantom, by displaying whole slices of the subtracted dose cubes. Shown in the images is the absolute difference D_{diff} between

the dose calculated using the pencil beam algorithm (D_{PB}) and the Monte Carlo simulated dose (D_{MC}), which is normalized to the reference dose value also used in the kernel calculation. The normalization factor for the MC-dose is the reference dose also used for the input of the kernel calculation and is necessary due to the used normalization of the input data. The colorscale for the display of the difference maps uses shades of red and yellow for positive differences (where D_{PB} is larger than D_{MC}) and shades of blue for negative differences (where D_{PB} is smaller than D_{MC}). To increase the visual discrimination between different groups of differences, distinct steps in the shades of red/blue are built in at ± 0.03 and ± 0.05. All differences of ± 0.1 and above are assigned the same color.

6.2. Single Photon Beam for a Large Rectangular Water Phantom

6.2.1. MC-Simulations and Pencil Beam Calculations

Monte Carlo Simulations

As the demanded geometry matches the one used for the simulation of the input data, dose distributions from the kernel input data simulations were used in this chapter. For the exact simulation geometry and parameters the reader is therefore referred to chapter 5.1.3, where the undertaken simulations are described in detail. As a reminder, the important simulation parameters are recalled here: All phase space files were obtained using the electron energy 121kV for the X-ray tube simulation. The main feature of the water phantom geometry is a voxel size in the central area of 3mm x 3mm x 3mm, and for the first voxel plane in z-direction: 3mm x 3mm x 2.5mm. The total phantom extension is 64.3cm x 64.3cm x 50.25cm, which is significantly larger than the field size, which varies from 1cm x 1cm to 35cm x 35cm for SSDs of ranging 70cm to 105cm.

Pencil Beam Calculations

All pencil beam dose calculations were executed using the developer version of the standard treatment planning system in our institution (VIRTUOS, Version 4.7.8,DKFZ Heidelberg) with a pencil beam dose calculation algorithm using the generated pencil beam kernels for the imaging energy range. The water phantom for the pencil beam dose calculation in VIRTUOS was created, so that the voxel sizes and positions of the dose distribution in the central area (larger than the largest field size) match the Monte Carlo simulation geometry. The extension of the phantom was chosen as 512x512x135 with a voxel size of 1.5mm x 1.5mm x 3mm, for the dose calculation it is downsampled to 256x256x135 with a voxel size of 3mm x 3mm x 3mm. As, for this phantom, the slice boundary z_0 in the planning system for the first voxel is determined from the z-positions of the centers of the first two voxels ($z_{center,1}, z_{center,2}$) as $z_0 = z_{center,1} + \frac{1}{2}(z_{center,1} - z_{center,2})$, the plane consisting of 3mm x 3mm x 2.5mm voxels in the Monte Carlo simulation was replaced by two 3mm x 3mm x 1.25mm voxel planes. The total phantom size is therefore 76.8cm x 76.8cm x 40.15cm. The photon beam for the irradiation was set to enter the phantom along the z-axis, as in the MC-simulation, the center of the beam in x- and y-direction was set to be in the center of a voxel for the dose distribution. To avoid the scaling of the pencil beam kernels depending on the Hounsfield Unit, which is built into the standard algorithm and will be described in the next chapter, the lookup table converting Hounsfields Units to electron density was manually adapted, so that all voxel are assigned the electron density of water.

6.2.2. Results

Comparison of dose ratios for varying SSDs

As the output factor and PDD input for the kernel calculation was adapted to specific inputs for each SSD for the algorithm used in this work, this part focuses on the validation of correct scaling of dose values and PDD shapes for different SSDs for a reference field size of 10cm x 10cm. To compare the shape of

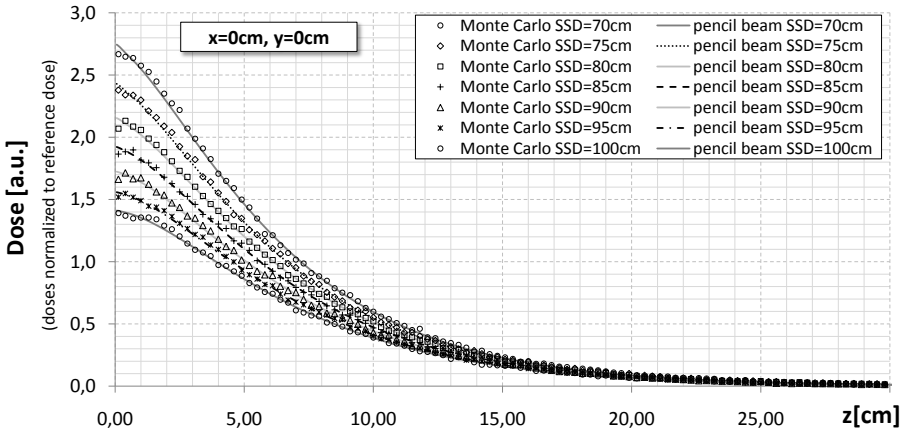

(a) *Depth dose curves*

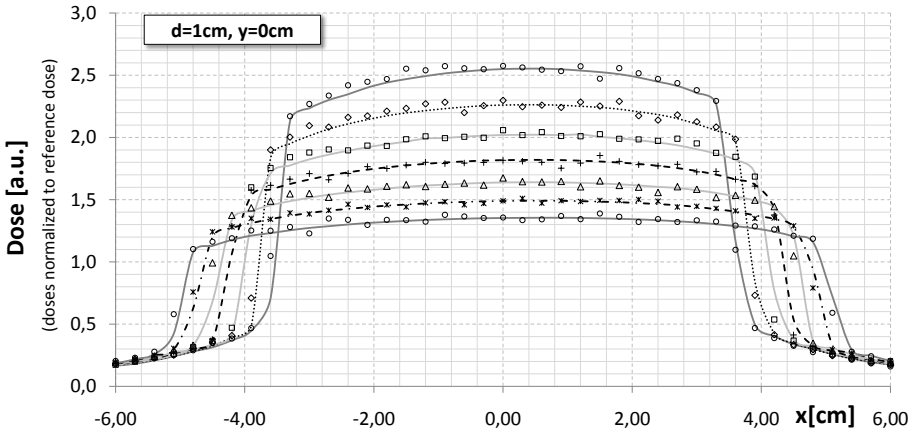

(b) *Profiles along the x-axis*

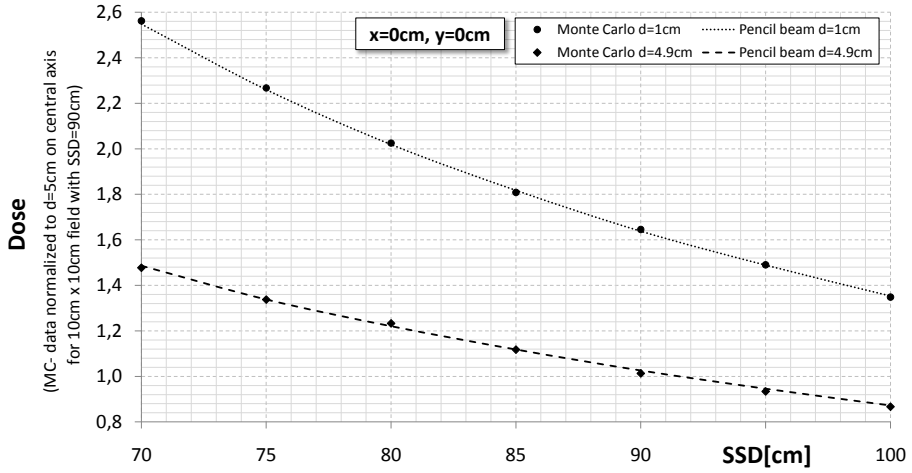

(c) *Comparison of the doses at a reference depth with changing SSD for a field size of 10cm x 10cm*

Figure 6.2.: *Comparison between calculated and simulated depth dose curves (a) and lateral profiles along the x-axis (b) at a depth of 1cm for 10cm x 10cm fields at different SSDs. The depth dose curves generally agree well. The pencil beam x-profiles also match the Monte Carlo simulated ones, also the field sizes at the depth of 1cm for the different SSDs agree well. c Comparison of the doses at a reference depth with changing SSD for a field size of 10cm x 10cm at depth of 1cm and 4.9cm. To decrease the influence of the statistical variation in the Monte Carlo simulation, the voxel size in x-direction for this plot was increased to 9mm for both dose distributions. For a better visual discrimination, the Monte Carlo data is displayed as datapoints, while the pencil beam doses are displayed as lines. This does not imply the availability of additional datapoints for the pencil beam datasets. For both depth, the central axis dose ratios for the different SSDs from the Monte Carlo simulation are well reproduced by the pencil beam algorithm.*

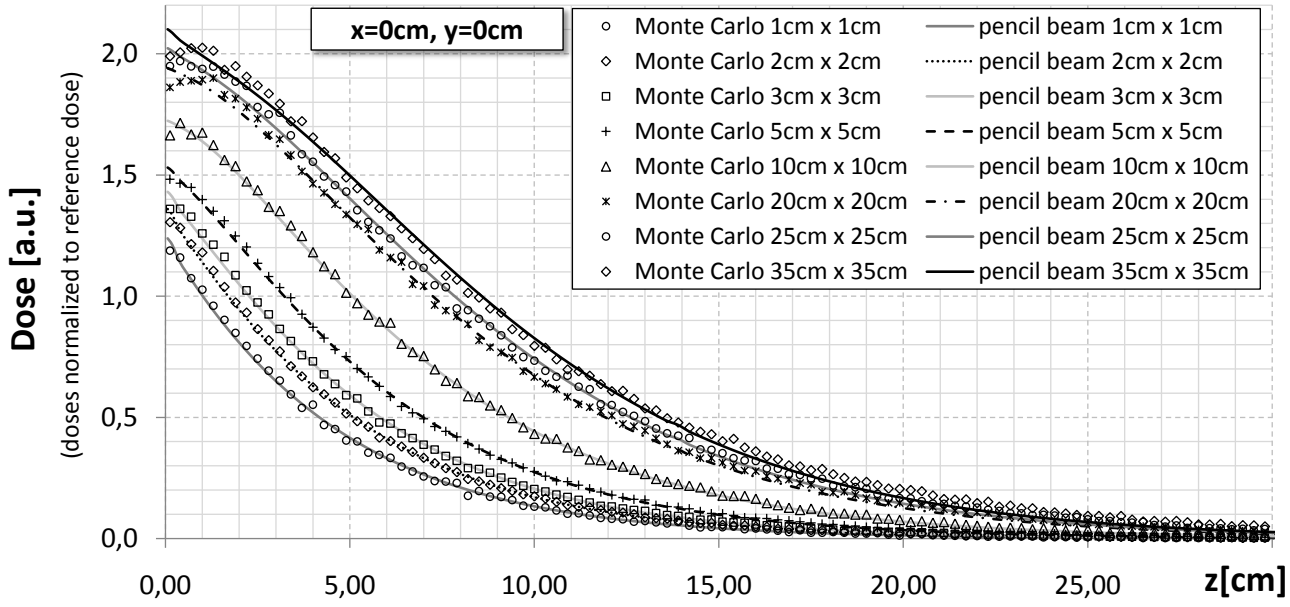

Figure 6.3.: *Comparison between calculated (pencil beam) and simulated (Monte Carlo) profiles along the z-axis. The Monte Carlo profiles are normalized to the dose at the reference point, which is placed at a depth of 5cm on the central axis. The pencil beam profiles are not normalized. Overall, the simulated and calculated profiles show a good visual agreement. Note that for higher depth, the calculated dose for the largest fields is lower than the simulated one.*

the dose distributions, depth dose profiles and lateral profiles were extracted from the dose distributions calculated with the pencil beam algorithm and compared to the normalized simulated profiles. Figure 6.2 shows the comparison for depth dose curves (a) and lateral profiles along the x-axis at a depth of 1cm (b) for SSDs ranging from 70cm to 100cm. For all SSDs, both profiles show a good visual agreement, also the field sizes at a depth of 1cm match the Monte Carlo simulation well. A statistical analysis of the differences between the profiles shows that app. 82.4% of the profile differences for $-24cm < x < 24cm$ are below 3% and almost 90% of the values are below 5%, with much higher differences for all voxels close to the field edges. For the investigation of the correct scaling of the dose at the different SSDs, Figure 6.2c shows the dependence of the dose at the central axis on the SSD at two different depths. To avoid the statistical variation in the Monte-Carlo simulation, the voxel size along the x-axis for this plot was increased to 9mm by averaging the center three voxels from the x-profiles. Even though some of the datapoints do not perfectly coincide, the general agreement between the dose calculated with the pencil beam algorithm and the Monte Carlo dose is good. All absolute differences are below 0.015 and appear randomly, no trend can be observed.

Dose comparison for varying field sizes

This part focusses on the comparison of dose distributions for different field sizes for one selected source-surface-distance to investigate the capability of the pencil beam algorithm to reproduce the matching simulated dose distributions. A key aspect is the dose distribution at points, which are not on the central axis, as this is not part of the input data. An analysis on the calculation of the MC- input data (PDDs and output factors) using the pencil beam algorithm is another point of interest.

Dose Profiles Figures 6.3 and 6.4 show profiles along the x-, y- and z-axis comparing the Monte Carlo simulated dose distribution and the dose distribution calculated with the pencil beam algorithm for different field length ranging from 1cm to 35cm. In general the visual agreement between the profiles is good, for a quantitative analysis see the next paragraph. Though most of the differences are due to the statistical variation of the simulated dose, systematic errors of the pencil beam dose calculation can be identified especially for the largest field considered.

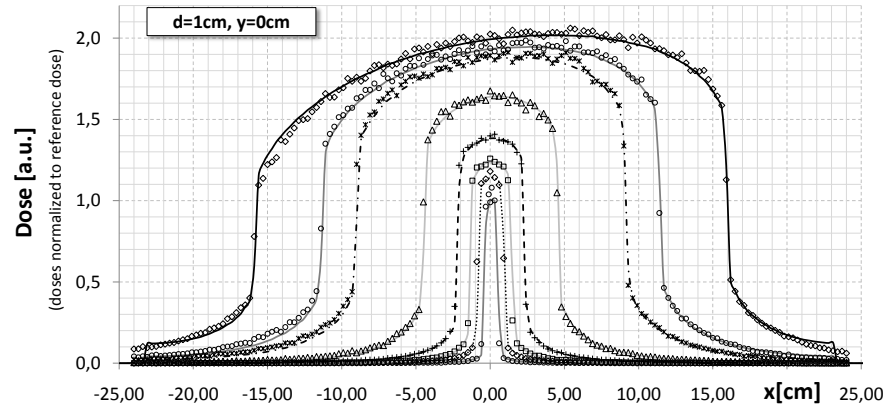

(a) *Profiles along x-axis at a depth of 1cm*

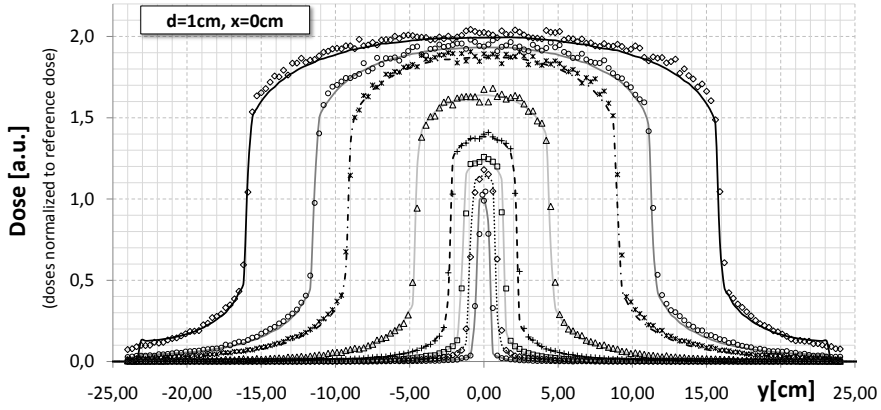

(b) *Profiles along y-axis at a depth of 1cm*

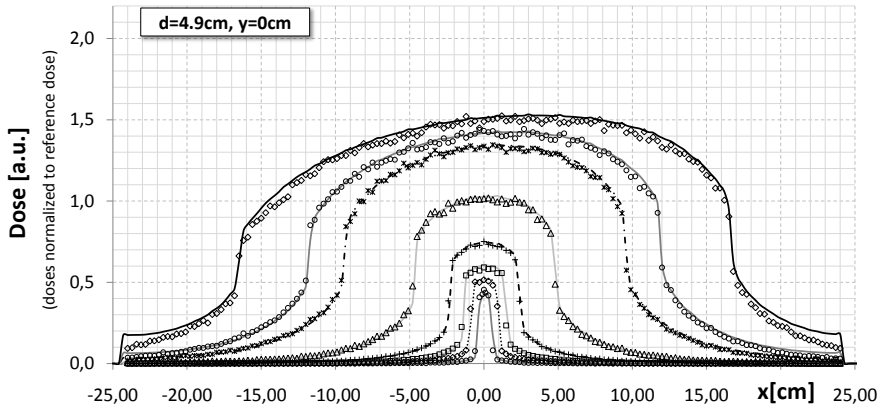

(c) *Profiles along x-axis at a depth of 4.9cm*

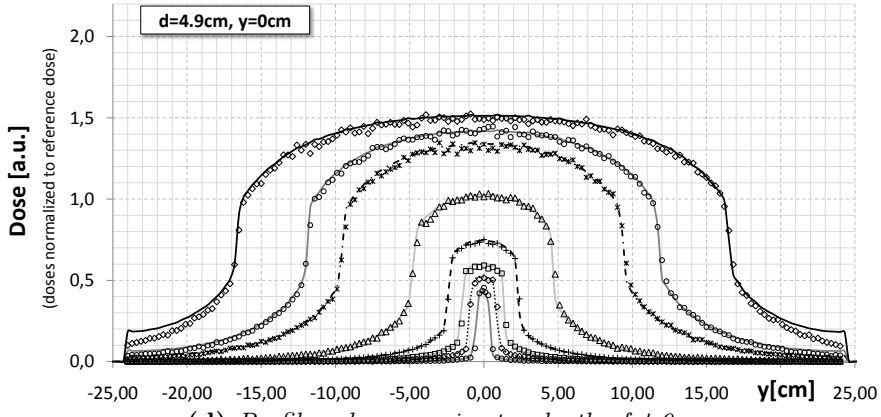

(d) *Profiles along y-axis at a depth of 4.9cm*

Figure 6.4.: *Comparison between calculated (pencil beam) and simulated (Monte Carlo) profiles along the x-, y- and z-axis. The Monte Carlo profiles are normalized to the dose at the reference point, which is placed at a depth of 5cm on the central axis. The pencil beam profiles are not normalized. (a) and (c): Profiles along the x-axis at depths of 1cm and 4.9cm. Again the profiles match well for most field sizes. For the largest field (35cm x 35cm) at a depth of 1cm the pencil beam calculation slightly underestimates the dose most of the voxels, for high negative x-values, the dose is overestimated by the pencil beam calculation. (b) and (d): Profiles along the y-axis at depths of 1cm and 4.9cm. As before, the profiles generally match for most field sizes. Again, for the largest field (35cm x 35cm) the pencil beam calculation slightly underestimates the dose at a depth of 1cm. This effect is not visible on either of the profiles at a depth of 4.9cm.*

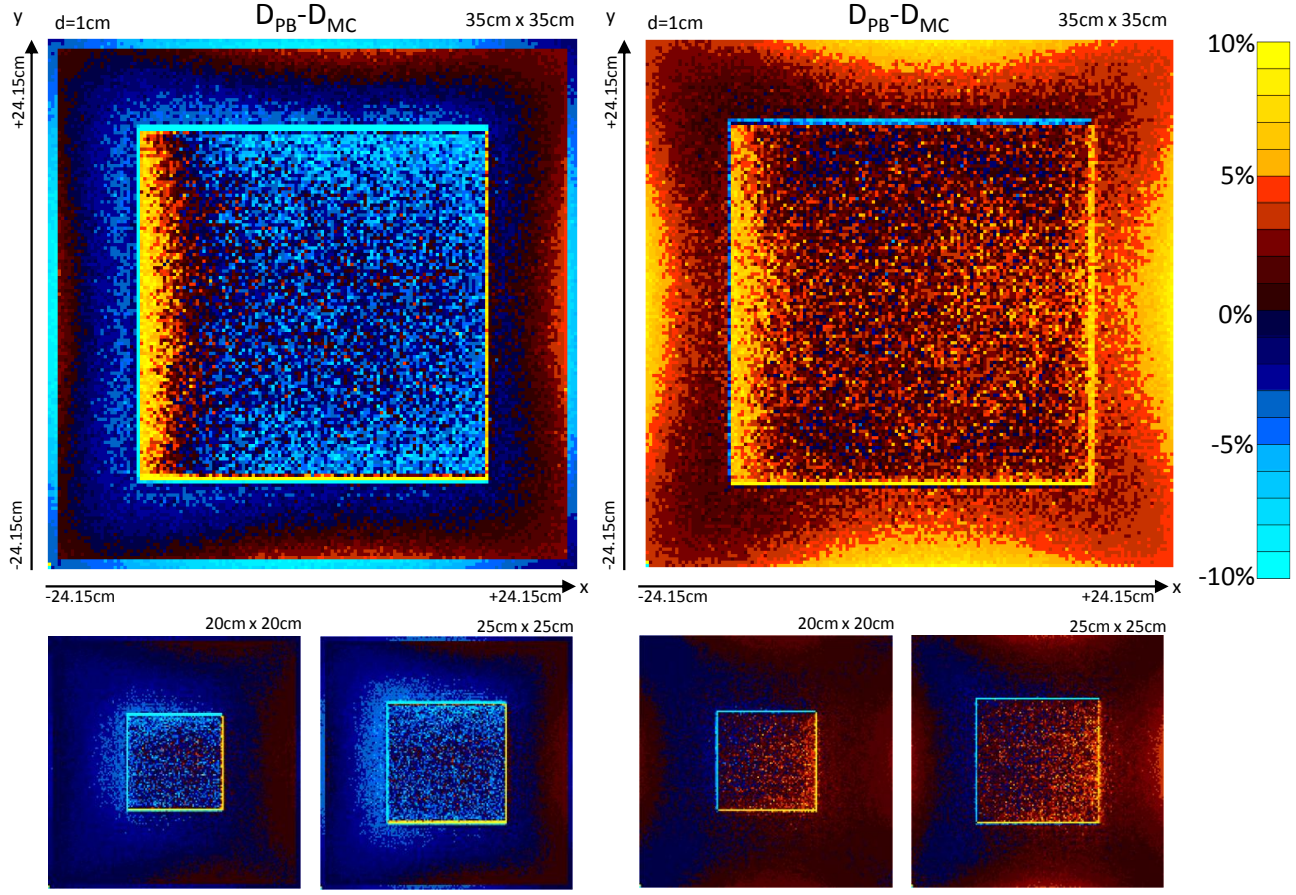

(a) *Slice perpendicular to the z-axis at a d=1cm* **(b)** *Slice perpendicular to the z-axis at d=4.9cm*

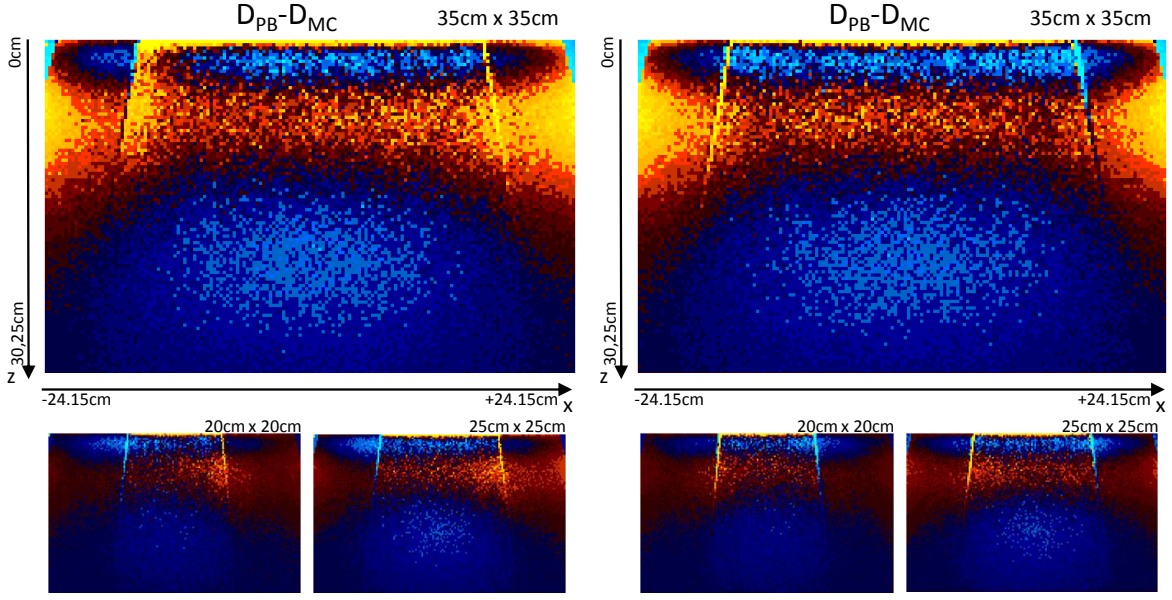

(c) *Slice perpendicular to the the y-axis* **(d)** *Slice perpendicular to the the y-axis*

Figure 6.5.: *Difference maps for larger fields at an SSD of 90cm. Displayed are the absolute differences between the pencil beam dose and the simulated dose in a subvolume of 48.3cm x 48.3cm x 30.25cm of the larger water phantom. The doses are normalized to the dose at a depth of 5cm on the central axis for the 10cm x 10cm field at the reference SSD of 90cm. (a) and (b) Slices perpendicular to the central axis at depths of 1cm and 4.9cm. The blueish appearance of a indicates an overestimation of the dose, the reddish appearance of b an underestimation. The orange/yellow area at the left field edge for both slices imply an overestimation of more than 0.05 in this area. (c) and (c) Slices perpendicular to the x-axis (top) and the y-axis (bottom). The effect of the overestimated dose for highly negative x-values at lower depth is clearly visible in the bottom image, the more prominent effect is the alternation between over- and underestimation with depth.*

The profiles along the central axis are plotted in Figure 6.3, a comparison of the calculated and simluated dose reveals that for the largest fields, especially the 35cm x 35cm field, the curvature of the depth dose curve is not reproduced by the pencil beam algorithm. For all large fields ($\geq 20cm$), the dose at very high depth is underestimated, and overstimated for very low depth. For the largest field smaller deviations are also clearly visible for most other depths.
The profile along the x- and y-axis for two different depth are shown in Figure 6.4. For both direction, the profiles match well for smaller fields, for the largest field (35cm), the pencil beam algorithm seems to slightly underestimate the dose at a depth of 1cm. This effect is not visible at a depth of 4.9cm.
Another effect is only visible in the x-profiles for the largest field: For high negative x-values the dose is overestimated inside the primary beam area and understimated outside the beam area. In combination, this implies a changed scatter behaviour of the photon beam in this area. This matches the fact, that in this area of the beam, the photon beam contains a smaller fraction of low energy photons due to absorption in the target, than in the center of the beam, where the kernel was calculated. This effect can also be observed a depth of 4.9cm, though to a lower extent.
For both profile directions at a depth of 4.9cm, another effect is visible for the larger fields for very high distances from the central axis. The dose outside the primary beam area is overestimated by the pencil beam algorithm until the geometric cutoff of the dose calculation algorithm is reached and the pencil beam dose is set to 0. This is an artfact due to the limited size of the pencil beam kernel calculation area, which depends on the kernel size itself. It only plays a role, if the field size is large enough, so that the dose outside the calculation area of the pencil beam is not negligible.

Difference maps To further quantify the observed differences but also to extend the investigation to points further away from the axis, difference maps as described above were employed. The display of a larger amount of voxels in the vicinity of a specific voxel allows for a statistic analysis of errors in certain areas of the beam. Due to the normalization of the dose cube, all difference values are also normalized to the dose value at reference conditions ((x,y,d)=(0,0,5)cm,SSD=90cm, fieldsize = 10cm x 10cm). All percentage values are also relative to that dose.
As the profiles for the 35cm x 35cm field showed the highest differences between pencil beam calculated and simulated dose distributions, a selection of the difference maps for a field side length of 35cm are shown in Figure 6.5. For comparison, the smaller maps show the situation in the same position for field side length of 25cm and 20cm . In all of the difference maps, the field edges are clearly visible as very high differences (positive or negative). This is due to the high gradient of the dose distribution in this area which leads to very high differences even for small deviation in the positioning of the field.
The trends, which could be observed in the profile plots, are also visible in the respective 2D-vizualisation of the differences. The general underestimation of the dose at a depth of 1cm (app. 2%), is represented by the blue color of most of the voxels inside the beam area in Figure 6.5a. The differences are larger in the corners of the field and to app 4.6%.
The overestimation of the dose for negative x-values is clearly visible as a yellow area at the left side of the field, which indicates that the difference exceeds 5% for a high fraction of voxels at the field edge. The yellow area is not visible for the 25cm x 25cm or the 20cm x 20cm field.
At a depth of 4.9cm (Figure 6.5b) most voxels are displayed in a shade of red or yellow indicating an obvious overestimation of the dose (app. 2%), which could hardly be seen in the profiles. At this depth, the yellow area at the edge of the field appears to be smaller and less intense, though the average difference close to the field edge at the left side is approximately the same as for a depth of 1cm. Again, the maps for the smaller field show, that the differences are much lower than for the large field, the distinct yellow area at the field edge is also not visible. Most voxels appear in very dark shades of red or blue, indicating, that the difference is below 3%.
All of the above can also be seen in the slices perpendicular to the x- and y-axis on the right side of Figure 6.5, when focussing at the respective depth. The most prominent feature of these slices is the alternating over- and underestimation of the dose for different depth in the phantom. Again, this effect is much lower for smaller fields.
To further analyze this pattern, Figure 6.6 shows a plot summarizing histograms of the differences as

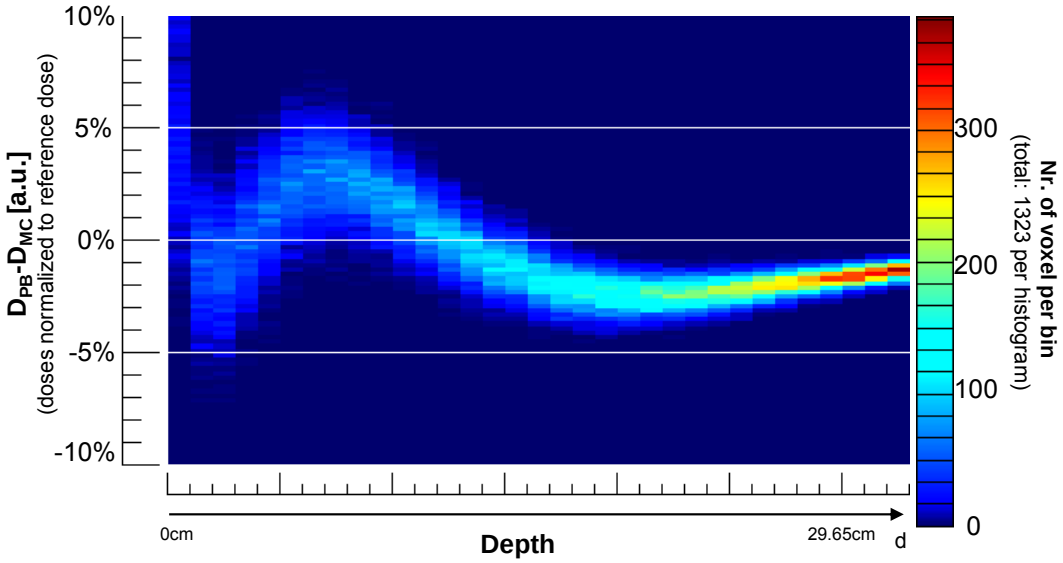

Figure 6.6.: *Summary of histograms of dose cube differences along the depth in water. Each column shows one histogram of differences between the pencil beam calculated dose and the normalized Monte Carlo dose. For every histogram a volume of 21x21x3 voxels was taken into account, histograms were calculated in steps of 9mm in depth with a binsize of 0.2%, the number of voxels per bin is colorcoded. Note that for the maxima, the shape of the curve is very similar to the plot of the difference between the PDD and the linear fit in the kernel calculation algorithm shown in Figure 5.8 in chapter 5.2.3.*

a function of depth. In this plot, the horizontal axis is the depth axis. Each histogram summarizes a volume of 21 x 21 x 3 voxels, histograms are calculated at steps of 3 voxels (9mm) using a binsize of 0.2%. The number of voxels per bin is color-coded, the respective difference value for the bin is denoted on the vertiacel axis. Considering only the maxima of the histograms, the similarity between this plot and the plot of the differences between the PDDs and the linear fit in the kernel calculation algorithm is obvious. Again the dose is overstimated for very low depth. This is followed by an area of underestimation and a larger area of overestimation. The extent of both is app. 3% on average. For larger depths, the dose is underestimated by 2%-3%. All of these features can be traced back to the fit of the PDDs in the kernel calculation algorithm. Also visible in the difference maps is the kernel size artefact for the 35cm x 35cm field, which produces the yellow areas outside the primary beam area at depth around 5cm, meaning that the dose is overestimated by app. 10%.

6.2.3. Summary

For fields of up to 25cm x 25cm, the pencil beam algorithm calculates dose distributions, that match the simulated distribution to less than a few percent. For larger fields, significant errors of up to 5% occur due to the fit of the PDDs. For high negative x-values the differences can even exceed 8-10%, due to the change in the photon spectrum caused by absorption of low energy photons in the target. For field sizes close to size of the pencil beam calculation area (e.g. 35cm x 35cm), which depends on the kernel size, a kernel size of 512 x 512 with a resolution of 1mm can lead to an overestimation of the scattered dose in the low dose region outside the primary beam area by app. 10%. For imaging applications, the beam size is usually below 30cm, so that a much lower effect is expectid in this case.

6.3. Single Photon Beam for a Small Cylindrical Phantom

Compared to the large water phantom, the small cylindrical phantom is more challenging for the pencil beam algorithm. To investigate the effect on the accuracy of the algorithm for a single beam direction, dose distributions simulated with Monte Carlo and calculated with the pencil beam algorithm were

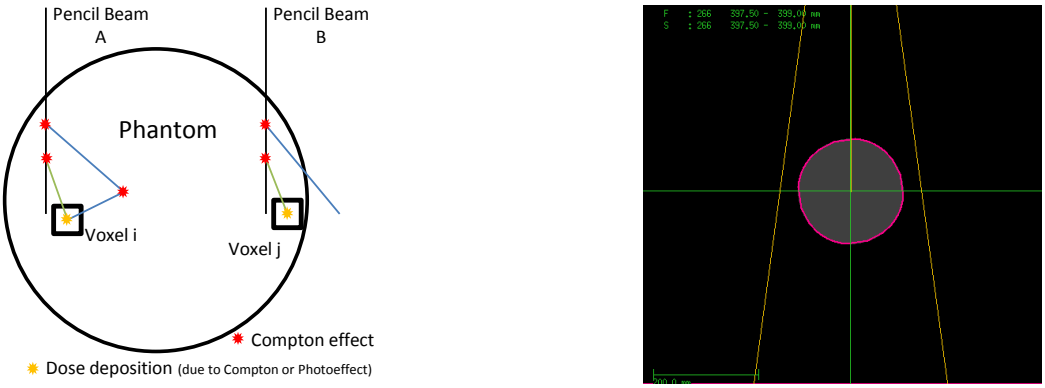

(a) *Scatter situation at the boundaries of cylinder* **(b)** *Cylindrical Phantom: Phantom and beam geometry*

Figure 6.7.: *Cylindrical Phantom: The cylindrical phantom is more challenging for the pencil beam algorithm due to the scatter situation shown in (a), where the difference between the blue path for pencil beam A and B cannot be accounted for. (b) shows the phantom and beam geometry used in this section.*

compared for a water phantom, which is closer to a real patient geometry but still offers a regular shape. The challenge of such a geometry is illustrated in Figure 6.7a. The pencil beam kernel model accounts for dose contributions due to scattered photons for the pencil beams A and B to an offaxis voxel i or j without knowing the exact path or primary interaction point of the scattered photon. E.g. the photon paths depicted in green and blue for pencil beam A cannot be distinguished in the pencil beam algorithm, when calculating the dose to voxel i. This gives rise to the problem, that in a situation as for pencil beam B, the blue path cannot be accounted for when calculating the dose distribution in voxel j. This leads to an overestimation of dose close phantom boundaries, which decreases with the angle between the boundary and the photon beam axis. The effect is more pronounced for smaller energies (e.g. keV range) than for larger energies (MeV range) due to the increased probability for high scatter angles and the decreased fraction of the energy transferred from the incoming photon to the outgoing electron in the Compton effect, and is therefore of special interest for this work.

6.3.1. MC-Simulation and Pencil Beam Calculations

Phantom Creation & Beam geometry

The cylindrical phantom with a radius of app. 20cm in the x-y-plane of the patient coordinate system was created using the planning system VIRTUOS. All voxels within the phantom were set to a Hounsfield Unit of 0HU, all voxels outside the phantom (CT-cube size: 76.8cm x 76.8cm x 40.5cm) were set to a value of -1024HU. For the Monte Carlo simulations, the phantom was imported to DOSXYZnrc as described in chapter 6.4.1, leading to the elemental composition of water with a mass density of $1 g/cm^3$ inside the phantom and air with a mass density of $0.0138 g/cm^3$ outside the phantom. For both dose calculation methods, the voxel size is 3mm x 3mm x 3mm. The isocenter was set to the central axis of the cylinder at app. half of the length of the cylinder with an irradiation of the phantom in along the y-axis of the patient coordinate system. A field size of 27cm x 27cm was used, meaning that the field boundaries are outside the phantom in the x-direction. Figure 6.7b shows the phantom and beam geometry in the x-y-plane in the planning system.

Monte Carlo Simulations

To achieve a field size of 27cm x 27cm in the DOSXYZnrc simulation, a BEAMnrc simulation of the second step of the X-ray tube simulation as described in chapter 5.1.3 on the kernel input data simulation was executed with a matching collimator opening, to obtain a phase space file at a distance of 60cm from the source with the respective field size. This phase space file contains app. $1.88 * 10^8$ particles, and was used as a phase space file source with a fixed beam direction. A total number of $5 * 10^9$ histories was simulated, each particle read from the phase space file was recycled 50 times.

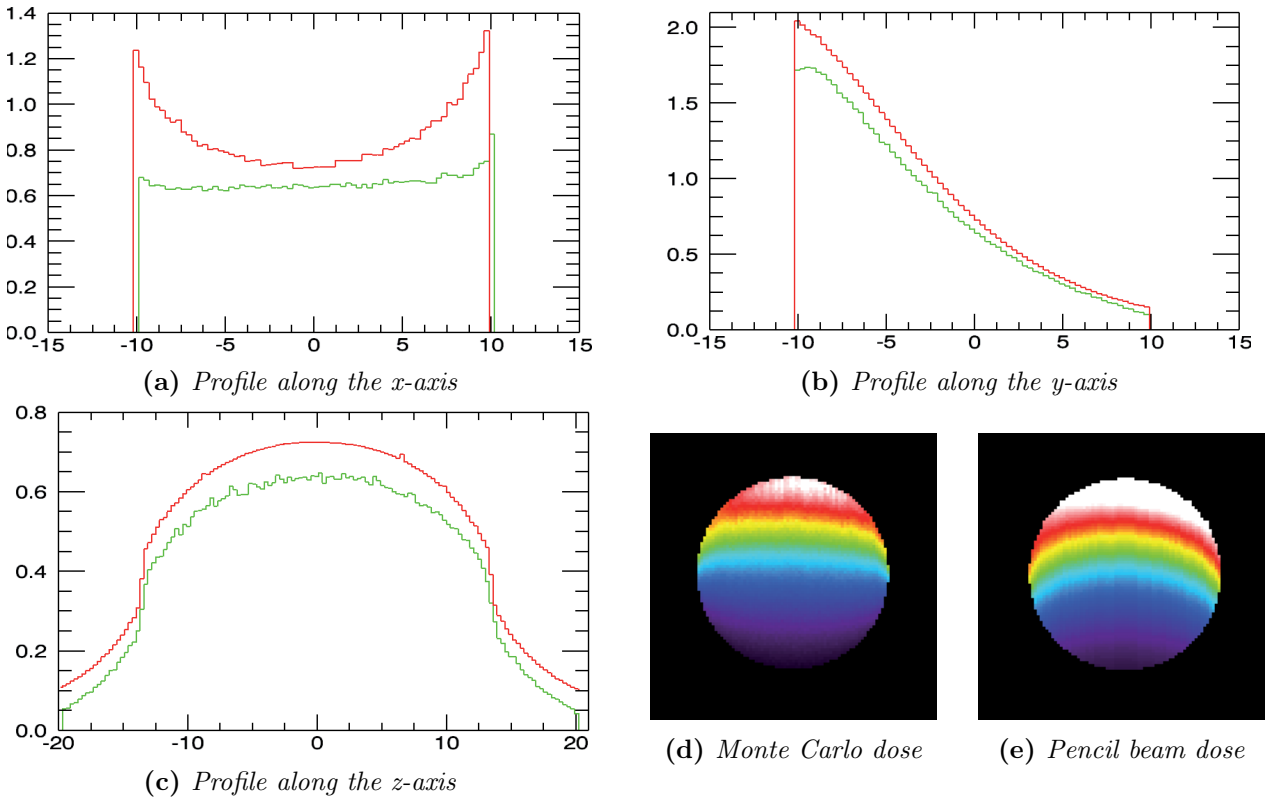

(a) *Profile along the x-axis*

(b) *Profile along the y-axis*

(c) *Profile along the z-axis*

(d) *Monte Carlo dose*

(e) *Pencil beam dose*

Figure 6.8.: *Cylindrical Phantom: (a) - (c) Profiles along the x-, y- and z-axis using the dose conversion factor derived in chapter 5.2.2. The pencil beam dose is plotted in red, the MC-dose is plotted in green. The additional dose in the pencil beam algorithm at the boundaries of the phantom due to the described scatter situation is clearly visible in (a). (d) Transversal slice of the dose distribution obtained in the Monte Carlo simulation. (e) Transversal slice of the dose distribution obtained with the pencil beam algorithm using the same colorscale as in (d).*

Pencil Beam Calculations

The pencil beam calculation was again executed using the planning system VIRTUOS (Version 4.7.5,DKFZ Heidelberg) using the obtained pencil beam kernel for a the 121kV-photon beam. The effect of the air outside the phantom is negligible, within the water phantom the unchanged pencil beam kernel was used. The gantry angle (which is used as the angle between the y-axis and the beam direction) was set to 0°.

6.3.2. Results

When comparing the simulated and pencil beam calculated dose distributions for the water filled patient outline, the obvious choice for the dose normalization factor is the dose conversion factor obtained in chapter 5.2.2 (to normalize the simulated dose). As the dose is calculated in water, this should match the dose normalization in the pencil beam calculation built into the pencil beam kernel. Figure 6.8 shows the result of the comparison between the simulated and the pencil beam dose distributions. Figures 6.8d and 6.8e show transversal slices of the respective normalized dose distributions using the same colorscale for both images. A general overestimation of the dose by the pencil beam algorithm is visible. As expected due to the effect described above, the overestimation of the dose increases towards the edges.
Figures 6.8a - 6.8c show dose profiles along the x-, y- and z-axis[1]. Again, the dose overstimation at the edges of the phantom, which can be seen in the x-profiles, is the most prominent feature, but an overestimation of the dose is also visible along the axis of the cylinder as well as in the y-profile (depth dose profile). The shift in x-direction by 1 voxel, which can be seen in the x-profile, is due to a different scaling algorithm upon the reduction of the CT resolution for the dose calculation. Figure 6.9a shows the difference $D_{PB} - D_{MC}$ for the same normalization. In the central area (of the x-axis), the difference

[1]Unless stated otherwise, all axis denominations refer to the patient coordinate system

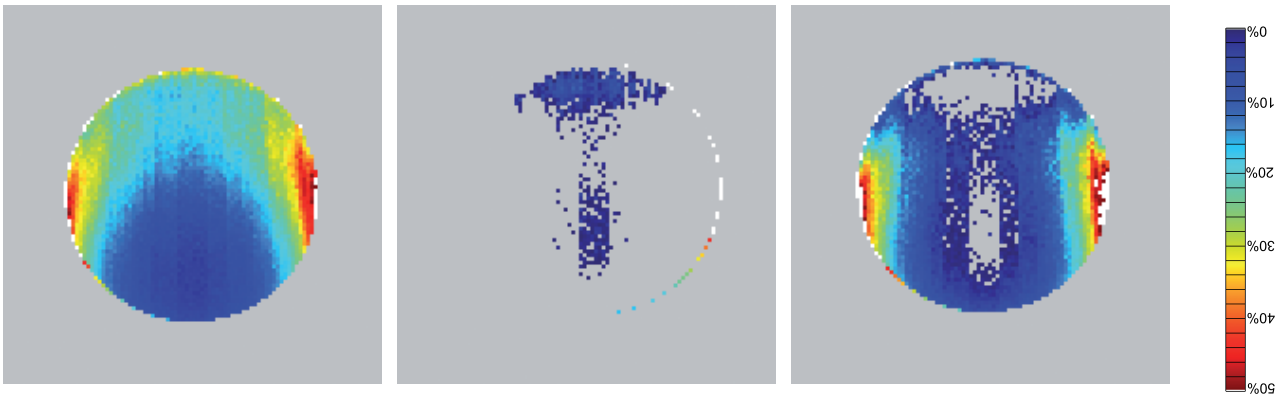

(a) *Normalized to normalization dose (positive differences)* **(b)** *Normalized to Isocenter (negative differences)* **(c)** *Normalized to Isocenter (positive differences)*

Figure 6.9.: *Cylindrical Phantom: Absolute dose differences for both normalizations. (a) shows the differences $D_{PB} - D_{MC}$ for the normalization using the dose conversion factor as described in chapter 5.2.2 using the displayed colorbar. (b) and (c) show the same difference for the normalization of both cube to their respective dose at the isocenter. For the negative differences, the colorbar is mirrored at 0%.*

is between 10% and 20% for app. the upper half of the phantom and decreases to below 10% for higher depth (All percentage values are absolute values and refer to the normalization dose). At both edges of the phantom, the difference increases to 40% to 50% for a small area at the boundaries (app. 3-5 voxels). Considering relative difference $(D_{PB} - D_{MC})/D_{PB}$ (no Figure), for the central area, the values again range between app. 10% and 20% with an increase towards higher depths. Due to the combination of a low absolute dose and a relatively high absolute difference, relative differences of the boundary voxels at higher depth (app. lower half circle, width 5 voxels) increase from app. 50% to 100%.
Normalizing both dose cubes to the respective dose at the isocenter (mean of 4x4x5 voxels) improves the agreement especially for the profiles along the y- and z-axis (Figure 6.10a). Still, the overestimation at the edges of the phantom cannot be compensated for.

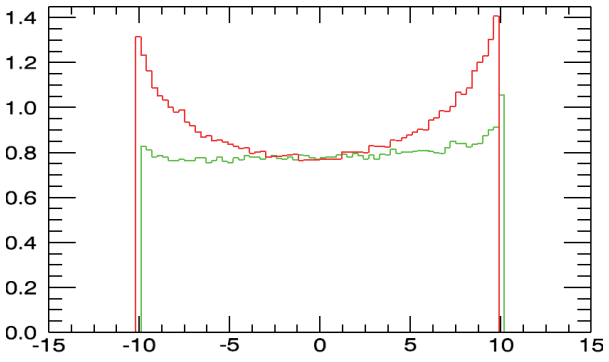

(a) *Profile along the x-axis*

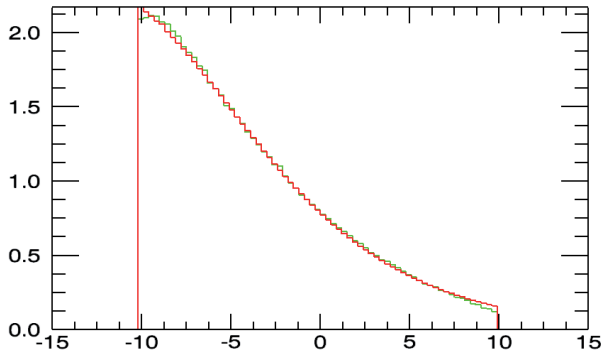

(b) *Profile along the y-axis*

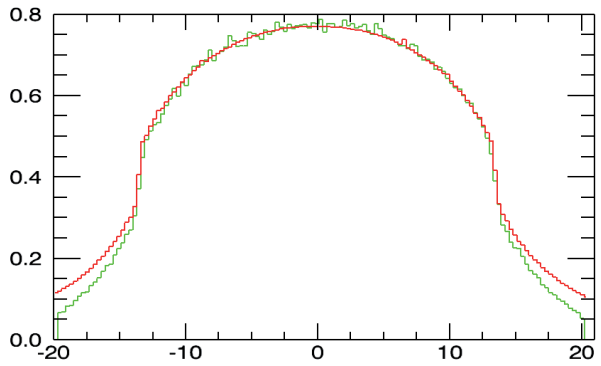

(c) *Profile along the z-axis*

Figure 6.10.: *Cylindrical Phantom: (a) - (c) Profiles along the x-, y- and z-axis normalized to the isocenter. The pencil beam dose is plotted in red, the MC-dose is plotted in green. Even though the profiles along the y- and z-axis show a much better agreement, the profile along the x-axis shows that the additional dose in the pencil beam algorithm at the boundaries of the phantom due to the described scatter situation cannot be compensated.*

Using this normalization, positive and negative differences $D_{PB} - D_{MC}$ occur. Transversal slices are shown in Figure 6.9b and b, for the negative differences, the colorbar is inverted to 0%–50% instead of 0%-50%. It can be seen, that for most of the voxels, an absolute difference of 10% is not exceeded for most of the voxels. Only at the very edges, the differences again increase to app. 50%. The relative differences are also decreased to values between -10% and 10% for most voxels, the area, where the relative differences increase from app. 50% to 100% is decreased to a width of 1 voxel and a smaller portion of the edge.

6.4. Cone Beam CT Acquisition for a Water-filled Patient Outline

Another step towards a dose calculation on patient geometries is the transition to a phantom with a real patient outline. To investigate the above described effect on the accuracy of the algorithm for a cone beam CT acquisition (360° rotation of the X-ray tube) with respect to patient geometries, dose distributions simulated with Monte Carlo and calculated with the pencil beam algorithm were compared for a water phantom, which is based on the outline of a real patient in a CT-dataset. The challenge of such a geometry is the same as described for the small cylindrical phantom in chapter 6.3, the irregular shape due to the anatomic features in the patient outline increase the surface of the phantom producing even more edges, but due to the rotating X-ray tube, the differences for different beam angles can be cancelled out, so that a quantification of the effect for a cone beam geometry provides important additional information.

6.4.1. MC-Simulation and Pencil Beam Calculation

Phantom Creation

To obtain the water filled patient outline, a patient CT-dataset was loaded into the planning system VIRTUOS. Volumes in the CT-dataset, such as the patient outline as well as organs at risk or target volumes were available from the treatment planning process for the patient. The isocenter was set to the center of the main target volume. All voxels within the patient outline were set to a Hounsfield value of 0HU, all voxels outside the outline to a value of -1024HU, which is the smallest possible HU-value in the used planning system.
To import the dataset into the DOSXYZnrc Monte Carlo simulation, the CT-dataset was converted to a .egsphant phantom definition file using a special conversion table consisting of only two materials: The first being air (material composition as specified in the Schneider conversion table) associated with a mass density $0.0138 g/cm^3$ for all voxels with a Hounsfield Unit of -1024. The second material was water with a mass density of $1 g/cm^3$ for all voxels with a Hounsfield Unit of above -950HU (meaning that the interpolated boundary voxels are also set to water). Due to the assignment of Hounsfield values in the planning system, no air voxels occur within the phantom (e.g. in the in the trachea).

Simulation Settings

A typical cone beam CT imaging geometry was chosen for the simulation, where the X-ray tube rotates 360° around the patient with a field size of 27cm x 27cm, with a distance between source and isocenter of 100cm. The phase space file described in 6.3.1 was used as the particle source. A total number of $5 * 10^9$ histories was simulated, each particle read from the phase space file was recycled 50 times. No electron transport was simulated, the cutoff energy for photon transport was set to 10keV. EGSnrc transport parameters were set as described in chapter 5.1.3.

Pencil Beam Calculation

The pencil beam calculation was again executed using the planning system VIRTUOS (Version 4.7.5,DKFZ Heidelberg) using the obtained pencil beam kernel for the 121kV-photon beam. The depth scaling factor

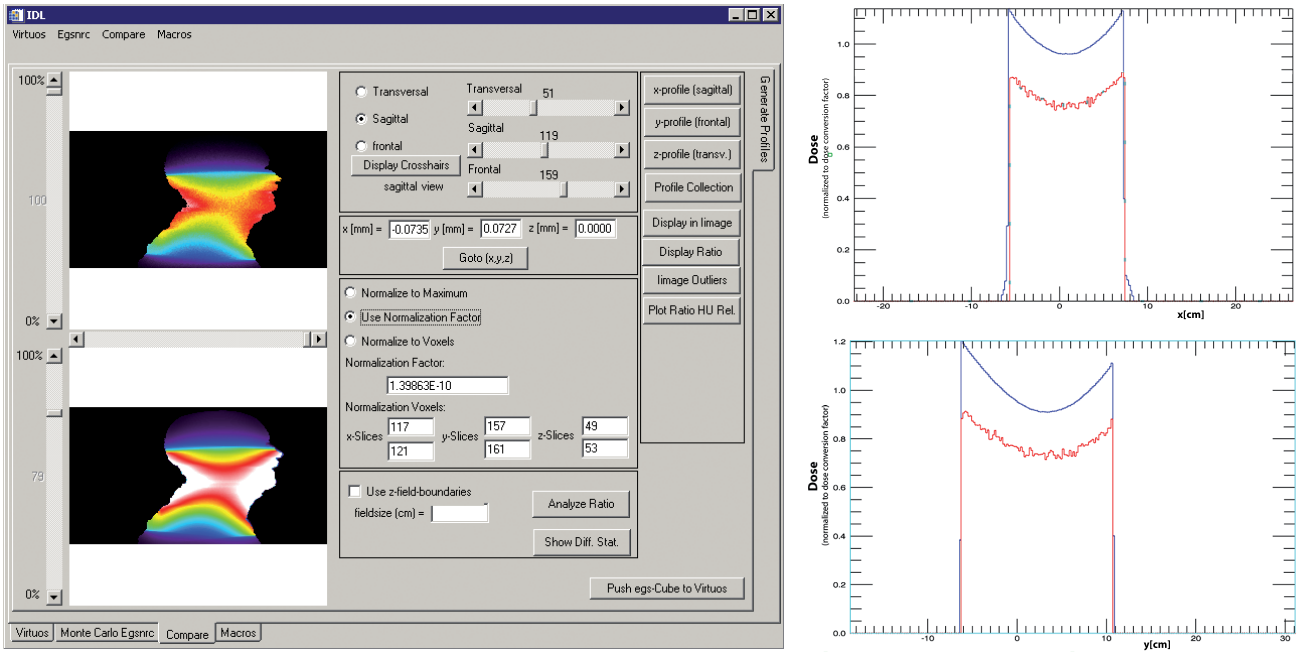

Figure 6.11.: *Sagittal Slices and x- and y-profile through the isocenter from the Monte Carlo and pencil beam dose distributions for the water filled patient outline. The simulated dose is displayed in the top image (in profiles: red), the pencil beam dose in the bottom image (in profiles: blue). The Monte Carlo simulated dose distribution is normalized using the normalization factor obtained in chapter 5.2.2 to match the pencil beam normalization. As expected, the dose is overestimated in most areas due to the scatter situation in the non-infinite phantom. In this display, the voxels are assumed to be isotropic, the stretch in the z-direction due to the larger slice thickness is not applied.*

for air (-1050HU - -950HU) was set to 0.001, so that the effect of the air around the water phantom is negligible, the depth scaling factor for water ($\geq$-949HU) was set to 1, so that the unchanged pencil beam kernel was used. A gantry rotation of 360° with angular steps of 5° between the beams resulted in the calculation of 72 beams, each with a field size of 27cm x 27cm in the isocenter plane and a beam weight of $\frac{1}{72}$ each.

6.4.2. Results

When comparing the simulated and pencil beam calculated dose distributions for the water filled patient outline, again the obvious choice for the dose normalization factor is the dose conversion factor obtained in chapter 5.2.2 (to normalize the simulated dose). Figure 6.11 shows sagittal slices through the isocenter of the resulting dose distributions from the MC-simulation and the pencil beam algorithm in the planning system using this normalization. As the simulated dose in the IDL-program is handled in $Gy/10^{10}$ source particles instead of Gy/source particle, the normalization factor displayed in the interface is 10^{10} times the reported factor. As for the single beam for the cylindrical phantom, the dose is overestimated in most areas due to the scatter situation in the non-infinite phantom. This can be seen in the dose slices, where the pencil beam dose (bottom image) is displayed in lighter colors (especially white instead of red) than the MC-dose (top image), as well as in the profile along the patients x-axis (perpendicular to the shown slices) and the y-axis, where the simulated dose is shown in red and the pencil beam dose is shown in blue. The overestimation is more pronounced in areas, where the phantom extensions are smaller (neck region), as in this case, all voxels are close to the boundaries and therefore affected by the above described problems with the scattered photons.
To investigate the potential of a different normalization, which will later be implicit due to the use of the dose scaling factors (see chapter 7 and 9.1.1), Figure 6.12 shows sagittal slices for a normalization of both dose distributions to the respective dose at the isocenter (normalization volume 5x5x5 voxels to increase statistics in MC). In the figure, the position of the isocenter is marked with crosshairs. In the interface, this can be achieved using the normalize to voxels option and setting the voxel boundaries accordingly.

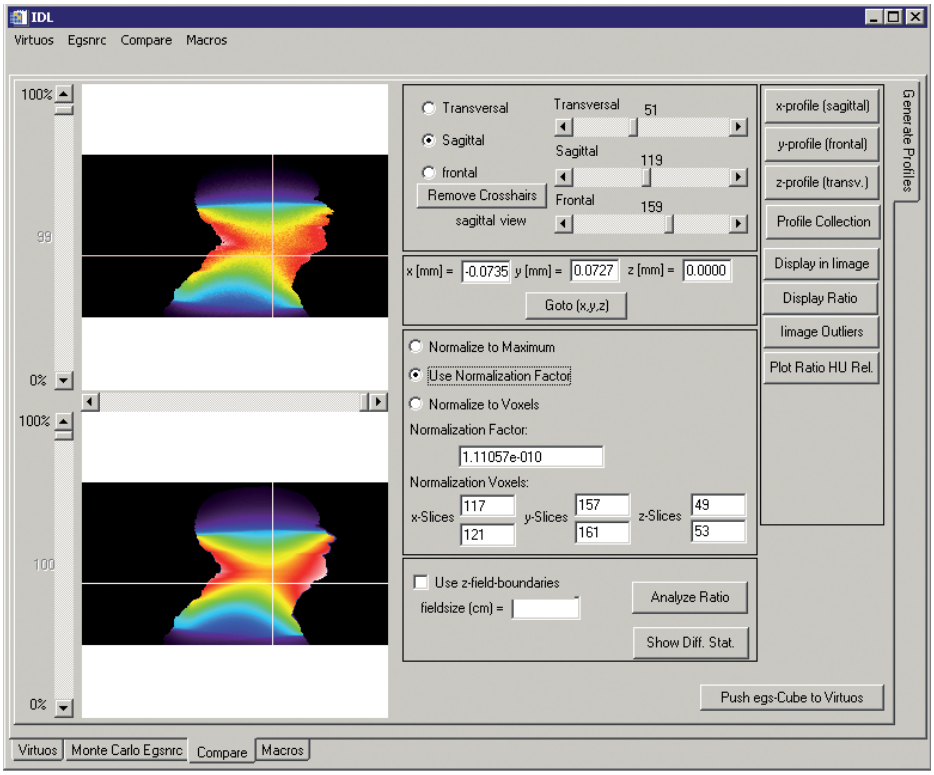

Figure 6.12.: *Sagittal Slices from the Monte Carlo and pencil beam dose distributions for the water filled patient outline normalized to isocenter (volume of 5x5x5 voxels). Using the normalize to voxels option in the GUI, the dose distributions are displayed using the normalization dose as the maximum value for the colorscale. In addition, the corresponding normalization factor is calculated and displayed. For display purposes, the calculated normalization factor was used, as in this case, the maximum for the colorscale is defined by the maximum of the pencil beam dose distribution and the MC-dose is scaled accordingly. Using this normalization, the similarity between the dose distributions is much higher.*

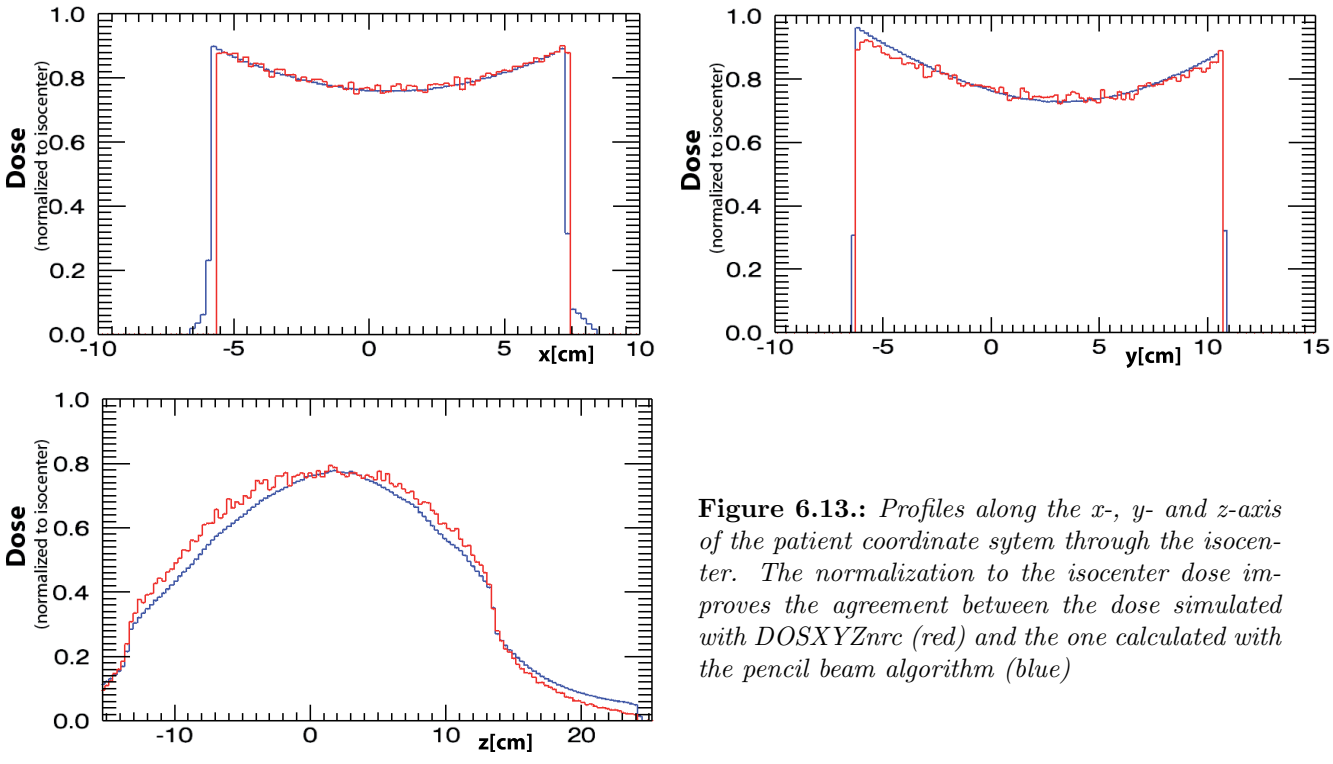

Figure 6.13.: *Profiles along the x-, y- and z-axis of the patient coordinate sytem through the isocenter. The normalization to the isocenter dose improves the agreement between the dose simulated with DOSXYZnrc (red) and the one calculated with the pencil beam algorithm (blue)*

A visual evaluation of the shown slices shows a much better agreement between the simulated and the calculated dose distribution for this normalization. This can also be seen in the profiles through the isocenter along the x-y- and z-axis of the patient coordinate system, which are shown in Figure 6.13. For this normalization, a statistical analysis of the relative difference ($D_{PB} - D_{MC}$) within the water phantom yields an average relative difference of 1.8% of the isocenter dose with a standard deviation of 5.6% within a range of $\pm 13.5cm$ (=1/2 * field side length) along the z-direction, for 99% of the voxels the difference falls within the interval [-10%,+10%]. In Figure 6.14 difference maps as described in chapter 6.1.1 for the absolute difference between the normalized dose distributions are plotted in addition to an isocentric frontal slice for both methods of dose assessment. The colorscale for the difference maps is also plotted in the Figure and ranges from -10% to +10%. In the frontal difference maps, a larger area of differences larger than 10% is visible between the shoulders and the neck.
This is due to the fact, that the pencil beam dose calculation algorithm assumes the deposition of dose due to scattered photons from pencil beams at the shoulder region of the patient. In the slices with the different orientations, within the water phantom, two major regions can be identified, where the absolute differences exceed 10% for a higher number of neighboring voxels: Firstly a very small area in the shoulders, where, due to the positioning of this special patient, a lack of backscattered photons from the air between the shoulder and the neck cannot be modeled by the pencil beam and secondly at the nose and chin, where the high curvature of the anatomical features causes the reduction of dose due to scattered photons, which is described above. The degree of the overestimation in the second area is highest at the chin, where differences of app. +15% occur in several voxels. At this height (position along the z-direction), a difference +10% is exceeded in most voxels up to a depth (distance from the surface) of app. 2.5cm. An underestimation of the dose by the pencil beam algorithm by more than -10% can only be observed for a small number of voxels in the chest area, the differences in this area for most voxels range between -5% and -10%.

6.4.3. Discussion

For the non-infinite water phantom based on the outline of a real patient combined with an irradiation from 360°, the accuracy of the pencil beam algorithm is much lower than for the single beam in the large water phantom. Using the initial factor for the conversion between simulated dose per source particle from the Monte Carlo simulation and the dose calculated with the pencil beam algorithm as in chapter 5.2.2, the pencil beam algorithm severely overestimates the dose in the phantom, due to the changed scatter situation. This is similar to the single beam for the cylindrical phantom in chapter 6.3. The pencil beam algorithm cannot account for the loss of dose in a voxel due to photons, which are scattered out of the phantom and would be scattered back in a larger phantom. Choosing the dose at the isocenter as the normalization dose for both dose distributions, improves the agreement to a great extent. Using this normalization, the two dose distributions agree to within ±10% for 99% of the voxels in the primary beam area, which is a much better agreement than for the single beam. Still in smaller areas, such as the nose and the chin, where the high curvature of the anatomic features enhances the above described effect, the pencil beam algorithm can exceed the simulated dose by more than 10%. Due to the increased radius of patient for other anatomic sites, such as the pelvic area, the effect of the patient outline is expected to be lower than for the head and neck area.

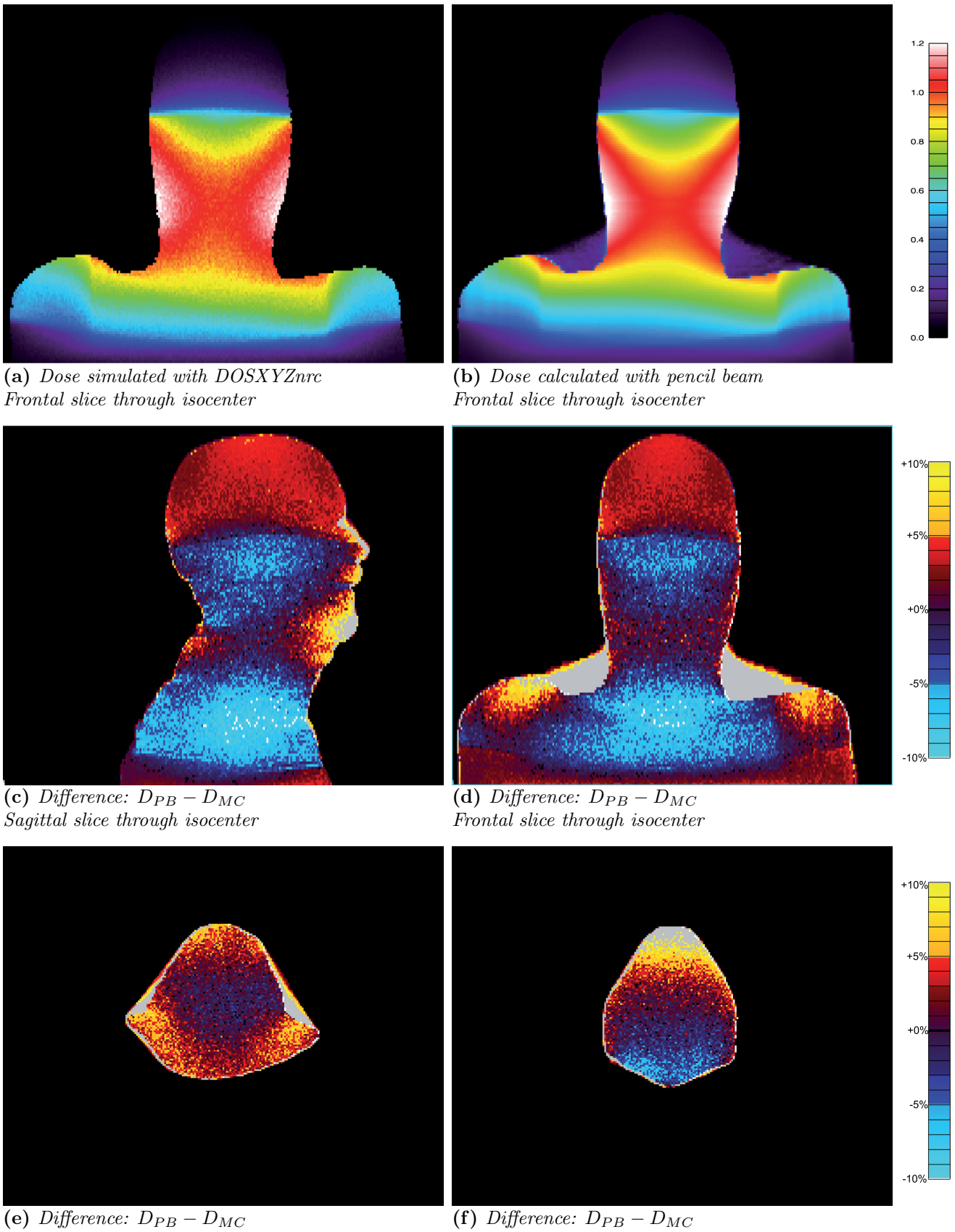

(a) *Dose simulated with DOSXYZnrc*
Frontal slice through isocenter

(b) *Dose calculated with pencil beam*
Frontal slice through isocenter

(c) *Difference:* $D_{PB} - D_{MC}$
Sagittal slice through isocenter

(d) *Difference:* $D_{PB} - D_{MC}$
Frontal slice through isocenter

(e) *Difference:* $D_{PB} - D_{MC}$
Transversal slice through isocenter

(f) *Difference:* $D_{PB} - D_{MC}$
Transversal slice (chin height)

Figure 6.14.: *Frontal slices and difference maps for simulated and pencil beam calculated dose distributions normalized to the respective dose at the isocenter. The differences exceed 10% in three major areas: the air between the shoulders and the neck, a small area at the shoulders and at the face, namely the chin and nose.*

7. Inhomogeneities: Scaling factors for depth and dose

In this chapter, the foundations for the integration and validation of inhomogeneous phantom geometries into the pencil beam algorithm for the keV energy range are layed. A use of the unchanged algorithm for MeV dose calculations is not possible due to the increased cross section of the photoeffect in the keV energy range and the resulting in a higher dependency of the photon absorption on the atomic number of the material in which the dose deposited. The developed algorithm to account for inhomogeneities in the pencil beam, which is based on the concept of scaling the depth and the dose with material dependent factors, is described in detail as well as the underlying principles, such as the depth scaling for the MeV pencil beam algorithm or material conversion tables. The actual calculation of the scaling factors is presented as well as the resulting factors themselves.

7.1. Dose to water vs. dose to medium

Most conventional dose calculation algorithms in radiation therapy calculate dose to water D_w. Reasons for this are on the one hand historical, as earlier dose calculations considered the patient to consist only of water, on the other hand most current dose calculation algorithms are based on input data derived from measurement or simulations in water. In contrast, most Monte Carlo simulations report the absorbed dose to medium D_{med}. On one hand, a conversion between the dose to water and the dose to medium is possible using the Bragg-Gray cavitity theory using the formula

$$D_w = D_{med} S_{W,med}, \tag{7.1}$$

where $S_{W,med}$ is the water-to-medium ratio of the unrestricted mass collision stopping powers (S_{water}, S_{medium}) averaged over the energy spectrum of primary electrons [72]. An overview of these stopping

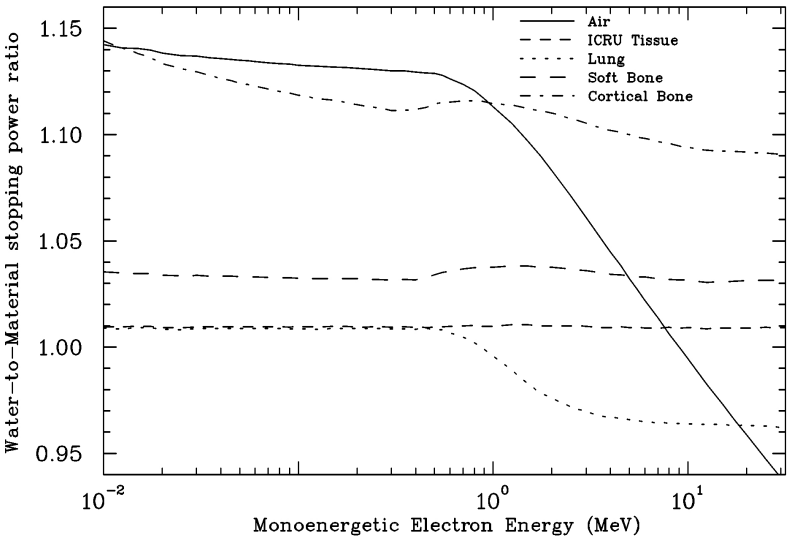

Figure 7.1.: *Water-to-medium mass collision stopping power ratios as a function of electron energy for different body tissues. Figure from [72].*

power ratios for different media and monoenergetic photons derived by Siebers et al. is shown in Figure 7.1. For energies between 10keV and 100keV, the conversion factors are quite stable and range from 1.01 for ICRU tissue and lung over 1.035 for soft bone to 1.14 for cortical bone.
Publications on the dose due to imaging procedures in radiotherapy often employ Monte Carlo simulations and report dose to medium instead of dose to water [16, 17, 62, 23]. In this work, Monte Carlo simulations were chosen as the Gold Standard for the dose calculation, the used pencil beam algorithm is therefore designed to also calculate dose to medium.

7.2. Methods

The next level in the complexity of pencil beam dose calculation is the transfer to inhomogeneous phantoms, which requires the introduction of media other than the medium for which the pencil beam kernel has been calculated. This gives rise to the question on how to adapt the pencil beam algorithm to account for the different absorption properties of the media, while the pencil beam kernel itself is calculated for water only.

7.2.1. Conventional Depth Scaling for MeV-Dose Calculation

In the MeV- pencil beam kernel based dose calculation algorithm, the consideration of additional media is based on O'Connors theorem [73] and the equivalent depth model, where the depth in the inhomogeneous phantom is assigned an equivalent depth in water (water equivalent depth). For a single pencil beam, lateral variations of the scattered dose due to the different traversed media are ignored. The conversion into water equivalent depth takes the changed absorption of the primary photon beam in the different media into account. According to Beer's Law, the intensity of the primary photon beam decreases exponentially with the thickness x of the traversed homogenous medium:

$$I(x) = I_0 e^{-\mu d}, \tag{7.2}$$

where d is the depth in the medium. As explained in chapter 3.3.2, the dependence of the absorption coefficient μ on the atomic number for the MeV energy range can be reduced to the one derived for the Compton effect, where the dependence on the atomic number Z can be summarized as a linear dependence on the electron density:

$$I(x) \approx I_0 e^{-\sigma_{Compton}(E_\gamma)\rho_e(Z)x} \tag{7.3}$$

To obtain the same intensity $I(x_1)$ at the same photon energy E_γ for a different electron density $\rho_e(Z_2)$ instead of $\rho_e(Z_1)$, the absorber thickness has to be adjusted accordingly to x_2:

$$\begin{aligned} \rho_e(Z_1)x_1 &= \rho_e(Z_2)x_2 \\ \Rightarrow x_2 &= \frac{\rho_e(Z_1)}{\rho_e(Z_2)}x_1 \end{aligned} \tag{7.4}$$

The water equivalent depth $d_{equ,hom}$ for a corresponding depth d_{med} in a homogenous medium with the electron density $\rho_e(Z_{med})$ is therefore defined as

$$d_{equ,hom} = \frac{\rho_e(Z_{med})}{\rho_e(Z_{H2O})} d_{med} \tag{7.5}$$

Under the assumptions, that the Compton effect is the dominant effect and the relation between atomic number Z and atomic weight A is app. constant for most relevant media, the dependence of the mass per volume and the deposited energy per volume on the mass density and the electron density is assumed to cancel each other out. For a homogeneous medium, this means, that the whole pencil beam kernel is scaled in the direction of the z-axis, the dose values in the kernel can be used as they are, but for a corrected depth. For an inhomogenous phantom, the equivalent depth for a total depth d lying within

the nth medium on the path of the beam is derived as the sum of traversed water equivalent depth for the individual media:

$$d_{equ,n} = \sum_{i=1}^{n-1} \frac{\rho_e(Z_i)}{\rho_e(Z_{H2O})}(d_{i,stop} - d_{i,start}) + \frac{\rho_e(Z_n)}{\rho_e(Z_{H2O})}(d - d_{i,start}) \tag{7.6}$$

where the medium i is located at depths lower than d and starts at $d_{i,start}$ and ends at $d_{i,stop}$.

7.2.2. Scaling Algorithm for the keV Energy Range

Several of the assumptions employed for the depth scaling with the electron density for the MeV-energy range do not hold for the keV-energy range. In this energy range, the Compton effect is no longer the dominant effect, but the photoeffect also plays an important role. Therefore for the intensity of the primary photon beam, the cross section σ can no longer be assumed to be independent of the atomic number Z, Equation 7.3 is no longer valid. Instead, the cross section also depends on the atomic number. Still a scaling of the depth is possible, the scaling factor in this case is directly the ratio of the absorption coefficients and is energy dependent:

$$\begin{aligned} d_{equ,hom} &= \frac{\mu(E_\gamma, Z_{med})}{\mu(E_\gamma, Z_{H2O})} d_{med} \\ &= \frac{\left(\frac{\mu}{\rho_m}\right)_{E_\gamma,med}}{\left(\frac{\mu}{\rho_m}\right)_{E_\gamma,H2O}} * \frac{\rho_{m,med}}{\rho_{m,H2O}} * d_{med} \\ &= \alpha(E_\gamma, Z_{med}, \rho_{m,med}) d_{med} \end{aligned} \tag{7.7}$$

The depth scaling factor $\alpha(E_\gamma, Z_{med}, \rho_{m,med})$ depends on the photon energy, the atomic number of the medium and the mass density. Assuming a constant density of water, the quantity

$$\alpha(E_\gamma, Z_{med}, \rho_{m,med}) = \frac{\left(\frac{\mu}{\rho_m}\right)_{E_\gamma,med}}{\left(\frac{\mu}{\rho_m}\right)_{E_{\gamma,H2O}} \rho_{m,H2O}} * \rho_{m,med} \tag{7.8}$$

is an energy dependent material specific property, which is proportional to the mass density $\rho_{m,med}$. The above equation for the equivalent depth holds only for the monoenergetic case. For a wider energy spectrum, the intensity for each contributing energy would have to be calculated separately using the respective absorption coefficient. For the calculation of the scaling factors, this is replaced by the use of a single effective absorption coefficient μ_{eff}, which is derived from the depth dose curves and therefore integrates scattered photons and beam hardening.For an inhomogeneous phantom, the estimation of the equivalent depth $d_{equ,n}$ in the nth medium is analog to the MeV case:

$$d_{equ,n} = \sum_{n-1}^{i=1} \alpha(E_\gamma, Z_i, \rho_{m,i})(d_{i,stop} - d_{i,start}) + \alpha(E_\gamma, Z_n, \rho_{m,n})(d - d_{i,start}) \tag{7.9}$$

where the medium i is located at depths lower than d and starts at $d_{i,start}$ and ends at $d_{i,stop}$. The higher dependency on the atomic number causes a higher increase in the absorbed energy in a volume than in the mass within the volume, which leads to an increase of dose for materials containing elements with a high atomic number Z. In the literature the multiplication of the preliminary dose distribution with different scaling factors for all bone voxels in a postprocessing step has been suggested [23, 24, 25]. This step is further discussed in chapter 9.1.1. To allow for a comparison of depth dose profiles for phantom geometries, only a short summary of the chosen concept is explained here. To account for the dependence of the local dose on the material of a voxel, another material specific scaling factor $\beta(Z)$ is introduced for the absolute dose in a medium n:

$$D_{n,pencil}(d) = \beta(Z) D_{water,pencil}(d_{equ,n}(d)) \tag{7.10}$$

Even though one would expect the factor $\beta(Z)$ to be close to the ratio of mass absorption coefficients for the medium and water, and therefore similar to the value of $\alpha(Z)/\rho_{m,mat}$, preliminary investigation showed, that this does not yield satisfactory results. Therefore another semi-empirical method was chosen for the estimation of the dose scaling factors $\beta(Z)$ for different materials.
The depth scaling factors α and β both depend on the atomic number Z and therefore for complex materials on the elemental composition. In addition, α depends on the mass density. Therefore a conversion table specifying the material and density for a given Hounfield Unit is needed. Such tables are commonly used for converting CT-data into simulation geomtries for Monte Carlo simulations. The principle of these tables as well as the specific tables used in this work are described in the following sections.
For the determination of the scaling factors for the different materials, an empirical approach was chosen in this work, where the factors are derived from Monte-Carlo simulated dose distributions. Other than the alternative of e.g. analytically calculating the effective μ from known absorption coefficients and the beam spectrum, the use of Monte Carlo simulations ensures a depth scaling for the dose instead of the intensity of the primary beam. As the pencil beam kernel itself represents a dose distribution and not an intensity, this lead to the choice of the described calculation algorithm for the depth scaling factors.The details of the calculation algorithm α is described in the following section. The derived scaling factors were implemented into the pencil beam algorithm by replacing the electron density ratio with the calculated depth scaling factors α for each material in the Hounsfield Unit-electron density conversion table usually used for depth scaling in the MeV pencil beam algorithm.
In this chapter, only a preliminary version of the dose scaling factors is used, to allow for the comparison of the depth scaled profiles with simulated profiles and to give an impression on the limitations of the employed method of single scaling factors per material. This preliminary method is described in the section following the next. The final algorithm employed for the dose calculation in patients is described in chapter 9.1.1. The obtained scaling factors are then used to correct the dose distribution calculated with the pencil beam algorithm and the depth scaling factors by scaling the dose voxel by voxel with the material dependent scaling factor. For each voxel, the respective scaling factor is selected based on the Hounsfield Unit. This part of the dose calculation was integrated in a graphical user interface, which was created using the program IDL (IDL version 6.2, ITT Visual Information Solutions, Boulder, Colorado).

7.2.3. Converting CT-data to material and density maps

The information contained in a CT-dataset is limited to the absorption coefficient for each voxel i in the geometry coded in Hounsfield Unit, which is defined as:

$$HU = 1000\frac{\mu_i - \mu_{water}}{\mu_{water}} \tag{7.11}$$

Based on this definition the Hounfield Units of -1000 HU for air and 0 HU for water are obvious. Typical values for body tissues are e.g. app. -100 HU for fatty tissue or 500 HU-2000 HU for bone. As the absorption coefficient and therefore the Hounsfield Unit depends not only on the atomic number of a material but also on the mass density, there is no direct correlation to determine both from the Hounsfield Unit. Due to the limited number of body tissues and a limited range of mass densities for each of the tissues, it is nevertheless possible to establish a conversion table, where different material bins are defined, which are associated to a certain range of Hounsfield Units. Two different of such conversion tables have been investigated in this work, the default table with four materials, which is suggested in the DOSXYZnrc manual [71] and based on tissue definitions by the International Commission on Radiation Units and Measurement and one described by Schneider et al.[74] based on tissue definitions by Woodard and White [75, 76]. The specific properties of the tables are described in full detail in the next section, the effect of the choice of the conversion table on the dose distribution is discussed in chapter 8.1.2. Both tables are based on the assumption that for each material with a fixed elemental composition, a maximum and minimum Hounsfield Unit ($HU_{i,max}, HU_{i,min}$) are defined and associated to a maximum and minimum density ($\rho_{m,i,max}, \rho_{m,i,min}$). The variation of the Hounsfield Unit within the intervall is

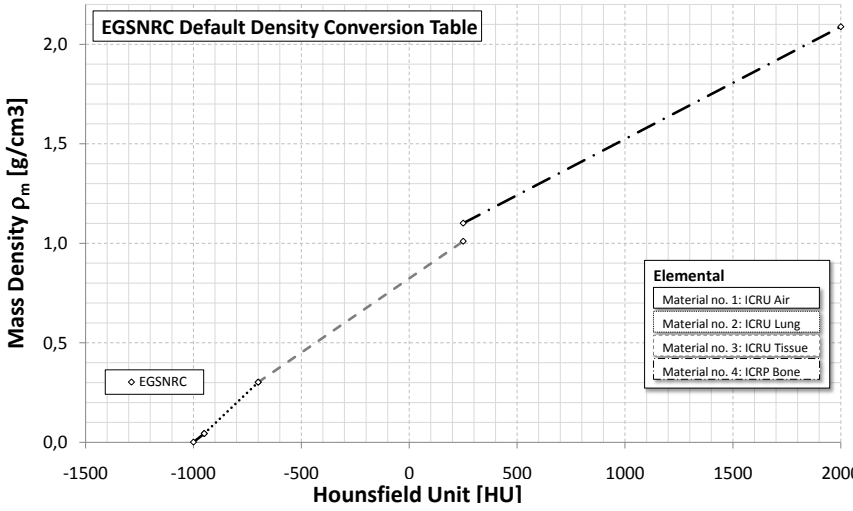

Table 7.1.: *EGSnrc Density and material conversion table*

Mat. Nr.	HU min	HU max	ρ_m min	ρ_m max
1	-1000	-950	0.001	0.044
2	-950	-700	0.044	0.302
3	-700	250	0.302	1.010
4	250	2000	1.101	2.088

Minimum and maximum Hounsfield Unit and corresponding minimum and maximum mass density for each material (with adapted bone soft tissue boundary).

Figure 7.2.: *EGSnrc Conversion table: Density as a function of Hounsfield Unit and Material assignment. A total number of 4 Materials is used in this conversion table, the variation in the absorption coefficient for each material is achieved by linear interpolation of the mass density.*

attributed to a proportional change in the density. For a given Hounsfield Unit HU, the density can therefore be linearly interpolated as:

$$\rho_m = \rho_{m,i,min} + \frac{\rho_{m,i,max} - \rho_{m,i,min}}{HU_{i,max} - HU_{i,min}}(HU - HU_{i,min}) \tag{7.12}$$

7.2.4. Material Conversion Tables

As described above, in this work, two different tables were investigated for the use in the imaging energy range. They differ mainly in the number of materials, which are defined, and the corresponding diversity of elemental compositions. While in one of the tables, all body tissues are roughly grouped into 3 groups (lung, soft tissue or bone), the other uses a more complicated definition, where mixtures of different tissue types are also allowed. E.g. for bone, this results in a stepwise increase of the calcium content over, which highly influences the absorption coefficient, so that a discrimition in the effective atomic number of e.g. cortical bone and femural bones is possible. As mentioned above, the effect of the choice of the conversion table on the dose distribution is discussed in chapter 8.1.2.

Egsnrc conversion table

This conversion table is used by default by the utility ctcreate, which is provided with the EGSnrc-coding system to convert CT-datasets from the fileformat DICOM into geometry files to be used in DOSXYZnrc simulations[71]; its derivation is described in detail in [77]. The table uses 4 materials: Air, Lung, Tissue and Bone. For all materials established elemental compositions as defined by the International Commission on Radiation Units and Measurement (ICRU) are employed. For bone, the elemental composition bone as defined by the International Commission on Radiological Protection (ICRP) is used. The materials used inthe the EGSnrc table are summarized in table 7.2. As explained above, for each material, a maximum and minimum Housfield Unit with corresponding minimum and maximum mass densities are provided (Table 7.1). For intermediate Hounsfield Units, the mass density is calculated by linear interpolation (Figure 7.2). Due to the low number of materials, the range of densities per material is relatively large. For the version of the egsnrc table used in this work, the Housfield Unit, which forms the boundary between soft tissue and bone was changed from 115HU to 200HU, as the use of the lower value lead to a clear missassignment of several voxels (such as singe voxels of bone within the brain). As this was attributed to a different calibration of the CT-Scanner, the density at the boundary was not adapted. Voxels exceeding the maximum defined Hounsfield Unit are assigned the maximum density and material number.

Table 7.2.: *EGSnrc Conversion table. Elemental Composition of Materials*

Material Number	Weight fraction [%]												
	H	C	N	O	NA	MG	P	S	CL	AR	K	CA	ZN
1		0.012	75.522	23.179						1.283			
2	10.3	10.5	3.100	74.898	0.2		0.2	0.3	0.3		0.2		
3	10.117	11.1	2.600	76.181									
4	4.723	14.433	4.199	44.609		0.22	10.497	0.315				20.993	0.01

Schneider Conversion table

Incorporating a total number of 24 materials, the conversion table based on Schneider et al. [74] uses a much higher number of different elemental compositions. The basic idea behind this conversion table is the interpolation of elemental compositions for body tissues over an interval of Hounsfield Units from known tissues, which form the boundaries of the intervall. E.g. all skeletal tissues, as the most intuitive case, are assumed to be a mixture of osseous tissue and bone marrow. Materials in the respective Hounsfield Unit range are therefore interpolated from the respective elemental compositions of these two tissues. For the soft tissue region, the situation is more complicated, an interpolation is only possible for a small range of tissues (Materials 3-7, see table 7.4). An additional bin is formed by averaging all tissues that fall within the respective Hounsfield range; another one is associated with connective tissue. The different material bins can again be grouped into the four major groups, air (Material no. 1), lung (Material no.2), soft tissues (Materials nos.s 3-9) and skeletal tissues (Materials nos. 10-24). The elemental compositions and the boundaries of the used material bins are summarized in Table 7.4. One of the main features of this table is the slow increase in high Z-element content for the skeletal tissues. The mass density ρ_m as a function of the Hounsfield Unit is again calculated using linear interpolation within fixed intervals (Figure 7.3); for most Hounsfield Units, the linear equation is explicitly specified in the publication[74]. Using these equations, the boundaries of the density interpolation intervals, which are summarized in Table 7.3 do not coincide with the boundaries of the material bins. To include the information on the density and the material in a single table, the linear interpolation of the density was carried out for the Housfield Unit boundaries of the material bins. All boundaries were then summarized in the final converison table. Again, voxels exceeding the maximum defined Hounsfield Unit are assigned the maximum density and material number.

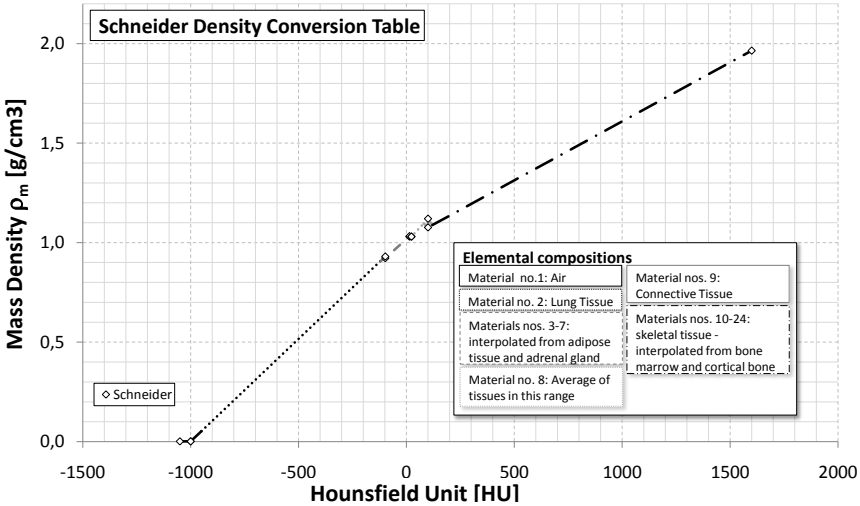

Table 7.3.: *Schneider density conversion table as specified in [74].*

HU min	HU max	ρ_m min	ρ_m max
-1050	-1000	0.00121	0.00121
-1000	-98	0.00121	0.93000
-98	14	0.92167	1.03176
14	23	1.03000	1.03000
23	100	1.02989	1.11990
100	1600	1.07620	1.96420

Minimum and maximum Hounsfield Unit and corresponding minimum and maximum mass density.

Figure 7.3.: *Schneider Density Conversion table. HU vs. mass density plot. The material groups, which are explained in the box on the right are marked with different linestyles.*

Table 7.4.: *Elemental compositions of the Schneider conversion table*

Mat. Nr.	Weight fraction [%]												HU_{min}	HU_{max}
	H	C	N	O	NA	MG	P	S	CL	AR	K	CA		
1			75.5	23.2				-		1.3			-1050	-950
2	10.3	10.5	3.1	74.9	0.2		0.2	0.3	0.3		0.2		-950	-120
3	11.6	68.1	0.2	19.8	0.1		0.0	0.1	0.1				-120	-83
4	11.3	56.7	0.9	30.8	0.1		0.0	0.1	0.1				-82	-53
5	11.0	45.8	1.5	41.1	0.1		0.1	0.2	0.2				-52	-23
6	10.8	35.6	2.2	50.9	0.0		0.1	0.2	0.2				-22	7
7	10.6	28.4	2.6	57.8	0.0		0.1	0.2	0.2		0.1		8	18
8	10.3	13.4	3.0	72.3	0.2		0.2	0.2	0.2		0.2		19	80
9	9.4	20.7	6.2	62.2	0.6		0.0	0.6	0.3				80	120
10	9.5	45.5	2.5	35.5	0.1		2.1	0.1	0.1		0.1	4.5	120	200
11	8.9	42.3	2.7	36.3	0.1		3.0	0.1	0.1		0.1	6.4	200	300
12	8.2	39.1	2.9	37.2	0.1		3.9	0.1	0.1		0.1	8.3	300	400
13	7.6	36.1	3.0	38.0	0.1	0.1	4.7	0.2	0.1			10.1	400	500
14	7.1	33.5	3.2	38.7	0.1	0.1	5.4	0.2				11.7	500	600
15	6.6	31.0	3.3	39.4	0.1	0.1	6.1	0.2				13.2	600	700
16	6.1	28.7	3.5	40.0	0.1	0.1	6.7	0.2				14.6	700	800
17	5.6	26.5	3.6	40.5	0.1	0.2	7.3	0.3				15.9	800	900
18	5.2	24.6	3.7	41.1	0.1	0.2	7.8	0.3				17.0	900	1000
19	4.9	22.7	3.8	41.6	0.1	0.2	8.3	0.3				18.1	1000	1100
20	4.5	21.0	3.9	42.0	0.1	0.2	8.8	0.3				19.2	1100	1200
21	4.2	19.4	4.0	42.5	0.1	0.2	9.2	0.3				20.1	1200	1300
22	3.9	17.9	4.1	42.9	0.1	0.2	9.6	0.3				21.0	1300	1400
23	3.6	16.5	4.2	43.2	0.1	0.2	10.0	0.3				21.9	1400	1500
24	3.4	15.5	4.2	43.5	0.1	0.2	10.3	0.3				22.5	1500	1600

Elemental Composition of materials and minimum and maximum Hounsfield Unit for each material as specified in [74]. A total number of 24 materials are used in this table. All skeletal tissues (materials no. 10-24) are interpolated from a mixture of red and yellow bone marrow and cortical bone. Note the slow increase of calcium for the skeletal material, which has a high influence on the deposited dose due to its high atomic number

7.2.5. Estimation of the depth scaling factors α

In this chapter, the empirical estimation of the material dependent depth scaling factors $\alpha(E_\gamma, Z_i, \rho_{m,i})$ for the pencil beam algorithm is described.
For each material, the effective absorption coefficient for a medium density of $1 g/cm^3$ is calculated according to equation 7.8 from a Monte Carlo simulation as described below. The scaling factor for other mass densities can be calculated from the value for a known mass density employing the proportionality of the scaling factor to the density.
Due to the different properties, all materials were grouped according to their high Z element content: one group of materials which only contain low Z materials (soft tissues, lung and air) and one group for materials containing high Z elements (all materials containing bone material).
While the dose simulation for the low Z materials was executed for a homogeneous phantom of the respective material, a slab geometry was chosen for the bony materials. Again, the mass density for all voxels was set to $1 \frac{g}{cm^3}$ to reduce the scaling effect to the influence of the material composition only.The material specific depth scaling factor for this density was then estimated as the ratio between an equivalent mass attenuation coefficient in the material and in water. For this central axis dose profiles D(d) along the beam direction were employed. To remove the dose dependency on the square of the distance from the source all dose values were corrected according to the SSD and the depth in water, resulting in the new dose profiles D':

$$D'(d) = \left(\frac{SSD + d}{SSD_{ref} + d_{ref}} \right)^2 D(d), \tag{7.13}$$

with

$$SSD_{ref} + d_{ref} = 100cm \tag{7.14}$$

The calculation algorithm is then based on the assumption that the dose D' decreases exponentially with

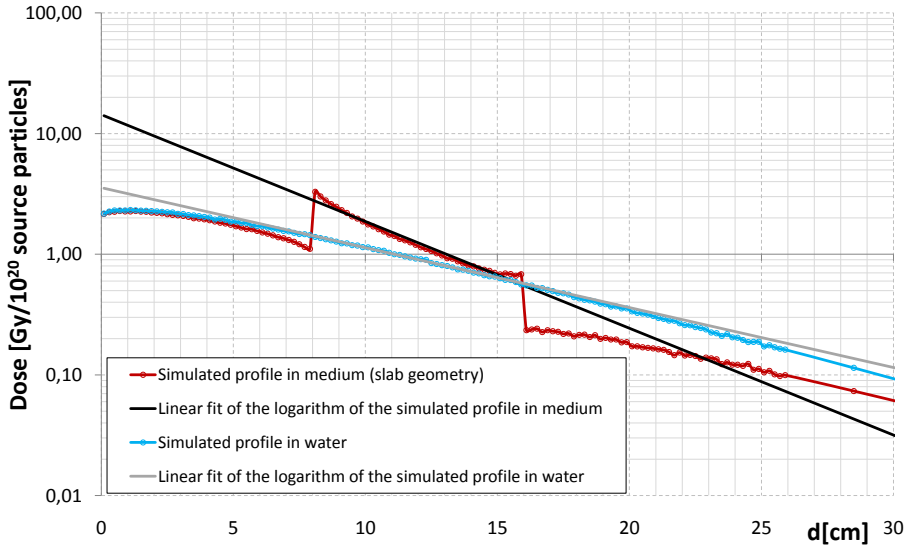

Figure 7.4.: *Linear fit of the logarithm of the simulated profiles in water and in the medium to obtain the effective mass absorption coefficients $\mu_{eq,water}$ and $\mu_{eq,material}$ as the slope of the linear fit.*

the depth in water:

$$D'(d) = D'(0)e^{-\frac{\mu_{eq}}{\rho_m}\rho_m d} \tag{7.15}$$

As the mass density is set to $1\frac{g}{cm^3}$, the slope of a linear fit of the logarithm of the respective dose profiles yields the effective attenuation coefficient μ_{eq} for water and the examined material (see Figure 7.4). For the high Z materials, the linear fit was executed only for the part of the doseprofiles within the respective material slab. The material dependent depth scaling factor $\alpha(E_\gamma, Z_i, 1g/cm^3)$ is then set to the ratio of the two attenuation coefficients:

$$\alpha(E_\gamma, Z_i, 1\frac{g}{cm^3}) = \frac{\mu_{eq,material}(\rho_m = 1\frac{g}{cm^3})}{\mu_{eq,water}(\rho_m = 1\frac{g}{cm^3})} \tag{7.16}$$

The different materials are specified in the conversion tables by maximum and minimum Hounsfield Unit and matching maximum and minimum mass density assuming a linear inscrease of the density over the interval. Due to the proportionality of the scaling factor $\alpha(E_\gamma, Z_{med}, \rho_{m,med})$ to the mass density, for each material a maximum and minimum scaling factor can be derived by multiplying the derived $\alpha(E_\gamma, Z_i, 1g/cm^3)$ with the minimum and maximum density of the materials. Scaling factors for other HU values within the interval can also be derived by linear interpolation.
In the MeV pencil beam dose calculation algorithm of the used planning system, the user supplies an HU vs. relative electron density table, specifying the electron density relative to water for a limited number of points. For other Hounsfield Unit values, the electron density is interpolated linearly. This mechanism was employed for the new scaling algorithm, by providing an HU vs. scaling factor table for the boundaries of the HU-intervals for each material, where the scaling factor can be linearly interpolated between the respective HU-boundaries.

7.2.6. Preliminary Dose Scaling Factors β

To allow for an evaluation of the scaling algorithm with single scaling factors per material for the case of homogeneous phantoms or slab phantoms, a very simple estimation of the dose scaling factor $\beta(Z)$ was used. The depth dose profiles employed for the calculation of the depth scaling factors were also used to determine $\beta(Z)$. The profiles resulting from the different steps of the factor calculation in addition to the profiles in water ($D'_{water}(d)$, light blue) and in the medium ($D'_{medium}(d)$, dark red) are plotted in Figure 7.5.The effect of the depth scaling procedure was simulated by calculating a depth in medium d_{med} for each datapoint (d,$D'_{water}(d)$) of the depth dose profile in water using the determined scaling factor $\alpha(E_\gamma, Z_i, 1g/cm^3)$ for the specific photon spectrum (short α_Z) according to

$$d_{med} = \alpha_Z * d \tag{7.17}$$

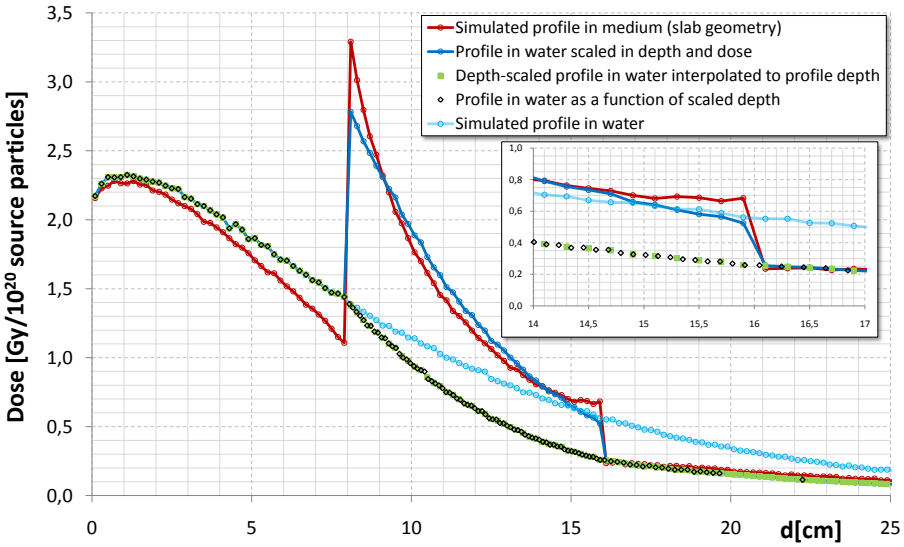

Figure 7.5.: *Profiles as created by the different steps of the factor calculation. In addition to the simulated profile in water $D'_{water}(d)$ (light blue) and in the medium $D'_{medium}(d)$ (dark red, in this case a slab geometry), the profile in water combined with the scaled depths $D'_{water,\alpha-scaled}(d_{med})$ (black diamonds), the interpolated version of the depth scaled profile (green rectangles) and the profile with the scaling factors α and β applied to the depth and the dose. In all plotted profiles, the inverse square dependency on the distance from the source is removed.*

for homogeneous phantoms and

$$d_{med} = \begin{cases} d & \text{with } d < d_1 \\ d_1 + \alpha_Z * (d - d_1) & \text{with } d_1 < d < d_2 \\ d_1 + \alpha_Z * (d_2 - d_1) + (d - d_2) & \text{with } d > d_2 \end{cases} \tag{7.18}$$

for slab phantoms, where a horizontal slab of a medium starting at the depth d_1 and ending at d_2 is embedded in an otherwise homogeneous waterphantom. These depth d_{med} combined with the dose values $D'_{water}(d)$ from the dose profile in water form a scaled water profile $D'_{water,\alpha-scaled}(d_{med})$ (black diamonds in Figure 7.5) with datapoints $(d_{med}, D'_{water}(d))$, which is then interpolated to match the evenly spaced depths of the depth dose profile datapoints from the dose distribution simulated for the respective medium (green rectangles in Figure 7.5). The dose scaling factor $\beta(Z)$ was then then set to the average ratio of the dose values in water and in the material at the same depth:

$$\beta(Z) = mean(\left(\frac{D'_{material}(d_{med})}{D'_{water,\alpha-scaled}(d_{med})}\right)) \tag{7.19}$$

Again for the high Z materials, only the dose values within the material slab were used ($d_1 < d < d_2$). Unlike the depth scaling factor alpha, the dose scaling factor $\beta(Z)$ does not depend on the mass density but only on the elemtnal composition of a material, so that a fixed value for each material is used. The profile, which combines both scaling factors but still has no inverse square dependence on the distance to the source is plotted in dark blue in Figure in Figure 7.5).The results from this estimation were not used in patient geometries, the estimation of these factors is described in chapter 9.1.1. As the material-mass density combinations used for the dose simulations, which yielded the used profiles, would have to be converted to Hounsfield Units outside the range for the respective material, the scaled water profile for the comparison with the simulated profile was not obtained using the planning system. Instead, the scaling for the homogeneous phantoms and the slab phantoms was reproduced manually: both scaling factors for the respective media were applied to the profile in water before restoring the dependence of the dose on the square of the distance to the source resulting in a fully scaled water profile $D_{water,scaled}(d_{med})$:

$$D_{water,scaled}(d_{med}) = \beta(Z_d) D'_{water,\alpha-scaled}(d_{med}) * \left(\frac{SSD_{ref} + d_{ref}}{SSD + d}\right)^2 \tag{7.20}$$

with d_{med} and $D'_{water,\alpha-scaled}(d_{med})$ as described above and $\beta(Z_d)$ being the determined dose scaling factor for the respective medium ($\beta(Z_{water}) = 1$).

7.3. Scaling Factor Estimation

7.3.1. Simulations

For all dose simulations described in this chapter, the phase space file with a field size of 25cm x 25cm generated in chapter 5.1.3 was used as the radiation source for dose simulations. The field size was chosen in the range of a typical field size for imaging purposes. All particles from the phase space file were used with a recycle factor of 10, resulting in the simulation of more than $1.6 * 10^9$ histories per dose simulation. No electron transport was simulated. Simulations were executed for all materials listed in the EGSnrc and the Schneider conversion table, which were described above (chapter 7.2.4). In addition, a simulation with a homogeneous water phantom was executed as needed for the scaling factor estimation. The phantom geometries were chosen as described in 7.2.5, the materials were grouped according to their high Z element content: one group of materials which only contain low Z materials (soft tissues, lung and air) and one group for materials containing high Z elements (all materials containing bone material). For the low Z materials a homogeneous phantom of the respective material was used, the phantom dimension were 60cm x 60cm x 46cm with a voxel side lengths in x- and y-direction of 0.5cm for the central 10cm and 0.2 in z-direction for the first 16cm. Outside this central area, voxel side length of 5cm were used to provide increase the size of the phantom. This setting was also used for the homogeneous water phantom. As described above, for the bony material, a slab geometry was chosen, where a horizontal slab of the respective medium was embedded in a water phantom of the above described dimensions. By setting the voxel planes no. 41-80 in z-direction to the respective medium, the slab thickness was set to 8cm starting at $d_1 = 8cm$ and ending at $d_2 = 16cm$. In both cases, the mass density for all materials was set to $1g/cm^3$ and an SSD of 90cm was used. The HOWFARLESS option [71] was activated for the homogeneous phantoms to increase the speed of the simulation.

7.3.2. Results & Discussion

Profile Comparison

The scaling factors $\alpha(E_\gamma, Z_i, 1g/cm^3)$ and $\beta(Z)$ were derived from the simulated dose distributions as described above. Figure 7.6 shows the depth dose profiles for a representative selection of the simulated materials from the Schneider table together with the scaled profile in water $D_{water,scaled}(d_{med})$ (For the definition of $D_{water,scaled}(d_{med})$ see chapter 7.2.6).
On the left side of the figure, profiles for air (a), lung (b), and different soft tissues (c-f) are displayed (each material set to a mass density of $1g/cm^3$). As visible in the respective plot, for lung and soft tissues, the scaled water profiles agree well with the simulated profile. To provide a quantitative analysis of the differences, Figure 7.6g shows the difference between the simulated and the scaled profiles for air (red), lung (blue) and all soft tissues (shades of green) used in the Schneider conversion table (differences normalized to the respective dose in water at 5cm depth). For all soft tissues, the difference is below 3% for all depth, for lung tissue the maximum difference is even below 2%. As it could already be seen in the profiles themselves, the difference for air is much higher, but due to the low density of air, the absorption in air will later play a very minor role in the dose calculation, so that the influence of the scaling for this material is negligible.
On the right of Figure 7.6 profiles for the slab geometries for different bony tissue materials are plotted. The slab of bony material is clearly visible as an area of increased dose in all profiles. For the bony tissues, the differences between the scaled and simulated profiles (Figure 7.6n+o) are much higher than for soft tissues and increase with the high Z content of the material.
Especially close to the upper boundary of the slab (d=8cm) in the bony material differences of up to -5%- -55% of the dose in water at a depth of 5cm occur, depending on the high Z content. This is due to

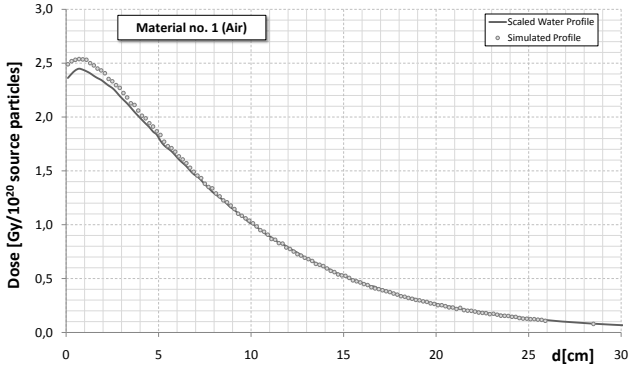

(a)

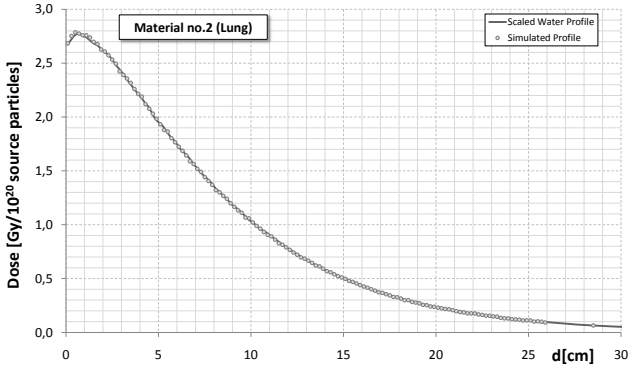

(b)

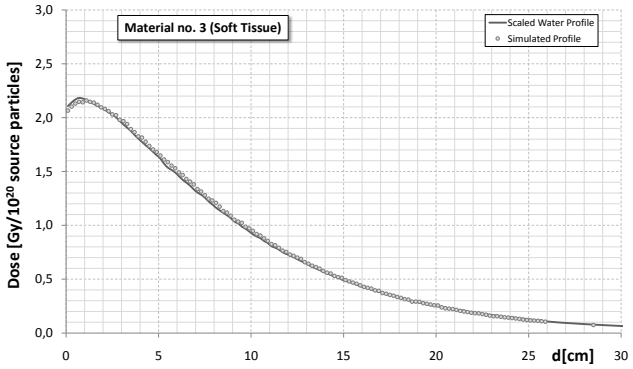

(c)

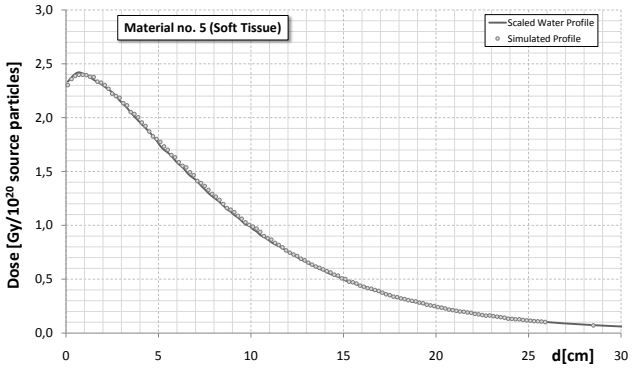

(d)

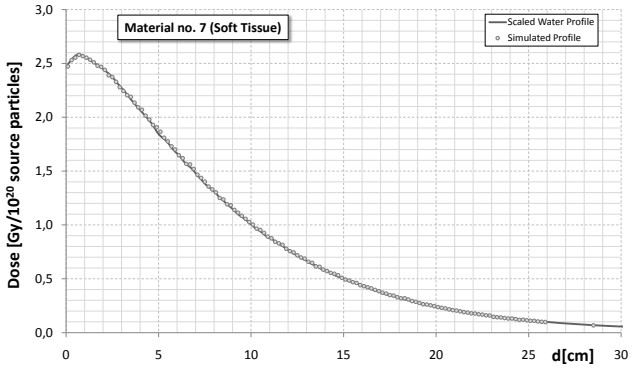

(e)

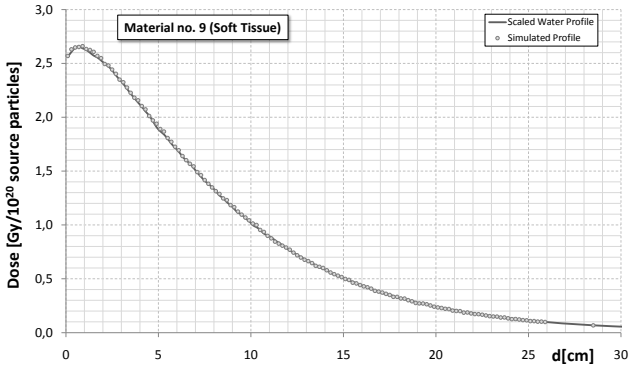

(f)

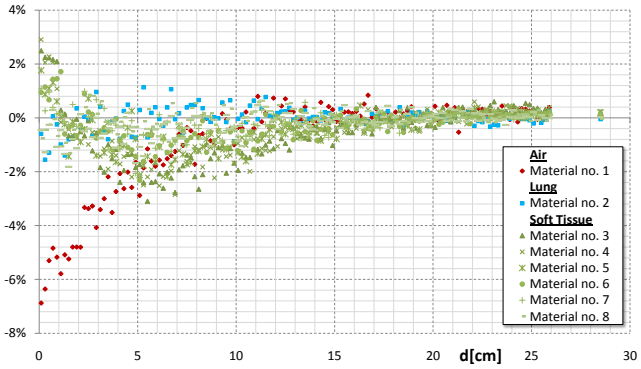

(g)

Figure 7.6.: *Dose profile comparison: Simulated depth dose profiles (Points) vs. scaled profiles in water (Line) for materials from the Schneider conversion table. The scaled profiles in water are obtained by applying the scaling factor $\alpha(E_\gamma, Z_i, 1g/cm^3)$ (obtained as the ration of effective absorption coefficients for the respective medium and for water) to calculate the equivalent depth in the medium and the dose scaling factor $\beta(Z_i)$ for the respective medium (see chapter 7.2.6). Figures (g), (n) and (o) show the differences between the two profiles for all materials.* *(Continued on page 70)*

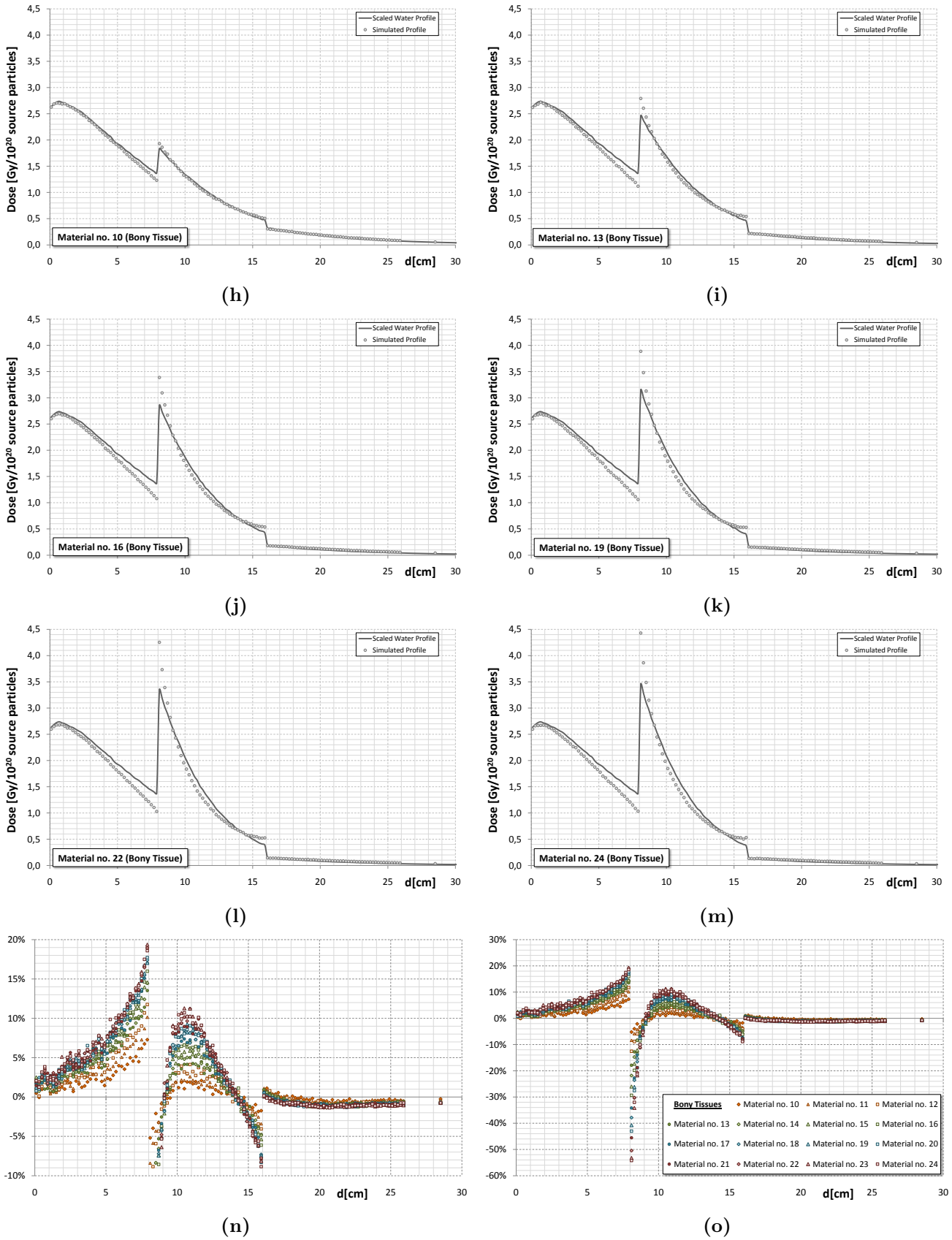

Figure 7.6.: *Continued from page 69*

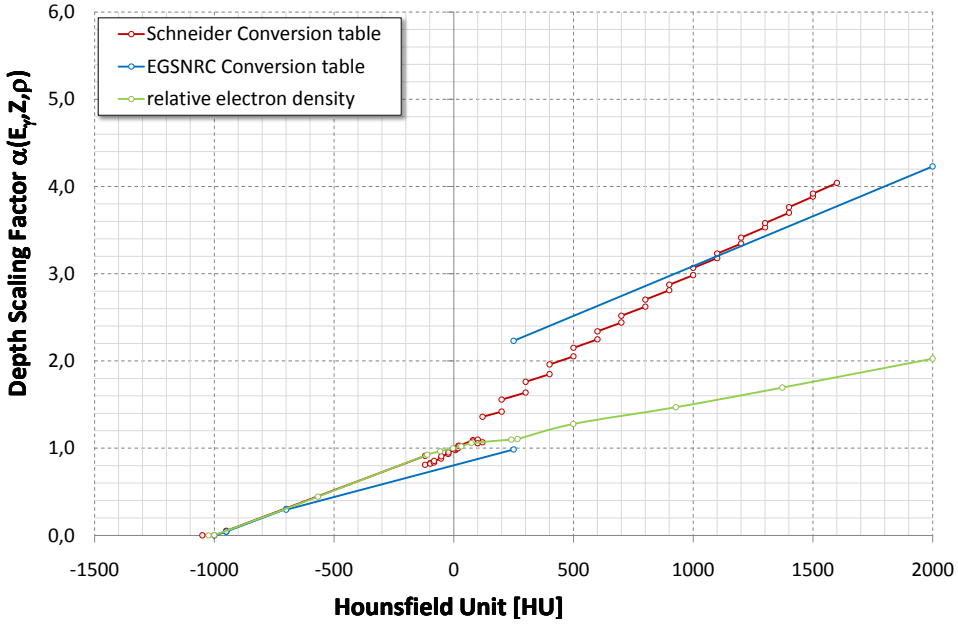

Figure 7.7.: *Estimated depth scaling factors α as a function of the Hounsfield value. The dependence of α on the elemental composition and the mass density ρ_m is implicit when combining the above plot with the material composition and mass densities for the respective Hounsfield Units specified in the matching material conversion tables. For comparison, the relative electron density is also plotted, which is used as the scaling factor in MeV applications.*

the high absorption in the bone slab compared to water, which causes an increased number of scattered photons from the water in front of the slab to reach the boundary voxels of the slab, which increases the dose in this area compared to a homogeneous situatuation. The opposite effect can be observed for the adjacent water, where the differences range between +5% and +20%. This in turn is caused by the decreased number of backscattered photons from within or behind the slab, which reach the water voxels at depth lower than the slab position but are absorbed within the slab with a higher absorption coefficient.
This scatter effect is larger for voxels that are closer to the slab than for those further away and cannot be modelled by the used scaling method, as the material of a voxel only influences the dose in the voxel itself (β-scaling) and for voxels at higher depth (α-scaling). The same effect causes the differences of -10% - -2% at the lower boundary (d=16cm) in the bone slab, where more backscattered photons reach the voxels at the end of the slab compared to a homogeneous situation. As the scaling factor β is set to an average value for all voxels in the depth dose curve of the respective material, in the center of the slab the dose in the scaled profile exceeds the simulated dose to compensate for the described underestimation at the slab boundaries.
For the above described scatter situation for the water voxels at depth lower than the slab boundary, the horizontal bone slab which extends over the whole width of the radiation field is a worst case situation, so that this effect will be much lower for bony structures with a smaller extension. This does not hold for the dose within the bony structures themselves, which, in combination with the results from chapter 6.4 leads to the different estimation of the dose scaling factors β for patient geometries to compensate for the underestimation of dose within smaller bony structures which is described in chapter 9.1.1 on dose calculation for patient geometries. The results for the materials from the EGSnrc conversion table are similar to those for the Schneider table, and are therefore not discussed in detail here.

Scaling Factors

The estimated depth scaling factors $\alpha(E_\gamma, Z_i, 1g/cm^3)$ were used to calculate $\alpha(E_\gamma, Z, \rho_m)$ for the material and densitity Hounsfield Unit boundaries by multiplication of $\alpha(E_\gamma, Z_i, 1g/cm^3)$ with the minimum and maximum mass density for each interval and supplied to the pencil beam algorithm, which uses linear interpolation for intermediate values. The resulting depth scaling factors for both conversion tables as a function of the Hounsfield value are plotted in Figure 7.7. As the plot shows, the scaling factors differ to a great extend for the two conversion tables. While the factors for the Schneider converison table show a slow increase with minor discontinuities at the material boundaries, the low number of materials in the EGSnrc conversion table causes a big jump in the depth scaling factors at the soft tissue/bone boundary.

The low number of materials also causes the scaling factors for the EGSnrc table to be much higher than for the Schneider table for low HU- bony structures and much lower for high HU-values. Again, it is not possible to identify the "true" situation, but the continouus increase for the Schneider table compared to the highly discontinouus boundaries in the EGSnrc table suggest, that a higher number of materials yields more plausible results.

8. The Use of CT Dataset for Monte Carlo Simulations

As Monte Carlo simulations were chosen as the Gold Standard for dose calculations in this work, any assumption that affects the simulated dose, also has an impact on the pencil beam algorithm itself. Due to the high dependency of the interaction cross section on the atomic number for the investigated energy range and the associated increase of dose in materials with high Z elements, the methods chosen for the import of CT-data into Monte-Carlo simulations and therefore the determination of the elemental content for each voxel, have a much higher influence on the dose distribution than for MeV dose simulations. In this chapter, the magnitude of this effect is investigated using two different conversion tables for the conversion of the CT-data into a simulation geometry.

8.1. Methods

A precondition for all Monte Carlo simulations is that either the cross sections for the different interaction processes is provided for each of the voxels of the simulation geometry separately, or the cross sections are supplied for a limited number of materials with a known elemental composition and each voxel is assigned one of these materials. In both cases, the mass density for each of the voxels has to be specified. A CT-dataset provides the absorption coefficient coded as Hounsfield Units, for the use in a MC-simulation, this has to be converted to material and density. These tables are the same as used for the material definition for the pencil beam algorithm, the principle of these tables and the definition of the specific tables used in this work are described in the sections 7.2.3 and 7.2.4. In this section, only the practical application for the import of CT-data into the DOSXYZnrc simulation is discussed as well as the graphical user interface, which was developed for this purpose.

8.1.1. .egsphant Phantom Files

The .egsphant file format is a file format, which can be used to import voxelized geometry data (e.g. from a patient CT) into a DOSXYZnrc simulation. The file format is described in full detail in [71], only a short summary shall be given here. The .egsphant file is a standard text file containing all relevant information about the desired phantom geometry. In addition to the material names, which are allotted a material number by their order, the phantom dimensions and the voxel boundaries in all 3 dimensions have to be specified. The rest of the file consists of a slice wise definition of the voxel materials (by numbers) and after completion of the whole geometry, the voxel mass densities. A review of the phantom orientation is possible using a text-editor. Due to the different appearance of the digits, the basic phantom geometry is discernible. Figure 8.1 shows such a phantom slice (upside down frontal slice through head and neck) as viewed in a text editor, with a high magnification, one can discern the single digits specifying the material number. As the original DOSXYZnrc code only accepted single digit material numbers and therefore a maximum number of 10 materials, the code was adapted so that two digits are read per material to permit the simulations using the Schneider conversion table.

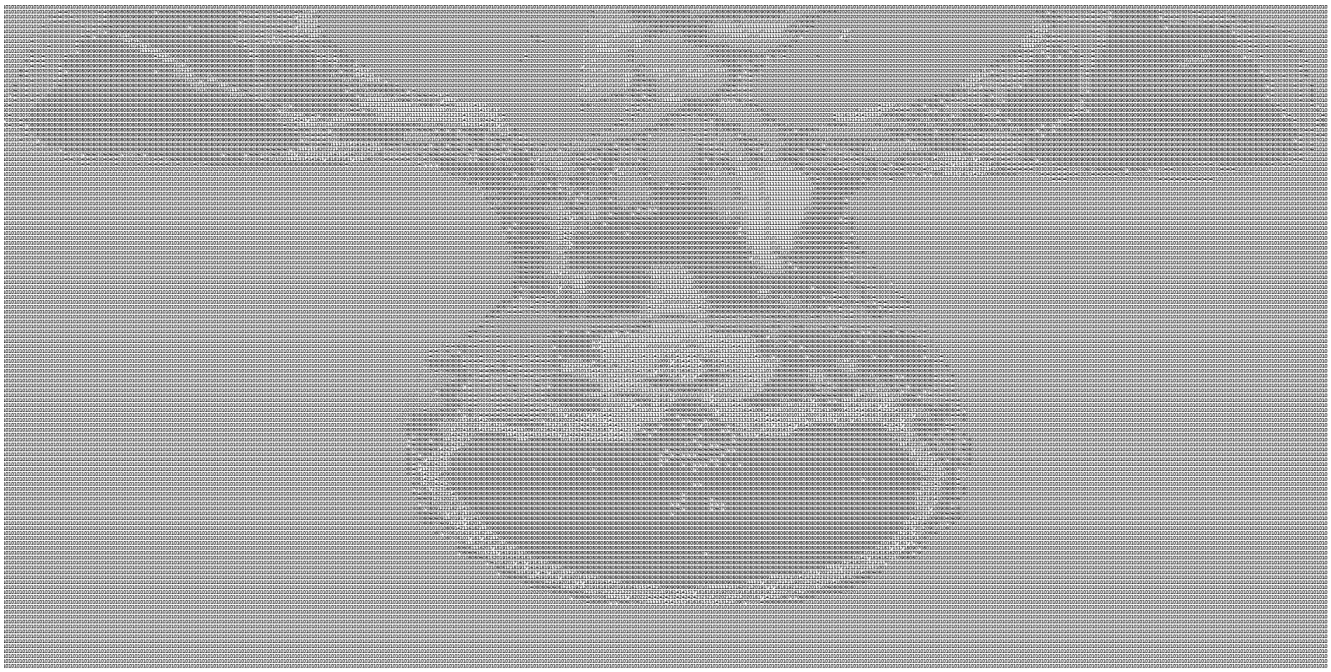

Figure 8.1.: *Screenshot of a phantom slice in a .egsphant file as viewed in a text editor. Due to the different appearance of the digits, the orientation and basic geometry of the head and neck patient is discernible. Due to the definition of the axis, the geometry is displayed upside down.*

8.1.2. Interface Realization

For the creation of .egsphant files and the visualization of the calculated material and density maps from CT-datasets in the format used by the planning system VIRTUOS, a graphical user interface was developed in IDL (IDL version 6.2, ITT Visual Information Solutions, Boulder, Colorado). The graphical user interface combines a number of applications occurring within the workflow of a dose comparison between pencil beam dose and Monte Carlo dose simulated with DOSXYZnrc. Within the interface, the following steps are necessary to derive a .egsphant file.

Loading a CT First a CT-dataset, which is available in the uncompressed VIRTUOS file format (.hed and .ctx) has to be loaded. For this a separate tab is available, where the path of the file can be specified and basic information, such as voxel size or cube dimensions, are displayed as well as transversal slices of the CT.

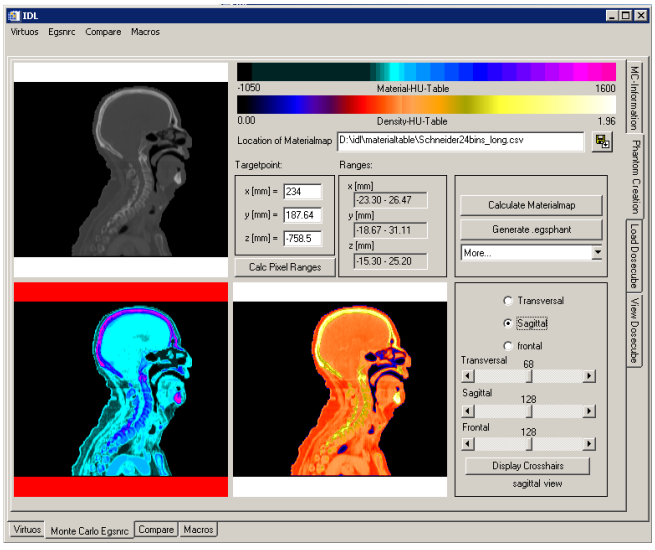

Figure 8.2.: *Material and density map created with the graphical user interface for the Schneider conversion tables. Before calculating the material and density for a phantom, one has to load a CT-cube, select a target point, which defines the isocenter and therefore the origin of the IEC coordinate system for the Monte Carlo simulation.*

CT cube reduction Analog to the pencil beam calculation the slice dimensions of the CT-cube have to be reduced to 256 x 256. This makes a direct comparison of the resulting dose cubes possible as well as it reduces the simulation time.

Conversion table selection The conversion tables themselves are saved as comma-separated values (CSV) specifying the number of boundary definitions in the file and for each defined interval the material name, the Hounsfield and mass density boundaries and if not trivial, the material number. The path of the conversion table can be specified in the graphical user interface (see Figure 8.2). It is also possible to display , an overview on the material boundaries specified in the chosen conversion table as a visualization in the two colorbars at the upper right of the tab, the upper one shows the colorcode and Hounsfield ranges for the materials, the lower one colorcoded mass densities as a function of Hounsfield Unit. The highest and lowest mass density in the conversion table are denoted at the respective ends of the colorbar.

Target point definition The targetpoint is specified in the coordinate system of the planning system and represents the isocenter. All voxel coordinates are calculated in relation to this point as it forms the origin of the IEC coordinate system, which is used in the Monte Carlo simulations. In the interface, the maximum and minimum x-,y- and z-positions of the voxel can be displayed.

Calculation of material and density map After completion of these steps, the material and density maps can be calculated and the .egsphant file can be created and displayed. This situation is illustrated in Figure 8.2 for the two different conversion tables. After the calculation, corresponding slices from the CT-cube (top), the resulting material map (lower left) and the density map (lower right) are visualized in the image frames of the graphical user interface. For a quantitative analysis, a function is available to open the slices in a separate image display.

8.2. Simulation Geometry and Settings

To assess the influence of the material conversion table on the simulated dose distribution, .egsphant phantom files were created from a head and neck CT using the two different conversion tables described above. The patient CT showed the patient only, any positioning devices were removed from the CT-dataset by replacing the Hounsfield Unit for all voxels outside the patient boundary with a Hounsfield Unit of -1000HU. Again, a typical cone beam CT imaging geometry was chosen with an X-ray tube rotation of 360° and a field size of 27cm x 27cm in the isocenter plane. The phase space file described in section 6.4 was used. A total number of $9 * 10^9$ histories was simulated for each of the phantom files using a recycle factor of 50 per particle. As both resulting dose cubes are normalized by DOSXYZnrc to show the dose per initial source particle, a direct comparison of the dose cube without any additional normalization is possible. EGSnrc transport parameters were set as described in chapter 5.1.3.

8.3. Results

8.3.1. Material and Density Maps

The material and density maps created with the two different conversion tables according to Schneider and EGSnrc, differ to a great extent. A comparison of a sagittal slice of the created maps for the head and neck case are shown in Figure 8.3. While the colorscale for the materials is unique for each of the conversion tables due to the different number of materials, the colorscale for the densities was adapted for this image to be common for both density maps.
Figures 8.3b and c show the estimated material maps for the EGSnrc table and the Schneider table. The main difference between the two is the usage of a much higher number of materials in the Schneider table, so that an additional discrimination can be seen, where the EGSnrc table yields the same elemental composition. E.g. the vertebrae are assigned a different material number and therefore a different

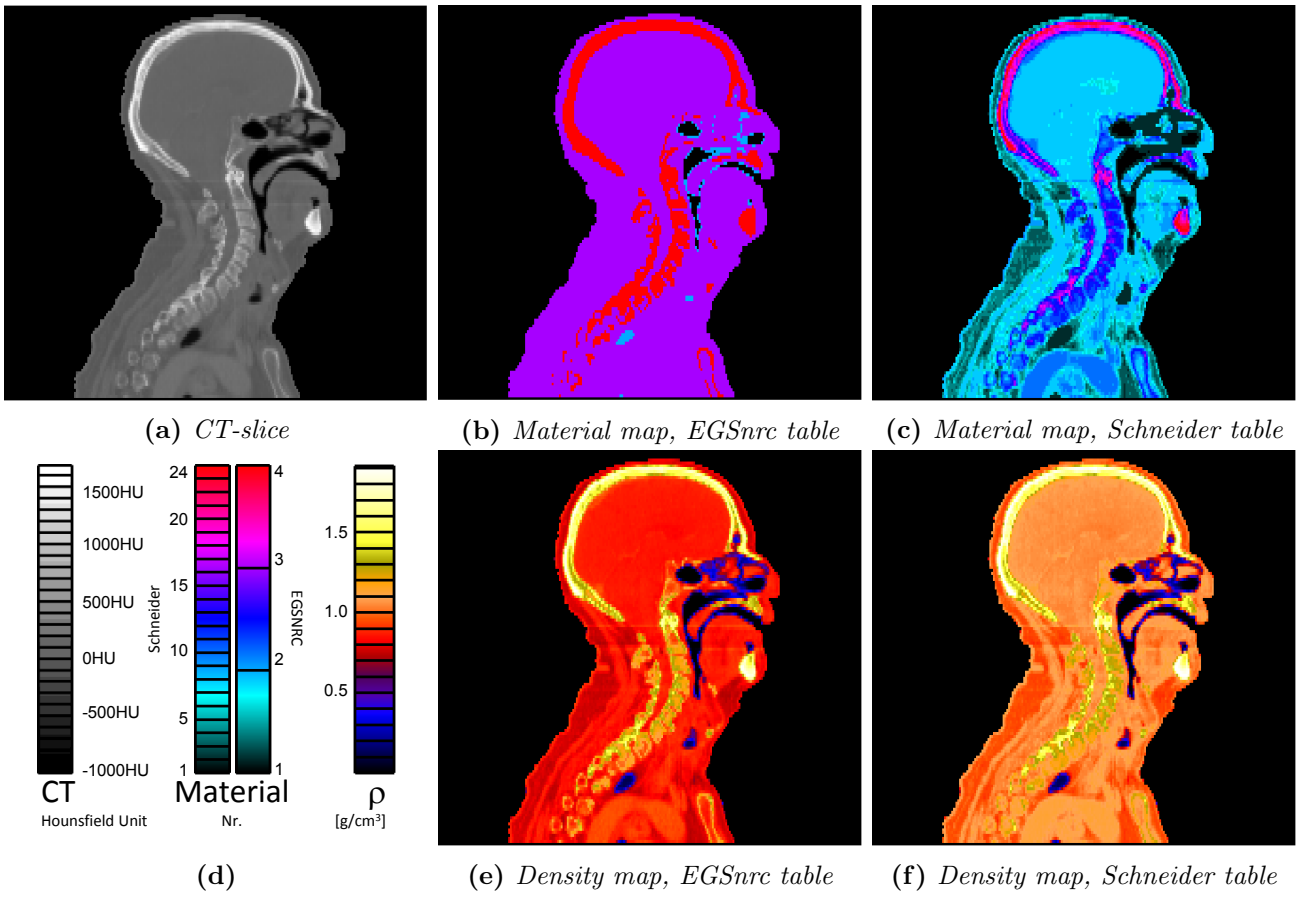

(a) *CT-slice* **(b)** *Material map, EGSnrc table* **(c)** *Material map, Schneider table*

(d) **(e)** *Density map, EGSnrc table* **(f)** *Density map, Schneider table*

Figure 8.3.: *Sagittal slices of the CT cube and the material maps (top) and density maps (bottom) for the EGSnrc conversion table (left) and the Schneider conversion table (right)*

elemental composition than the cortical bone, while the EGSnrc table assigns the same material (ICRP bone) to both. The same effect can be seen for the soft tissues.
For both cases, the elemental composition of lung material is not only assigned to the lung itself but also to some voxels, where the CT value is averaged from a voxel containing air and one containing soft tissue upon reduction of the slice dimension. The number of these voxels is relatively low, they are spread along the surface, so that the influence on the dose distribution is assumed to be very low.
Important to note is that the Schneider table does not lead to severe fluctuations in the material number within smaller areas, which would indicate a high number of missassigned voxels due to noise in the CT-image. Only in the fatty tissue, which is located directly underneath the skin e.g. at the back of the patient, such fluctuations are visible, this matches the fact, that the width of the bins for these tissues is relatively small (app. 30HU).
As it can already be seen, when comparing the Hounsfield Unit vs. density conversion tables shown in Figures 7.2 and 7.3, the mass densities calculated using the Schneider table are significantly higher than the ones calculated with the EGSnrc table. This effect is more pronounced for the soft tissues than for bony materials and can also be seen in Figure 8.3 in the bottom row, where the visualization of the sagittal slice of the density map for the Schneider table (left) is displayed in lighter colors than the one calculated with the EGSnrc table (right).
Considering the material composition and mass density at the same time, it can be summarized, that the Schneider table tends to lead to higher densities coupled with an elemental composition with a lower effective Z than the EGSnrc table. This corresponds to the fact, that the elemental compositions assumed in the EGSnrc table are tend to have an above average content of higher Z materials compared to the set of materials from the Schneider table for the same Hounsfield Unit range.

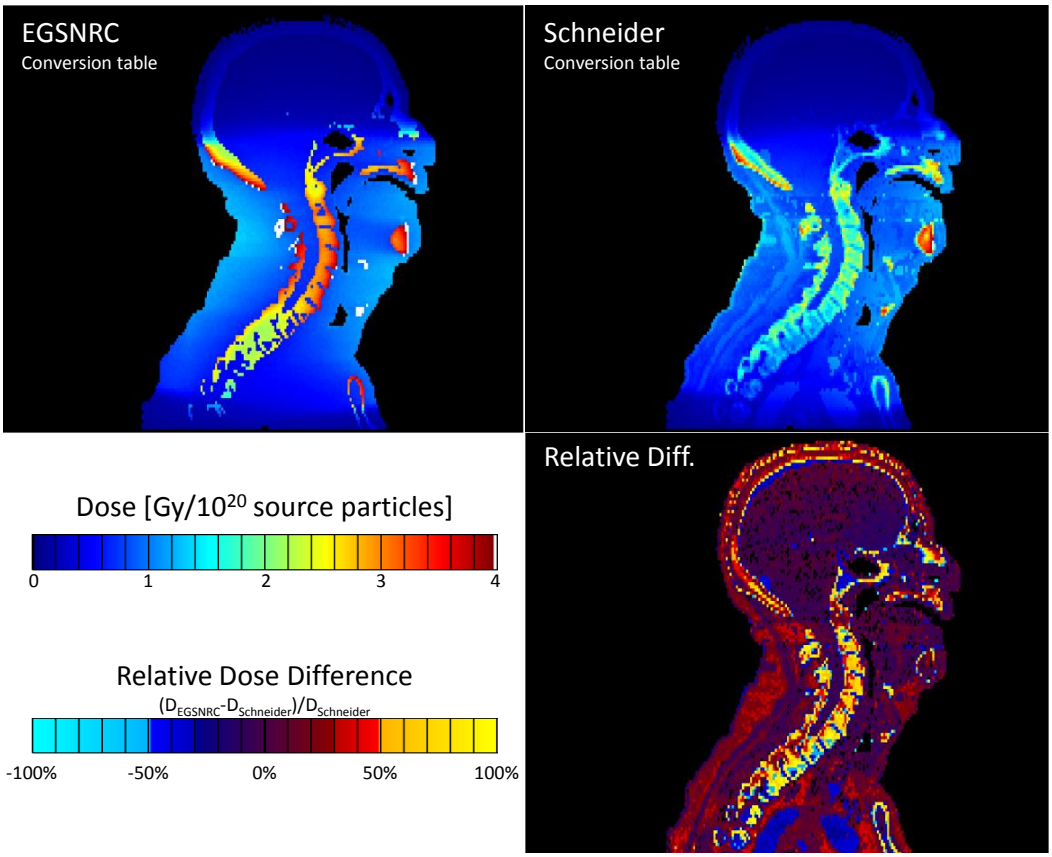

Figure 8.4.: *Comparison of sagittal slices of the dose distributions for the Schneider and the EGSnrc conversion table and the differences between them. Especially in bony structures such as the vertebrae, where the Schneider table assigns a material with a relatively high bone marrow content compared to the osseous tissue content, the differences are very high and even exceed 100% in a high number of voxels.*

8.3.2. Dose Distributions for a CBCT acquisition

The simulated dose cubes for the two conversion tables also show significant differences. Figure 8.4 shows the simulated dose distributions for the same sagittal slices as the material and density maps in Figure 8.3. Due to the dose normalization in the Monte Carlo simulations to a dose per source particle, the dose is displayed in Gy per 10^{20} source particles.
The main difference compared to typical dose distribution in MeV therapy planning is, that due to the high dependency of the dose on the atomic number, the anatomy of the patient is reflected in the dose distributions by highly varying dose levels within the different tissues. Upon comparison of the two simulated dose distributions, even a visual comparison of the shown slices reveals that due to the different assigned elemental compositions, major differences in dose occur especially in bony structures.
In Figure 8.4, the relative difference of the doses $((D_{EGSnrc} - D_{Schneider})/D_{Schneider}$ is shown in the image in the bottom row, the colorscale ranges from -100% to +100%. For the vertebrae and most other bony structures, dose differences of more than 50% are clearly visible, a more detailed analysis shows, that the use of the EGSnrc table yields doses in the vertebrae, which are more than 200% of the ones simulated with the Schneider table. For some other tissues, such as the brain tissue, the differences are much lower and do not exceed 15%. On the other hand, there are also soft tissues, such as the fatty tissue at the back of the patient, where the dose differences are between 30% and 50%.
This is also shown in the profile plots in Figure 8.5 (all axis denominations in this chapter refer to the patient coordinate system). It can also be seen in these plots, that even though the effect of the different elemental compositions on the absolute dose value in the voxel itself is quite high, the effect on the dose to other voxels is relatively low. For instance in the profile along the y-axis, the dose in the soft tissue agrees well despite the high differences in the elemental composition of the surrounding bony structures for the two conversion tables.

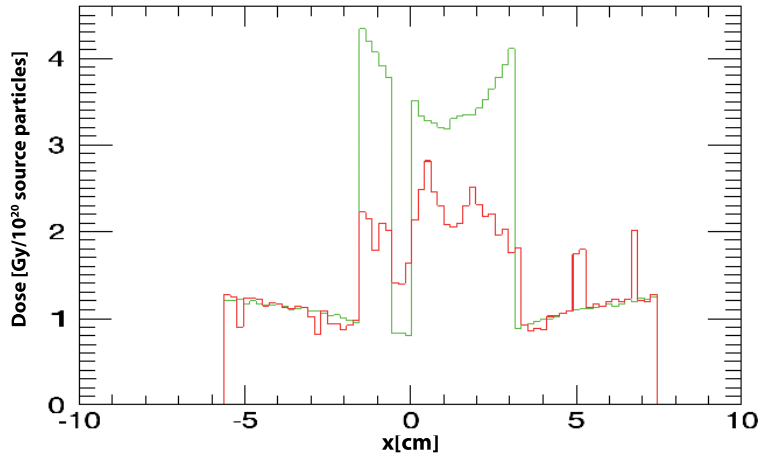

(a) *Profile along the x-axis of the patient coord. system*

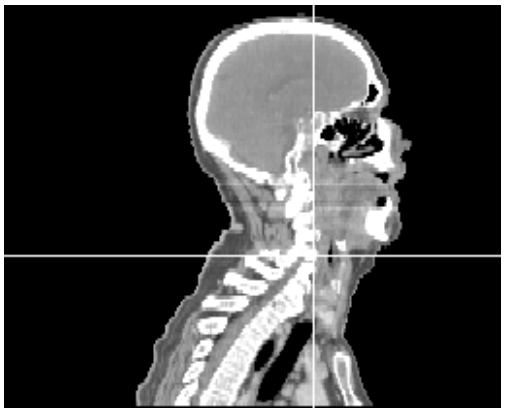

(b) *Sagittal view, marked isocenter*

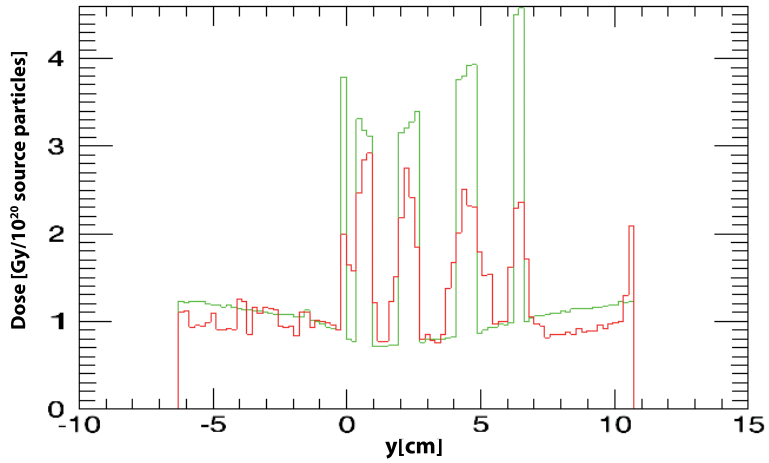

(c) *Profile along the y-axis of the patient coord. system*

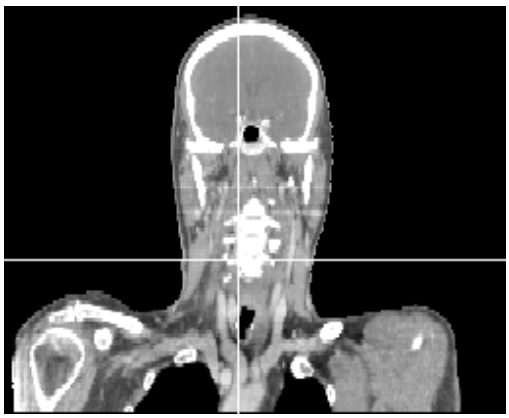

(d) *Frontal view, marked isocenter*

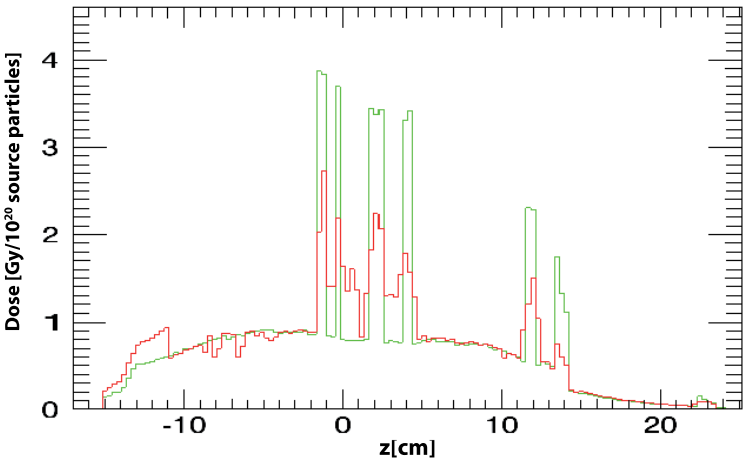

(e) *Profile along the z-axis of the patient coord. system*

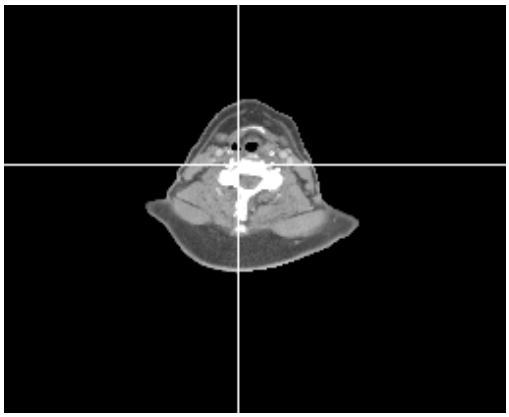

(f) *Transversal view, marked isocenter*

Figure 8.5.: *Dose profile comparison for conversion tables according to Schneider (red) and EGSnrc(green): profiles through the isocenter. The position of the isocenter and the axes is illustrated on the CT-slices at the right side.*

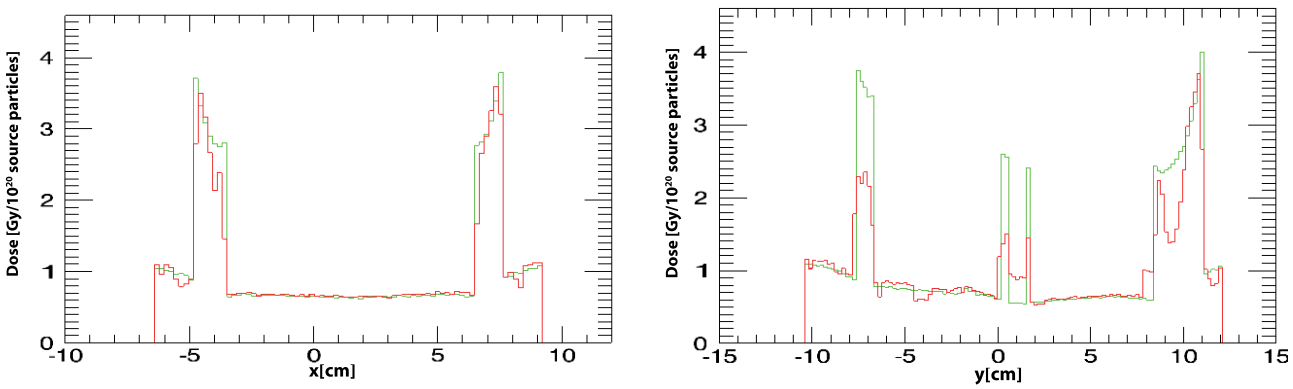

(a) *Profile parallel to the x-axis of the patient coord. system*

(b) *Profile parallel to the y-axis of the patient coord. system*

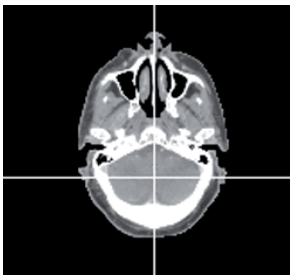

Figure 8.6.: *Dose profile comparison for conversion tables according to Schneider (red) and EGSnrc (green): profiles through the brain. On the CT-slice, which is situated 10.5cm above the isocenter, the position of the profiles and the covered anatomy is pictured. The profile along the x-axis (left) shows a good agreement for the different conversion tables within the brain tissue (central area). In this case, the dose within the bony structures is also similar for both tables, as the assigned materials for this special Hounsfield unit have similar elemental compositions. In the y-profile, larger differences can be observed, for the different bony structures, while the dose within the brain again shows only minor differences.*

Voxels with a similar composition for the two conversion tables, e.g. in the brain, where the Schneider material no.8 and the EGSnrc soft tissue are assigned, show a relatively low deviation even though the photons beam is attenuated by a number of differing materials before reaching this voxel. This is also shown in Figure 8.6, where profiles through the lower part of the brain are plotted. The profile along the x-axis even shows a similar dose in the bone for both dose distributions. This is due to the fact, that the material composition used in the EGSnrc table is close to cortical bone, as is the material used for the respective Hounsfield Unit range in the Schneider table. In the profile along the y-axis, where the two conversion tables assign very different elemental compositions to the bony structures, the dose in these structures again shows high differences.

8.4. Discussion

To simulate dose distributions for patient geometries obtained from a CT scan using a Monte Carlo system, one first has to convert the Hounsfield Units given in the CT dataset to allow for an estimation of the cross sections for the different interaction processes in the simulation. In this chapter, it has been shown, that for the keV energy range the choice of the conversion table, which maps the Hounsfield Unit to a given elemental composition and mass density, highly influences the simulated dose distribution. For the two investigated tables consisting of 4 materials (EGSnrc table), which is often used for dose simulations, and 24 materials (Schneider table), the differences in dose in the bony structures regularly exceed 100%, for some of the soft tissue materials used in the Schneider table (e.g. fatty tissues), the differences still vary between 30% and 50%. It is not possible to decide, which of the dose distributions is closer to the "true" dose distribution, without measuring doses within a patient. For choosing a conversion table, the following arguments have to be considered: While a high number of materials is desirable to reproduce the elemental compositions in the body as accurate as possible, one argument for a lower number of materials is the smaller number of missassigned voxels due to noise in the CT dataset. For the investigated table with 24 materials, fluctuations in the material number for neighboring voxels, which

would be expected subsequent to a missassignment due to noise, could not be observed. Therefore, for the remainder of this work, the conversion table as suggested by Schneider et al. [74] was used, though some investigations were undertaken for both conversion tables, as the table consisting of only 4 materials is widely used for Monte Carlo dose simulations on patient geometries.

9. Pencil Beam Dose Calculation for Patient Geometries

In this chapter, the accuracy of the pencil beam algorithm for the application on patient data is evaluated. Two different sites were chosen for this investigation, the head and neck region and the pelvic area. As the pencil beam algorithm is known to yield poor results in the lung region even for the calculation of MeV dose [78, 79, 80], this anatomic site is not included in the investigation. For each anatomic site, two different typical imaging beam geometries are investigated. The first geometry is a photon beam from a single direction as it would be used for motion monitoring with fluoroscopic imaging. The second geometry simulates the acquisition of a cone beam CT as used for daily positioning with a 360° rotation of the X-ray tube. This choice of beam geometries represents the two most extreme cases considering the degree to which they challenge the algorithm. The single photon beam at 0° represents the most challenging situation even compared to other single photon beam angles. The results for the different beam configurations therefore form the upper and lower boundaries for the accuracy of the algorithm for other imaging geometries, such as a 200° CBCT acquisition or a 360° CBCT acquisition with a shifted detector.

9.1. Methods

9.1.1. keV Dose Scaling

Literature Review

The use of dose scaling factors for the correction of a preliminary dose distribution in bones has been proposed in several publications [23, 24, 25]. All of these publications use their respective adaptation method for all voxels above a certain Hounsfield Unit in the CT-data, different compositions of bony tissues are not considered. This is the case for both, the correction method itself and eventual Monte Carlo simulation methods used for comparison. Also all of the publications use a dose distribution as the starting point, which is calculated considering only the changes in the electron density and no other dependency on the atomic number Z. This dose distribution is obtained either using a superposition algorithm with a scaling of the kernel according to the relative electron density, or Monte Carlo simulations.
In the publication by Alaei et al. [24], the used dose scaling factor represents the theoretical factor if only the additional attenuation of the primary photon beam and no scatter effects are considered: the ratio of the mass absorption coefficients of bone and water for a specific beam energy. This method results in dose differences of up to 30% compared to phantom measurements for the pelvic region.
The method of dose scaling proposed by Ding et al. [23] takes the changed scatter due to voxels with a high effective atomic number into account. It therefore applies scaling factors not only to the dose in the bone voxels themselves but also voxels lying upstream and downstream along the beam direction. Despite the use of only one bone material, the method includes a high number (10) of energy dependent adjustable parameters, which are obtained in a Monte Carlo simulation for a phantom geometry similar to the calculation of depth scaling factors described in chapter 7.2.5. While this method provides a very good estimation of the dose in the soft tissue, again differences of app. 25% occur in the shown profiles for a head and neck patient. As the scaling method requires the knowledge of the beam direction,

another disadvantage of this method is, that it adds the calculation time of a beam angle dependent postprocessing step to the already relatively high calculation time of the superposition algorithm.
In their very recent publication, Pawlowski et.al. [25] use a dose distribution simulated with Monte Carlo as their preliminary dose distribution, which, similar to the other publications, only considers changes in the density of the voxels, not the atomic number. Their proposed method of dose scaling considers the beam hardening, which occurs to a much higher extent, when the beam traverses voxels with a high atomic number. The dose scaling factor is therefore given as a function of a quantity called effective bone thickness. This is the only publication including different anatomic sites. As mentioned above, only one type of bone voxels is considered in this method. An adaption of this method to the use of more materials would require major changes in the definition of the effective bone thickness. Accuracies of 3% of the maximum dose to soft tissue or better are reported for soft tissue voxels for this correction method, at app. 4.5% - 13% the reported accuracy for bone voxels is significantly lower. Considering the speed of the method, the calculation for the required effective bone thickness the correction is beam angle dependent, so that it has to be executed repeatedly for a rotation of the X-ray tube. Again, this calculation time is added to the time needed for the calculation of the preliminary dose distribution.

Estimation of Dose Scaling Factors β

In this work, the dose scaling method was optimized with respect to calculation speed, while still maintaining a good accuracy for the dose calculation. Due to the high influence of the material definition, which was shown in chapter 8 a differentiation between different bony materials and also different soft tissues should also be possible for the applied method. For this reason, a simple method of dose scaling was chosen, where a single dose scaling factor per material is employed. Due to this the postprocessing step does not include a calculation depending on the beam angle as in [23] and [25], which makes the algorithm very fast. To still incorporate the beam hardening, which also depends on the anatomic features and the beam configuration, dose scaling factors specific for the anatomic site and beam configuration were used. This is in accordance with other algorithms proposed in the literature [23]. In contrast to other dose scaling methods suggested in the literature, the use of material dependent dose scaling factors is not restricted to a single bone material. The dose scaling factors can be estimated for an arbitrary number of considered materials, which also allows the desired differentiation between different soft tissues.
The algorithm for the calculation of a specific set of dose scaling factors consists of the following steps:

Selection of the Reference Patient For each anatomic site, a reference patient has to be chosen. The reference patient should reflect the typical anatomy for this site, a patient with very special anatomic features should not be used as the reference patient. The position of the target point and the anatomic structures for this patient should be typical for this site, otherwise, the beam hardening situation cannot be assumed to be equivalent to that for other patients.

Monte Carlo Dose Simulation For the reference patient, a dose simulation with a Monte Carlo program (in this case EGSnrc) has to be executed. For this, the patient geometry has to be converted into a simulation geometry suitable for Monte Carlo simulations using the material conversion table of choice as described in 8.1. The irradiation geometry such as a single photon beam or a CBCT acquisition combined with a typical field width should be used in the simulation.

Pencil Beam Dose Calculation For the same irradiation geometry and patient as in the simulation, a pencil beam dose calculation has to be carried out. For this calculation, the energy specific pencil beam kernels (as derived in chapter 5) and depth scaling factors $\alpha(HU)$ for the respective energy spectrum and conversion table (as derived in chapter 7) have to be employed.

Dose Ratio Evaluation The dose scaling factor $\beta(Z)$ is defined according to

$$D_{pencil}(x, y, z) = \beta(Z) D'_{PB}(x, y, z), \tag{9.1}$$

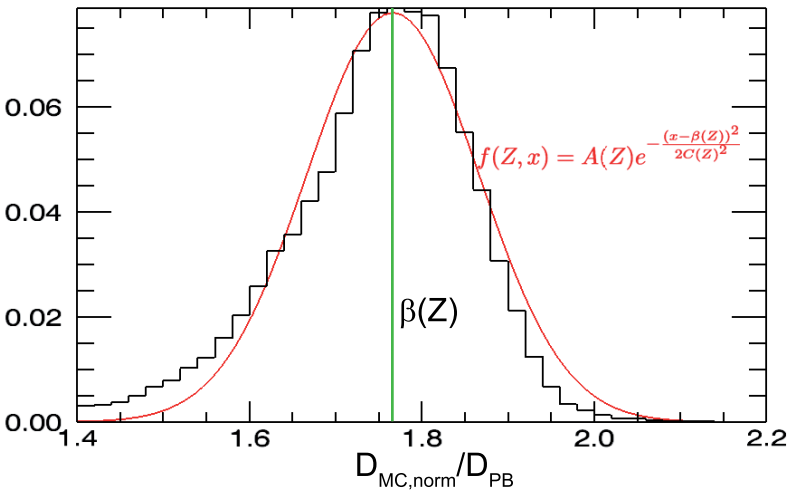

Figure 9.1.: *Determination of β as the mean value of a gauss fit (red) of the histogram (black). This analysis is done for each material in the conversion table to obtain the material specific scaling factors.*

where in the optimal case, the dose distribution D_{pencil} is equal to the simulated dose distribution $D_{MC}(x, y, z)$, and the dose distribution $D'_{PB}(x, y, z)$ is the result of the pencil beam calculation with the adapted depth scaling in the planning system. The optimal dose scaling factor for a single voxel would therefore be the ratio $\beta_{opt}(x, y, z) = D_{MC}(x, y, z)/D'_{PB}(x, y, z)$ of the available dose distributions. To obtain average dose scaling factors $\beta(Z)$ separately for each material, a histogram of the optimal scaling factors $\beta_{opt}(x, y, z)$ is calculated employing the respective conversion table to determine the material for each voxel. For each of the histograms of optimal scaling factors $\beta_{opt}(x, y, z)$, the dose scaling factor for the material is calculated as the mean value for a Gaussian fit.
The use of the mean of the Gaussian fit instead of the direct mean value of the ratios for all voxels of the respective material compensates for the fact, that while very high ratios are possible for single voxels, the smallest possible ratio is 0, so that the very high ratios would significantly increase the dose scaling factor. Even though this would lead to a higher accuracy for the single high dose voxels, the dose in many other voxels would be overestimated.
To optimize the factors to reproduce the dose within the primary beam area as good as possible, the scaling factors can be calculated using a restricted range of voxels along the z-direction. In the graphical user interface, which was developed for this purpose, this setting can be chosen combined with a given field size, which will restrict the considered volume to voxels with z-values within ± half of the given field side length.

9.1.2. General Remarks on the Measure of Accuracies

Summarizing the accuracy of a dose calculation algorithm in a single number is a very difficult if not impossible task. IN other publications concerning dose calculation for keV imaging procedures, each publication uses a different measure for the evaluation. If a numerical value is given, it is mostly based on a statistical analysis of the differences between the calculated values and reference values either obtained in a measurement or in a Monte Carlo simulation.
In this work not only statistical values summarizing the differences for all voxels were presented but also exemplary analyses of dose slices pointing out characteristic features of the dose differences. Even though the statistical values also play an important role in judging the accuracy of the calculation algorithm, one also has to keep in mind, that they do not contain any information about whether the analyzed differences occur randomly or systematically.
Another remark has to be included concerning the standard deviation of the absolute differences relative to the maximum dose in soft tissue as a measure of the accuracy of the dose calculation as in [25]. Considering this value upon comparison with a Monte Carlo dose calculation as the reference, one has to keep in mind that the absolute differences are normalized to the maximum dose value in soft tissue obtained in a Monte Carlo simulation. As calculations with Monte Carlo methods underlie statistical

variations, the maximum value might be derived from a single voxel with an unusually high dose. This means that a low accuracy of the Monte Carlo simulation will improve the calculated accuracy of the dose calculation algorithm. In addition the estimated accuracy depends on the amount of voxels outside the primary beam area, which are included in the analysis. These voxels typically receive a very low dose associated with a low absolute dose difference or no dose at all and therefore distort the statistical data. Therefore in this work, only voxels within the primary beam area are included in statistical analyses.

9.1.3. Dose normalization

All Monte Carlo dose distributions were normalized so that the dose values were available in Gy/10^{20} source particles. Due to the chosen normalization factor for the Monte Carlo dose upon calculation of the scaling factors, the resulting pencil beam dose will be also be available in Gy/10^{20} source particles, to obtain the total dose for an imaging procedure, one has to multiply the dose with the number of source particle, which is defined by the charge Q crossing the X-ray tube, the so called mAs-setting as it is measured as a current (in mA) over a known time (in s). A typical mAs value for the acquisition of one projection image is 2mAs [10], from which the number of source electrons with the elemental charge $e \approx -1.602 * 10^{-19} C$ per projection image N_{1proj} can be calculated as

$$N_{1proj} = \frac{Q_{1proj}}{e} = \frac{2mAs}{1.602 * 10^{-19} C} \approx 1.248 * 10^{16}. \tag{9.2}$$

Combined with the unit of dose being Gy/10^{20} source particles this yield the following conversion:

$$D[\frac{mGy}{projection}] \approx 0.1248 * D[\frac{Gy}{10^{20} source\ particles}]. \tag{9.3}$$

Assuming one projection image per degree for a cone beam acquisition with a centered detector, this means that one 360° degree rotation of the X-ray tube is equal to a number of

$$N_{360proj} = \frac{360 * Q_{1proj}}{e} \approx 4.493 * 10^{18} \tag{9.4}$$

source electrons reaching the target for the photon production. Analog to the single projection, this yields

$$D[\frac{mGy}{CBCT}] \approx 44.93 * D[\frac{Gy}{10^{20} source\ particles}]. \tag{9.5}$$

9.2. MC-simulations and Pencil Beam Calculations

9.2.1. Phantom Creation

For each of the patients, the CT-dataset in combination with defined volumes for the patient outline, target volume and organs at risk was available from the treatment planning process for the patient. As the patient fixation material was not included in the investigation, all voxels in the CT outside the patient outline were set to a value of -1000HU. For the Monte Carlo simulation for each patient, a phantom definition file was created using the center of the target volume as the isocenter and the Schneider material conversion table to derive the elemental composition and mass density for each voxel [74].

9.2.2. Beam geometry

As described above, two different beam geometries were investigated: a single photon beam and a cone beam CT acquisition. As the shape of the anatomic structures in the head is most challenging for the pencil beam algorithm due to a high curvature of the face and a high number of bony structures under the surface, a photon beam at an angle of 0° was chosen for the investigation of a single photon beam. For the cone beam CT acquisition, a rotation of the X-ray tube by 360° around the target point of the patient was assumed.

For both beam geometries, a field size of 27cm x 27cm in the isocenter plane was used, with a distance between the radiation source and the isocenter of 100cm. This matches the approximate dimensions for a maximum field of view at our Siemens ARTISTE (Oncology Care Systems, Siemens Medical Solutions, Concord, CA, USA).

9.2.3. Simulation Settings

Apart from the beam direction, all settings for the simulations in DOSXYZnrc were chosen to be common for all patient dose simulations. To achieve the field size of 27cm x 27cm, the phase space file described in 8.2 was used. For the first simulations (360° rotation for Patient A and B), a total number of $9 * 10^9$ was simulated in each simulation, in all other simulations, the number of histories was reduced to $5 * 10^9$ with a minimal loss in simulation accuracy. No electron transport was simulated, the transport of photons was simulated with a cutoff energy at 10keV. All EGSnrc transport options were set as described in chapter 4.1.2. As described above, all Monte Carlo dose distributions were normalized so that the dose values were available in Gy/10^{20} source particles.

9.2.4. Pencil Beam Calculations

The pencil beam calculation with the depth scaling was executed using the planning system VIRTUOS (Version 4.7.5,DKFZ Heidelberg) with the obtained depth scaling factors $\alpha(HU)$ supplied in the table usually used as the HU-electron density table (see chapter 7), resulting in the dose distribution $D'_{PB}(x, y, z)$.
The normalization of the dose scaled pencil beam dose is inherently included in due to the estimation process of the scaling factors, so that the final dose values from the pencil beam algorithm are also available in Gy/10^{20} source particles. The scaling factors $\beta(Z)$ were calculated for the reference patient for the respective anatomic site. To obtain the final pencil beam dose distribution $D_{PB}(x, y, z)$ for each patient, the dose scaling factors were applied to the respective depth scaled pencil beam dose distribution $D'_{PB}(x, y, z)$ from the planning system. To increase the calculation speed for the cone beam CT geometry, a stepsize of 5° was chosen, as a further decrease of the stepsize did not result in significantly different dose distributions. This lead to a calculation of 72 beams per plan, with a total weight of all beams of 1 to obtain a dose distribution, which is independent of the number of beams. This is also the case for the simulated dose, which is normalized to the number of source particles. The same scaling factors can therefore also be used for a 360°-rotation calculated with the pencil beam algorithm with a stepsize of 10° or 2° or 1°.

9.3. Head & Neck Patients

This section focuses on the accuracy of the developed pencil beam algorithm for patient CTs in the head and neck area. In addition to a combined part on the calculated dose scaling factor themselves, the results in this chapter are split into two major parts according to the irradiation geometry (single beam or cone beam CT acquisition). For each geometry, three major characteristics are evaluated: trends in the dose slices and their differences, a statistical analysis of the accuracy and the accuracy of the pencil beam algorithm in predicting doses to organs at risk for the respective site.

9.3.1. Patient Description

As the reference patient for the head and neck region, a patient was chosen, were the targetpoint lies approximately in an intermediate position, so that the fields for most target points in the brain or face, as well as for most target points in the neck region in z-direction overlap with the simulated field to a high extent. The material map for the reference patient as created with the graphical user interface is shown in Figure 9.2a. The reference patient for the site head and neck is also referred to as Patient A in this chapter. The two other patients (Patient B and Patient C), which are used to investigate the accuracy of

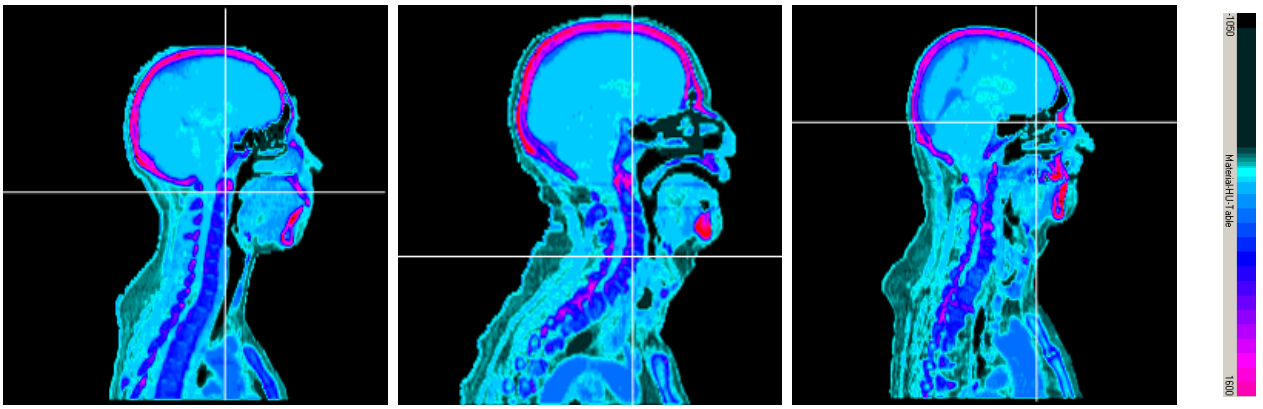

(a) *Patient A* **(b)** *Patient B* **(c)** *Patient C*

Figure 9.2.: *Material map and targetpoints for the head and neck patients. The crosshairs mark the frontal and transversal position of the targetpoint, which is used as the isocenter. The target points for the Patients B and C lie in opposite directions compared to the reference patient, Patient A, so that different tumor sites in the head and neck area are covered.*

the pencil beam algorithm, if the simulated dose is not known beforehand are shown in Figure 9.2b and c. They represent two very different sites within the head and neck region, the target point for Patient B is located in the neck region, while for Patient C, the target point is situated in the frontal region at the height of the root of the nose. For all three patients, the target point is not located within the shown slice, but shifted towards the right or left of the patient.

9.3.2. Dose Scaling Factors $\beta(Z)$

The scaling factors $\beta(Z)$ were derived separately for each beam geometry. The dependence of β on the atomic number and therefore the elemental composition was converted into a dependence on the Hounsfield Unit value using the Schneider material conversion table, which was also used for the Monte Carlo simulations. As described above, histograms of the ratio between the normalized Monte Carlo dose D_{MC} in Gy/10^20 source particles and the pencil beam dose D_{PB} were calculated.

Dose ratio histograms

Figure 9.3 shows a summary of the ratio histograms for a single photon beam at an angle of 0° and for a 360° rotation. The most prominent common characteristic in these plots is the increase of the average ratio with increasing Hounsfield Unit. This was also expected due to the increasing content of high Z elements in the materials. Another important feature in the plot is, that especially for the single beam direction, the distribution of ratios within one material is much wider than for the CBCT acquisition. This is due to the beam hardening, which leads to a varying energy spectrum for voxels at different depth, which also lead to a different increase in dose. For the rotation, the voxels are irradiated from different directions, so that on average, the beam spectrum for all voxels is similar. This effect will also influence the accuracy of the scaled pencil beam algorithm, as a single scaling factor per material cannot compensate for a wide distribution of dose ratios.

Derived Dose Scaling Factors

The resulting scaling factors as a function of the Hounsfield Unit for the reference patient A are plotted in Figure 9.4 (red). In addition, the plot shows the scaling factor if calculated for Patient B (blue) and Patient C (green). It can be seen that even though the dose scaling factors for the single beam and the tube rotation are similar, significant differences occur especially for the bony materials with a higher content of high Z elements. This reflects the beam hardening, which has a higher influence for the single beam leading to different dose ratios at different depth.

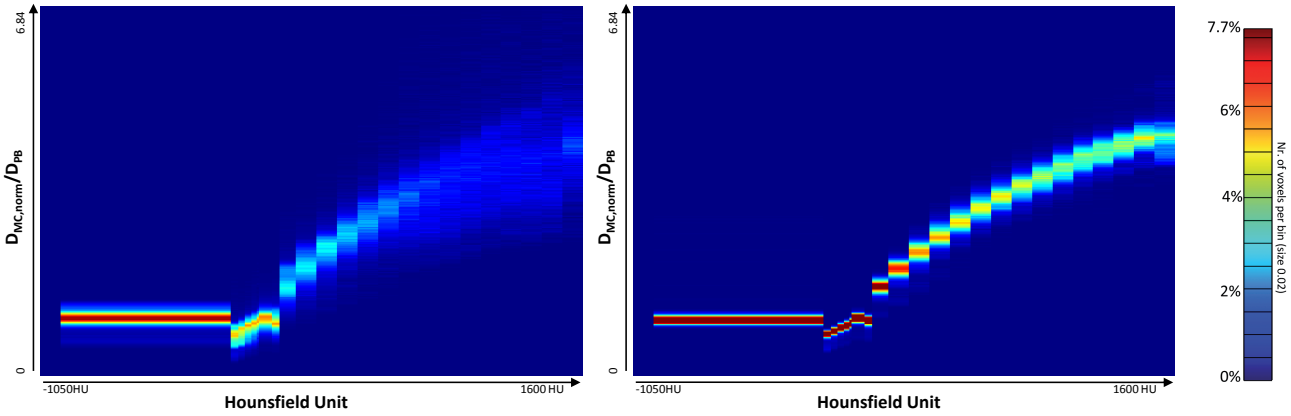

(a) *Single Beam at 0°* **(b)** *CBCT: 360° tube rotation*

Figure 9.3.: *Summary of dose ratio histograms as a function of the Hounsfield Unit. For each material, one histogram is calculated and displayed for the associated Hounsfield Unit range. a shows the situation for a single photon beam at an angle of 0° (front of the patient), b for a 360° rotation of the X-ray tube. The main difference, which can be seen between the different beam geometries is, that while the histograms for the 360° rotation are relatively narrow, for the single photon beam, a wide distribution of dose ratios occurs in each material.*

The beam hardening effect also explains the increased scaling factors for Patient B compared to the other patients: For this patient a smaller part of the head with the skull directly underneath the surface is included in the primary beam, leading to a softer energy spectrum of the beam averaged over all voxels.
Another aspect can be investigated, when comparing the dose scaling factors for the different patients: As the dose will later be obtained by multiplication with the scaling factor, trends of the factors between the patients will translate into adverse affects in the average dose difference for the respective patient, so that an estimated scaling factor which is higher for the patient himself than for the reference patient suggests that the dose for this patient will be systematically underestimated (As the optimal scaling factor would be the one calculated from the dose ratios of the patient himself). Evaluating the ratio of the different scaling factors in that respect, e.g. an underestimation of the dose is expected for the CBCT acquisition for Patient B.

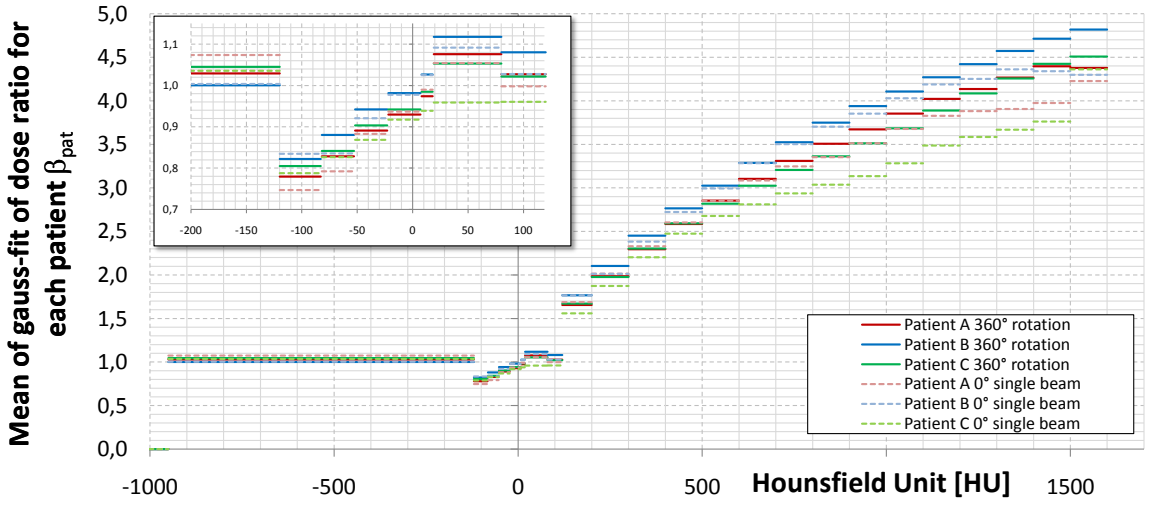

Figure 9.4.: *Dose scaling factors β as calculated for all head and neck patients for both beam configurations.*

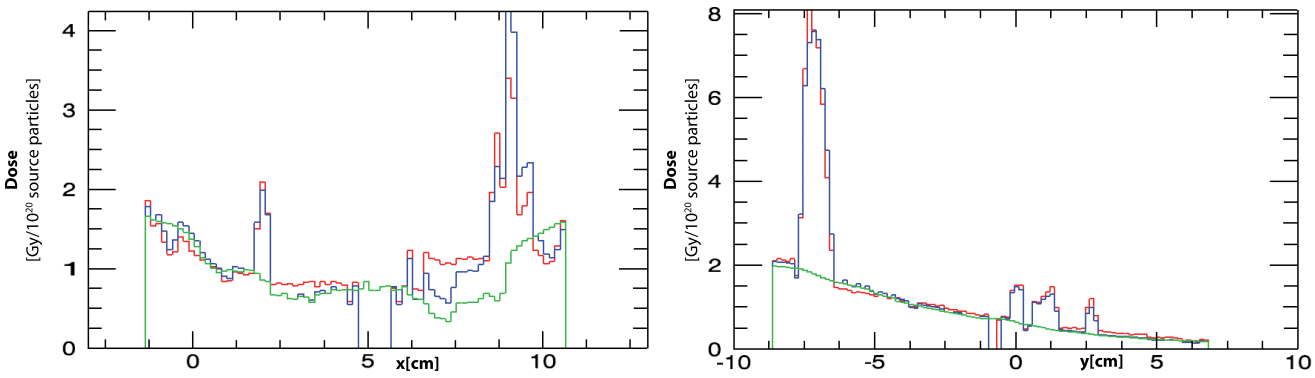

(a) *Profile parallel to the x-axis* **(b)** *Profile parallel to the y-axis*

Figure 9.5.: *Dose profiles along the x-, y- and z-axis of the patient coordinate system for the reference patient for a single photon beam at 0°. The simulated dose is plotted in red, the pencil beam dose is plotted in blue. The positions of the profiles are marked in the CT with crosshairs.*

9.3.3. Single beam - Dose Comparison

Analysis of Dose and Difference Slices

For all patients, the pencil beam dose was calculated using the dose scaling factors originating from the dose ratios for the reference patient, Patient A. The evaluation of the accuracy of the pencil beam therefore has to be mainly based on the results for Patients B and C, as these patients represent all future patients, where the simulated dose distribution is not known. Still, the results for Patient A can offer additional information.

As a first impression for the effect of the dose scaling algorithm, Figure 9.5 shows profiles of the different dose distributions parallel to the x- and y-axis of a transversal slice in the lower jaw region of the reference patient for a single beam at 0°. Shown are the simulated dose D_{MC} (red), the depth scaled pencil beam dose distribution D'_{PB} as calculated by the planning system (green) and the final pencil beam dose D_{PB} with the dose scaling factors applied (blue). It is obvious in this plot, that the application of the scaling factors highly improves the shape of the pencil beam profiles compared to the Monte Carlo simulation. Nevertheless, significant differences can be observed for smaller regions, e.g. in the x-profile at app. 6.5cm $<$ x $<$ 7.5cm.

The cause of the deviations is difficult to analyze in the profile alone, as only a very limited view on the dose distribution is offered. Figure 9.6 shows the matching transversal slice, the positions of the profiles are marked with white lines. In addition to the dose slices themselves, a map of the absolute difference

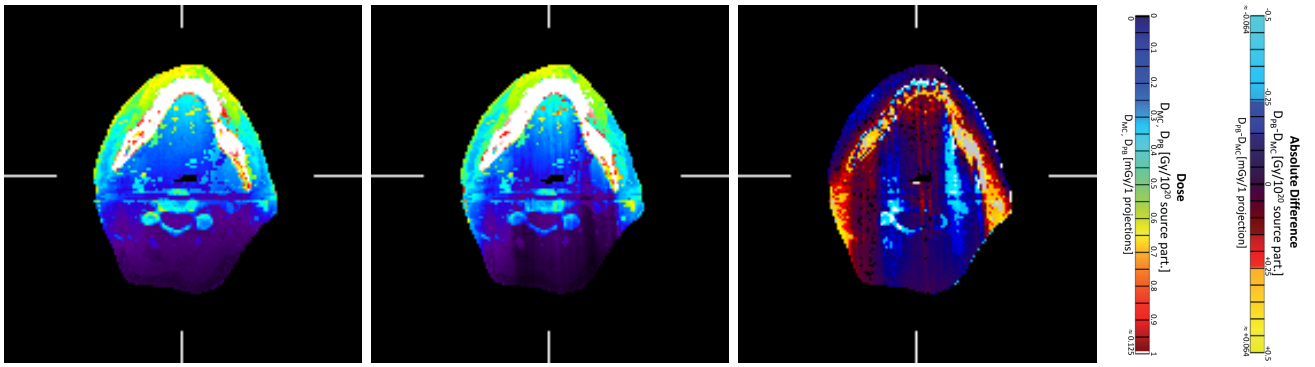

(a) *Simulated dose* D_{MC} **(b)** *Pencil beam dose* D_{PB} **(c)** *Abs. diff.* $D_{PB} - D_{MC}$

Figure 9.6.: *Transversal slices of the simulated and pencil beam dose distribution for Patient A for a single photon beam at 0°. In addition, the absolute difference between the two dose distributions is shown in (c). Note, that an underestimation of the dose by the pencil beam algorithm occurs behind dental fillings or bony structures, which can be identified as darker stripes in the dose slices and as blue stripes in the difference map.*

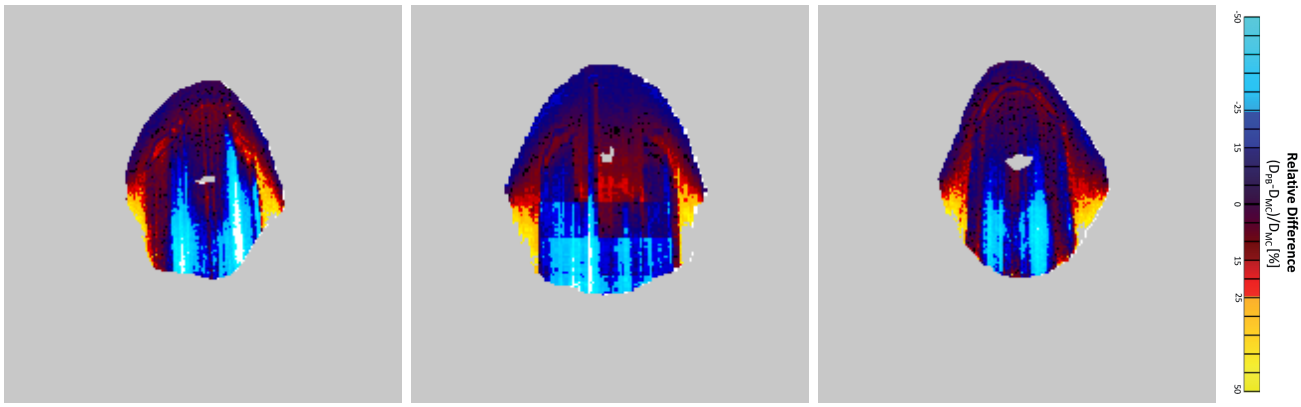

(a) *Patient A* **(b)** *Patient B* **(c)** *Patient C*

Figure 9.7.: *Transversal slices of the absolute difference between simulated and pencil beam dose distribution for all head & neck patients. Note the similarities between the patients: behind the bony structures / teeth at the front of the patient, the pencil beam underestimates the dose. At the sides, where no bony structures are present, an area of severe overestimation of the dose can be identified for all patients.*

$D_{PB} - D_{MC}$ is shown. In this plot, it can be seen, that the decrease in the pencil beam dose described above for the profiles is due to a very high absorption most probably in a dental filling or implant situated at the front of the patient. The associated decrease in dose in the direct photon path behind the fillings for the pencil beam algorithm can be identified as a darker stripe in the dose distribution in anterior posterior direction or as a blue stripe in the difference map. For the simulated dose, the gradient in the dose behind the filling is less steep, as a high fraction of the photons of the pencil beam with the primary beam path through the filling are scattered around the high absorption area.
When considering the relative difference maps for this anatomic region for all head and neck patients in Figure 9.7 (more dose slices are shown in Appendix B), one can see a pattern of over- and underdosage, which is common for all patients: in the skin region in front of the teeth, the dose is underestimated by the pencil beam algorithm, behind the bony structures of the lower jaw, an area of underestimation can be identified for all patients. At the sides, where the pencil beams do not cross any bony structures, the dose is overestimated. As the dose is very low in most of these areas, the very high relative differences translate into absolute dose differences comparable to that in the other voxels.
The above described trend is visible in all transversal slices, as it can be seen in the relative difference maps for the sagittal view (Figure 9.8): For all patients, the dose in front of the trachea and the vertebra is calculated with a relative difference of less than 15% for most voxels. In the area behind the vertebra the bony structures cause a stripelike pattern, which depends on the exact patient anatomy.
The other important trend visible in the sagittal slices regards the dose outside the primary beam area, where very high relative differences (>> 50%) can be observed for all patients. While the absolute difference for the soft tissue in this area is low (<10% of the soft tissue dose in the frontal region), the absolute difference observed for the bony structures is app. 3 times higher.

Statistical Analysis

To quantify the overall accuracy of the algorithm difference, histograms were calculated for the relative differences for all patients considering all voxels in the primary beam area (within a range of z-values of ± 1/2 of the field side length). These histograms are shown in Figure 9.9a. For Patient B, the histogram shows a shift of the maximum indicating a systematic underestimation of app. 10%. As described above, this effect was expected due to the different dose ratios for this patient as shown in Figure 9.4. For the investigated non-reference patients, Patients B and C, the fraction of the considered voxels with a relative difference below ±20% is below 70% (63.34% for Patient B and 66.24% for Patient C), for 30% the fraction increases to almost 80% in both cases.

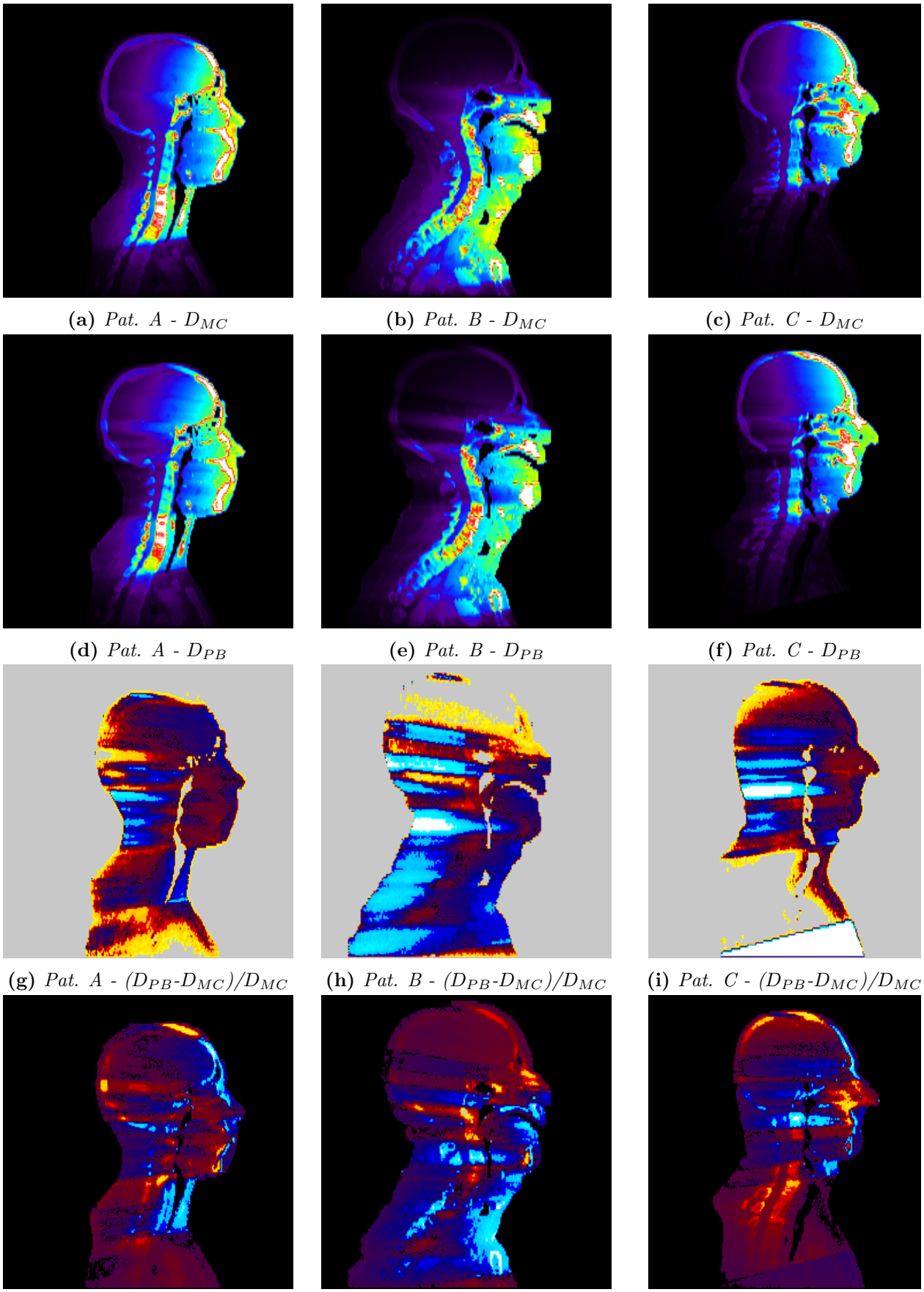

(a) *Pat. A - D_{MC}* **(b)** *Pat. B - D_{MC}* **(c)** *Pat. C - D_{MC}*

(d) *Pat. A - D_{PB}* **(e)** *Pat. B - D_{PB}* **(f)** *Pat. C - D_{PB}*

(g) *Pat. A - $(D_{PB}$-$D_{MC})/D_{MC}$* **(h)** *Pat. B - $(D_{PB}$-$D_{MC})/D_{MC}$* **(i)** *Pat. C - $(D_{PB}$-$D_{MC})/D_{MC}$*

(j) *Pat. A - D_{PB}-D_{MC}* **(k)** *Pat. B - D_{PB}-D_{MC}* **(l)** *Pat. C - D_{PB}-D_{MC}*

Figure 9.8.: *Single photon beam at 0°: Sagittal slices of the dose distributions and difference maps for all head and neck patients. Note that for the area in front of the trachea and the vertebrae the relative difference is below 15% for all patients, while in the low dose area behind the spine, very high relative differences occur. The same colorscale as in Figures 9.6 and 9.7 was used.*

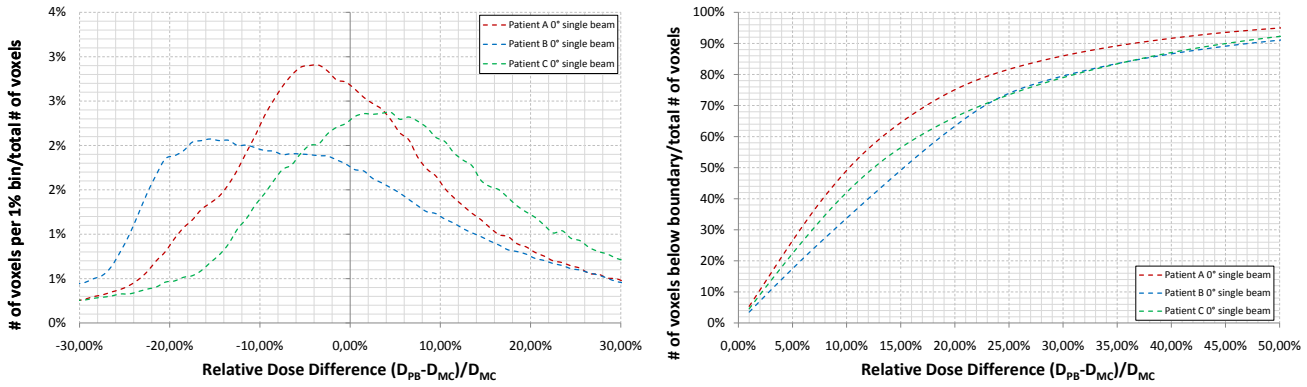

(a) **(b)**

Figure 9.9.: *(a) Histogram of differences for all patients for a beam at 0°. (b) Integrated histogram of differences for all patients for a beam at 0° showing the number of voxels within the boundaries, e.g. the number of voxels with differences between -10% and +10% divided by the total number of voxels.*

Evaluation of Organ Doses

To evaluate the accuracy of the pencil beam algorithm for the calculation of doses in the organs at risk, the pencil beam dose distribution and the simulated dose distribution were imported into the treatment planning system, which offers a number of tools for the evaluation of doses in organs at risk. As Monte Carlo simulation underlie statistical variations, only the mean dose per organ was calculated for both dose estimation methods and compared, the maximum and minimum dose were not included in the analysis. Only organs at risk, which were delineated in at least 2 patients, were included in the analysis.
To compare the accuracy of the algorithm to the method currently in use, which is the simulation or measurement for a single phantom geometry, the relative error was calculated not only for the comparison between Monte Carlo dose and Pencil Beam dose, but also for the comparison of the Monte Carlo doses for Patient A and the respective other patient. Table 9.1 shows the result of the analysis of the mean values. Despite the wide distribution of differences, which was reported in the quantitative description, the mean dose for almost all organs at risk for patient B and C could be predicted with an accuracy better than 10%. The only exception is the parotis for Patient B, where the relative difference was 18.63%, which is still below the difference resulting from a fixed reference value.

Table 9.1.: *Mean Organ doses - Pencil Beam vs. Monte Carlo - Single beam at 0° - Head & Neck*

	Patient D			Patient E				Patient F			
Organ	D_{MC} [mGy]	D_{PB} [mGy]	$\frac{D_{PB}-D_{MC}}{D_{MC}}$	D_{MC} [mGy]	D_{PB} [mGy]	$\frac{D_{PB}-D_{MC}}{D_{MC}}$	$\frac{D^A_{MC}-D_{MC}}{D_{MC}}$	D_{MC} [mGy]	D_{PB} [mGy]	$\frac{D_{PB}-D_{MC}}{D_{MC}}$	$\frac{D^A_{MC}-D_{MC}}{D_{MC}}$
Outline	0.080	0.081	1.56%	0.080	0.076	-4.69%	0.00%	0.042	0.046	8.82%	88.24%
Spinal Cord	0.061	0.061	0.00%	0.064	0.060	-5.88%	-3.92%	0.030	0.031	4.17%	104.17%
Brain Stem	0.092	0.095	2.70%	0.057	0.061	6.52%	60.87%	0.081	0.085	4.62%	13.85%
Parotis left	0.102	0.129	25.61%	0.127	0.151	18.63%	-19.61%	-	-	-	-
Eye right	0.255	0.228	-10.29%	-	-	-	-	0.226	0.206	-8.84%	12.71%
Eye left	0.243	0.217	-10.77%	-	-	-	-	0.236	0.215	-8.99%	3.17%
N.opticus right	0.206	0.205	-0.61%	-	-	-	-	0.172	0.172	0.00%	19.57%
N.opticus left	0.201	0.195	-3.11%	-	-	-	-	0.177	0.180	1.41%	13.38%
Chiasm	0.125	0.121	-3.00%	-	-	-	-	0.107	0.105	-2.33%	16.28%

Mean organ doses in mGy/projection image for head and neck patients for a single photon beam at 0°. All organ doses were calculated in the planning system VIRTUOS. Only organs at risk were included, wich were delineated in patient A and at least one additional patient. As an indicator for the accuracy of the pencil beam algorithm, the relative difference $D_{PB} - D_{MC}/D_{MC}$ between the pencil beam dose (D_{PB}) and the simulated dose (D_{MC}) is shown. For comparison, the relative difference $D^D_{MC} - D_{MC}/D_{MC}$ between the simulated dose for each patient and the dose simulated for Patient A (D^A_{MC}) is shown, which simulates the effect of using a fixed reference value obtained for a single geometry.

9.3.4. CBCT - Dose Comparison

For the new beam configuration, the corresponding scaling factors for Patient A were applied to the depth scaled pencil beam dose distributions from the planning system to calculate the final pencil beam dose distributions for all head & neck patients. These distributions are then compared to the simulated dose distributions. As already indicated by the comparison of dose ratio histograms for the reference patient for the different beam geometries, the agreement between the simulated and the pencil beam dose is expected to be much better for the CBCT acquisition, than for the single photon beam.

Analysis of Dose and Difference Slices

A first impression on the agreement between the dose distribution simulated with Monte Carlo and the one calculated with the pencil beam algorithm is again given in a profile plot for Patient A. Figure 9.10c shows the same profiles as Figure 9.5 but for the new beam configuration. As it can already be seen in the profiles plot, the differences between the two dose distributions are much smaller for the 360° rotation of the X-ray tube than for the single beam.
This is also visible in the respective dose slices and relative difference plot shown in Figure 9.10. Due to the application of photon beams from all directions, the dose is more evenly distributed throughout the patient: The maximum dose in the soft tissue at the front of the patient in reduced, while the dose in the voxels at the back of the patient is increased. While using a colorscale, which still offers some contrast within the bony structures, it is virtually impossible to see a difference between the simulated and the pencil beam dose slices for this beam configuration.
The map of relative dose differences in this slice confirms the good agreement, the relative difference in almost all voxels is below 20% and even does not exceed 10% in the voxels further away from the teeth (Note the different colorscale (Figure 9.24a) for the relative difference compared to the section above). This distribution of relative differences is a systematic effect, which occurs for all patients to a different degree. This is shown in the sagittal slices in Figure 9.13 as well as in the transversal slices of relative differences in Figure 9.12. Figure 9.12 also shows the comparison with a transversal slice of the relative differences for the water-filled patient outline investigated in chapter 6.4, which is created from the CT dataset for Patient B. The comparison shows, that the characteristic distribution of differences in the head & neck region can at least to some extent be assigned to the scatter effect described in chapter 6.4.
Another effect, which can be seen for all of the patients, is, that again in the area outside the primary beam area, the dose is overestimated by the pencil beam, with an increase in the relative difference with the distance to the primary beam. For bony structures located in the region just outside the photon field, the absolute difference is again much higher than for the soft tissue, where the absolute difference is negligible.

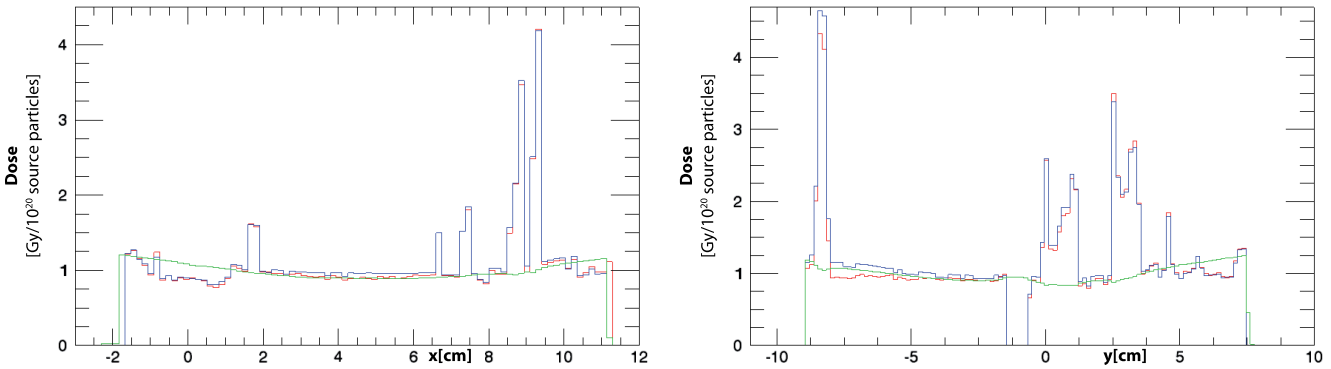

(a) *Profile parallel to the x-axis* **(b)** *Profile parallel to the y-axis*

(c) *CBCT Acquisition, 360° tube rotation: Dose profiles along the x-, and y-axis for Patient A. The simulated dose is plotted in red, the final pencil beam dose is plotted in blue. In addition to the final dose distribution, the pencil beam dose without the dose scaling factors applied is shown in green.*

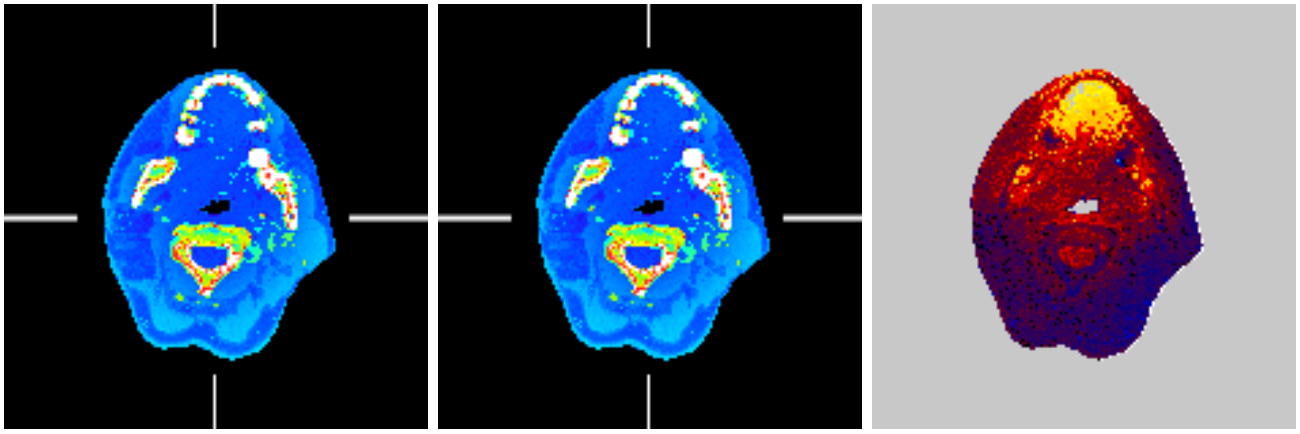

(a) *Simulated dose* D_{MC} **(b)** *Pencil beam dose* D_{PB} **(c)** *Rel. diff.* $(D_{PB} - D_{MC})/D_{MC}$

Figure 9.10.: *Transversal slices of the simulated and pencil beam dose distribution for Patient A for a CBCT acquisition (360° tube rotation). In addition, the relative difference between the two dose distributions is shown in (c). Note that in the frontal region, the dose tends to be overestimated by up to 20% (grey voxels), while in the posterior region, a slight underestimation by less than 6% is visible (dark blue voxels). The colorscales for this plot are shown in Figure 9.11.*

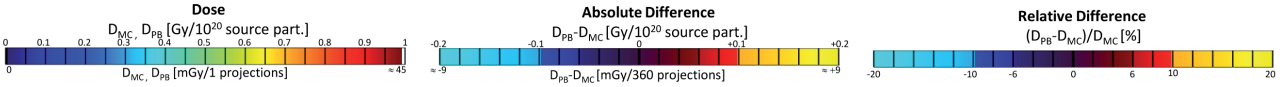

Figure 9.11.: *Colorscale for all plot in the section head and neck - CBCT Acquisition.*

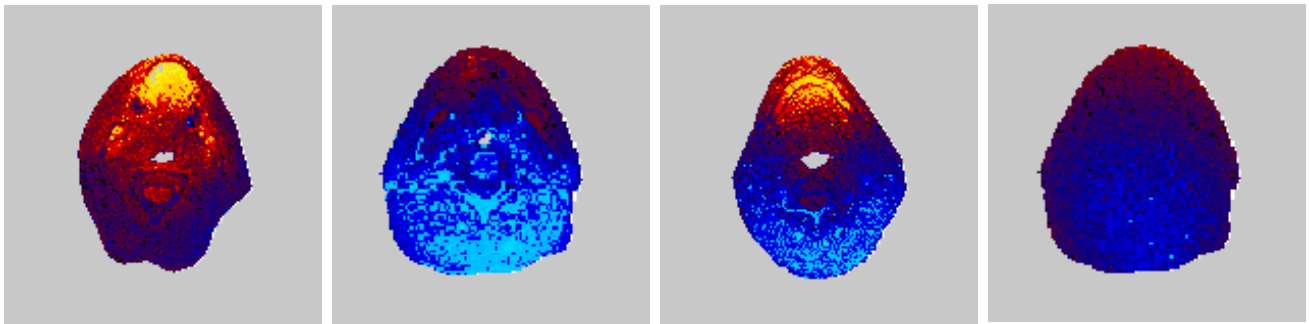

(a) *Patient A* **(b)** *Patient B* **(c)** *Patient C* **(d)** *Patient Outline only*

Figure 9.12.: *Transversal slices of relative differences between the simulated and the pencil beam dose distributions for a CBCT acquisition for all head & neck patients. For comparison, a transversal slice of the difference map for the water-filled patient outline investigated in chapter 6.4, which is actually based on the outline of Patient B is shown. The normalization of the dose distributions for this plot was adapted to match the one for Patient B. Note the similarities between the difference maps for the different patient geometries. The colorscale for this plot is shown in Figure 9.11.*

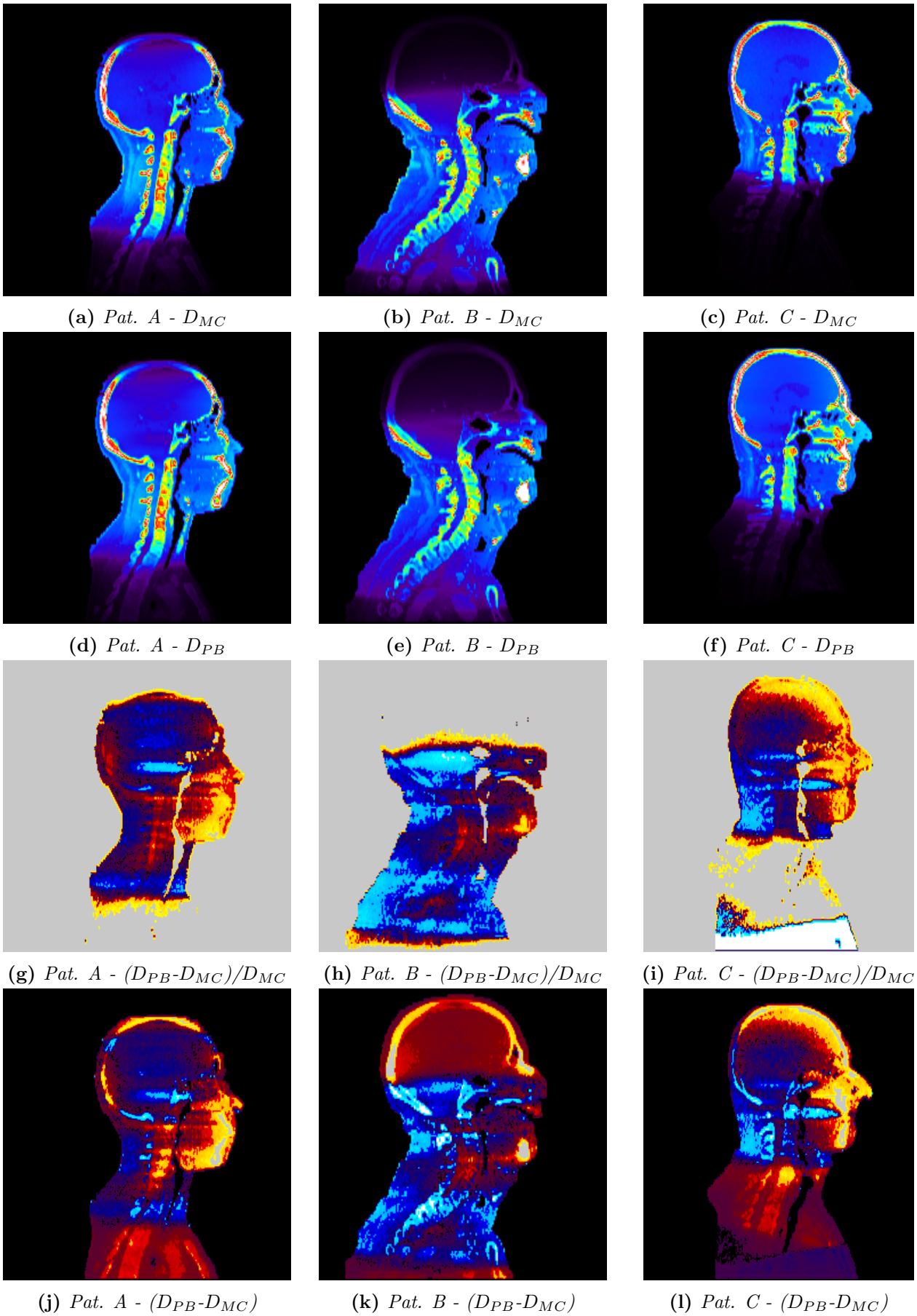

(a) *Pat. A - D_{MC}* **(b)** *Pat. B - D_{MC}* **(c)** *Pat. C - D_{MC}*

(d) *Pat. A - D_{PB}* **(e)** *Pat. B - D_{PB}* **(f)** *Pat. C - D_{PB}*

(g) *Pat. A - $(D_{PB}$-$D_{MC})/D_{MC}$* **(h)** *Pat. B - $(D_{PB}$-$D_{MC})/D_{MC}$* **(i)** *Pat. C - $(D_{PB}$-$D_{MC})/D_{MC}$*

(j) *Pat. A - $(D_{PB}$-$D_{MC})$* **(k)** *Pat. B - $(D_{PB}$-$D_{MC})$* **(l)** *Pat. C - $(D_{PB}$-$D_{MC})$*

Figure 9.13.: *CBCT acquisition: Sagittal slices of the dose distributions and difference maps for all head and neck patients. The colorscales for this plot are shown in Figure 9.11.*

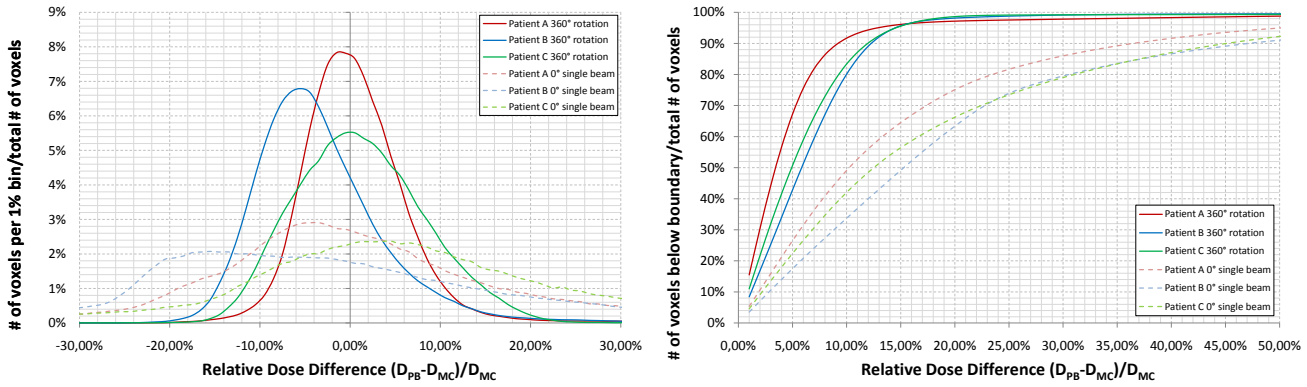

(a) **(b)**

Figure 9.14.: *(a) Histogram of differences for all patients for a beam at 0°. (b) Integrated histogram of differences for all patients for a beam at 0° showing the number of voxels within the boundaries, e.g. the number of voxels with differences between -10% and +10% divided by the total number of voxels.*

Statistical Analysis

The better agreement between the pencil beam dose and the simulated dose compared to the single beam direction is also reflected in the histogram of the relative differences for both cases as shown in Figure 9.14. The distribution of the differences is much wider for the single beam than for the tube rotation. For the reference patient A, the statistical analysis of the voxels within the primary beam, yields app. 92% of the voxels with a difference of below 10% and app. 97% of the differences below 20%. For both other patients, which represent the application of the algorithm to patients without knowing the simulated dose distribution first, still more than 80% of the voxels show a relative difference of less than 10% and more than 98% a difference of less than 20%. Similar to the single beam, a systematic underestimation of the dose for Patient B is visible.
When grouping the materials for all voxels (also outside the primary beam) into the four major groups air, lung, soft tissue and bone, the absolute difference in relation to the maximum dose in the soft tissue can be investigated. This analysis yields a mean dose error ranging from -1% to +1% between the patients with a standard deviation of 4.15% to 4.19% for soft tissues, which indicates the dose difference variation. A mean difference of 0.03% was found for bony tissues with a standard deviation ranging between 8.27% and 8.98%, meaning that for these tissues, the accuracy of the pencil beam algorithm combined with the proposed depth and dose scaling is comparable to the effective bone thickness correction algorithm described by Pawlowski et al. [25].

Evaluation of Organ Doses

Table 9.2 shows the mean doses for the organs at risk for a CBCT acquisition in mGy for 360 projections. Comparing the mean values to the measured values by Kan et al. [11] which were reported in chapter 2.4, the calculated values are in the range of app. half of the dose reported by Kan et al. This matches the fact, that in the publication, a total of 1330 to 1400 mAs were used to acquire the CBCT, while in this work, 720mAs were assumed (360 projections a 2mAs). For almost all of the organs at risk, the mean dose could be predicted with an accuracy better than 10%, the only exception being the brain stem for Patient B, where the deviation was 10.61%.
For all organs at risk located in the neck region, the prediction of the mean dose could be improved compared to the use the dose for Patient A as the fixed reference dose. This is especially the case for the spinal cord, which extends over the boundaries of the radiation field for Patient A and C.
The variation of mean doses between the patients for organs at risk located in the upper head, such as the eyes or the optical nerve, is much lower, so that for these organs, the fixed reference value was already a very good predictor.
The trend of a higher variation for the organs at risk in the lower region could also be seen in the

Table 9.2.: *Mean Organ doses - Pencil Beam vs. Monte Carlo - CBCT: 360° tube rotation - Head & Neck*

Organ	Patient D			Patient E				Patient F			
	D_{MC} [mGy]	D_{PB} [mGy]	$\frac{D_{PB}-D_{MC}}{D_{MC}}$	D_{MC} [mGy]	D_{PB} [mGy]	$\frac{D_{PB}-D_{MC}}{D_{MC}}$	$\frac{D^A_{MC}-D_{MC}}{D_{MC}}$	D_{MC} [mGy]	D_{PB} [mGy]	$\frac{D_{PB}-D_{MC}}{D_{MC}}$	$\frac{D^A_{MC}-D_{MC}}{D_{MC}}$
Outline	28.0	28.9	3.17%	27.1	26.7	-1.64%	3.28%	17.4	17.8	2.56%	61.54%
Spinal Cord	24.9	26.7	7.14%	27.1	27.1	0.00%	-8.20%	19.6	19.6	0.00%	27.27%
Brain Stem	34.3	32.0	-6.49%	29.4	26.2	-10.61%	16.67%	38.3	36.9	-3.49%	-10.47%
Parotis left	52.9	52.5	-0.84%	50.7	48.5	-4.39%	4.39%	-	-	-	-
Eye right	45.8	47.2	2.91%	-	-	-	-	47.2	49.8	5.66%	-2.83%
Eye left	46.3	46.7	0.96%	-	-	-	-	48.0	50.7	5.56%	-3.70%
N.opticus right	42.7	44.5	4.17%	-	-	-	-	43.6	44.9	3.06%	-2.04%
N.opticus left	44.9	45.8	1.98%	-	-	-	-	44.0	44.9	2.02%	2.02%
Chiasm	34.3	33.4	-2.60%	-	-	-	-	37.4	36.9	-1.19%	-8.33%

Mean organ doses in mGy/projection image for head and neck patients for a CBCT- acquisition (360° tube rotation) for the same organs at risk as for the single beam. Again the relative difference $D_{PB}-D_{MC}/D_{MC}$ between the pencil beam dose (D_{PB}) and the simulated dose (D_{MC}) is shown in addition to the relative difference $D^D_{MC}-D_{MC}/D_{MC}$ between the simulated dose for each patient and the dose simulated for the reference patient, Patient A (D^A_{MC}).

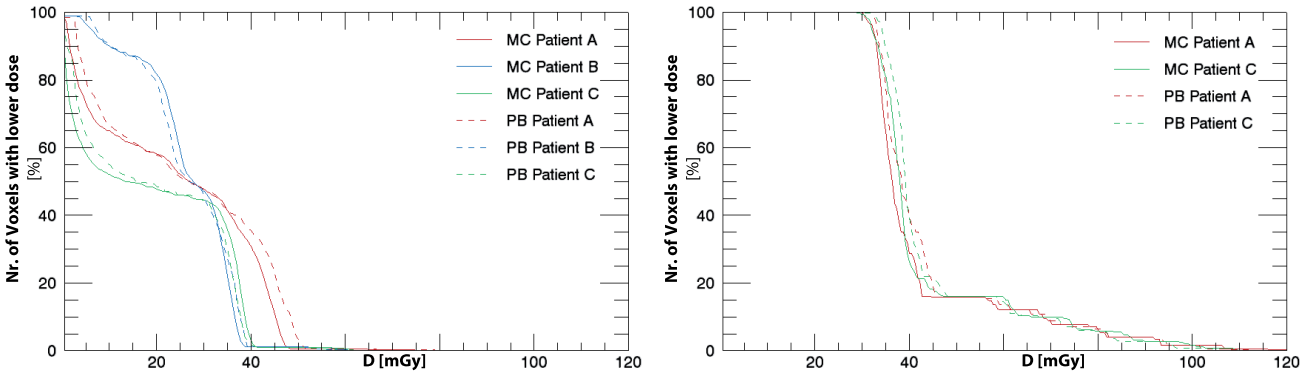

(a) *Spinal Cord* **(b)** *Right optic nerve*

Figure 9.15.: *Dose volume histograms (DVHs) for the spinal cord (a) and the right optic nerve (b) for a CBCT acquisition. The differences between the patients for the spinal cord are much bigger than for the optic nerve, where a fixed reference value already provides a good estimation of the organ dose. In both cases, the pencil beam algorithm predicts the DVH with a good accuracy (see also Table 9.2).*

histograms for the respective organ, e.g. Figure 9.15 shows the integral dose volume histograms (DVHs) for the spinal cord and the right optic nerve. Similar to the mean values, the DVH for the right optic nerve shows only a very small variation between patients A and C.
For the spinal cord, a typical steplike shape can be identified for all patients, which reflect the position of the spinal cord with respect to the primary beam. A high number of voxels receive a relatively low dose, these voxels are located outside the primary beam area. The fraction of voxels, where the step towards a higher dose is observed varies between the patients, this behavior is well predicted by the pencil beam algorithm. Also the maximum dose, which is received by a higher number of voxels (e.g. 10%) in the spinal cord also highly depends on the patient anatomy or the positioning of the target point. Again this is well predicted by the pencil beam algorithm.

9.4. Pelvis Patients

As the second anatomic region, the accuracy of the developed pencil beam algorithm for patient CTs in the pelvic area without any patient fixation is discussed. Again, a single photon beam at 0 ° and a 360° rotation are investigated, to simulate the different imaging options.

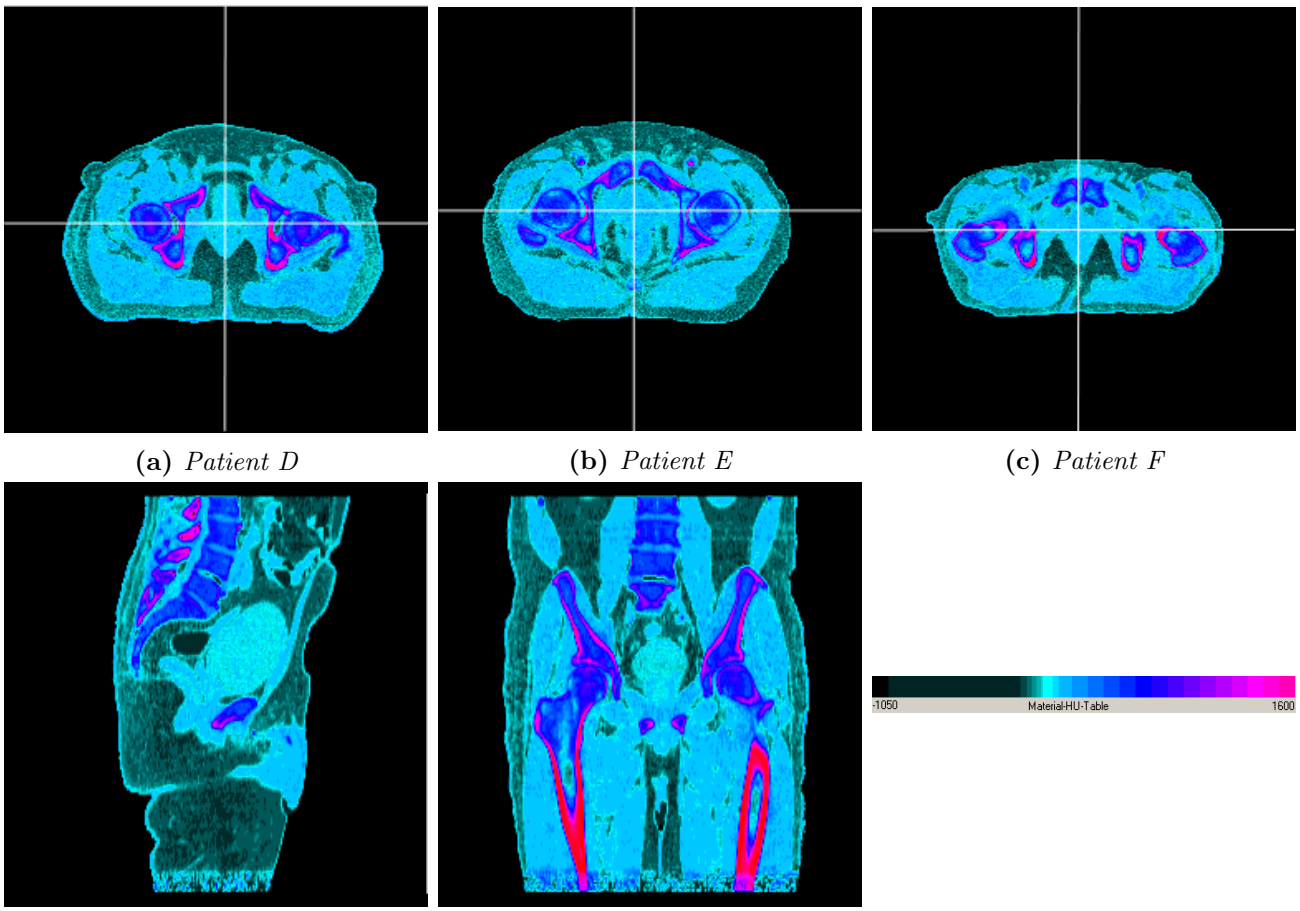

(a) *Patient D* **(b)** *Patient E* **(c)** *Patient F*

(d) *Patient D, sagittal* **(e)** *Patient D, frontal*

Figure 9.16.: *Material and density map for the pelvis patients. The crosshairs mark the isocenter, which is located in the shown transversal slice. As all of the patients are treated for prostate cancer, the variation of the position of the target point in relation to the anatomic structures is much lower than for the head & neck region. To illustrate the distribution of materials in this anatomic region, a sagittal and frontal slice of the material maps are also shown for patient A. While the bar itself shows the definition of materials according to the Hounsfield Unit each material bin is represented by a single color.*

9.4.1. Patient Description

All three patients for this anatomic site are patients treated for prostate cancer, which is one of the major indications for radiotherapy in the pelvic area. Due to the common indication, the variation of the target point position varies much less between the patients than for the head and neck patients. Again, no patients with visible CT-artifacts due to metal implants were considered. In contrast to the head and neck region, the number of bony tissues close to the surface, which are very challenging for the pencil beam algorithm, is limited.
The material and density maps for the reference patient (Patient D) is shown in Figure 9.16a,9.16d and 9.16e. The additional slice orientations are added to give an impression on the distribution of materials in this anatomic region. The maps for Patient E and F are shown in Figures 9.16b and c.
The extension of Patient F in anterior posterior direction is significantly lower than for the other patients. For patients E and F small structures, which are assigned the material of bony tissues, are visible in the material map. This is due to the administration of a contrast medium prior to the CT-acquisition. Within the primary beam area, this leads to the assignment of a bone material to the major veins. As this is the case for the simulation as well as for the pencil beam algorithm and the structures are small compared to other anatomic structures in this area, this is not expected to have a major influence on the analysis of the accuracy of the pencil beam algorithm.

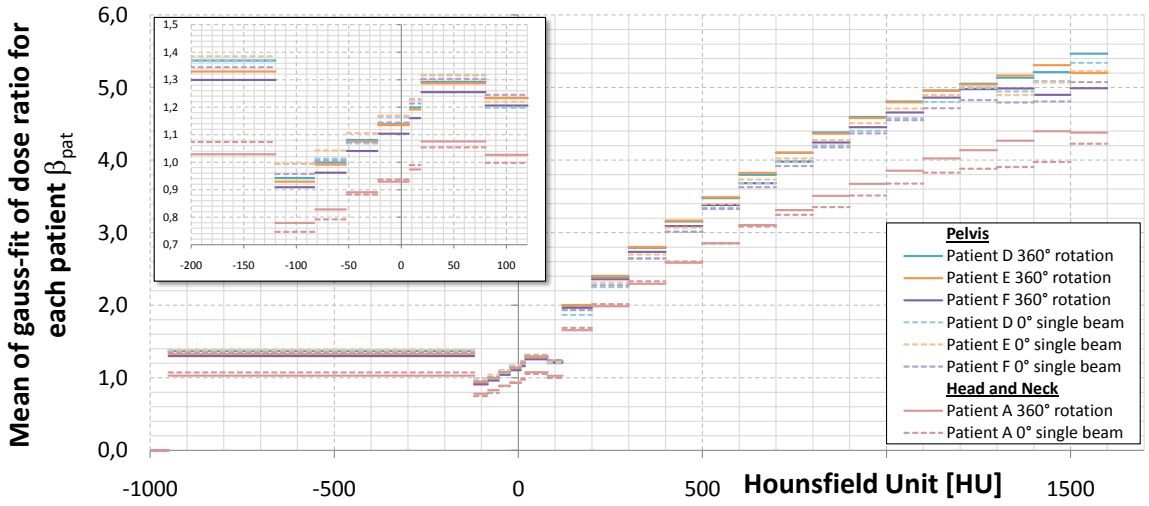

Figure 9.17.: *Dose scaling factors β as calculated for all pelvis patients. For comparison, the scaling factors for the head & neck reference patient are also plotted.*

9.4.2. Dose Scaling Factors $\beta(Z)$

As for the head and neck patients, the scaling factors β as a function of the Hounsfield Unit were derived from histograms of the ratio between the normalized simulated ($D_{MC,norm}$) and the calculated dose D'_{PB}. This was done separately for each beam geometry using the Schneider conversion table.
The ratio histograms show a similar behavior as described for the head and neck region: The factors increase for increasing content of high Z material, the distributions for the single pencil beam are much wider than for the 360° rotation, which facilitates a lower accuracy of the pencil beam algorithm for the single beam. Again, this is due to the beam hardening, which is of higher importance for the single beam, as it will also be seen in the comparison of the dose distributions described below.
Figure 9.17 shows the resulting values of $\beta(HU)$ for all patients. For comparison, the dose scaling factors for the 360° beam rotation for the reference patient of the head and neck region is plotted. The scaling factors for the pelvic region are significantly higher than for the head and neck case, which can be explained by the bony structures at the surface of the patient in most areas of the head, which leads to increased beam hardening compared to soft tissues and therefore a shift of the energy spectrum towards higher energies, where the scaling factor is lower (For MV beams the dose is not scaled at all, the scaling factor is 1). The scaling factors for the single beam at 0° tend to be slightly lower than for the 360° rotation of the tube, which can also be attributed to the same effect.
As before, the difference of the scaling factors between the patients can be considered to predict systematic over- and underestimation of the dose by the pencil beam algorithm compared to an optimal scaling factor for the respective patient. As the plot of the scaling factors shows, for the 360° rotation of the X-ray tube, a systematic overestimation of the dose for Patient F is expected for all materials but the one with the highest content of high Z elements. For Patient E, no clear trend is visible.

9.4.3. Single Beam - Dose Comparison

Analysis of Dose and Difference Slices

For the reference patient, profiles of the dose distributions simulated with Monte Carlo and calculated with the pencil beam algorithm are shown in Figure 9.18. The shown profiles are oriented along the x- and y-axis of the patient coordinate system and go through the isocenter, the matching anatomic structures are shown in Figure 9.16a. The basic shape of the profiles matches well, even though deviations in single voxels occur.
The decrease of the dose with increasing depth in the traversed soft tissue is reproduced well by the pencil beam algorithm. This is not the case, where bony structures are in the path of the beam, which can be

seen in the transversal slices of the dose distributions for the reference patient and the maps of relative and absolute differences shown in Figure 9.19.
While the relative difference of the doses in front of the femoral bones is displayed in shades of dark blue and dark red indicating an accuracy of 15% or better, behind the femoral bones, the dose is underestimated by more than 50% in some areas and overestimated by almost the same amount outside the central area, where the decreased scattered dose caused by the femoral bones is not correctly reproduced. This behavior is again common for all patients as shown in Figure 9.20. On the other hand, the absolute dose difference in most voxels of the soft tissue is only app. 10% of the dose in the soft tissue at the front of the patient. This is much lower than the absolute differences observed for the single beam in the head and neck region for a number of voxels.

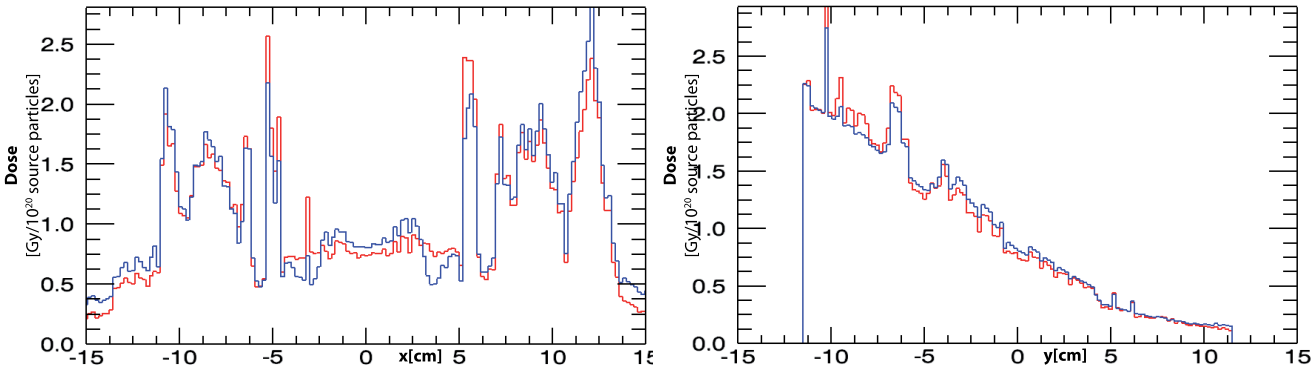

(a) *x-profile* **(b)** *y-profile*

Figure 9.18.: *Profiles along the x- and y- axis of the patient coordinate system through the isocenter for the dose distribution originating from DOSXYZnrc (red) and the pencil beam algorithm (blue) for the reference Patient D for a single beam at 0°. The general shape of the profiles matches well, though differences are visible. It has to be mentioned that for this specific profile along the y-axis, which is parallel to the beam direction, no bony structures are in the path of the beam.*

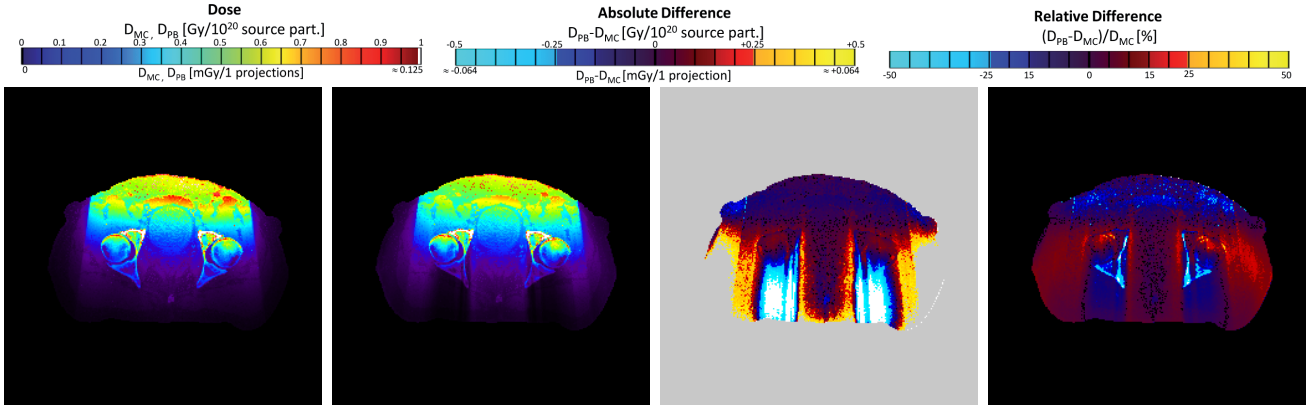

(c) *Simulated dose* D_{MC} **(d)** *Pencil beam dose* D_{PB} **(e)** *Rel. diff.* $(D_{PB}\text{-}D_{MC})/D_{MC}$ **(f)** *Abs. diff.* $D_{PB}\text{-}D_{MC}$

Figure 9.19.: *Transversal slices of the simulated and pencil beam dose distribution for Patient D for a single photon beam at 0°. In addition, the absolute difference between the two dose distributions is shown in (c). Note that an underestimation of the dose by the pencil beam algorithm occurs behind the pelvic bones, which can be identified as darker stripes in the dose slices and as blue stripes in the difference map. The colorscale for this plot is the same as for the single beam in the head & neck region.*

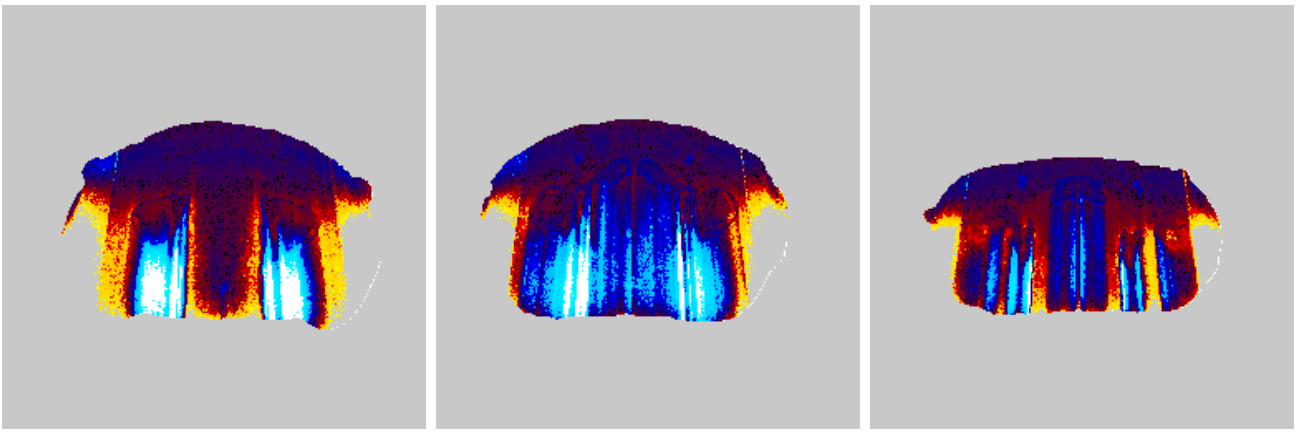

(a) *Patient D* **(b)** *Patient E* **(c)** *Patient F*

Figure 9.20.: *Transversal slices of the relative differences between simulated and pencil beam dose distribution for all pelvis patients. Note the similarities between the patients: behind the femoral heads, the pencil beam underestimates the dose. At the sides, where no bony structures are present, an area of overestimation of the dose can also be identified for all patients. The colorscale for this plot is the same as for the single beam in the head & neck region and is shown in Figure 9.19.*

Statistical Analysis

Again, all voxels within a range of z-values of $\pm$ 1/2 of the field side length were considered for the statistical analysis. In addition to the primary beam area, this includes a small number of voxels at the side of the phantom, which lie outside the primary beam. The statistical analysis of the differences as shown in Figure 9.21 shows that even though for an average fraction of only app. 70% (app. 80%) of the voxels, the relative difference is below 20% (30%) for Patients D,E and F. More than 93% of the voxels show an absolute difference of less than 10% and 70% an absolute difference of even less than 5% of the approximate average dose in the soft tissue at the front of the patient.

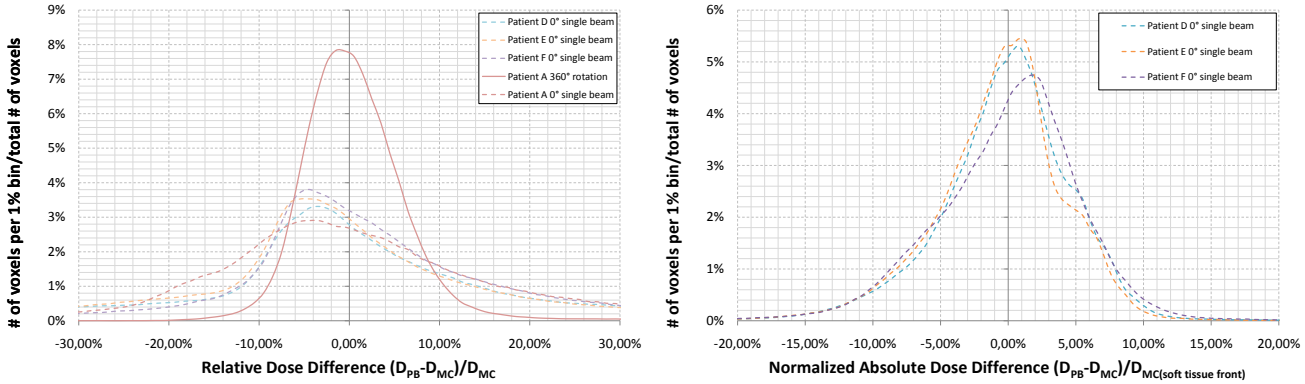

(a) *Relative Difference* **(b)** *Absolute Difference*

Figure 9.21.: *Histograms for the absolute differences of the dose distributions for Patient D for a single beam at 0°. (a) shows the plot of the relative differences $(D_{PB} - D_{MC})/D_{MC}$. For comparison, the same plot for the reference patient for the single beam at 0° and for the 360° rotation are shown. In (b), the x-axis shows the absolute difference instead of the relative difference.*

Evaluation of Organ Doses

Compared to the head and neck region the organs at risk in the pelvic area are larger and show a higher variation in size and position. The organs at risk for the pelvic area, which already receive a high dose due to the radiation treatment and therefore are of special interest, are the bladder, the rectum, the

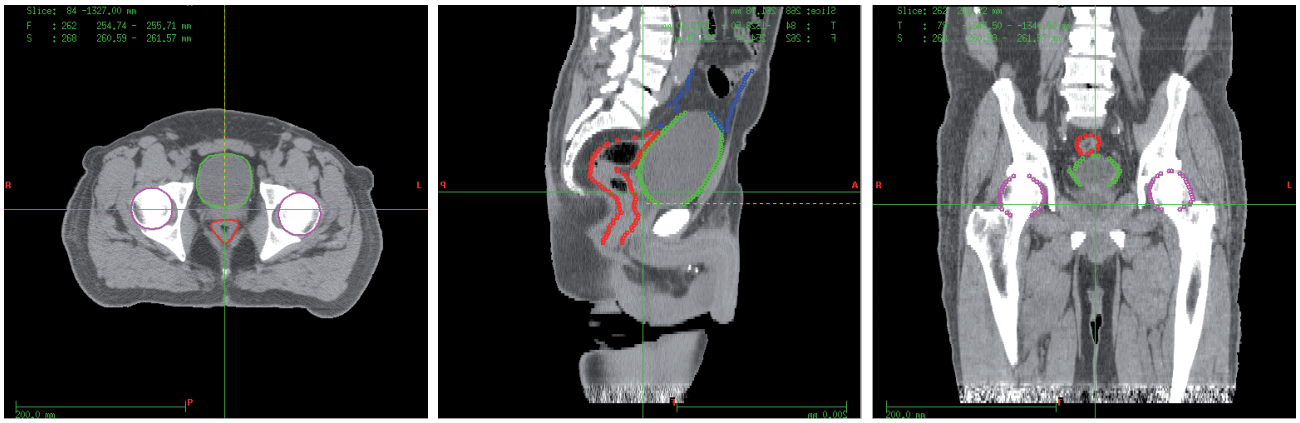

(a) *transversal view* **(b)** *sagittal view* **(c)** *frontal view*

Figure 9.22.: *Position of organs at risk for the pelvic area. The main organs at risk in radiotherapy are the bladder (green) and the rectum (red), which are located adjacent to the target volume and therefore receive a dose close to the tolerance dose in the radiotherapy treatment. Other organs at risk are the heads of the femoral bones (pink) and the intestine (blue). To match the display orientation of Figure 9.16d, the sagittal slice from the planning system was mirrored.*

intestine and the femoral heads. To give an overview on the position of the different organs at risk, the organs at risk for the reference patient are shown in Figure 9.22).
Table 9.3 again shows the mean doses for the main organs at risk. For all organs, but the rectum for patient E, the mean doses could be predicted with an accuracy better than 5%. The mean dose for the only organ with a higher difference (rectum patient E), which lies in between the femoral bones, was underestimated by 12%. Especially the dose in the femoral heads could be estimated with an accuracy better than 2%, which is a significant improvement compared to the use of a reference value (dose for reference patient D), which would cause deviations of app. 10% for Patient E and more than 35% for Patient F. Also for the intestine, whose position is outlined very differently for the different patients, the pencil beam algorithm allows a prediction of the mean dose with an accuracy better than 4% compared to deviations above 30%, if a reference value was used.
This can also be seen in the integral dose volume histograms shown for these two organs in Figure 9.23. Even though the DVHs for the pencil beam calculated dose are slightly less steep than the simulated ones, the agreement is still much better than if the one for one of the other patients were used. The accuracy for the prediction of maximum values was much lower than for the mean values. This is most probably due to very high doses in single voxels occurring in the Monte Carlo simulation, which leads to a high uncertainty of the simulated value itself.

Table 9.3.: *Mean Organ doses - Pencil Beam vs. Monte Carlo - Single beam at 0° - Pelvis*

	Patient D			Patient E				Patient F			
Organ	D_{MC} [mGy]	D_{PB} [mGy]	$\frac{D_{PB}-D_{MC}}{D_{MC}}$	D_{MC} [mGy]	D_{PB} [mGy]	$\frac{D_{PB}-D_{MC}}{D_{MC}}$	$\frac{D^{D}_{MC}-D_{MC}}{D_{MC}}$	D_{MC} [mGy]	D_{PB} [mGy]	$\frac{D_{PB}-D_{MC}}{D_{MC}}$	$\frac{D^{D}_{MC}-D_{MC}}{D_{MC}}$
Outline	0.059	0.060	2.13%	0.056	0.056	0.00%	4.44%	0.076	0.077	1.64%	-22.95%
Bladder	0.180	0.176	-2.08%	0.176	0.170	-3.55%	2.13%	0.171	0.170	-0.73%	5.11%
Rectum	0.066	0.066	0.00%	0.062	0.055	-12.00%	6.00%	0.072	0.072	0.00%	-8.62%
Intestine	0.091	0.089	-2.74%	0.069	0.066	-3.64%	32.73%	0.070	0.070	0.00%	30.36%
Femur right	0.157	0.156	-0.79%	0.176	0.178	1.42%	-10.64%	0.251	0.253	1.00%	-37.31%
Femur left	0.158	0.160	0.79%	0.177	0.176	-0.70%	-10.56%	0.248	0.251	1.01%	-36.18%

Mean organ doses in mGy/projection image for pelvis patients for a single photon beam at 0° for the main organs at risk in this anatomic region. Again the relative difference $D_{PB} - D_{MC}/D_{MC}$ between the pencil beam dose (D_{PB}) and the simulated dose (D_{MC}) is shown in addition to the relative difference $D^{D}_{MC} - D_{MC}/D_{MC}$ between the simulated dose for each patient and the dose simulated for the reference patient, Patient D (D^{D}_{MC}).

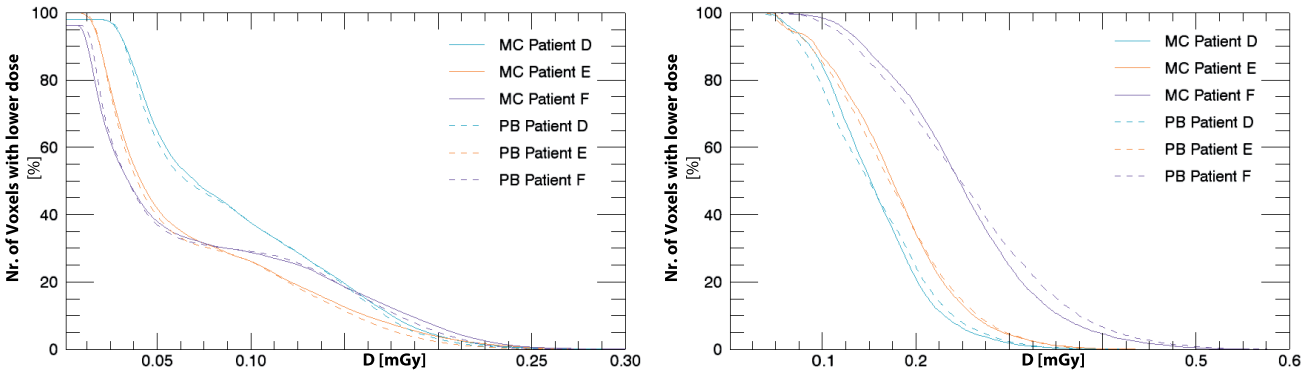

(a) *Small intestine* **(b)** *Right femoral head*

Figure 9.23.: *Dose volume histograms (DVHs) for the intestine and the right femoral head for a single photon beam at 0°. In both cases, the pencil beam algorithm provides a much better estimation of the DVHs than the use of a reference curve for a single anatomy (e.g. DVH for patient D) (see also Table 9.3).*

9.4.4. CBCT - Dose Comparison

Analysis of Dose and Difference Slices

Analog to the preceding sections, the scaling factors were applied to the depth scaled pencil beam dose distribution from the planning system leading to the final dose distribution, which is compared to the simulated dose distribution.
Similar to the CBCT case for the head & neck region, in Figure 9.24, virtually no difference can be seen between the two dose distributions for the reference patient with the same colorscale as before. Despite the good accuracy in a large number of voxels, a trend in the dose distribution differences can be seen in the absolute difference maps also shown in Figure 9.24. As for the single beam, the absorption in the femoral heads causes an underestimation of 10-20% for the shown reference patient for the dose in the area, which is shielded from the radiation by bony structures for a high number of beam angles (in this case between the femoral heads).
To compensate for the underestimation in the central area (the scaling factor is chosen as an average dose ratio), the dose in the outer region of the patient is overestimated by app. 5-10% in the soft tissue and 10-20% within the bones. This trend is similar for all pelvis patients, which can be seen in Figure 9.25 in the transversal slices of the relative differences between the simulated and the pencil beam dose distribution. The degree of the effect depends on the exact anatomy of the respective patient, and can be explained by the beam hardening in the bones, which cause a smaller increase in dose with a hardening of the beam in high Z materials than at the surface.
As already indicated by the comparison of the dose scaling factors derived for Patient F compared to those for the reference patient, the dose is systematically overestimated for this patient by app. 5%.

Statistical Analysis

For the pelvic region, the comparison between the accuracy for the single beam and the 360° rotation is similar to the head and neck region: The accuracy for the 360° rotation is significantly higher than for the single beam. This can also be seen in the histograms of the differences shown in Figure 9.26 which show, that for all patients, for more than 92% of the voxels within a range of z-values of ± 1/2 of the field side length, the pencil beam algorithm predicts the simulated dose with an accuracy better than 10%. For app. 99% of the voxels, the relative difference is below 20%.
To compare the accuracy of the pencil beam algorithm to the values reported by Pawlowski et al. [25], again a statistical analysis for the absolute dose differences normalized to the maximum dose in soft tissue is executed. This analysis yields a mean dose difference of 0.63% to 2.21% for the soft tissues and 0.02% to 0.06% for bony tissues. The average standard deviations for this anatomic site were 2.84% and 8.15%, which is for bony structures comparable to the accuracy of the method suggested in the publication. For

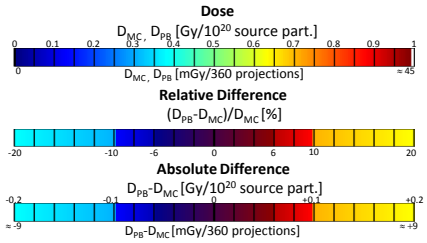

(a) *Colorscale*

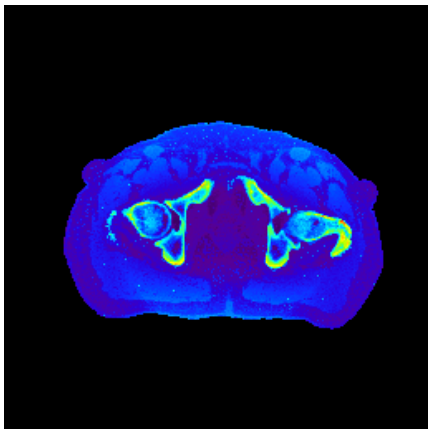

(b) *Simulated dose* D_{MC}

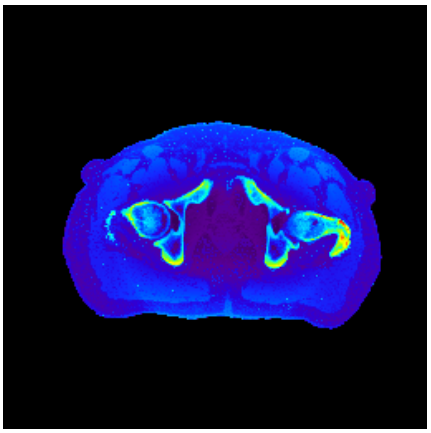

(c) *Pencil beam dose* D_{PB}

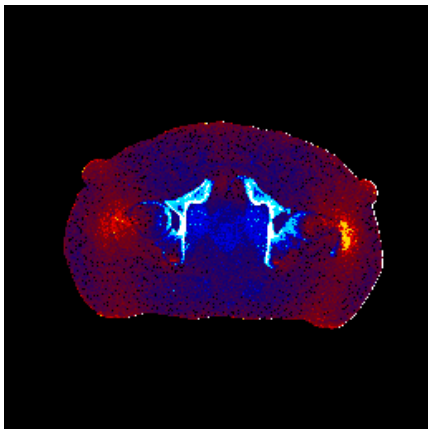

(d) *Abs. diff.* $(D_{PB} - D_{MC})$

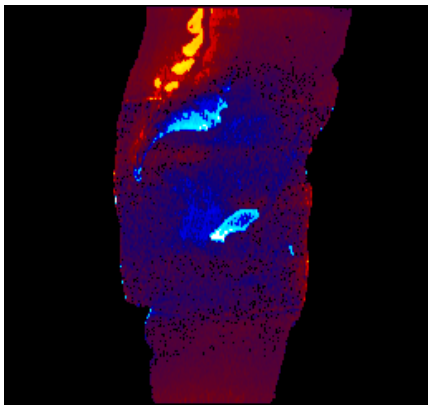

(e) *Abs. diff.* $(D_{PB} - D_{MC})$

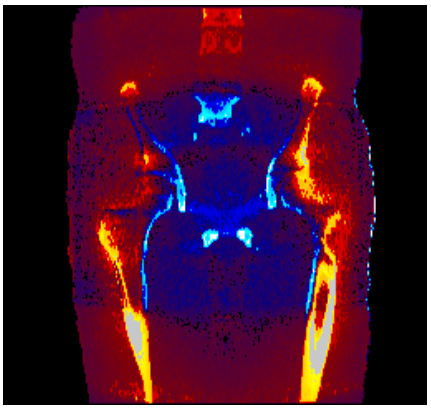

(f) *Abs. diff.* $(D_{PB} - D_{MC})$

Figure 9.24.: *Transversal slices of the simulated and pencil beam dose distribution for Patient D for a CBCT acquisition (360° tube rotation). In addition, the absolute difference between the two dose distributions for different orientations is shown in (d-f). Note that in the central region, the dose is slightly underestimated, while it is overestimated in the outer regions. The colorscale for this plot is the same as for the CBCT acquisition in the head and neck area.*

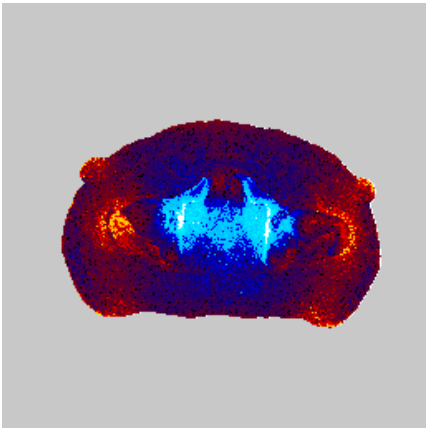

(a) *Patient D*

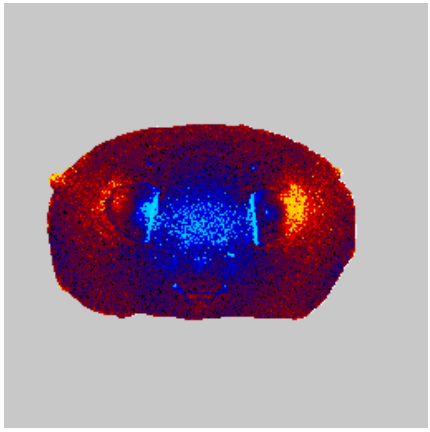

(b) *Patient E*

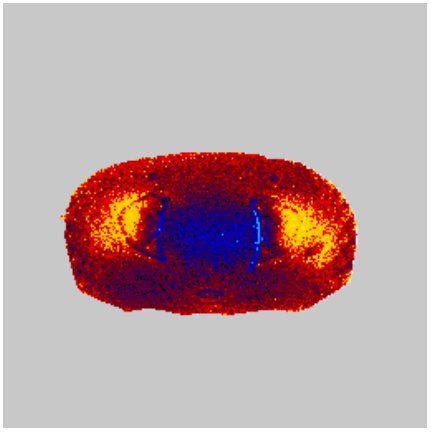

(c) *Patient F*

Figure 9.25.: *Transversal slices of the relative difference for all pelvis patients for a CBCT acquisition (360° tube rotation). Note the common pattern of under- and overestimation of the dose for all of the patients. The colorscale for this plot is the same as for the CBCT acquisition in the head and neck area and is shown in Figure 9.24a.*

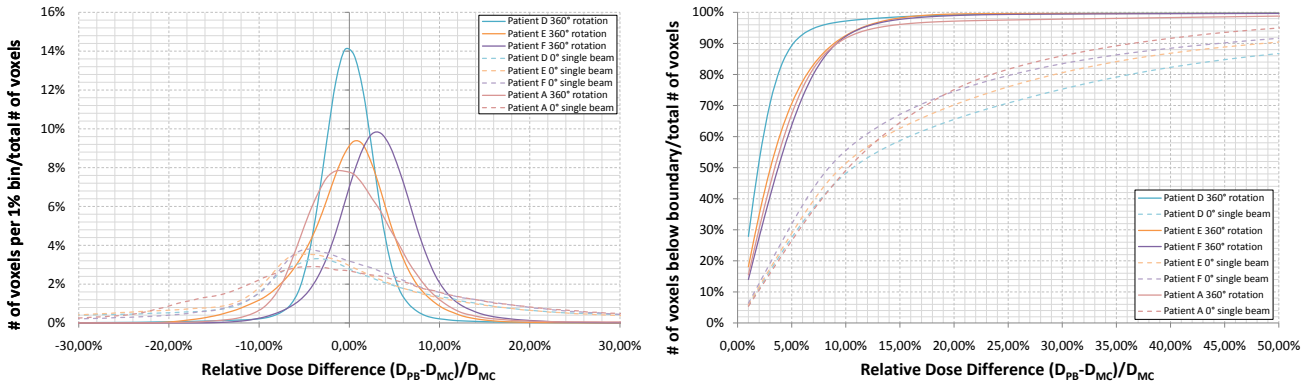

(a) **(b)**

Figure 9.26.: *(a) Histogram of differences for all patients for a 360° tube rotation. (b) Integrated histogram of differences for all patients for a 360° tube rotation showing the number of voxels within the boundaries, e.g. the number of voxels with differences between -10% and +10% divided by the total number of voxels.*

Table 9.4.: *Mean Organ doses - Pencil Beam vs. Monte Carlo - CBCT - Pelvis*

	Patient D			Patient E				Patient F			
Organ	D_{MC} [mGy]	D_{PB} [mGy]	$\frac{D_{PB}-D_{MC}}{D_{MC}}$	D_{MC} [mGy]	D_{PB} [mGy]	$\frac{D_{PB}-D_{MC}}{D_{MC}}$	$\frac{D^D_{MC}-D_{MC}}{D_{MC}}$	D_{MC} [mGy]	D_{PB} [mGy]	$\frac{D_{PB}-D_{MC}}{D_{MC}}$	$\frac{D^D_{MC}-D_{MC}}{D_{MC}}$
Outline	19.6	20.0	2.27%	18.2	18.7	2.44%	7.32%	24.0	25.4	5.56%	-18.52%
Bladder	26.7	27.1	1.67%	28.0	26.2	-6.35%	-4.76%	29.8	29.4	-1.49%	-10.45%
Rectum	23.6	22.2	-5.66%	26.2	23.6	-10.17%	-10.17%	30.7	29.8	-2.90%	-23.19%
Intestine	15.1	15.1	0.00%	12.0	12.0	0.00%	25.93%	12.0	12.9	7.41%	25.93%
Femur right	46.7	46.7	0.00%	48.5	50.3	3.67%	-3.67%	61.8	64.1	3.60%	-24.46%
Femur left	48.5	50.3	3.67%	48.0	48.9	1.85%	0.93%	61.4	64.5	5.07%	-21.01%

Mean organ doses in mGy for pelvis patients for a cone beam CT acquisition for the main organs at risk in the pelvic region assuming 360 projections and 2mAs per projection. As in the other sections, the relative difference $D_{PB} - D_{MC}/D_{MC}$ between the pencil beam dose (D_{PB}) and the simulated dose (D_{MC}) is shown in addition to the relative difference $D^D_{MC} - D_{MC}/D_{MC}$ between the simulated dose for each patient and the dose simulated for the reference patient, Patient D (D^D_{MC}).

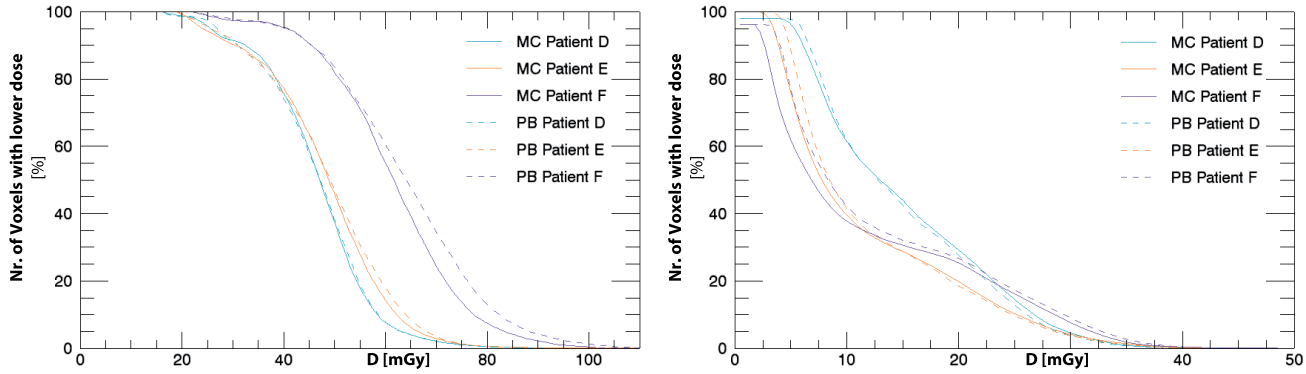

(c) *Spinal Cord* **(d)** *Right optic nerve*

Figure 9.27.: *Dose volume histograms (DVHs) for the right femoral head (c) and the intestine (d) for a CBCT acquisition.*

soft tissues, the accuracy is only slightly smaller.

Evaluation of Organ Doses

The mean organ doses resulting from the Monte Carlo simulation and the pencil beam calculation, are summarized in Table 9.4. The obtained mean organ doses and the measured doses reported by Kan et al. are again approximately in the same range when considering, that an approximately doubled mAs setting has been used for the measurement.
For almost all considered organs at risk, including the femoral heads, the mean dose was predicted with an accuracy of 10% or better. Especially the case for Patient F, where the simulated doses for most organs are significantly different to those for patient D due to the smaller size of the patient, the calculation of the dose with the pencil beam algorithm is a significant improvement compared to the use of the mean dose for a single geometry (Patient D) as a fixed reference value for each organ. This is also visible in the dose volume histograms for the different organs, which are shown for the intestine and the right femoral head in Figure 9.27. The only exception for the described accuracy is the rectum for Patient B, where the dose is underestimated by 12%, as it is situated in the region between the femoral head described above.

10. Discussion and Outlook

In this work, the development of a pencil beam algorithm for a fast calculation of keV dose due to imaging procedures in radiation therapy was presented. Using a standard pencil beam dose calculation algorithm as the starting point, pencil beam kernels for the investigated energy range were established for the calculation of dose in water, the algorithm was improved to meet the energy specific requirements for the keV energy range. This included the introduction of depth scaling factors into the pencil beam to account for the increased dependence of the absorption of photons on the atomic number due to the relative importance of the photon effect compared to MeV radiation. In addition, dose scaling factors were established to reflect this material dependent increased photon absorption, not only as a decreased dose in voxels at a higher depth, but also in a higher local dose. The accuracy of the resulting algorithm was evaluated by comparison with Monte Carlo simulations, which were established as the gold standard for patient dose calculation over the course of this work. The separate steps presented in this work will now be discussed in this chapter.

10.1. Monte Carlo Gold Standard

The used model of the X-ray tube was validated against a relative dose measurement in a water phantom. Including the uncertainty of the simulation as well as for the measurement, the Monte Carlo model was found to reproduce the measured relative dose values accurately for most measurement points. In addition to steeper gradients at the field edge, for some measurement points at relatively high distances from the central axis, deviations of up to app. 8% were found, which exceeded the combined uncertainties of the measurement and the simulation. As the Monte Carlo model was nevertheless accepted as the gold standard for all following comparisons, this additional uncertainty has to be considered if conclusions are drawn from the comparison with Monte Carlo regarding the accuracy of the pencil beam dose calculation vs. measurements.

A much bigger uncertainty has to be considered, when Monte Carlo dose calculations are employed for the calculation of dose based on CT-datasets. The use of different tables for the conversion between the Hounsfield Unit, which is available in the CT dataset and the elemental composition and mass density needed for the Monte Carlo simulation, was studied in chapter 8. The two investigated tables result in significantly different dose distributions, with differences of up to 100% in bony structures. Even for soft tissues, the inclusion of different elemental compositions, such as fatty tissue or connective tissue, instead of a single soft tissue composition, can lead to dose differences of app. 25%. This step introduces a major uncertainty into the chosen gold standard, as it is not known, which conversion table causes the dose distribution closest to the "true distribution". The advantage of using a high number of material definitions is obvious, as smaller variations in the elemental composition can also be accounted for. On the other hand, a high number of materials also leads to the definition of relatively small Hounsfield Unit bins, which favors the assignment of a "wrong" material for single voxels.

Even though the effect of the conversion table on the simulation of dose distributions in the keV energy range significantly influences the resulting dose distribution, the authors often do not mention, which table and how many materials have been used (e.g. [16, 62]). If the conversion table is mentioned, most Monte Carlo simulations are based on a conversion table with only four materials : Air, lung, soft tissue and bone (e.g. [17, 18, 25]). All other changes in the Hounsfield Unit value are assigned to changes in

the mass density.
As a conclusion of this investigation for this work, the use of a conversion table with more than the standard four materials is an important part of an accurate calculation of keV dose distributions. For this reason, the Schneider table [74] was used as the standard material conversion table for the Monte Carlo simulations as well as for the pencil beam algorithm for all investigations on patient geometries.
As the choice of the material conversion table was shown to have a major impact on the dose distribution, this aspect has to be investigated in further detail in future studies.

10.2. Pencil Beam Kernel Calculation and Dose in Water

The first step for the application of the pencil beam algorithm for a new beam energy is the calculation of a pencil beam kernel. The pencil beam algorithm used in this work is based on the algorithm described by Bortfeld et al. [60], which requires the decomposition of the pencil beam kernel. The decomposed kernel is derived from depth dose curves using a kernel calculation algorithm and combined with a 2-dimensional primary fluence calculated in the same algorithm. The existing kernel calculation usually used for the MeV energy range was found to be suitable for the use in the keV energy range with only minor changes.
To use same pencil beam kernel for all pencil beam locations throughout the photon beam, the employed pencil beam algorithm is based on the assumption, that the beam spectrum is invariant to translation. Due to the setup for the photon beam production in the X-ray tube and the associated absorption of the photon beam in the target, this assumption introduces a systematic error into the dose calculation for very large fields. The dose comparison for a large water phantom showed that this effect plays a role for the investigated field size of 35cm x 35cm, but is negligible for field sizes used in imaging.
The investigations on the cylindric phantom and the water-filled patient outlined in chapter 6.3 and 6.4 focused on another limitation of the pencil beam algorithm, which plays a larger role for the very large keV photon beams than for the smaller therapeutic MeV-beams. Due to the increased probability for high scattering angles and the low fraction of energy transferred to electrons in a Compton interaction in the lower energy range, the likelihood of multiple scattering of photons is also increased. As explained in chapter 6.3, for the convex shape of the investigated phantoms, this leads to a significant overestimation of dose at the phantom boundaries. While this effect is very high for a single photon beam, it can be compensated for with a different normalization for a 360° rotation of the X-ray tube as in a CBCT acquisition.

10.3. keV Depth- and Dose-Scaling

To account for the higher dependence of the attenuation of the primary photon beam on the atomic number, a combination of depth scaling factors and dose scaling factors were employed in the pencil beam algorithm. The depth scaling factors, which are obtained for a specific beam spectrum from simulated depth dose profiles for an extended field, replace the relative electron density in the MeV algorithm for the scaling of the pencil beam kernels, while the dose scaling factors account for the increase of the absolute dose value for the respective voxel itself.

10.3.1. Depth Scaling Factors

In contrast to the MeV case, the depth scaling factors depend on the beam energy, the elemental composition of the voxels in the geometry and are proportional to the respective mass density. As the only information available in a CT-dataset is Hounsfield Units, the same tables for the conversion from Hounsfield Unit to material and mass density were employed as for Monte Carlo simulations. For a given conversion table, the depth scaling factors can therefore be supplied to the pencil beam algorithm as a function of the Hounsfield Unit.
For the scattered dose, the method of the scaling of the pencil beam along a single direction takes the

decrease of primary photons into account, for scattered photons also the depth scaled pencil beam is used, leading to a decrease in scattered dose in voxels which do not lie on the pencil beam axis. All changes in lateral scatter are neglected. Additional photons scattered into bony tissue or reduced backscatter for voxels at depth lower than the bone cannot be accounted for in the depth scaling algorithm.
While the adapted method to incorporate the additional dependence on the atomic number in the pencil beam algorithm offers very short calculation times, there are also several disadvantages. The derived set of scaling factors depends on a number of variables: the energy spectrum of the photon beam, the chosen conversion table and finally the phantom simulation geometry employed for the estimation of the scaling factors including the observed beam hardening. Regarding the phantom geometry and the associated beam hardening, it would also be possible to adapt the geometry to better reproduce the conditions for the desired application (mostly specified by the size and positioning of bony structures), but this would lead to an additional dependency of the depth scaling factors on the anatomic site. In principle it would also be possible to include at least the beam hardening in soft tissue into the scaling algorithm by adding a dependence on the equivalent depth, which would lead to a 2-dimensional table of the depth scaling factors. Still, this would not solve the problem of additional beam hardening in bony structures.

10.3.2. Dose Scaling Factors

The dose scaling factors in this work mainly account for the increase or decrease in local dose due to the dependence of the interaction cross section for the photoeffect on the atomic number. The use of site and geometry specific factors optimized the calculated dose for different conditions regarding beam hardening and the additional scattering of photons from the soft tissue into bony structures. Similar to the depth scaling factors, the dose scaling factors depend on the material, which requires the use of a conversion table to derive the material from the known Hounsfield Unit for each voxel. To obtain the final dose distribution, the dose in each voxel is multiplied with the dose scaling factor for the respective material.
The algorithm chosen for the calculation of the dose scaling factors is again based on Monte Carlo simulations. For each anatomic site, the scaling factors for each material are derived as the typical ratio between the simulated dose distribution and the preliminary dose distribution for all voxels, which fall into the Hounsfield Unit range for the respective material. In this work, a single reference patient was used to derive the factors, which are then used for all other patients. For a higher number of patients, it would also be possible to average the scaling factors for a number of reference patients to reduce the influence of unique anatomic features compared to a single reference patient.
A clear advantage of the chosen method is the calculation speed. A single scaling factor is used for each voxel, which - due to the use of the conversion table - only depends on the Hounsfield Unit of the respective voxel and the anatomic site. In the used implementation in IDL (Version 6.2, ITT Visual Information Solutions, Boulder, Colorado), the postprocessing step takes app. 8-10 seconds for a full patient CT dataset, when using 24 materials.
The chosen method of a single scaling factor per material also leads to different limitations of the calculation algorithm. The most important limitation is, that the scaling factors highly depend on the photon energy and beam hardening can only be considered to a very small extent: in the site dependency of the scaling factors, which is equal to assuming an average beam spectrum for all voxels. Also the increase of dose in bony structures and the decrease in the soft tissue at soft tissue/bone interfaces due to scattered photons crossing the interface cannot be accounted for.

10.3.3. Comparison with Existing Algorithms

The accurate calculation of keV imaging dose in IGRT with methods other than Monte Carlo calculations, has been the subject of investigations of several recent papers. In this section, the advantages and disadvantages of the developed algorithm compared to other methods proposed in the literature are discussed.
All major publications on the topic of keV dose calculation algorithms can be split into two groups. The first group are investigations on complete dose calculation algorithms, where the dose is calculated

from scratch. This group includes the work by Alaei et al. [20, 21, 24], which presents a superposition algorithm to calculate dose in soft tissues, and the approach by Kouznetsov et al. [81], where the dose in a single point of interest is calculated using a combination of deterministic and Monte Carlo techniques. As this method only allows the fast calculation of dose in single points of interest and not a complete dose distribution it is not further discussed. The second group of publications was already presented in chapter 9.1.1 and studies methods to improve a preliminary dose distribution by the use of multiplicative factors [23, 24, 25]. As a full description of the respective method is beyond the scope of this work, only the main differences and similarities to the presented algorithm are pointed out.
The superposition algorithm presented by Alaei et al. [20, 21, 24] is based on a standard superposition algorithm for MeV dose calculation combined with point spread kernels for the new energy range. Similar to the algorithm presented in this work, Alaei et al. suggest the use of an adapted scaling factor to account for the additional absorption of photons in the algorithm. In contrast to the definition of materials based on the Hounsfield Unit and the empirical estimation of material specific depth scaling factors described above, Alaei et al. suggest a scaling factor equal to the relative electron density to the power of 2.5 for relative electron densities larger than 1 [21] for the special case of a lung phantom investigated in this publication. In later publications, this adapted scaling approach was no longer pursued and the author suggests the use of postprocessing corrections [24], which leads to the discussion of the second group of publications. The main advantage of the pencil beam algorithm presented in this work is the cost in calculation time compared to a superposition algorithm.
Three major publications are included in this discussion, the publications, Ding et.al. and Pawlowski et al. [23, 25]. The publication by Alaei et.al. [24] uses a constant dose scaling factor for all bone voxels and the author himself suggests to use a more complex postprocessing method. Both publications consider only two different materials within the body: tissues or bone. The postprocessing step then tries to model the impact of the voxels defined to be bone on the dose distribution. Due to the high effect, that the choice of materials had on the Monte Carlo dose distributions, the inclusion of a high number of different body tissues was one of the major goals upon the development of the scaling factor concept. While the desired differentiation of body tissues is possible in the approach chosen in this work, the adaptation of the methods by Ding et al. and Pawlowski et al. to a higher number of materials not only for bony structures but also for soft tissues would require major changes in the concept of the respective algorithm.
This leads to the comparison of the pencil beam algorithm presented in this work with the algorithm suggested by Ding et.al. [23]. Even though their method is used as a postprocessing step on a dose distribution, which already accounts for changes in the electron density, the additional dependency on the atomic number is accounted for in a way, which is very similar to a pencil beam algorithm: For the calculation of the dose in a single voxel, all soft tissue-bone interfaces within the same primary pencil beam path have to be considered. Depending on the material of the each voxel, a factor is derived which accounts for a decrease in the primary photon beam and additional (within bone) or decreased (in soft tissue) dose contributions from backscattered photons. The only investigated geometry for this algorithm is a head and neck like phantom and a head and neck patient. In contrast to the algorithm suggested by Ding et al., in the pencil beam algorithm presented in this thesis, the effect of backscattered photons is not explicitly accounted for. Due to the site specific definition of the dose scaling factors as an average dose ratio, an average change of the dose in each material due to the above described scatter effect is accounted for in the scaling factors. The contribution of this effect to the scaling factors depends on the size of the bony structures and decreases with an increasing size.
The approach of Pawlowski et al. [25] includes the additional absorption due to the photoeffect implicitly by using a scaling factor, which depends on the distance that a pencil beam would travel through bone before reaching the voxel. A parameterization of the scaling factor as a function of the depth in bone is derived for a group of reference patients for different anatomic sites. The same set of functions describing the scaling factors for a specific energy spectrum can then be used for other patients for all anatomic sites, which is the main advantage of this method. This concept allows to include the effect of additional beam hardening in bony structures into account, which is not possible in the current implementation of the presented pencil beam algorithm.

A major difference between the dose scaling methods proposed by Ding et al. and Pawlowski et al. compared to the dose scaling algorithm presented in this thesis is the dose distribution used as a starting point for the postprocessing step. This dose distribution is almost the same in both publications: A dose distribution, which is corrected only for the dependence of the absorption coefficient on the electron density and no additional dependence on the atomic number. This dose distribution is obtained either using the superposition algorithm described above or a Monte Carlo simulation. The additional dependency on the atomic number Z, which reduces the number of primary photons, when the beam traverses a voxel with a different elemental composition with a higher effective Z, is not accounted for in this preliminary dose distribution and therefore can only be modeled in the postprocessing step. In both approaches, the dose in a single voxel is corrected with a single factor depending on the anatomic structures in the same primary beam path of this voxel. This includes a scaling of the scattered dose with the same factor, and does not allow for a change in the fraction of dose due to scattered photons originating from other pencil beam path. This is a major advantage of the algorithm described in this work, where the use of depth scaling factors accounts for this effect already upon calculation of the preliminary dose distribution. The depth scaling reduces the primary pencil beam dose as well as the scattered dose taking the reduced number of photons available for scattering into account.
Considering calculation speed, both correction methods from the literature add the calculation time for a correction step, which includes repetitive calculations for different beam angles to the calculation time needed to calculate a preliminary dose distribution with the above described superposition algorithm. In contrast, the cost in calculation time for the pencil beam algorithm and the proposed dose scaling method is very, as also described in the next section.
As a part of future work, the adaptation of other dose scaling factors reported in the literature would be of interest. Especially the algorithm proposed in the recent publication by Pawlowski et al. would allow for the inclusion of beam hardening into the algorithm, which is a major limitation of the current implementation. Also the application of the proposed depth and dose scaling factors to a superposition algorithm would be of interest.

10.4. Calculation Speed

A main goal of this work was to develop a very fast algorithm for the calculation of dose due to keV imaging procedures in radiotherapy. The developed algorithm is therefore based on the fastest type of algorithms available for the dose calculation for therapeutic MeV beams. Also in the design of the postprocessing step, the cost in calculation time was part of the consideration.
In the current implementation, the presented algorithm needs app. 10-12 minutes to calculate the preliminary pencil beam dose distribution for 72 beam directions. Experiences with the MeV pencil beam algorithm show that the use of a newer version of the pencil beam algorithm, which includes parallel execution on several CPUs can speed up the calculation significantly. For instance, on a computer with 4 CPUs, the calculation time can be reduced to approximately one third.
The resulting dose cube and the matching CT dataset are imported into the IDL program, where the postprocessing step is executed within app. 8-10s. As the time needed for the postprocessing step is currently very low compared to the pencil beam calculation time, an investigation of more complex postprocessing algorithms should be considered in future work.

10.5. Accuracy of the Developed Algorithm

The accuracy of the developed algorithm was investigated for two different anatomic sites. For both sites, two beam configurations were considered to simulate typical imaging procedures: 1. Fluoroscopic imaging with a photon beam from a single direction and 2. a cone beam CT acquisition with a rotation of the X-ray tube by 360°. As the pencil beam algorithm is known to yield poor results for the calculation of dose in the lung region, this anatomic region was excluded from the investigation.
The two investigated scenarios challenge the proposed algorithm to a very different degree. The single

photon beam at 0° represents the most challenging situation even compared to other single photon beam angles. In contrast, the 360° rotation of the X-ray tube represents the most forgiving one. While in the single beam situation even differences in low dose areas are visible and can lead to very high relative differences between the calculated dose distribution and the reference value from the simulated dose distribution, for a 360° rotation, this area is overlaid with the high dose area for a different beam angle. Therefore for other imaging scenarios such as a 200° cone beam CT acquisition or a cone beam CT acquisition with a shifted detector, an accuracy is expected, which lies in between the two considered cases.
In general, for the same beam configuration, a better accuracy could be achieved for the pelvic region than for the head and neck region. This is due to the different anatomic features of the respective anatomic site. While in the pelvic area, the outer region consists of soft tissue and the bony structures are located at a certain depth, in the head and neck region, the skull and jaws lie directly underneath the skin. This leads to a high amount of beam hardening which is not accounted for in the presented algorithm. In addition, a lot of smaller bony structures are located in the head and neck creating a high lateral variation in the absorption. The consideration of lateral inhomogeneities is a known limitation of the pencil beam algorithm.

10.5.1. Single Photon Beams

For both anatomic sites, a comparison of the pencil beam dose distribution with the simulated dose distribution revealed high relative differences especially for the low dose area. For both anatomic sites, the same trend could be observed: The dose was underestimated in areas behind bony structures. As the dose scaling factor is calculated as a mean dose ratio, this underestimation of the dose behind bony structures is compensated for by an overestimation of the dose in other areas. As most of these voxels lie in the low dose region, the high relative difference still translates into relatively small absolute differences. As the application of fluoroscopic imaging in the pelvic region and especially in the head and neck region is very limited and the chosen beam direction highly challenges the pencil beam algorithm due to the high curvature of the face, the given accuracy has to be understood as a lower boundary of the accuracy when other imaging options such as the 200° CBCT scan are employed.
The lowest accuracy was achieved for the single beams in the head and neck region. For this site and beam configuration, the relative dose difference in more than 30% of the voxels exceeded 20%. As most of the high relative differences occur in low dose regions, the result improves to 85% of the voxels below 10%, when considering absolute differences in relation to the maximum dose in soft tissue. Due to the different beam hardening, significant differences in the dose ratios were found for treatment sites in the head and in the neck region, so that a separation of scaling factor for these two regions has to be considered.
For the pelvic area, a much higher accuracy could be achieved even for the single beam configuration. Even though the relative differences showed similar statistics as for the head and neck region, an average fraction of 86% of the voxels showed an absolute difference of less than 5% and even 98% of the voxels below 10% of the maximum dose in soft tissue. Also the mean doses for the organs at risk could be predicted with an accuracy better than 4% for most organs at risk. Especially for the intestine and the femoral heads, the prediction of the mean dose could be significantly improved compared to a fixed reference value, which is the method currently in use in most institutions.

10.5.2. CBCT Acquisitions

As expected, the accuracy for the 360° rotation of the X-ray tube was significantly increased compared to the single photon beams. For the head and neck region, a systematic overestimation of the dose could be observed for the frontal region, while the dose in the posterior region was underestimated. The comparison with the water-filled patient outline showed, that to a certain extent, this effect is not caused by inhomogeneities or their corrections but by the influence of the patient outline on the pencil beam algorithm itself. Therefore a significant improvement can only be expected if a different type of dose calculation algorithm is chosen. For the pelvic area, the same limitations of the algorithm could be observed as for the single beams: The dose shielded from the radiation by bony structures is

systematically underestimated. The observation of this effect for different beam geometries suggests that the depth scaling factors estimated for the slab phantom geometries overestimate the absorption in a real patient situation. A revised algorithm for the estimation of depth scaling factors could therefore lead to an increased accuracy of the presented pencil beam algorithm.
For the head and neck region, 80% of the voxels were found to show a relative difference of less than 10% and more than 98% a relative difference of less than 20%. The mean doses in the organs at risk could be predicted with an accuracy better than 6% for most organs at risk. With app 8.5% for bony tissues, the standard deviation of absolute differences normalized to the maximum dose in soft tissue for all voxels are comparable to those reported for the same anatomic site for the algorithm reported by Pawlowski et al.[25]. For soft tissue the value of app. 4.2% is slightly higher than the reported average of 2.3%.
Again for the pelvic region, an even higher accuracy could be achieved. For more than 92% of the voxels, a relative difference of less than 10% was found. The average standard deviations of the absolute differences normalized to the maximum dose in soft tissue for this anatomic site were 2.84% for soft tissues and 8.15% for bony materials. Again for bony structures this is comparable to the accuracy reported in the publication. For soft tissues, the accuracy is only slightly smaller than the reported 2.6% for this anatomic site.

11. Conclusion

Image guidance with keV photon beams offers a high potential benefit in radiation therapy, even though they may deliver a considerable amount of additional dose to the organs at risk. Unlike in a diagnostic procedure this dose is added to an already high dose applied in the radiation treatment, which has to be considered in the treatment planning process.
In this work, a fast dose calculation algorithm for the application in the keV energy range has been developed and evaluated. The algorithm is based on a MeV pencil beam algorithm, and extended to account for the characteristics specific for the new energy range. To account for tissue inhomogeneities, the concept of semi-empirical depth scaling factors was introduced. Furthermore, site specific dose scaling factors ensure an accurate calculation of dose in media other than water. The accuracy of the algorithm was investigated for different steps in the development process by comparison with Monte Carlo simulations. For the application to patients, the calculated dose distributions were evaluated focusing on systematic effects, the overall accuracy and the implications on the dose calculation for organs at risk. The presented algorithm has been shown offer predictions of the mean dose in organs at risk for all beam geometries with an accuracy better than 10% in most cases. For cone beam CT acquisitions the calculation of dose distributions for the full patient geometry is also possible with a high accuracy: Within the primary beam area, the Monte Carlo dose distribution could be predicted with an accuracy of 10% for 80% of the voxels in the head and neck region and for 92% of the voxels in the pelvic region. The developed algorithm therefore allows for an inclusion of the dose due to keV imaging procedures into the planning process in radiotherapy.

A. Summary of Simulation parameters

A.1. Common Settings

A.1.1. All simulations

EGSnrc Transport Parameters as set in input file:

```
Global ECUT= 0.512
Global PCUT= 0.01
Global SMAX= 1e10
ESTEPE= 0.25
XIMAX= 0.5
Boundary crossing algorithm= EXACT
Skin depth for BCA= 0
Electron-step algorithm= PRESTA-II
Spin effects= On
Brems angular sampling= KM
Brems cross sections= NIST
Bound Compton scattering= On
Pair angular sampling= Simple
Photoelectron angular sampling= On
Rayleigh scattering= On
Atomic relaxations= On
Electron impact ionization= On
Photon cross sections= xcom
```

A.1.2. X-ray tube simulation

Source
Source Type: Electron beam from the side (isource nr. 13)
Particle Type: Electrons
Electron Energy: monoenergetic, 110keV or 121keV
Beam direction: antiparallel to x-axis
Beam size: 0.1cm x 0.1cm

Target
Target Angle: 12°
Target material: Tungsten
Target thickness: 1cm
Target holder material: Copper (no electron transport)

Filters
Aluminum Filter: 2.5mm at z=6.2cm

Copper Filter: 0.2mm at z=10.2cm

Other Settings
Directional Bremsstrahlung Splitting (DBS) activated
DBS-splitting factor: 2000
Electron transport cutoff (ECUT): 521keV
Photon Transport Cutoff (PCUT): 10keV
Electron range rejection below: 531keV
Phase space scoring plane position: z=20cm

A.1.3. Collimator simulation

Source
Source Type: Phase space file (isource nr. 21)
Particle Type: as defined in phase space
Phase Space File: File created in X-ray tube simulation
Nr. of particles: All particles in phase space file

Collimator
X-Jaw Position: z_{sim}=0.01cm -0.4cm
Y-Jaw Position: z_{sim}=0.41cm -0.8cm
Jaw edge: focussed (same fieldsize in isocenter plane for upper and lower edge)
Collimator Material: lead (no signifiacnt difference to tungsten found)

Other Settings
Air slab of differing thickness behind collimator
Phase space scoring plane behind air
DBS deactivated
Electron transport cutoff (ECUT): 521keV
Photon Transport Cutoff (PCUT): 10keV
Electron range rejection below: 531keV

A.1.4. Dose deposition simulation

Source
Source Type: Phase space file stationary or rotating (isource nr. 2 or 8)
Particle Type: as defined in phase space
Phase Space File: File created in Collimator simulation
Source position: Dependent on thickness of air slab in collimator simulation
Constant distance isocenter/target of 100cm

Other Settings Electron transport cutoff (ECUT): 1MeV (no electron transport)
Photon Transport Cutoff (PCUT): 10keV

A.2. Individual Parameters

Table A.1.: *Individual Sources & other parameters*

	X-ray tube simulation				Collimator simulation					Dose deposition simulation					
	E_{elec} $[keV]$	Nr. of Part.	DBS radius/ z_{pos} $[cm]$	Phase Space Radius $[cm]$	app. Nr. of Part.	Field Side Length $[cm]$	z_{pos} of Phase Space $[cm]$	Phase Space Radius $[cm]$	app. Nr. of Part. in Phase Space	app. Nr. of Part.	Part. recycle factor	Beam-size set to $[cm]$	SSD $[cm]$	HOW-FAR-LESS	source angle
Tube Verification	110	$7*10^9$	40/70	10	$2.0*10^9$	35	60	25	$4.8*10^8$	$4.8*10^9$	10	-	80	on	2
Input Sim. 1.1-1.8	121	$3.5*10^9$	40/70	10	$1.3*10^9$	1	60	25	$2.6*10^5$	$1.3*10^7$	50	-	70-105	on	180°
Input Sim. 2.1-2.8	121	$3.5*10^9$	40/70	10	$1.3*10^9$	2	60	25	$1.1*10^6$	$3.2*10^7$	30	-	70-105	on	180°
Input Sim. 3.1-3.8	121	$3.5*10^9$	40/70	10	$1.3*10^9$	3	60	25	$2.4*10^6$	$7.2*10^7$	30	-	70-105	on	180°
Input Sim. 4.1-4.8	121	$3.5*10^9$	40/70	10	$1.3*10^9$	5	60	25	$6.7*10^6$	$2.0*10^8$	30	-	70-105	on	180°
Input Sim. 5.1-5.8	121	$3.5*10^9$	40/70	10	$1.3*10^9$	10	60	25	$2.7*10^7$	$2.7*10^8$	10	-	70-105	on	180°
Input Sim. 6.1-6.8	121	$3.5*10^9$	40/70	10	$1.3*10^9$	20	60	25	$1.1*10^8$	$1.1*10^9$	10	-	70-105	on	180°
Input Sim. 7.1-7.8	121	$3.5*10^9$	40/70	10	$1.3*10^9$	25	60	25	$1.6*10^8$	$1.6*10^9$	10	-	70-105	on	180°
Input Sim. 8.1-8.8	121	$3.5*10^9$	40/70	10	$1.3*10^9$	35	60	25	$3.1*10^8$	$3.1*10^9$	10	-	70-105	on	180°
Input Sim. 9.1-9.8	121	$4.0*10^9$	60/100	20	$1.9*10^9$	-	70	50	$1.9*10^9$	$2.0*10^9$	10	60	70-105	on	180°
Input Sim. 10.1-10.8	121	$4.0*10^9$	60/100	20	$1.9*10^9$	-	70	50	$1.9*10^9$	$2.0*10^9$	10	80	70-105	on	180°
Input Sim. 11	121	$4.0*10^9$	60/100	20	$1.9*10^9$	-	90	50	$1.9*10^9$	$2.0*10^9$	10	-	90	on	180°
Rectang. Waterph.	see input data simulations														
Cylindric Waterph.	121	$3.5*10^9$	40/70	10	$1.3*10^9$	27	60	25	$1.9*10^9$	$5*10^9$	30	-	phantom	off	0°
Water-filled Outline	121	$3.5*10^9$	40/70	10	$1.3*10^9$	27	60	25	$1.9*10^9$	$5*10^9$	50	-	phantom	off	0°-359°
Depth Scaling hom.	121	$3.5*10^9$	40/70	10	$1.3*10^9$	25	60	25	$1.6*10^8$	$1.6*10^9$	10	-	90	on	180°
Depth Scaling slab	121	$3.5*10^9$	40/70	10	$1.3*10^9$	25	60	25	$1.6*10^8$	$1.6*10^9$	10	-	90	off	180°
Pat. A&B - CBCT	121	$3.5*10^9$	40/70	10	$1.3*10^9$	27	60	25	$1.9*10^9$	$9*10^9$	50	-	phantom	off	0°-359°
Other Pat.s - CBCT	121	$3.5*10^9$	40/70	10	$1.3*10^9$	27	60	25	$1.9*10^9$	$5*10^9$	50	-	phantom	off	0°-359°
All Pat.s - single	121	$3.5*10^9$	40/70	10	$1.3*10^9$	27	60	25	$1.9*10^9$	$5*10^9$	50	-	phantom	off	0°

Table A.2.: *Non-CT geometries: Voxel definitions*

		x-direction		y-direction		z-direction	
	voxel boundary range	voxel-size	nr. of voxels	voxel-size	nr. of voxels	voxel-size	nr. of voxels
Tube Verification	x: -32.150cm - +32.150cm	8cm	1	8cm	1	0.125cm	1
	y: -32.150cm - +32.150cm	0.3cm	161	0.3cm	161	0.25cm	100
	z: -20.000cm - +55.125cm	8cm	1	8cm	1	10cm	5
Input Sim. 1.1-1.8		8cm	1	8cm	1		
	x: -32.150cm - +32.150cm	0.3cm	80	0.3cm	80	0.25cm	1
	y: -32.150cm - +32.150cm	0.1cm	3	0.1cm	3	0.3cm	100
	z: $z_{min} = SSD - 100cm$	0.3cm	80	0.3cm	80	10cm	2
	z_{max}=$z_{min} + 50.25cm$	8cm	1	8cm	1		
Input Sim. 2.1-8.8	x: -32.150cm - +32.150cm	8cm	1	8cm	1	0.25cm	1
	y: -32.150cm - +32.150cm	0.3cm	161	0.3cm	161	0.3cm	100
	z: $z_{min} = SSD - 100cm$	8cm	1	8cm	1	10cm	2
	z_{max}=$z_{min} + 50.25cm$						
Input Sim. 9.1-10.8	x: -60cm - +60cm	9cm	1	9cm	1	0.25cm	1
	y: -60cm - +60cm	2cm	51	2cm	51	0.3cm	100
	z: $z_{min} = SSD - 100cm$	9cm	1	9cm	1	10cm	2
	z_{max}=$z_{min} + 50.25cm$						
Rectang. Waterph.	see input data simulations						
Depth Scaling Factors	x: -30cm - +30cm	5cm	5	5cm	5	0.2cm	130
	y: -30cm - +30cm	0.5cm	20	0.5cm	50	5cm	4
	z: -10cm - +36cm	5cm	5	5cm	5		

For the calculation of depth scaling factors for air, lung and soft tissues, all voxels were set to the respective material. For the slab phantoms for bony tissues, voxel 1-40 ($d = 0cm - 8cm$) and all voxels above 81 ($d > 16cm$) in z-direction were set to water, voxel 41-80 ($d = 8cm - 16cm$) were set to the respective material. All voxels were set to a density of $1g/cm^3$.

B. Simulated vs. pencil beam dose slices

In this section, transversal, sagittal and frontal slices of the dose distribution simulated with Monte Carlo, the dose distribution calculated with the pencil beam algorithm and the relative and absolute differences are shown, to provide additional information for the reader. For each patient and beam configuration, isocentric slices are shown. Due to the high variation in the target point/ isocenter position, for the head and neck patients, central slices showing similar anatomic features for all patients are additionally shown. The colorscale used for the images is the same as used in chapter 9, again different colorscales were used for the single beam at 0° than for the cone beam CT aqcuisition (360° rotation of the X-ray tube). The colorscales are shown in the respective figure.

B.1. Single Beam - Head and Neck

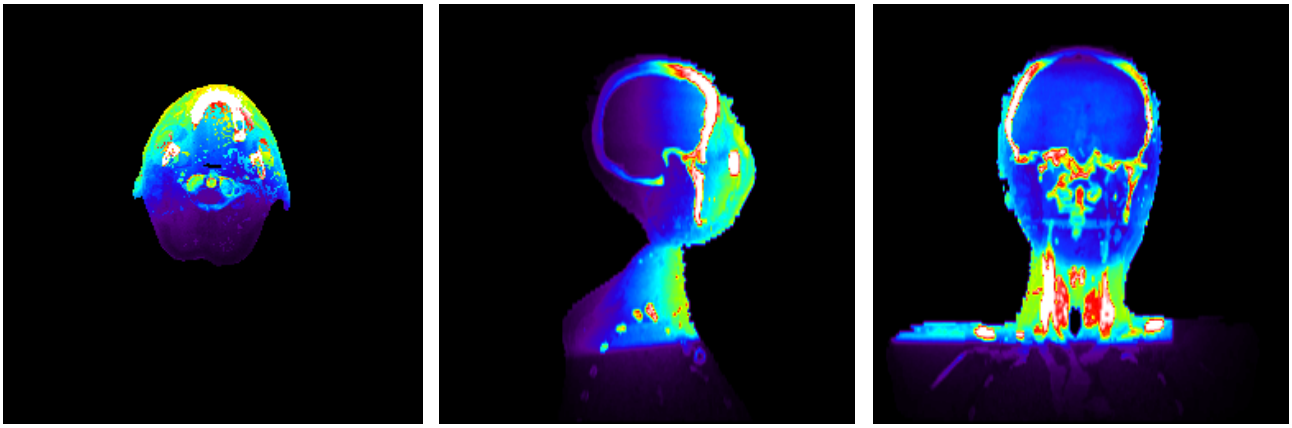

(a) *trans., Pat. A,* D_{MC} **(b)** *sag., Pat. A,* D_{MC} **(c)** *front., Pat. A,* D_{MC}

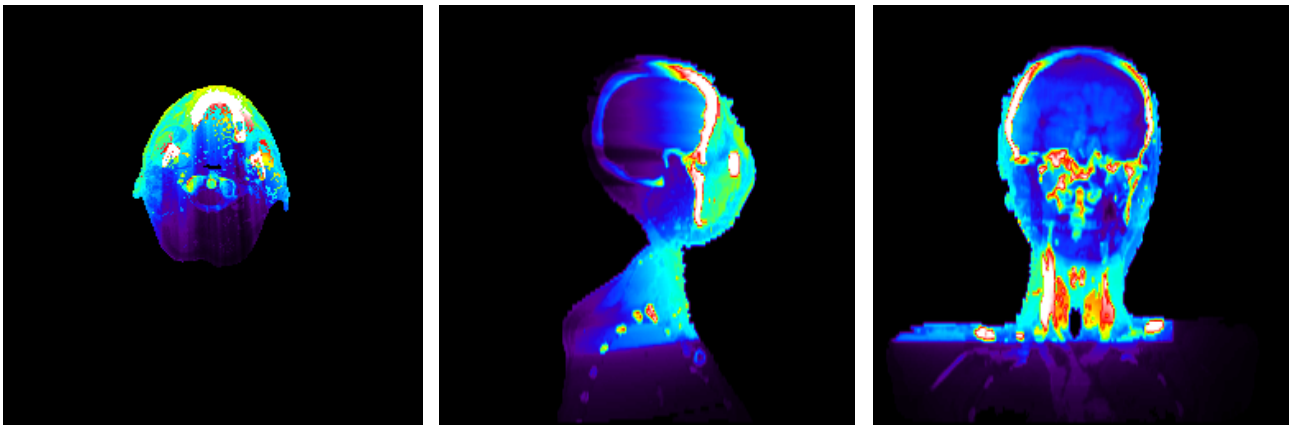

(d) *trans., Pat. A,* D_{PB} **(e)** *sag., Pat. A,* D_{PB} **(f)** *front., Pat. A,* D_{PB}

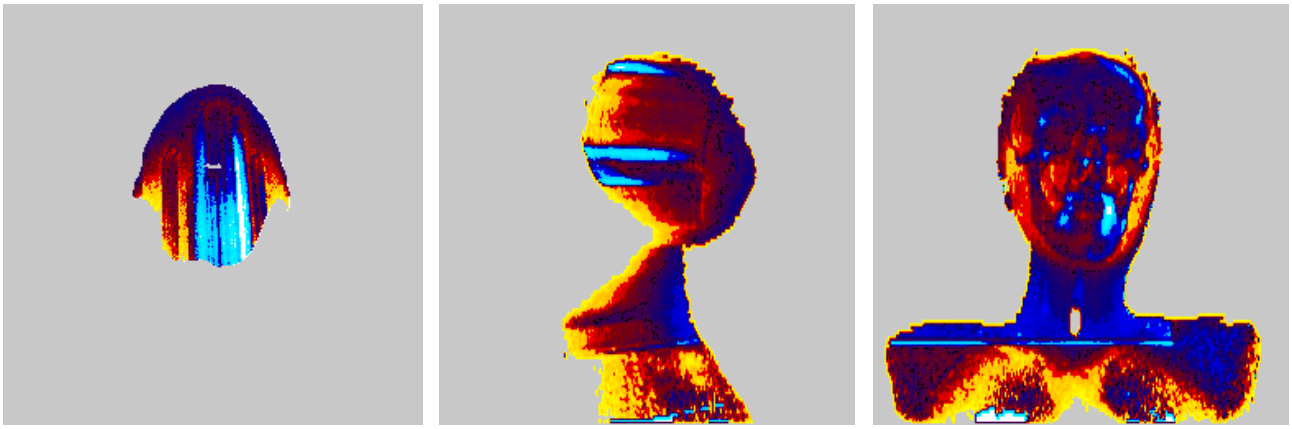

(g) *trans., Pat. A,* $\frac{D_{PB}-D_{MC}}{D_{MC}}$ **(h)** *sag., Pat. A,* $\frac{D_{PB}-D_{MC}}{D_{MC}}$ **(i)** *front., Pat. A,* $\frac{D_{PB}-D_{MC}}{D_{MC}}$

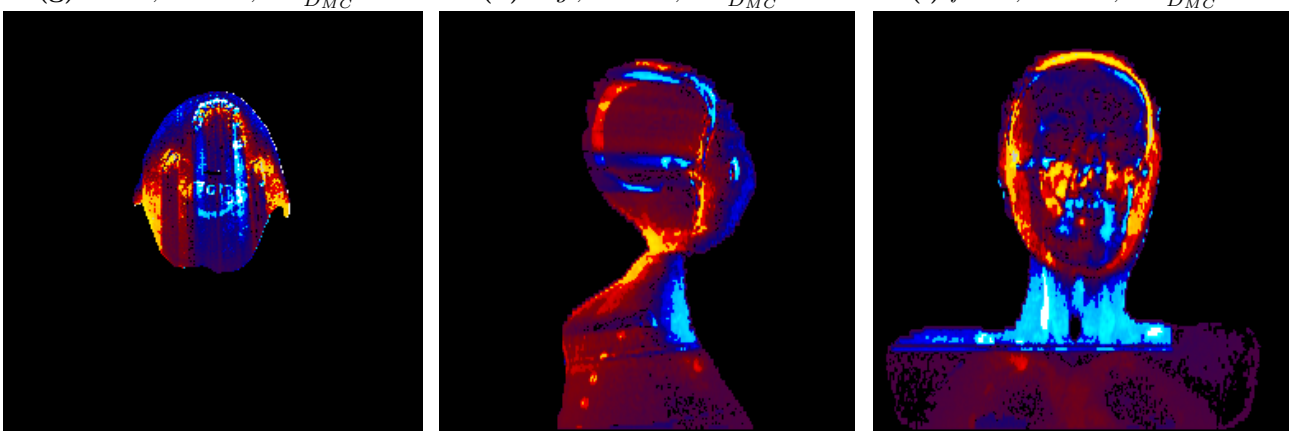

(j) *trans., Pat. A,* $D_{PB} - D_{MC}$ **(k)** *sag., Pat. A,* $D_{PB} - D_{MC}$ **(l)** *front., Pat. A,* $D_{PB} - D_{MC}$

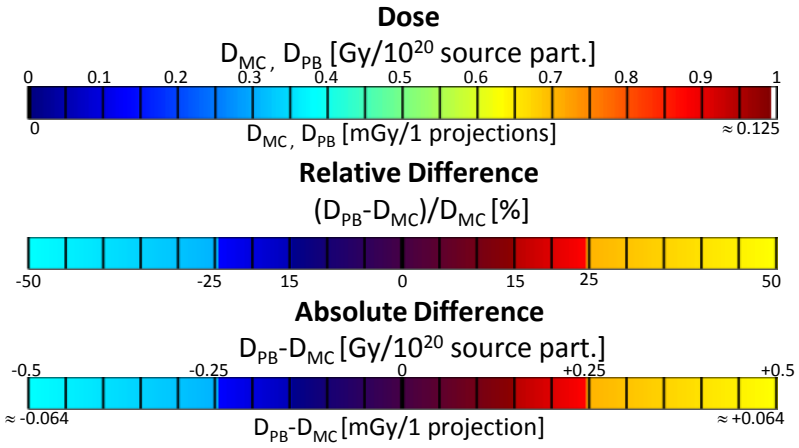

(m) *Colorscale for single projection image*

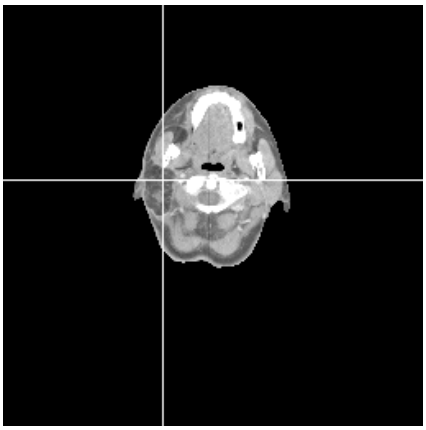

(n) *trans., Pat. A, CT*

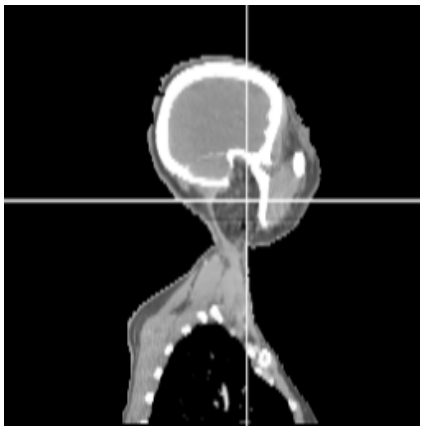

(o) *sag., Pat. A, CT*

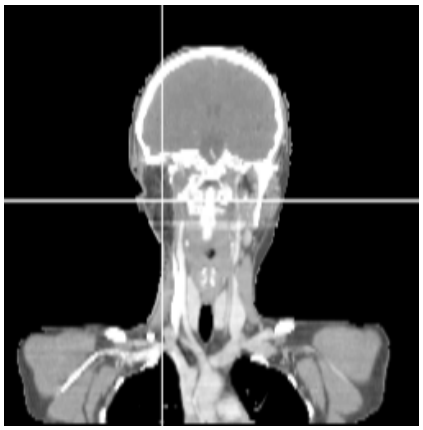

(p) *front., Pat. A, CT*

Figure B.1.: *Isocentric slices for Pat. A for a single beam at 0°. The slice positions are marked in the CT-slices shown in (n) - (p).*

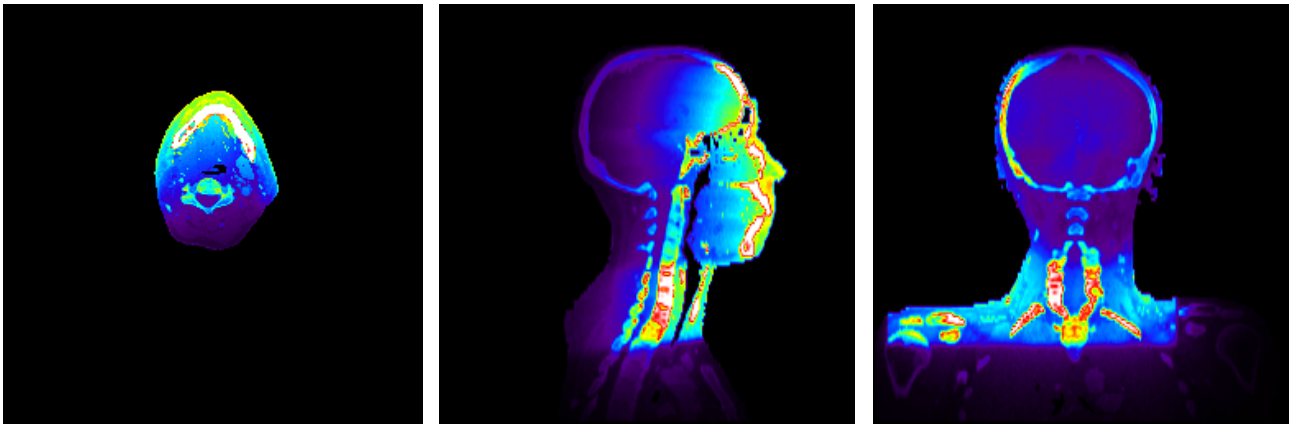

(a) *trans., Pat. A,* D_{MC} **(b)** *sag., Pat. A,* D_{MC} **(c)** *front., Pat. A,* D_{MC}

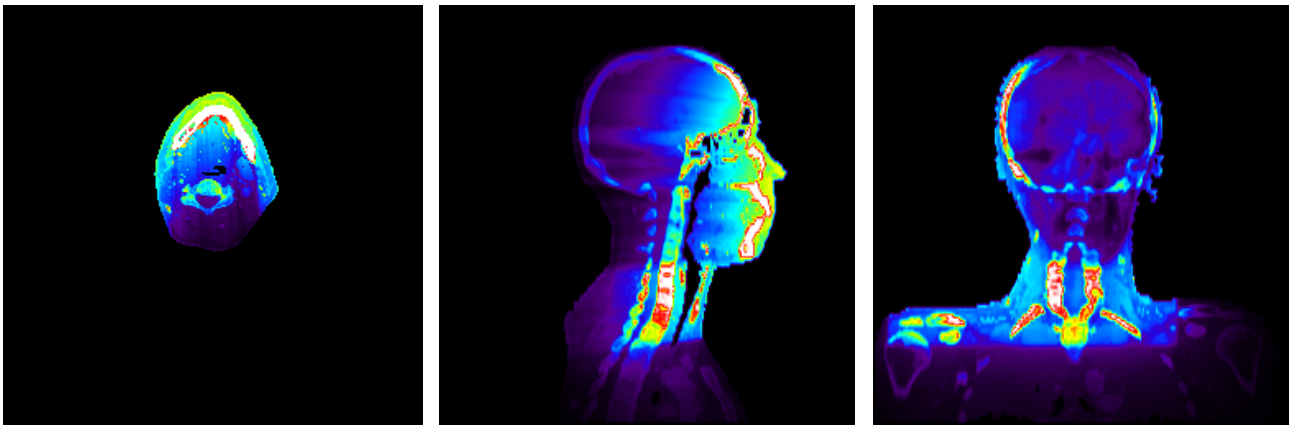

(d) *trans., Pat. A,* D_{PB} **(e)** *sag., Pat. A,* D_{PB} **(f)** *front., Pat. A,* D_{PB}

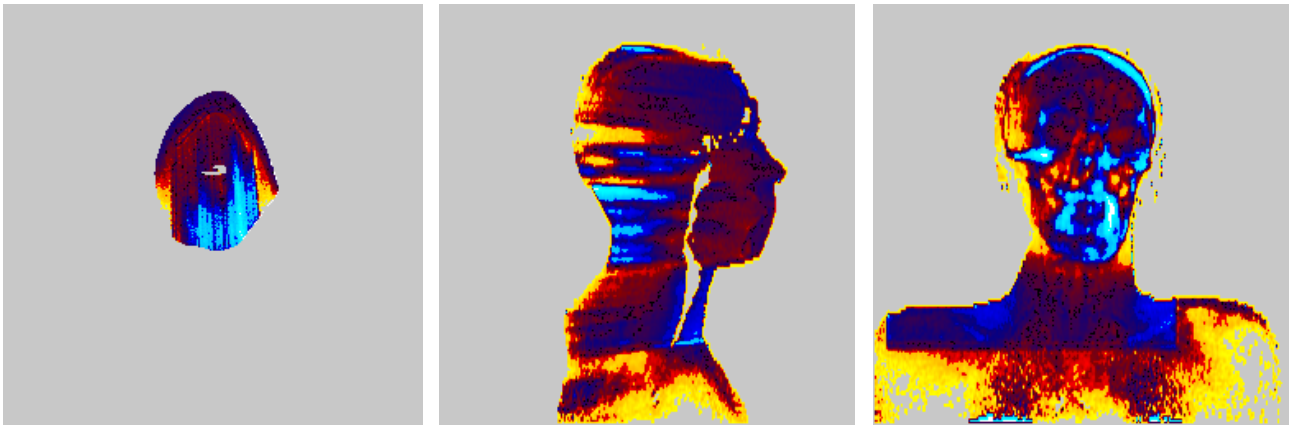

(g) *trans., Pat. A,* $\frac{D_{PB}-D_{MC}}{D_{MC}}$ **(h)** *sag., Pat. A,* $\frac{D_{PB}-D_{MC}}{D_{MC}}$ **(i)** *front., Pat. A,* $\frac{D_{PB}-D_{MC}}{D_{MC}}$

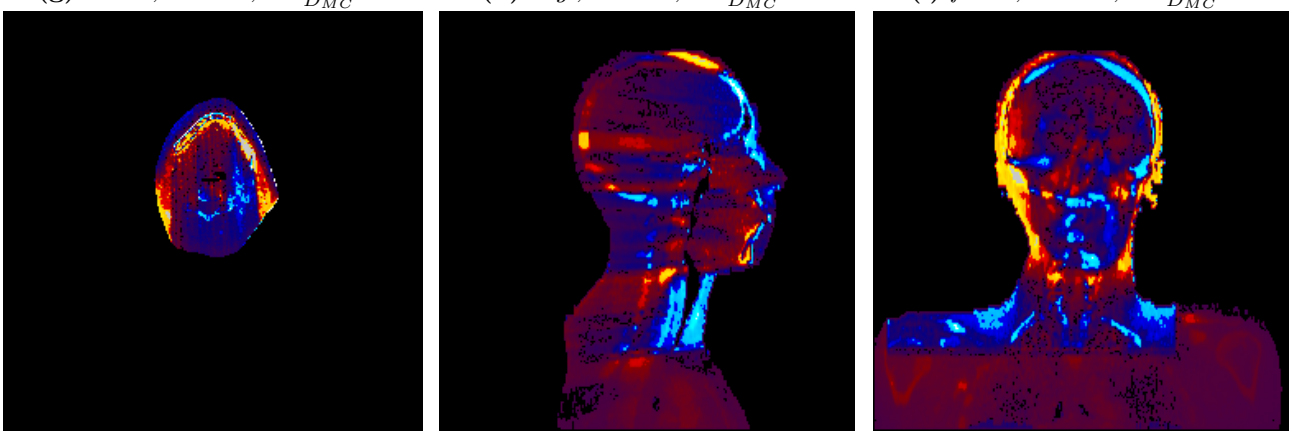

(j) *trans., Pat. A,* $D_{PB} - D_{MC}$ **(k)** *sag., Pat. A,* $D_{PB} - D_{MC}$ **(l)** *front., Pat. A,* $D_{PB} - D_{MC}$

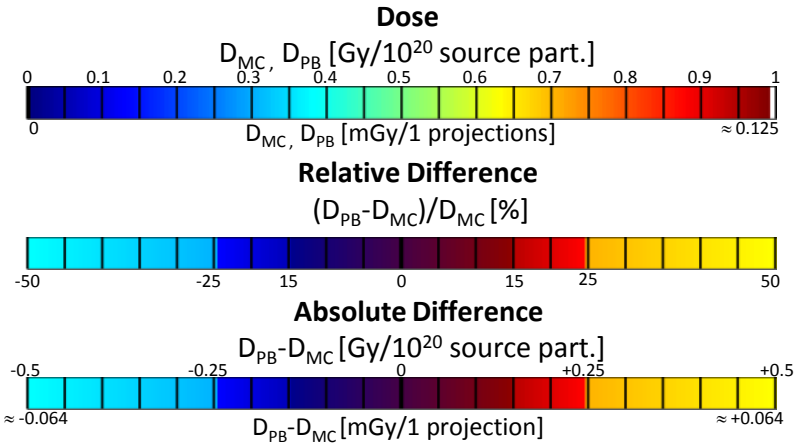

(m) *Colorscale for single projection image*

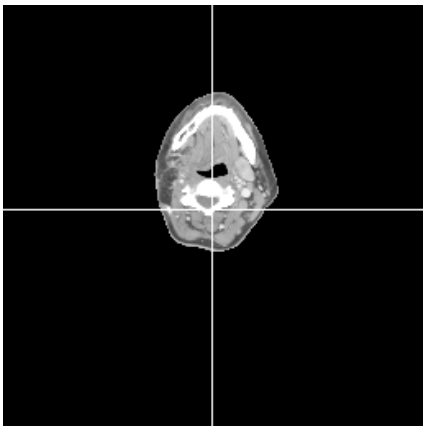

(n) *trans., Pat. A, CT*

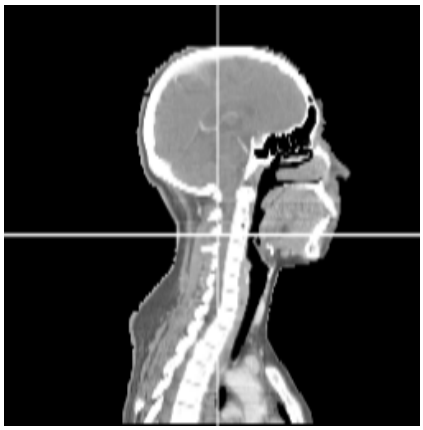

(o) *sag., Pat. A, CT*

(p) *front., Pat. A, CT*

Figure B.2.: *Central slices for Pat. A for a single beam at 0°. The slice positions are marked in the CT-slices shown in (n) - (p).*

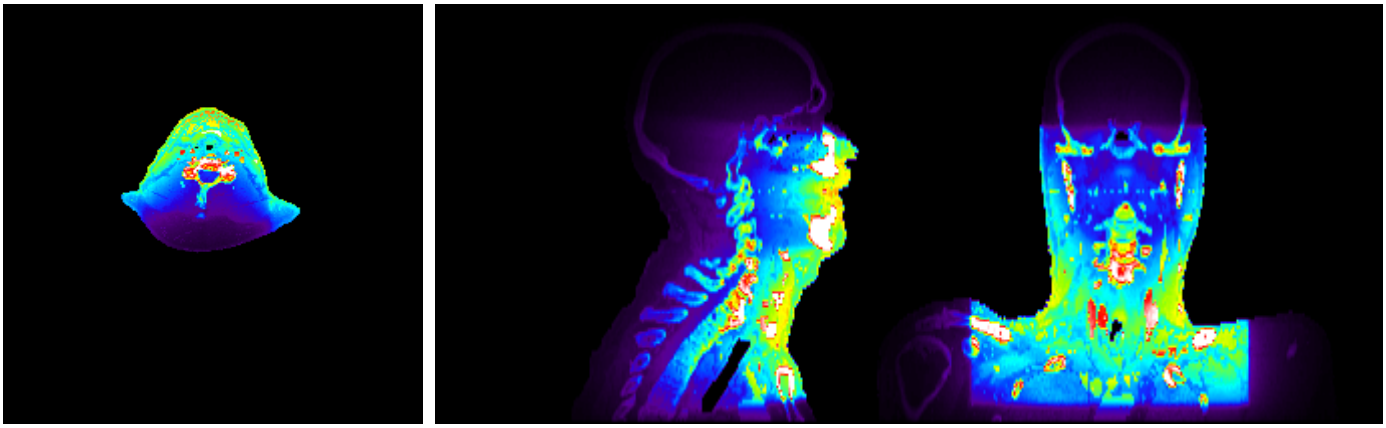

(a) *trans., Pat. B,* D_{MC} **(b)** *sag., Pat. B,* D_{MC} **(c)** *front., Pat. B,* D_{MC}

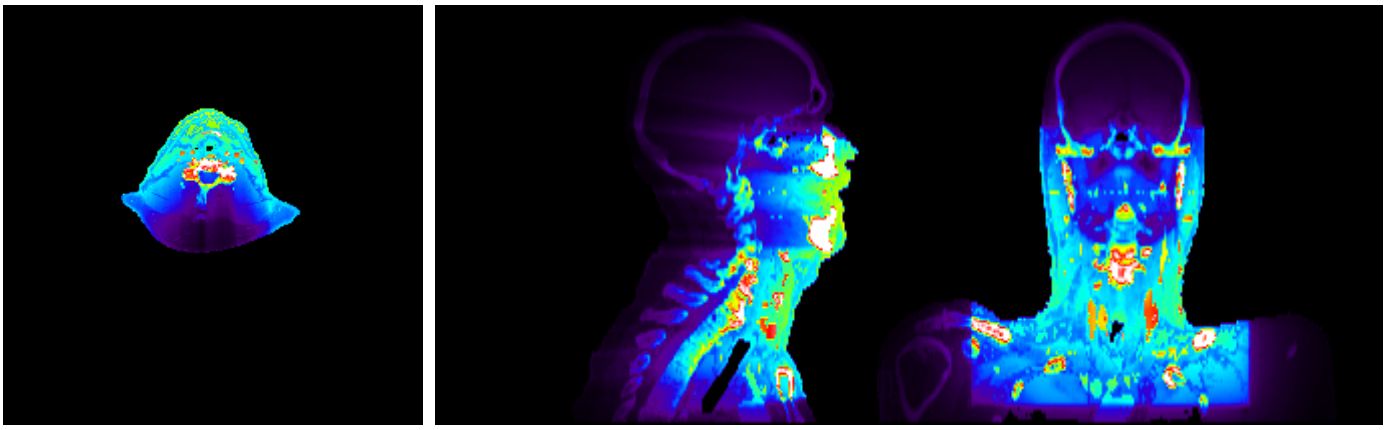

(d) *trans., Pat. B,* D_{PB} **(e)** *sag., Pat. B,* D_{PB} **(f)** *front., Pat. B,* D_{PB}

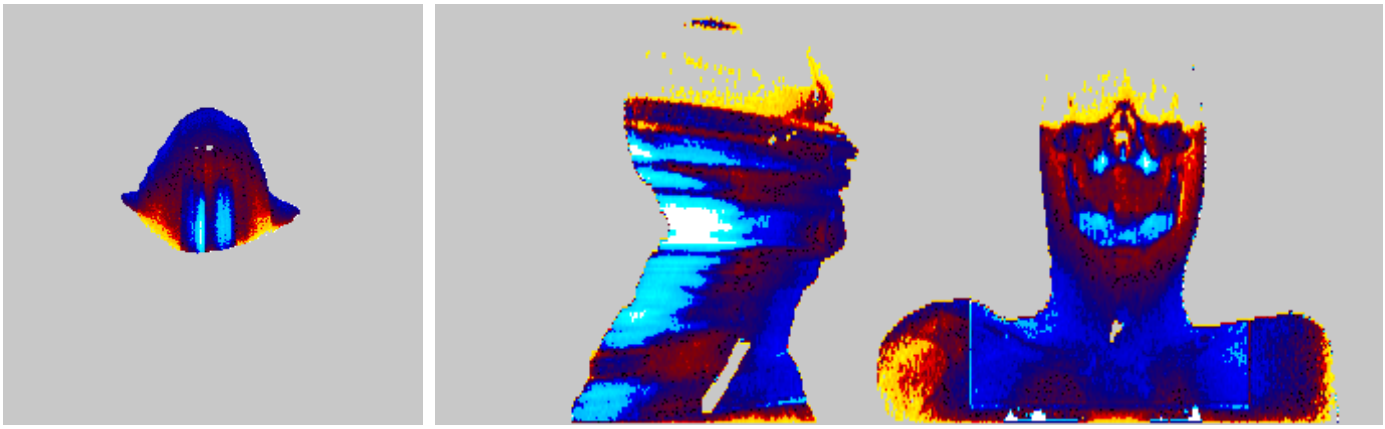

(g) *trans., Pat. B,* $\frac{D_{PB}-D_{MC}}{D_{MC}}$ **(h)** *sag., Pat. B,* $\frac{D_{PB}-D_{MC}}{D_{MC}}$ **(i)** *front., Pat. B,* $\frac{D_{PB}-D_{MC}}{D_{MC}}$

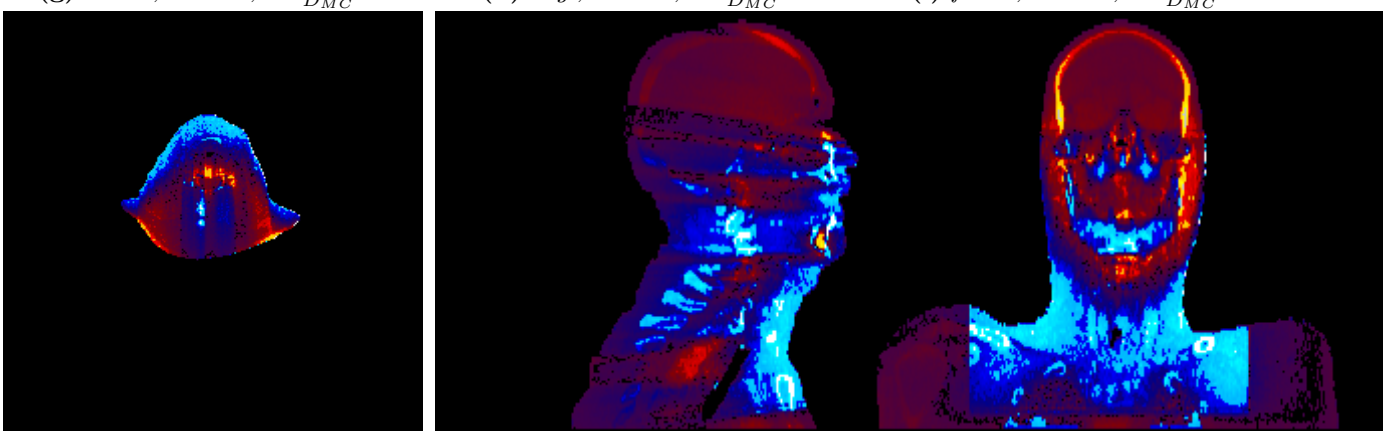

(j) *trans., Pat. B,* $D_{PB} - D_{MC}$ **(k)** *sag., Pat. B,* $D_{PB} - D_{MC}$ **(l)** *front., Pat. B,* $D_{PB} - D_{MC}$

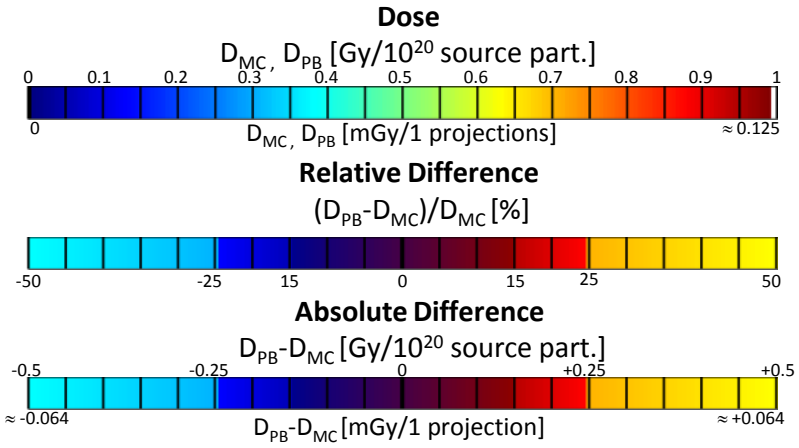

(m) *Colorscale for single projection image*

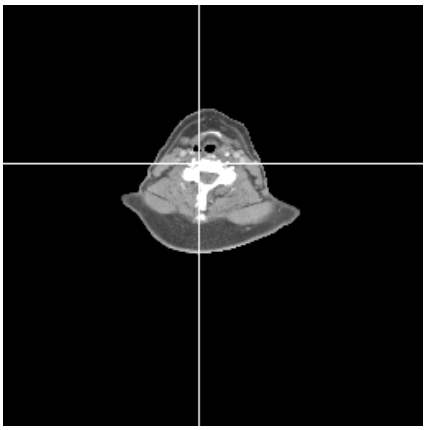

(n) *trans., Pat. B, CT*

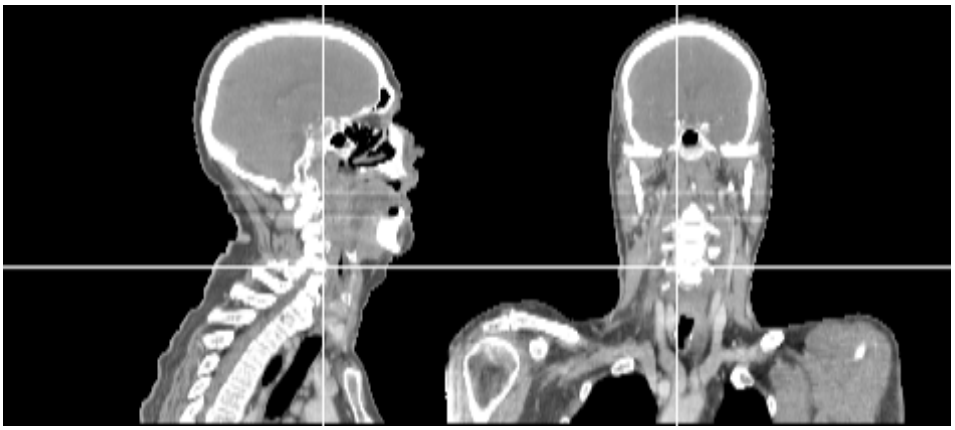

(o) *sag., Pat. B, CT* **(p)** *front., Pat. B, CT*

Figure B.3.: *Isocentric slices for Pat. B for a single beam at 0°. The slice positions are marked in the CT-slices shown in (n) - (p).*

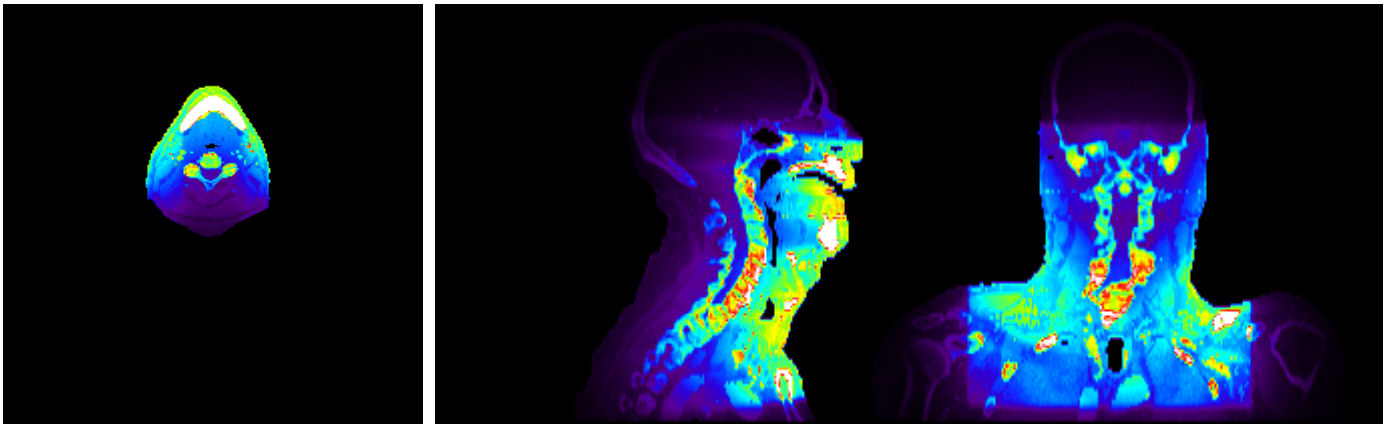

(a) *trans., Pat. B,* D_{MC} **(b)** *sag., Pat. B,* D_{MC} **(c)** *front., Pat. B,* D_{MC}

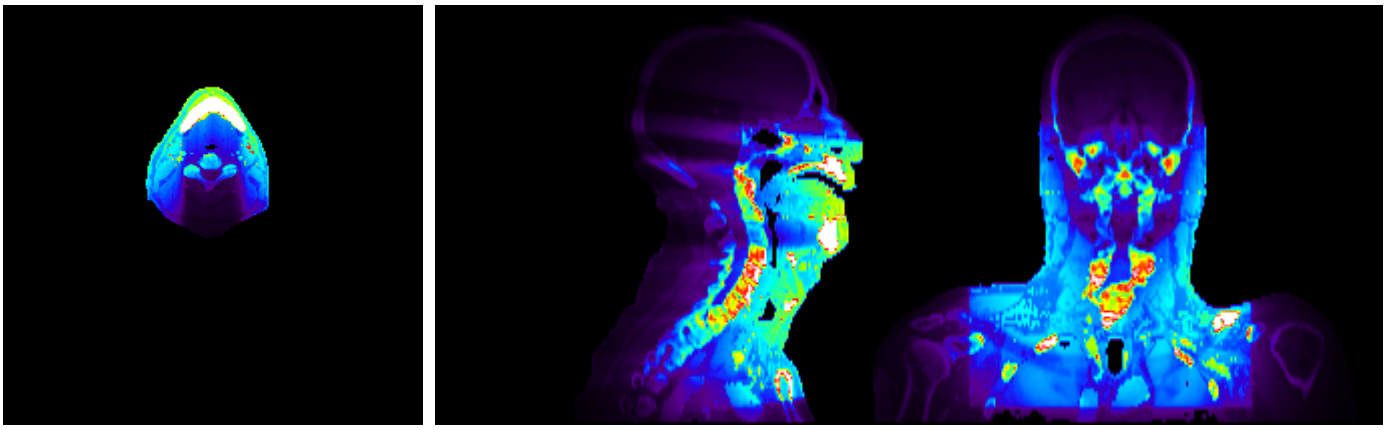

(d) *trans., Pat. B,* D_{PB} **(e)** *sag., Pat. B,* D_{PB} **(f)** *front., Pat. B,* D_{PB}

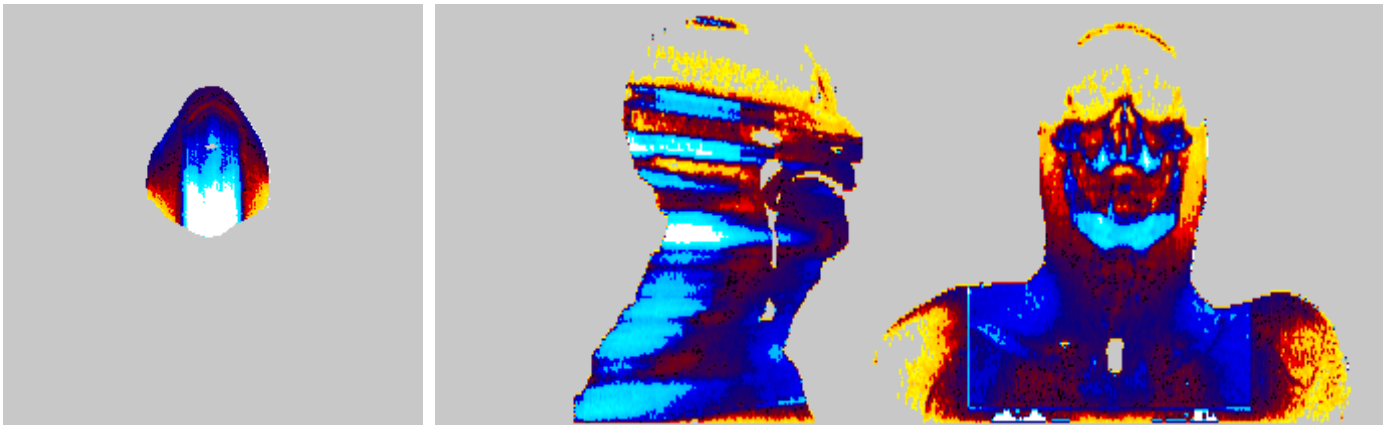

(g) *trans., Pat. B,* $\frac{D_{PB}-D_{MC}}{D_{MC}}$ **(h)** *sag., Pat. B,* $\frac{D_{PB}-D_{MC}}{D_{MC}}$ **(i)** *front., Pat. B,* $\frac{D_{PB}-D_{MC}}{D_{MC}}$

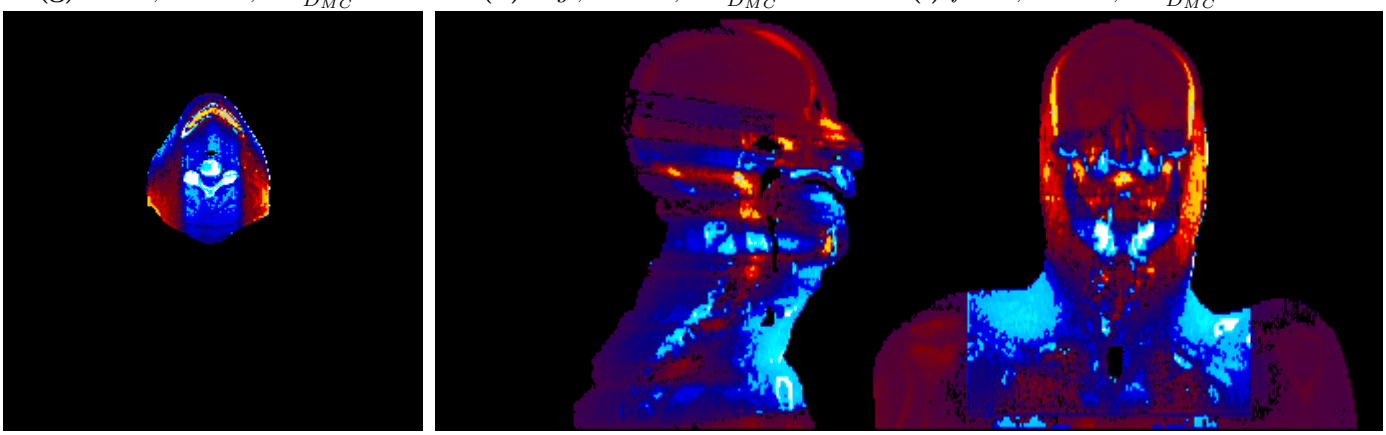

(j) *trans., Pat. B,* $D_{PB} - D_{MC}$ **(k)** *sag., Pat. B,* $D_{PB} - D_{MC}$ **(l)** *front., Pat. B,* $D_{PB} - D_{MC}$

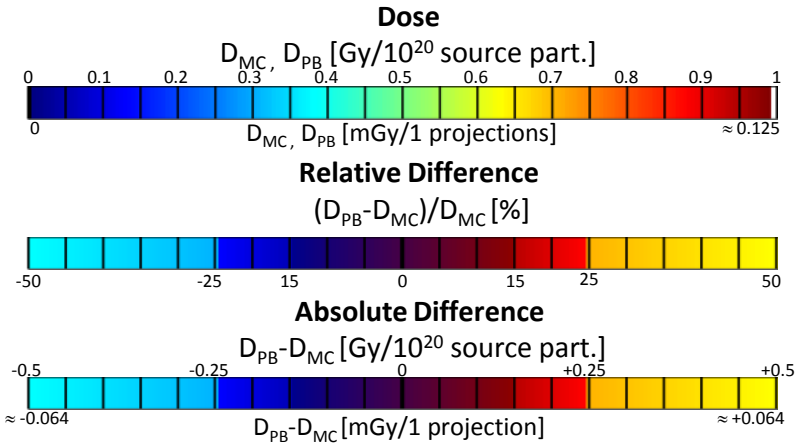

(m) *Colorscale for single projection image*

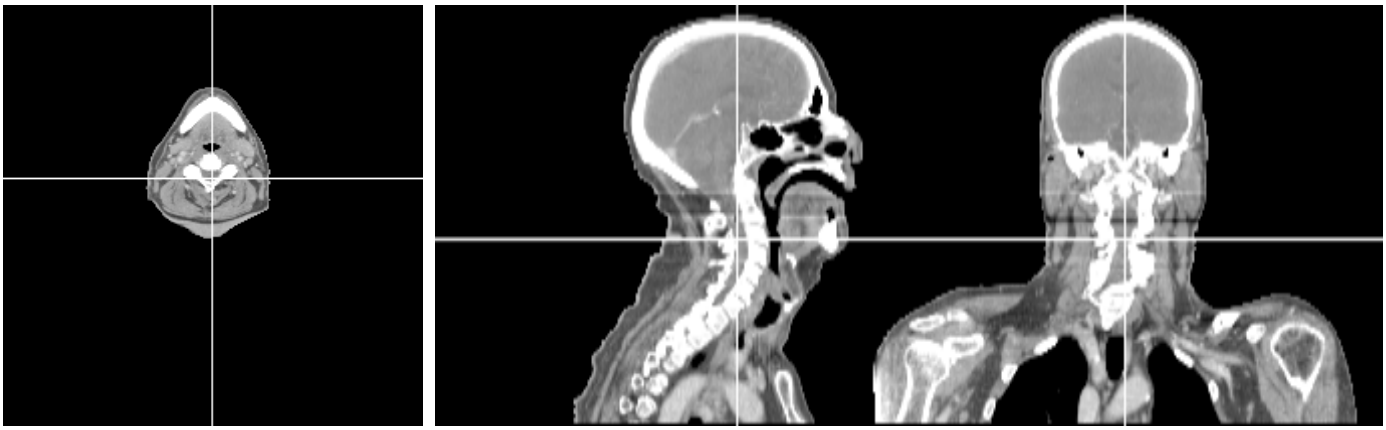

(n) *trans., Pat. B, CT* **(o)** *sag., Pat. B, CT* **(p)** *front., Pat. B, CT*

Figure B.4.: *Central slices for Pat. B for a single beam at 0°. The slice positions are marked in the CT-slices shown in (n) - (p).*

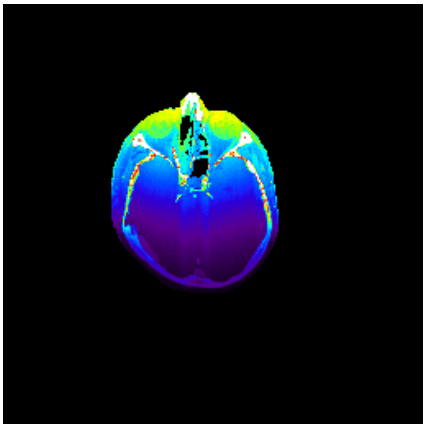

(a) *trans., Pat. C,* D_{MC}

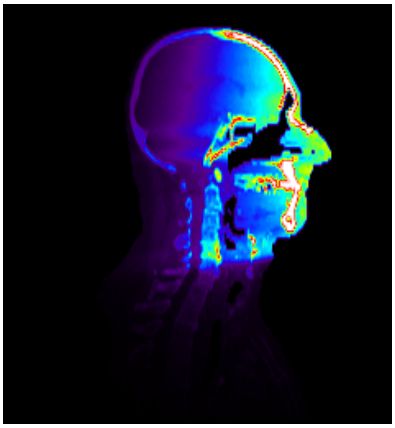

(b) *sag., Pat. C,* D_{MC}

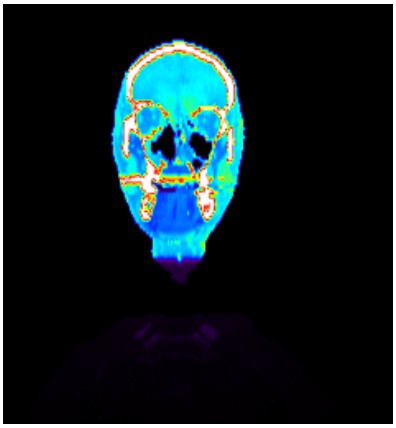

(c) *front., Pat. C,* D_{MC}

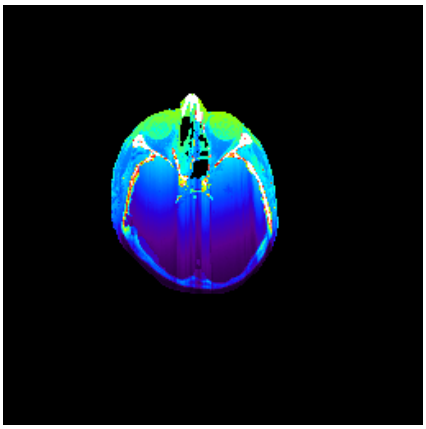

(d) *trans., Pat. C,* D_{PB}

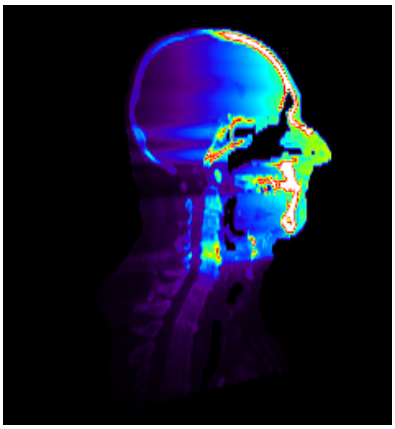

(e) *sag., Pat. C,* D_{PB}

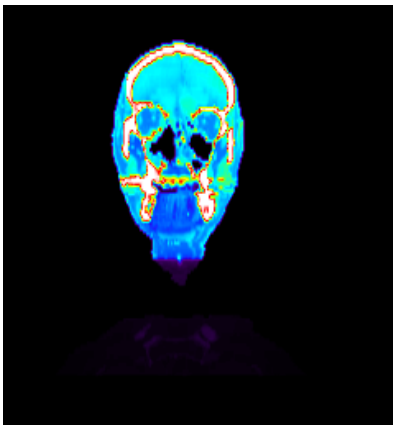

(f) *front., Pat. C,* D_{PB}

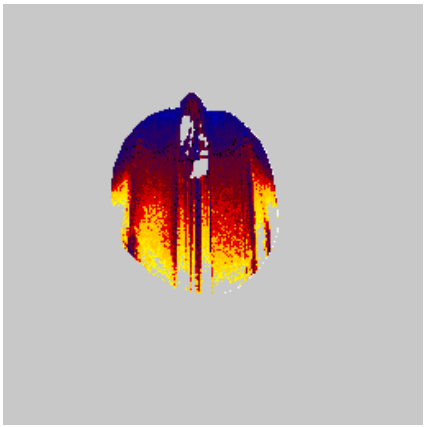

(g) *trans., Pat. C,* $\frac{D_{PB}-D_{MC}}{D_{MC}}$

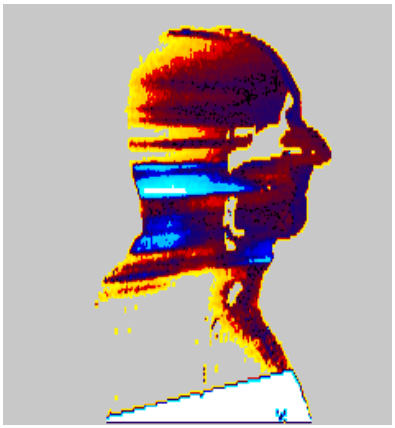

(h) *sag., Pat. C,* $\frac{D_{PB}-D_{MC}}{D_{MC}}$

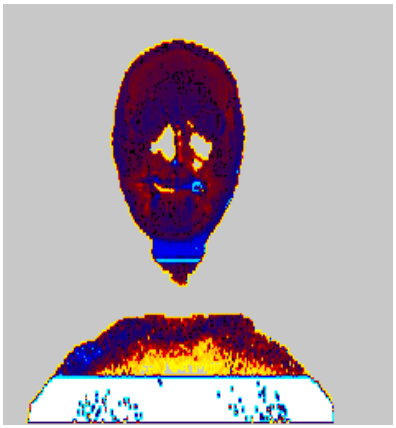

(i) *front., Pat. C,* $\frac{D_{PB}-D_{MC}}{D_{MC}}$

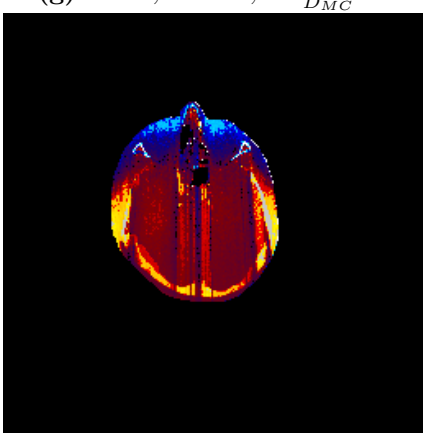

(j) *trans., Pat. C,* $D_{PB} - D_{MC}$

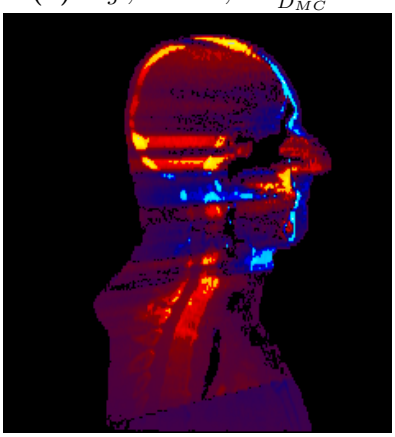

(k) *sag., Pat. C,* $D_{PB} - D_{MC}$

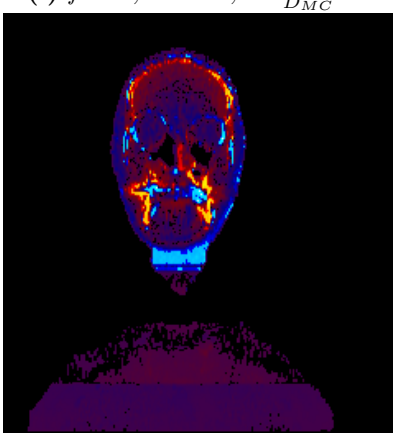

(l) *front., Pat. C,* $D_{PB} - D_{MC}$

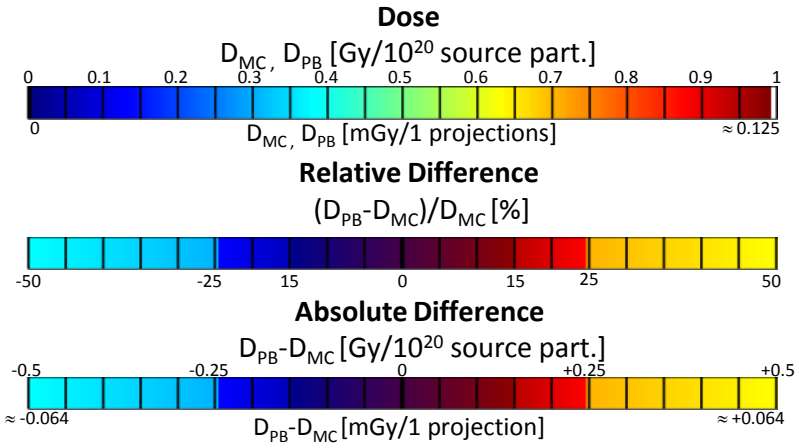

(m) *Colorscale for single projection image*

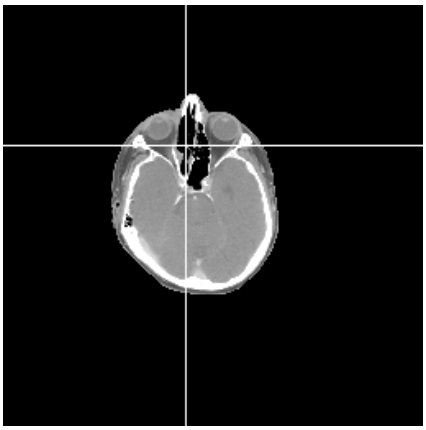

(n) *trans., Pat. C, CT*

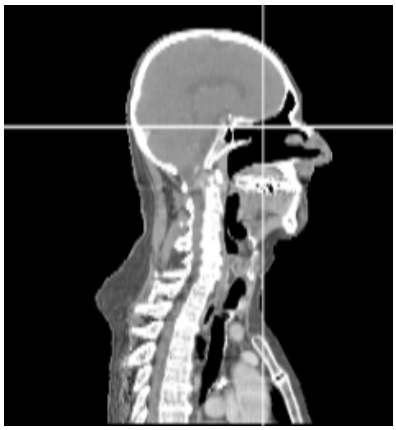

(o) *sag., Pat. C, CT*

(p) *front., Pat. C, CT*

Figure B.5.: *Isocentric slices for Pat. C for a single beam at 0°. The slice positions are marked in the CT-slices shown in (n) - (p).*

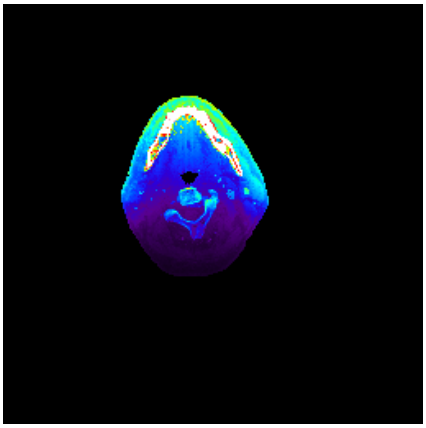

(a) *trans., Pat. C,* D_{MC}

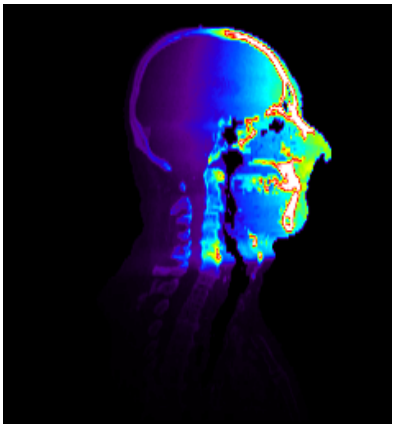

(b) *sag., Pat. C,* D_{MC}

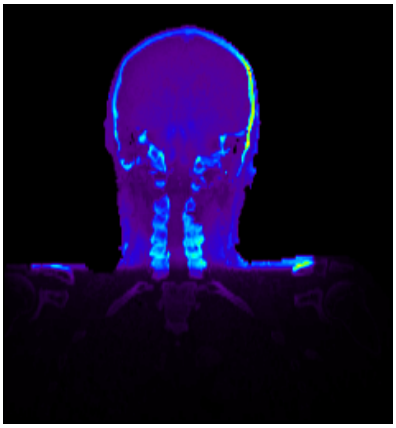

(c) *front., Pat. C,* D_{MC}

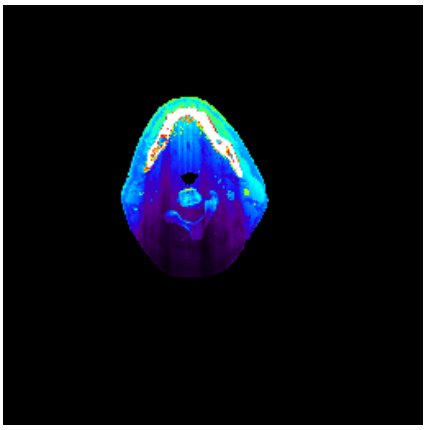

(d) *trans., Pat. C,* D_{PB}

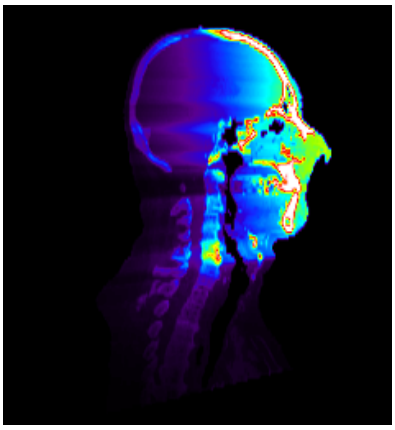

(e) *sag., Pat. C,* D_{PB}

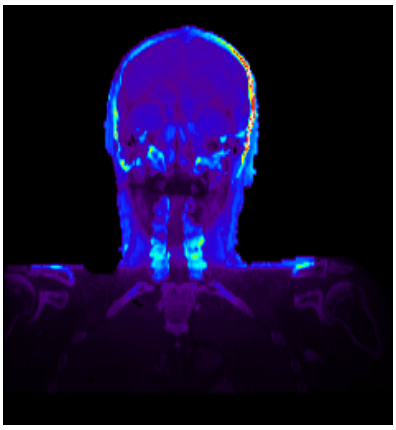

(f) *front., Pat. C,* D_{PB}

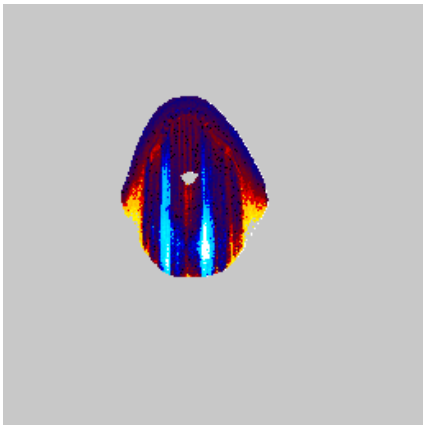

(g) *trans., Pat. C,* $\frac{D_{PB}-D_{MC}}{D_{MC}}$

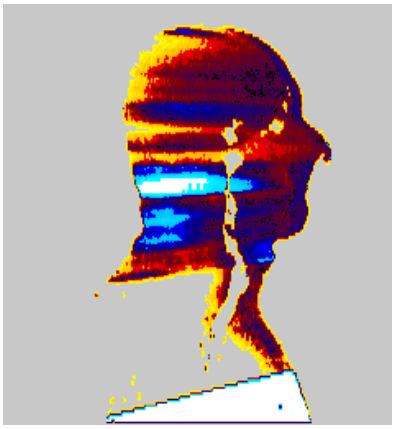

(h) *sag., Pat. C,* $\frac{D_{PB}-D_{MC}}{D_{MC}}$

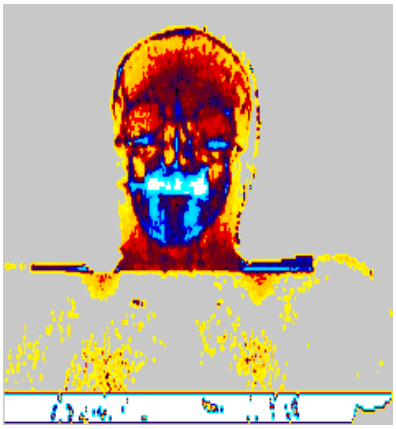

(i) *front., Pat. C,* $\frac{D_{PB}-D_{MC}}{D_{MC}}$

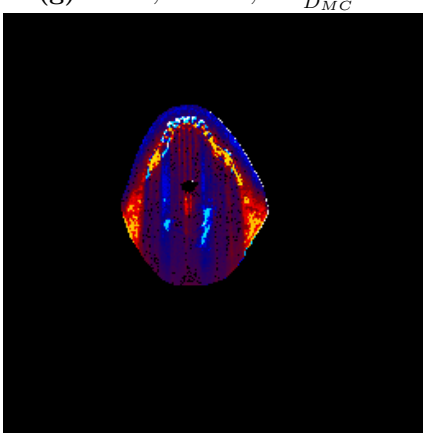

(j) *trans., Pat. C,* $D_{PB} - D_{MC}$

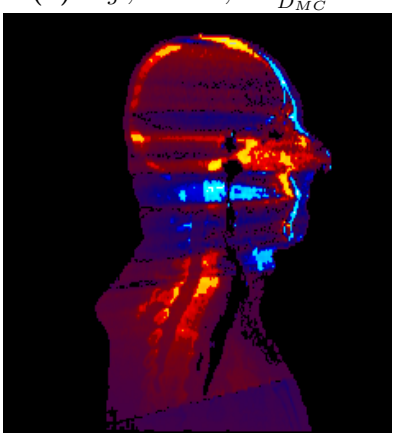

(k) *sag., Pat. C,* $D_{PB} - D_{MC}$

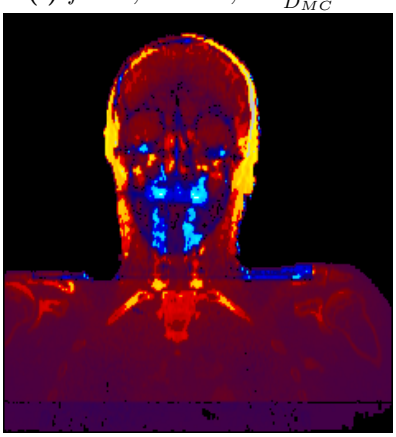

(l) *front., Pat. C,* $D_{PB} - D_{MC}$

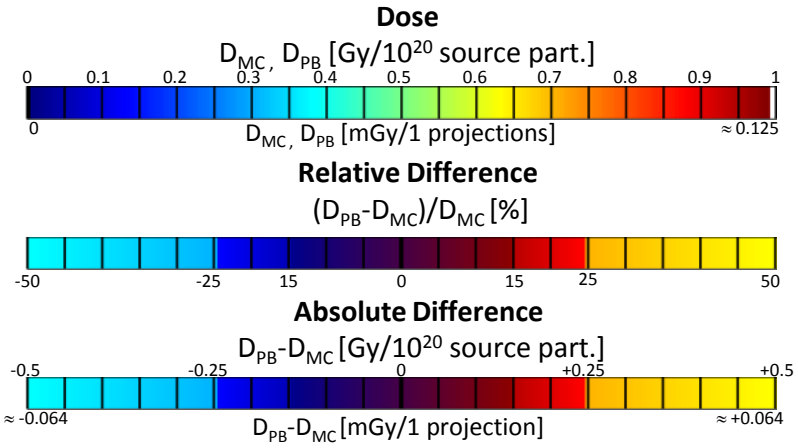

(m) *Colorscale for single projection image*

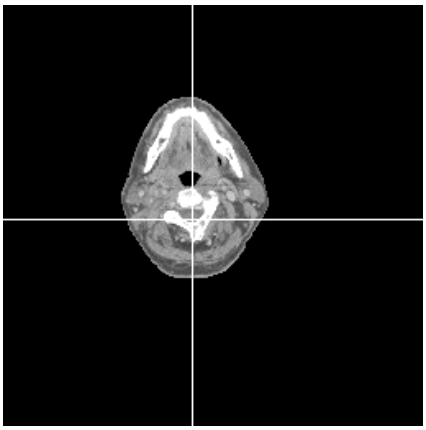

(n) *trans., Pat. C, CT*

(o) *sag., Pat. C, CT*

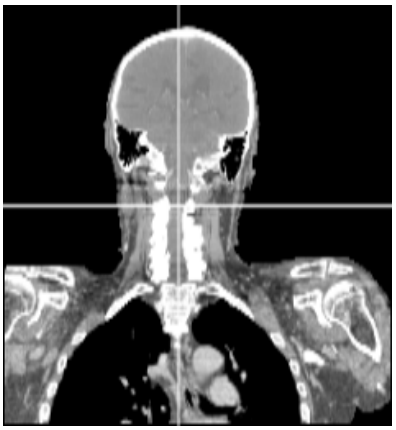

(p) *front., Pat. C, CT*

Figure B.6.: *Central slices for Pat. C for a single beam at 0°. The slice positions are marked in the CT-slices shown in (n) - (p).*

B.2. Cone beam CT - Head and Neck

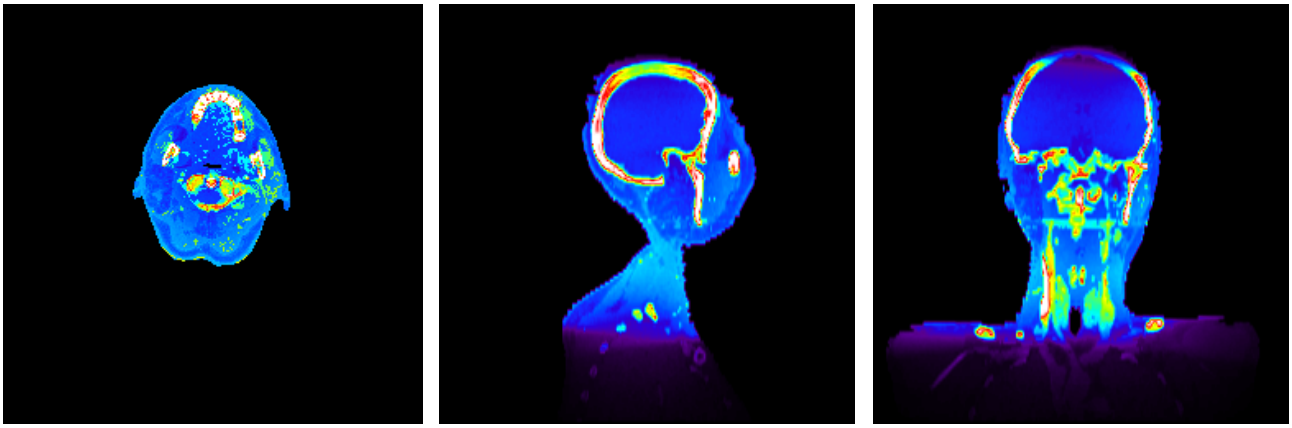

(a) *trans., Pat. A,* D_{MC} **(b)** *sag., Pat. A,* D_{MC} **(c)** *front., Pat. A,* D_{MC}

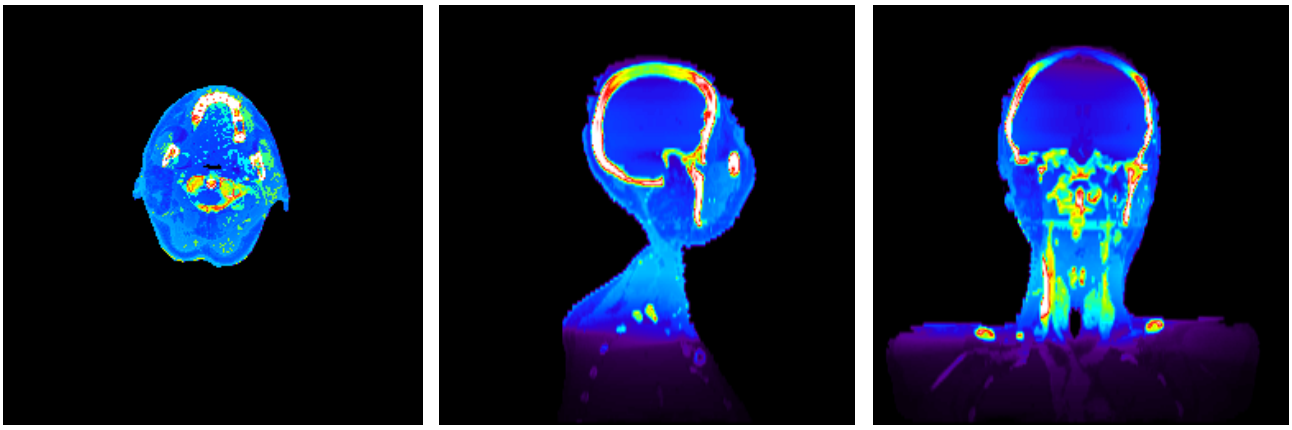

(d) *trans., Pat. A,* D_{PB} **(e)** *sag., Pat. A,* D_{PB} **(f)** *front., Pat. A,* D_{PB}

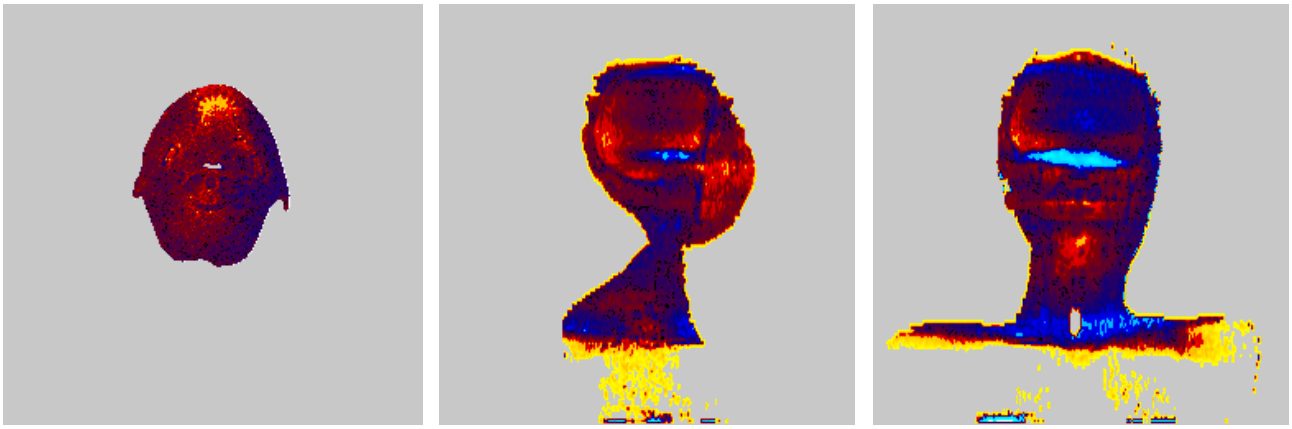

(g) *trans., Pat. A,* $\frac{D_{PB}-D_{MC}}{D_{MC}}$ **(h)** *sag., Pat. A,* $\frac{D_{PB}-D_{MC}}{D_{MC}}$ **(i)** *front., Pat. A,* $\frac{D_{PB}-D_{MC}}{D_{MC}}$

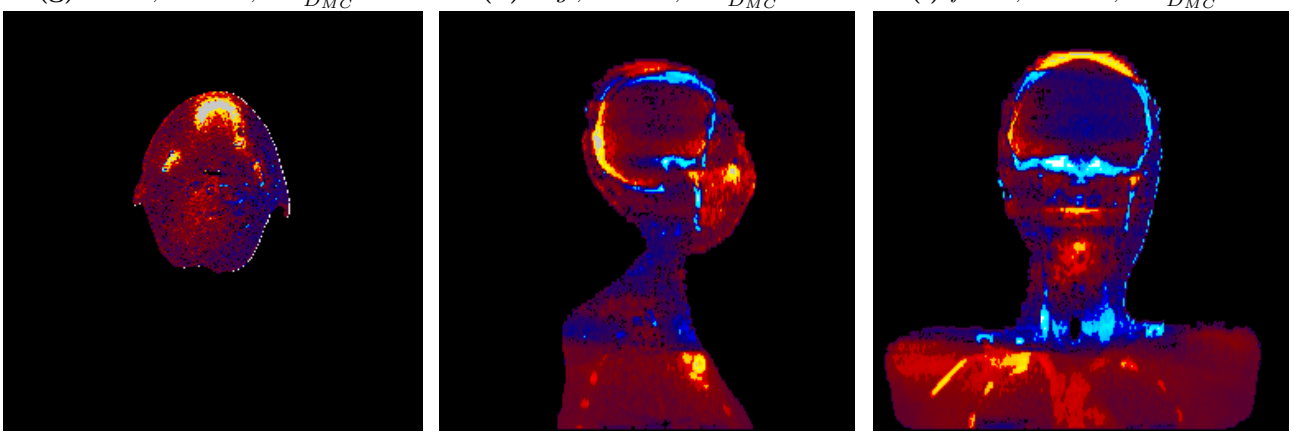

(j) *trans., Pat. A,* $D_{PB} - D_{MC}$ **(k)** *sag., Pat. A,* $D_{PB} - D_{MC}$ **(l)** *front., Pat. A,* $D_{PB} - D_{MC}$

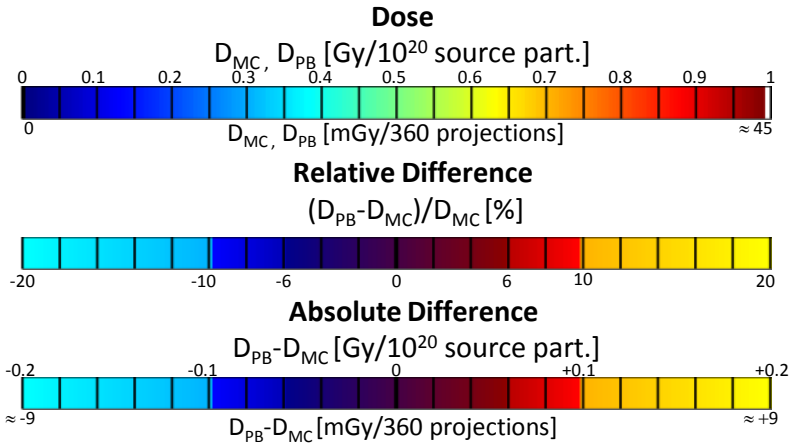

(m) *Colorscale for single projection image*

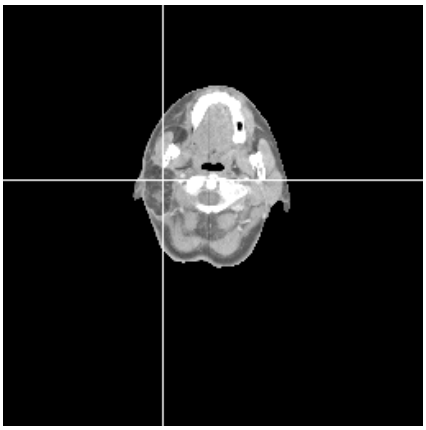

(n) *trans., Pat. A, CT*

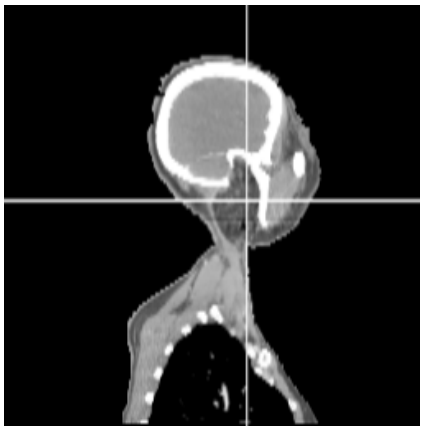

(o) *sag., Pat. A, CT*

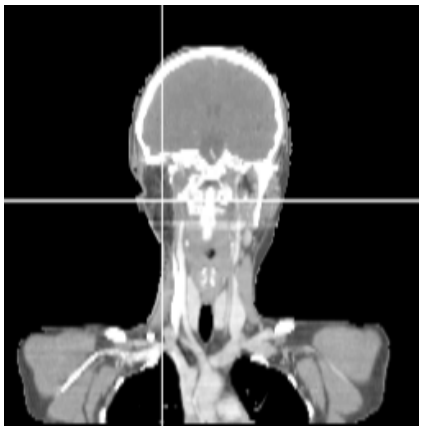

(p) *front., Pat. A, CT*

Figure B.7.: *Isocentric slices for Pat. A for a cone beam CT acquisition (360° tube rotation). The slice positions are marked in the CT-slices shown in (n) - (p).*

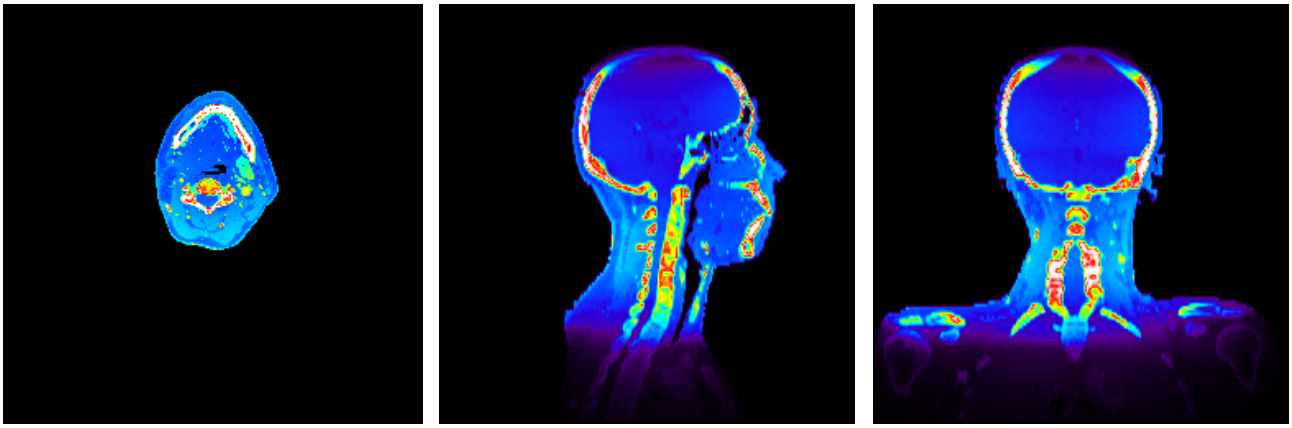

(a) *trans., Pat. A,* D_{MC} **(b)** *sag., Pat. A,* D_{MC} **(c)** *front., Pat. A,* D_{MC}

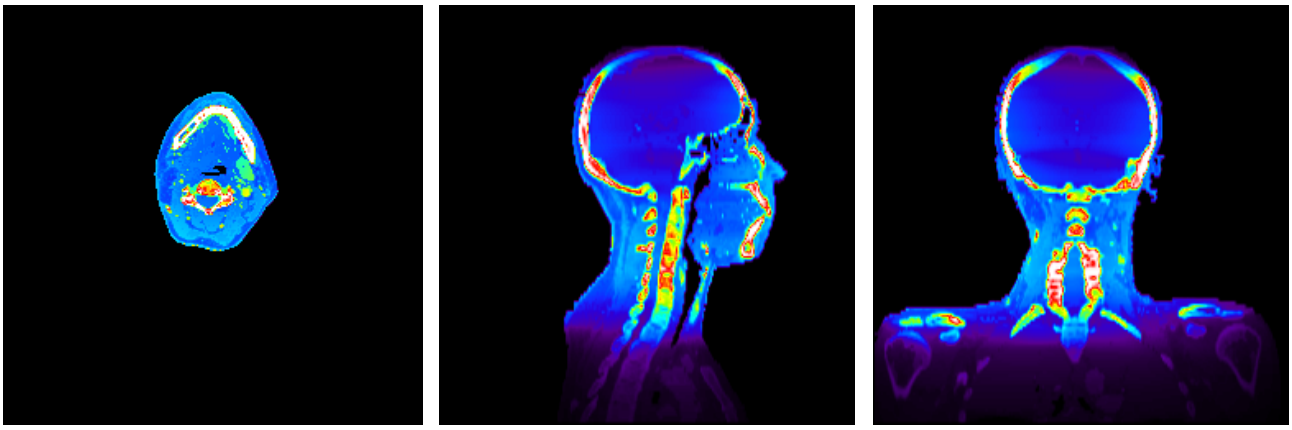

(d) *trans., Pat. A,* D_{PB} **(e)** *sag., Pat. A,* D_{PB} **(f)** *front., Pat. A,* D_{PB}

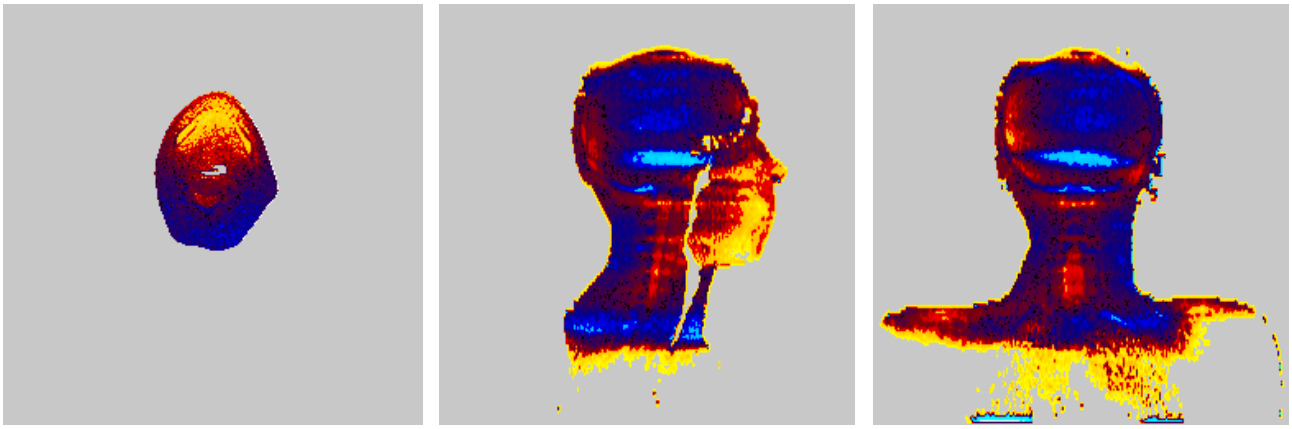

(g) *trans., Pat. A,* $\frac{D_{PB}-D_{MC}}{D_{MC}}$ **(h)** *sag., Pat. A,* $\frac{D_{PB}-D_{MC}}{D_{MC}}$ **(i)** *front., Pat. A,* $\frac{D_{PB}-D_{MC}}{D_{MC}}$

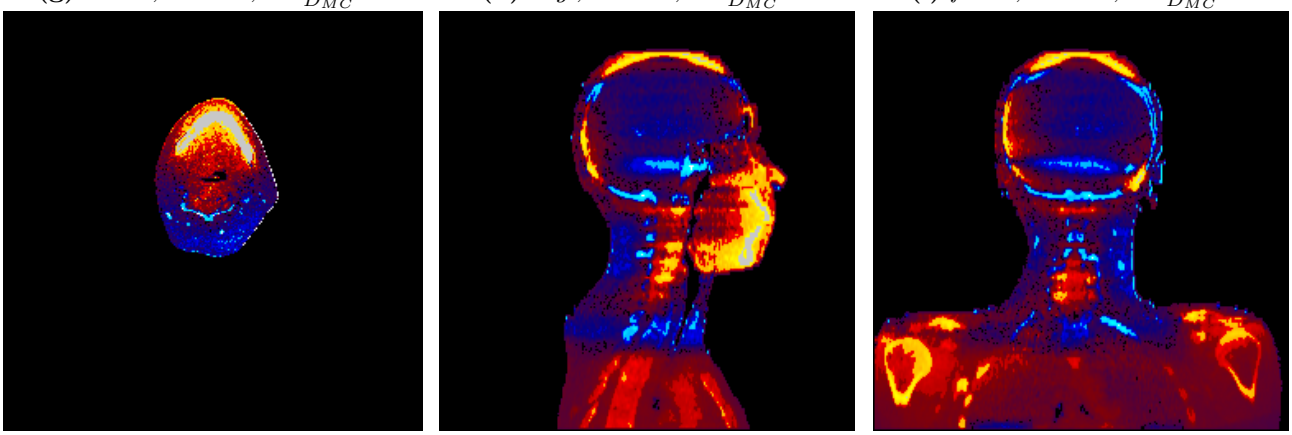

(j) *trans., Pat. A,* $D_{PB} - D_{MC}$ **(k)** *sag., Pat. A,* $D_{PB} - D_{MC}$ **(l)** *front., Pat. A,* $D_{PB} - D_{MC}$

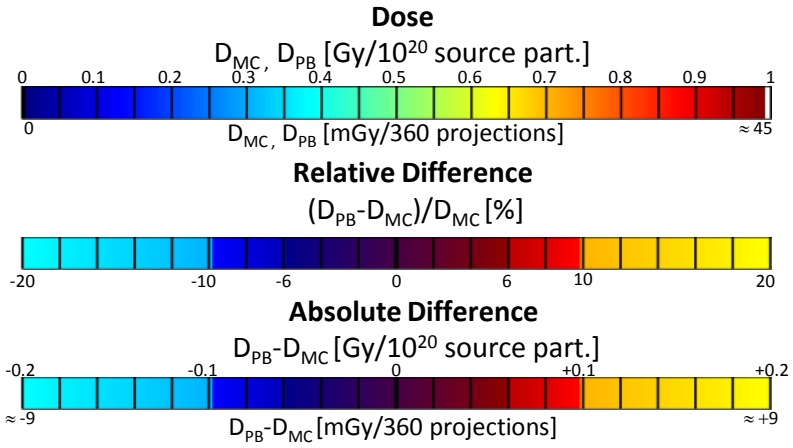

(m) *Colorscale for single projection image*

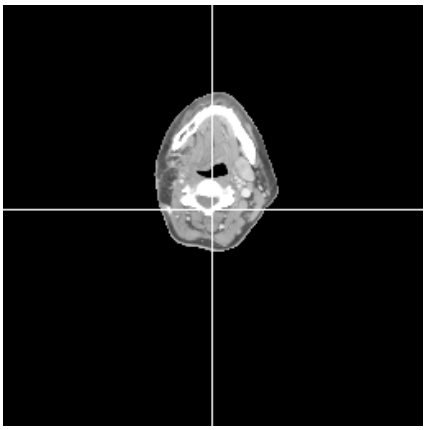

(n) *trans., Pat. A, CT*

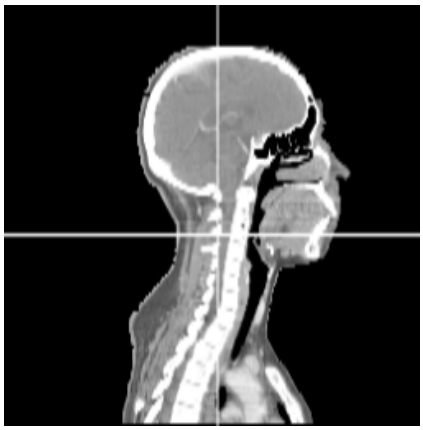

(o) *sag., Pat. A, CT*

(p) *front., Pat. A, CT*

Figure B.8.: *Central slices for Pat. A for a cone beam CT acquisition (360° tube rotation). The slice positions are marked in the CT-slices shown in (n) - (p).*

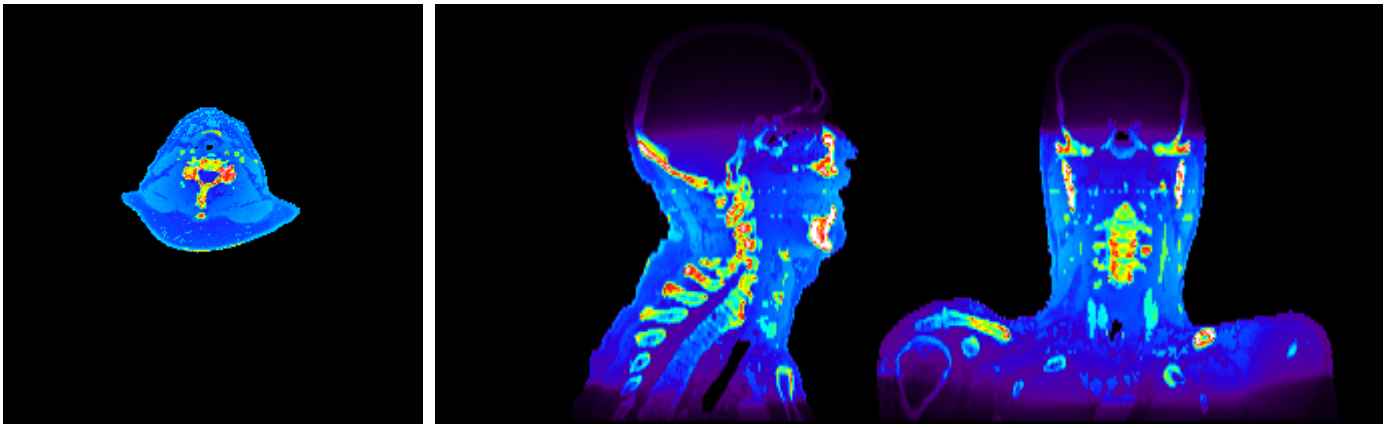

(a) *trans., Pat. B,* D_{MC} **(b)** *sag., Pat. B,* D_{MC} **(c)** *front., Pat. B,* D_{MC}

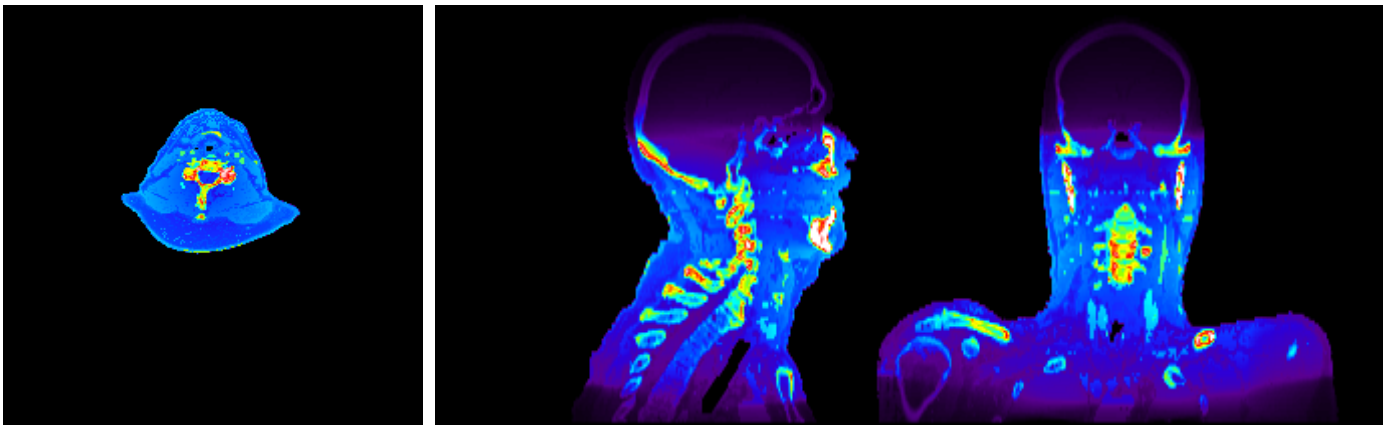

(d) *trans., Pat. B,* D_{PB} **(e)** *sag., Pat. B,* D_{PB} **(f)** *front., Pat. B,* D_{PB}

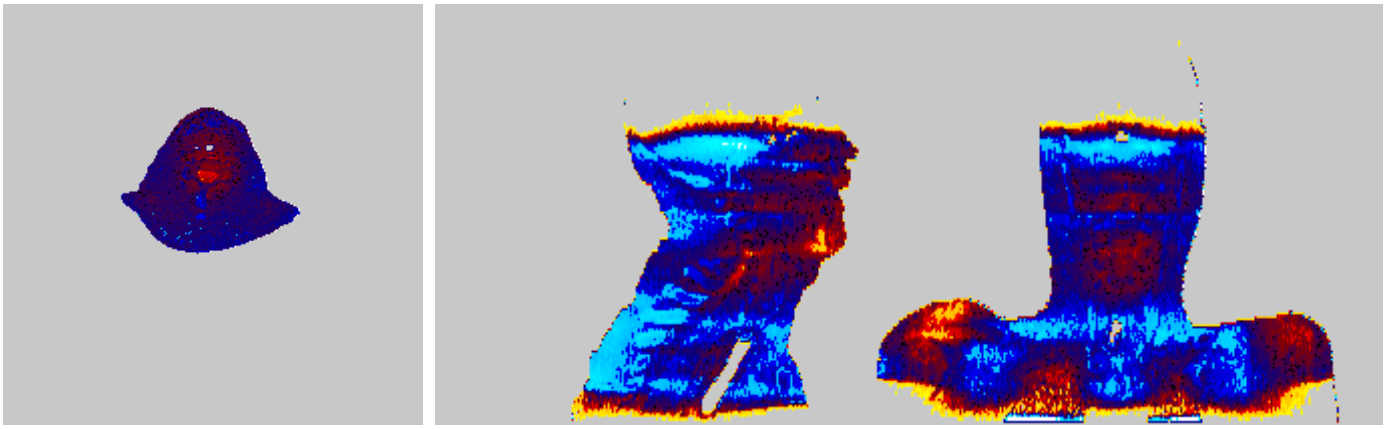

(g) *trans., Pat. B,* $\frac{D_{PB}-D_{MC}}{D_{MC}}$ **(h)** *sag., Pat. B,* $\frac{D_{PB}-D_{MC}}{D_{MC}}$ **(i)** *front., Pat. B,* $\frac{D_{PB}-D_{MC}}{D_{MC}}$

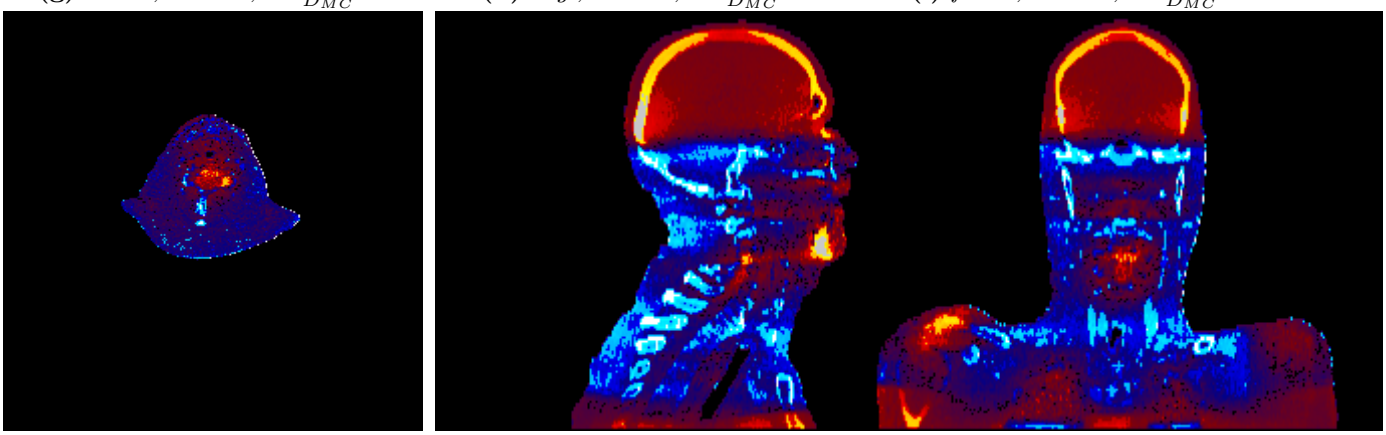

(j) *trans., Pat. B,* $D_{PB} - D_{MC}$ **(k)** *sag., Pat. B,* $D_{PB} - D_{MC}$ **(l)** *front., Pat. B,* $D_{PB} - D_{MC}$

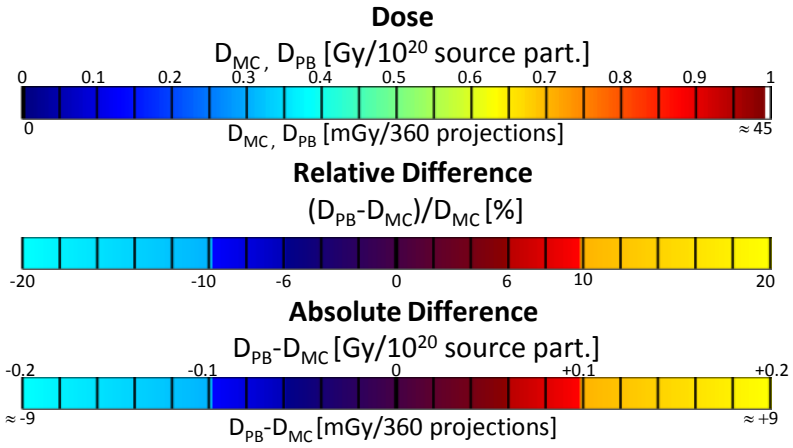

(m) *Colorscale for single projection image*

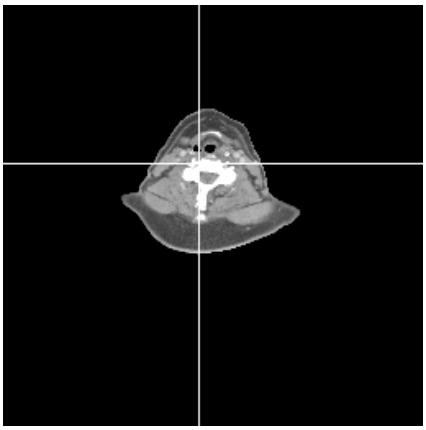

(n) *trans., Pat. B, CT*

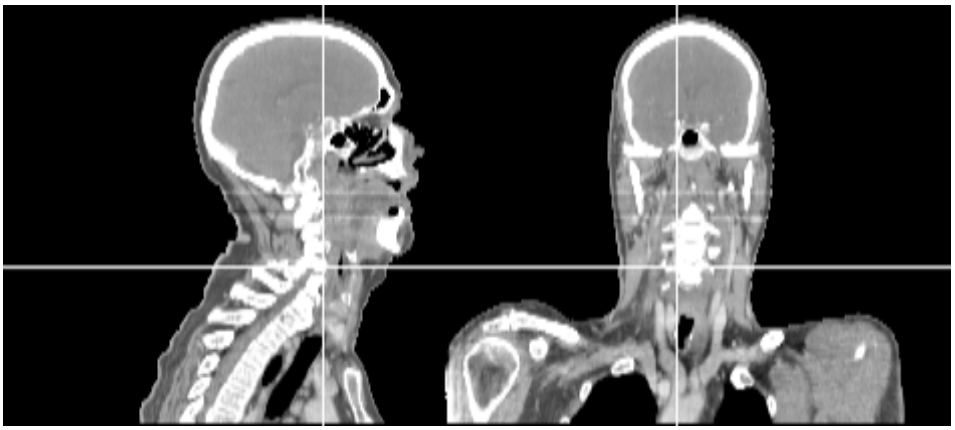

(o) *sag., Pat. B, CT* **(p)** *front., Pat. B, CT*

Figure B.9.: *Isocentric slices for Pat. B for a cone beam CT acquisition (360° tube rotation). The slice positions are marked in the CT-slices shown in (n) - (p).*

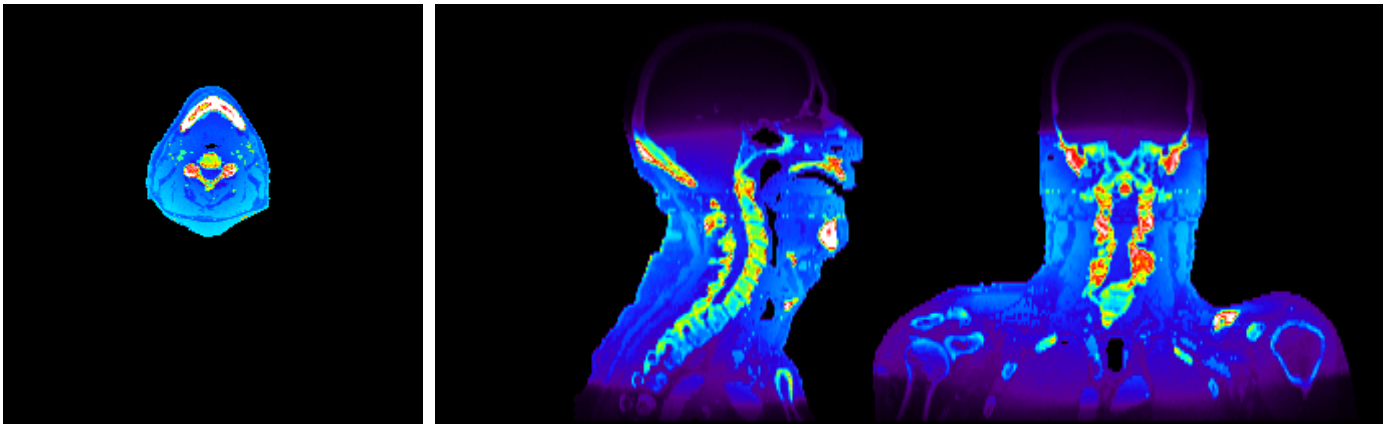

(a) *trans., Pat. B,* D_{MC} **(b)** *sag., Pat. B,* D_{MC} **(c)** *front., Pat. B,* D_{MC}

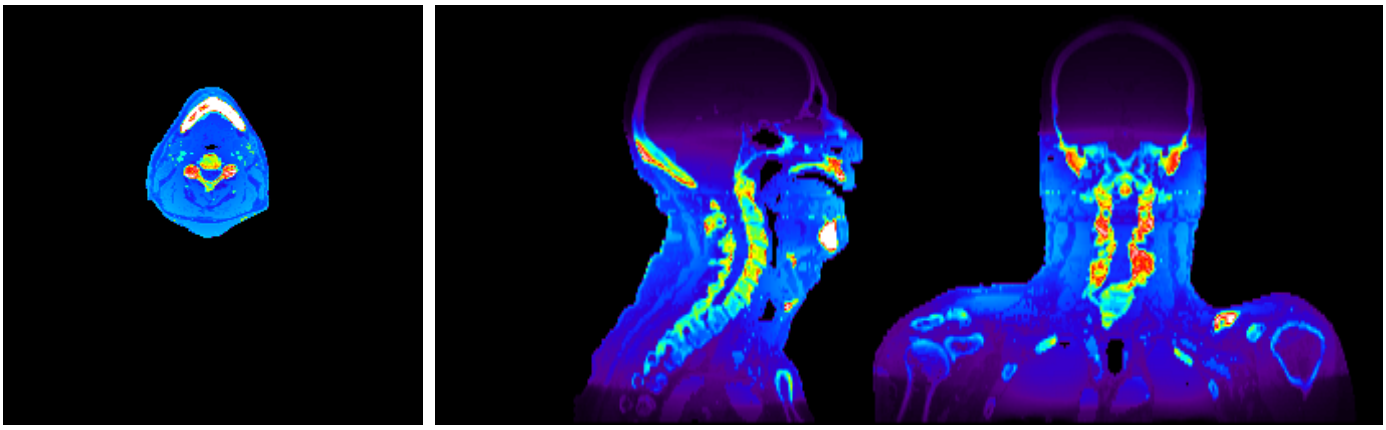

(d) *trans., Pat. B,* D_{PB} **(e)** *sag., Pat. B,* D_{PB} **(f)** *front., Pat. B,* D_{PB}

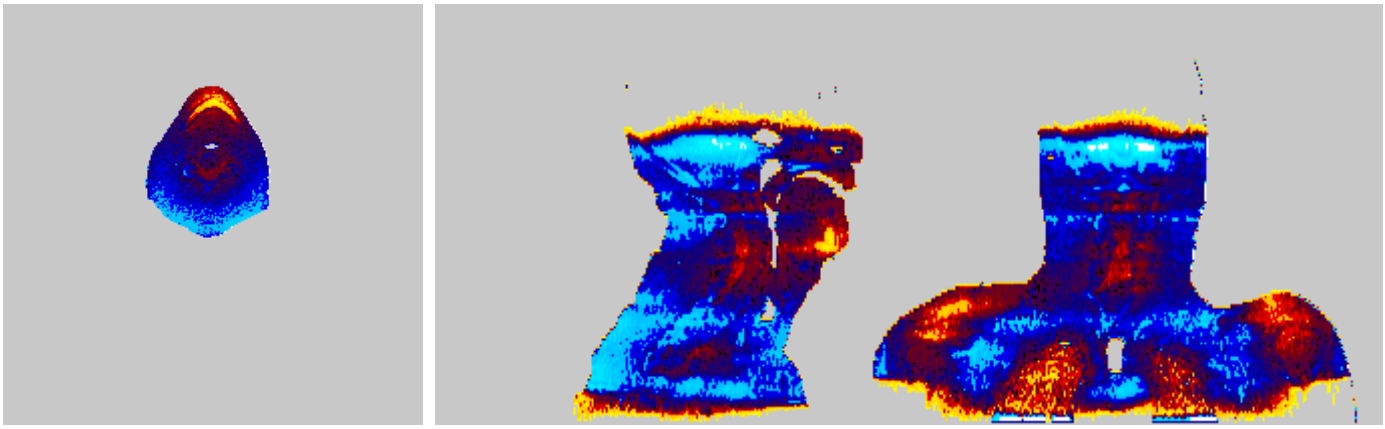

(g) *trans., Pat. B,* $\frac{D_{PB}-D_{MC}}{D_{MC}}$ **(h)** *sag., Pat. B,* $\frac{D_{PB}-D_{MC}}{D_{MC}}$ **(i)** *front., Pat. B,* $\frac{D_{PB}-D_{MC}}{D_{MC}}$

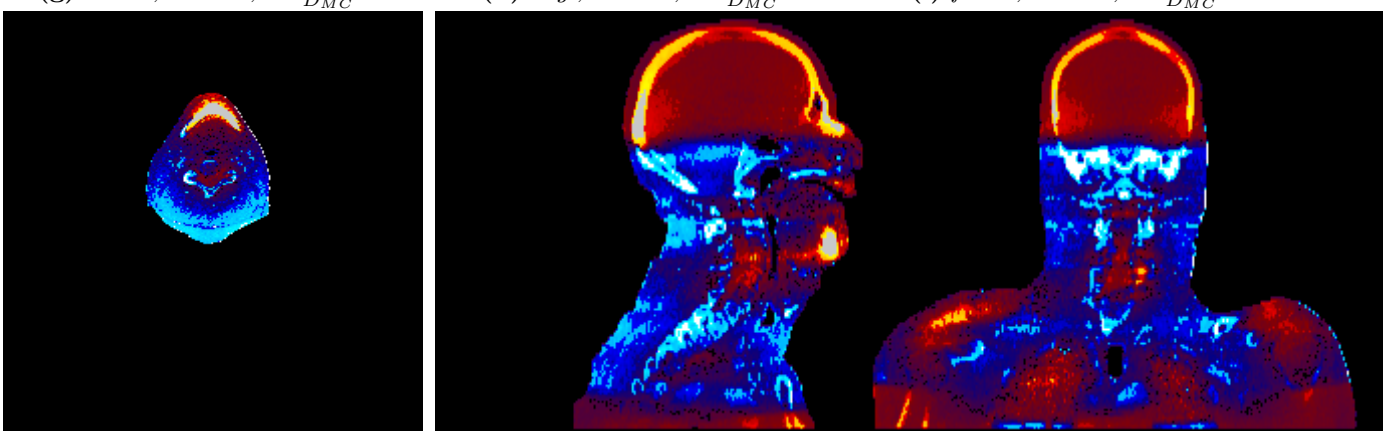

(j) *trans., Pat. B,* $D_{PB} - D_{MC}$ **(k)** *sag., Pat. B,* $D_{PB} - D_{MC}$ **(l)** *front., Pat. B,* $D_{PB} - D_{MC}$

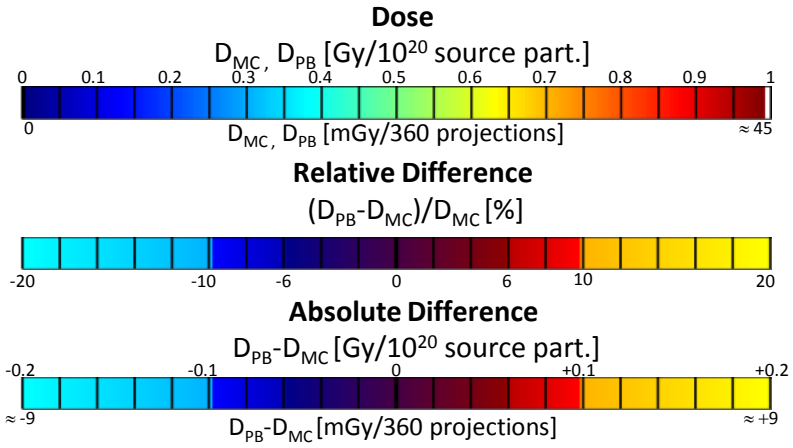

(m) *Colorscale for single projection image*

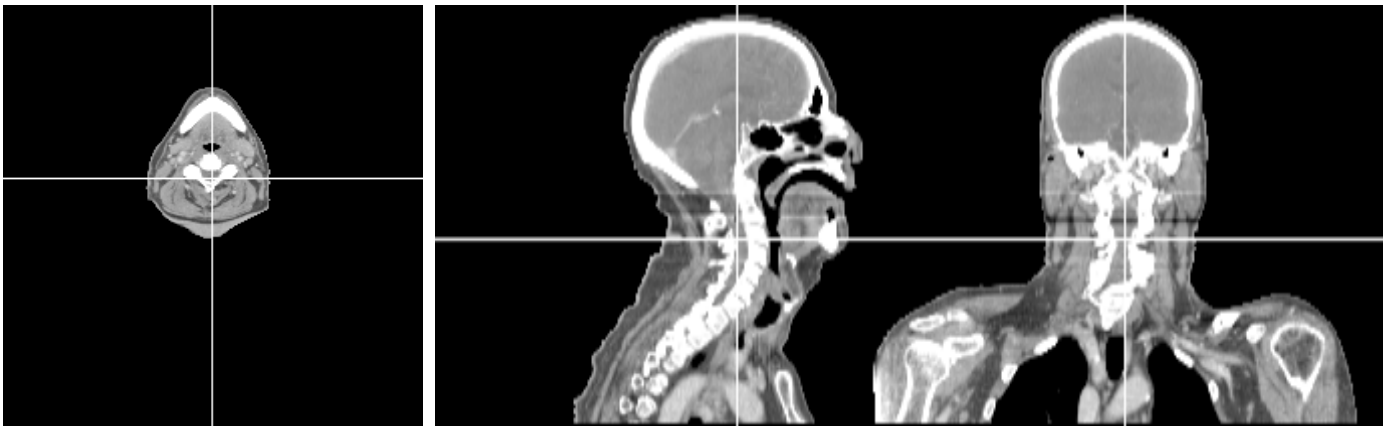

(n) *trans., Pat. B, CT* **(o)** *sag., Pat. B, CT* **(p)** *front., Pat. B, CT*

Figure B.10.: *Central slices for Pat. B for a cone beam CT acquisition (360° tube rotation). The slice positions are marked in the CT-slices shown in (n) - (p).*

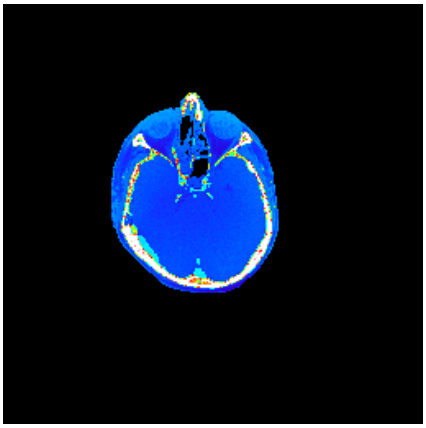

(a) *trans., Pat. C,* D_{MC}

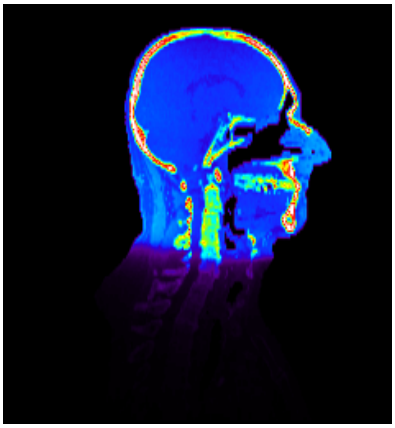

(b) *sag., Pat. C,* D_{MC}

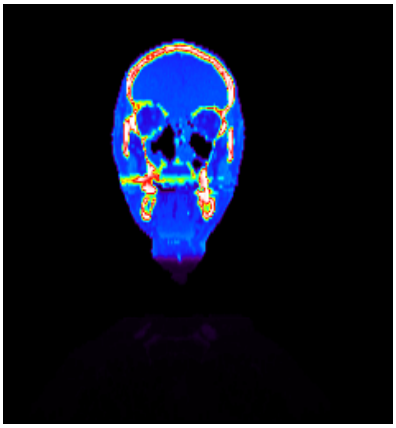

(c) *front., Pat. C,* D_{MC}

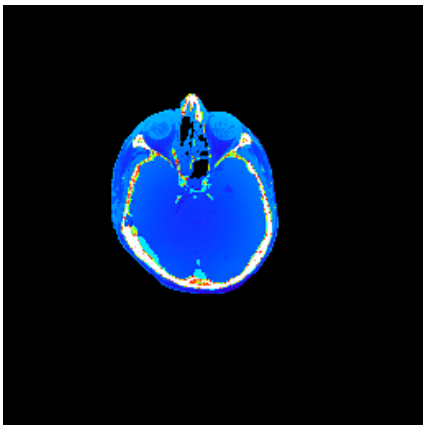

(d) *trans., Pat. C,* D_{PB}

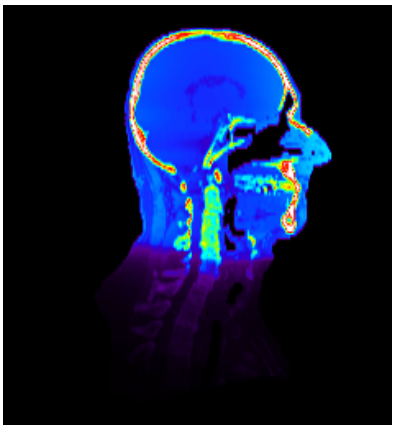

(e) *sag., Pat. C,* D_{PB}

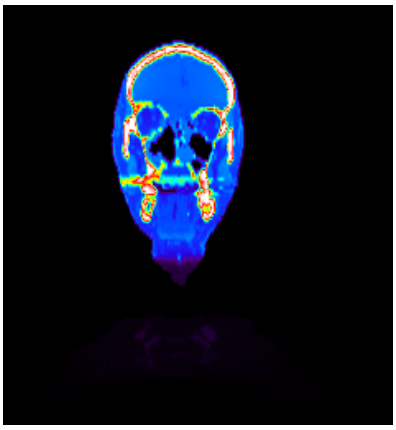

(f) *front., Pat. C,* D_{PB}

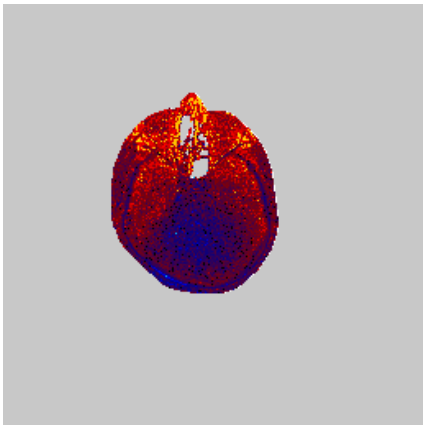

(g) *trans., Pat. C,* $\frac{D_{PB}-D_{MC}}{D_{MC}}$

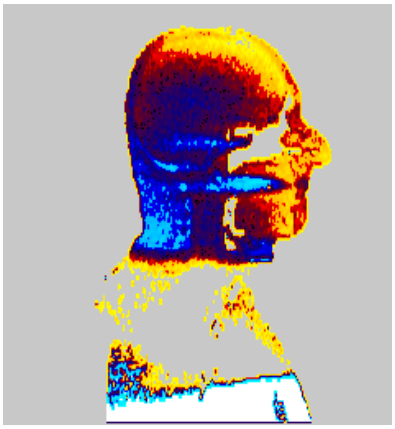

(h) *sag., Pat. C,* $\frac{D_{PB}-D_{MC}}{D_{MC}}$

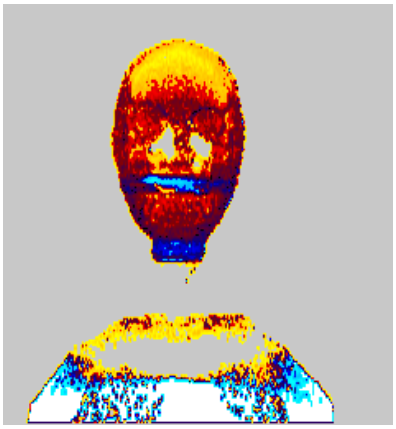

(i) *front., Pat. C,* $\frac{D_{PB}-D_{MC}}{D_{MC}}$

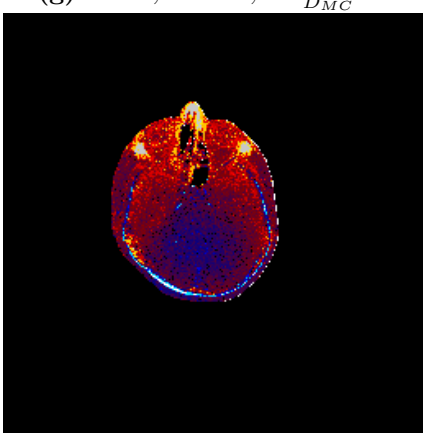

(j) *trans., Pat. C,* $D_{PB} - D_{MC}$

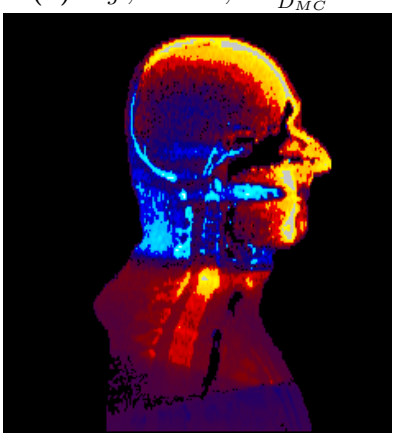

(k) *sag., Pat. C,* $D_{PB} - D_{MC}$

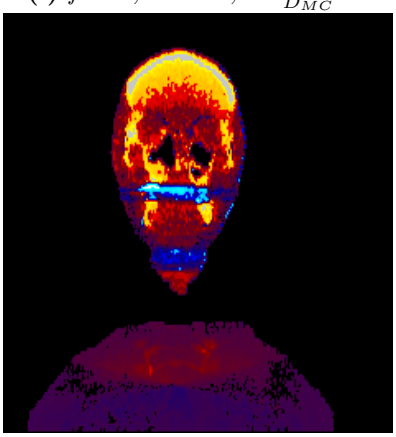

(l) *front., Pat. C,* $D_{PB} - D_{MC}$

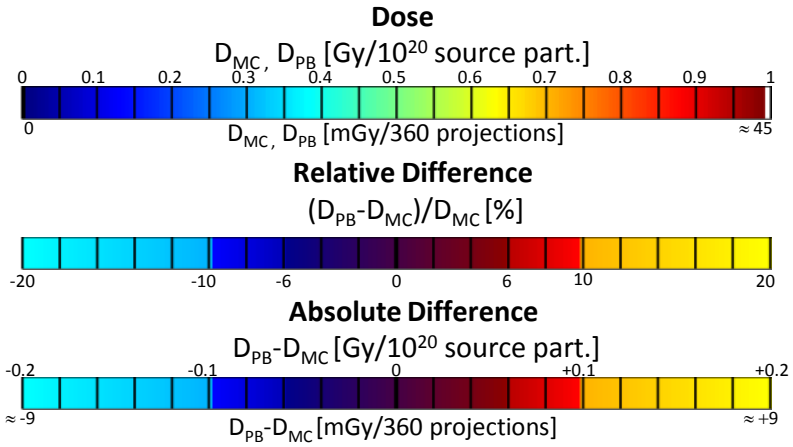

(m) *Colorscale for single projection image*

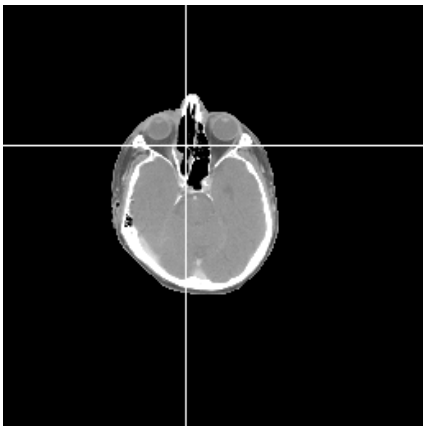

(n) *trans., Pat. C, CT*

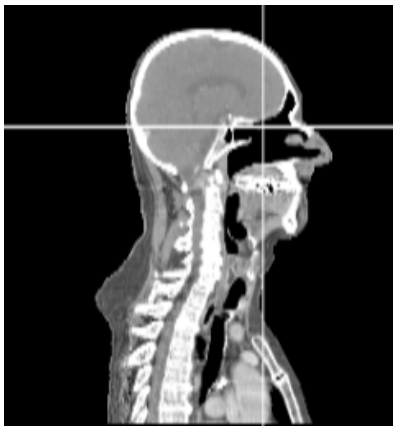

(o) *sag., Pat. C, CT*

(p) *front., Pat. C, CT*

Figure B.11.: *Isocentric slices for Pat. C for a cone beam CT acquisition (360° tube rotation). The slice positions are marked in the CT-slices shown in (n) - (p).*

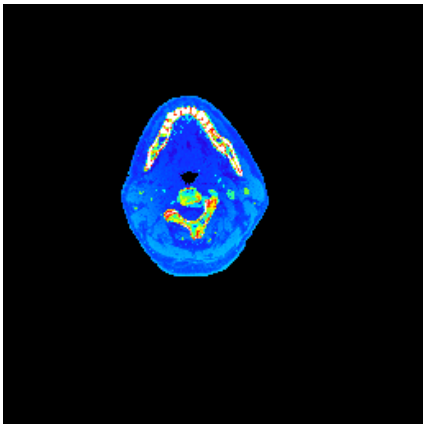

(a) *trans., Pat. C,* D_{MC}

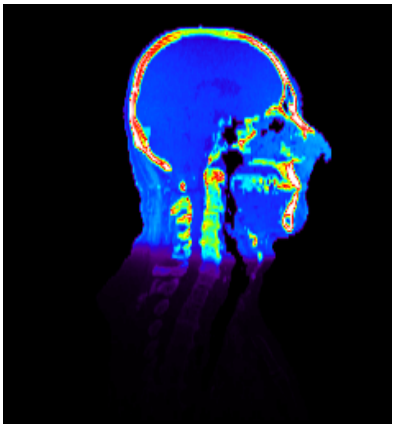

(b) *sag., Pat. C,* D_{MC}

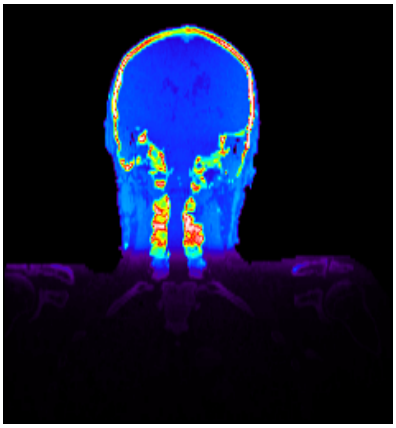

(c) *front., Pat. C,* D_{MC}

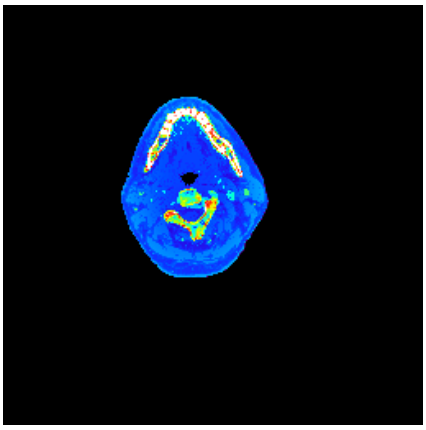

(d) *trans., Pat. C,* D_{PB}

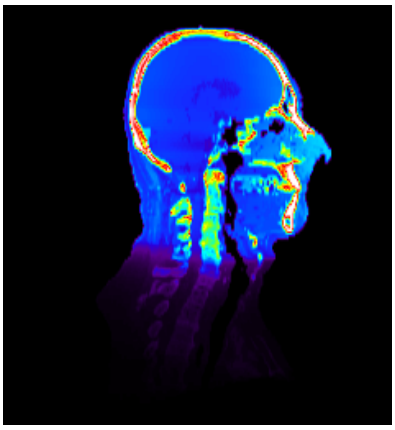

(e) *sag., Pat. C,* D_{PB}

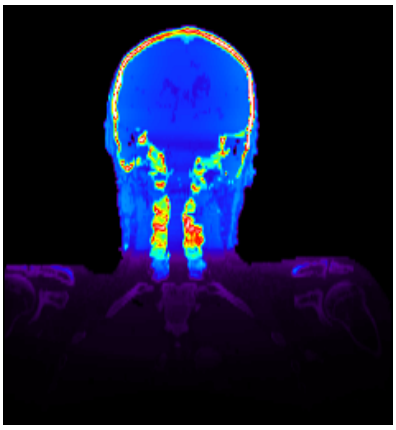

(f) *front., Pat. C,* D_{PB}

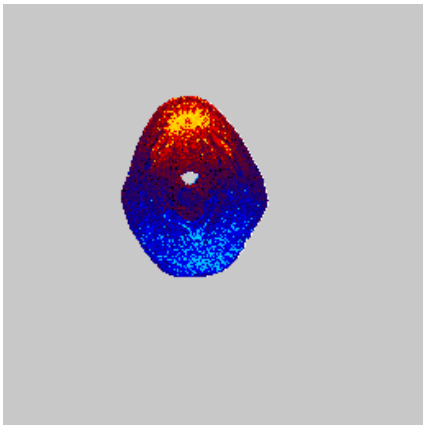

(g) *trans., Pat. C,* $\frac{D_{PB}-D_{MC}}{D_{MC}}$

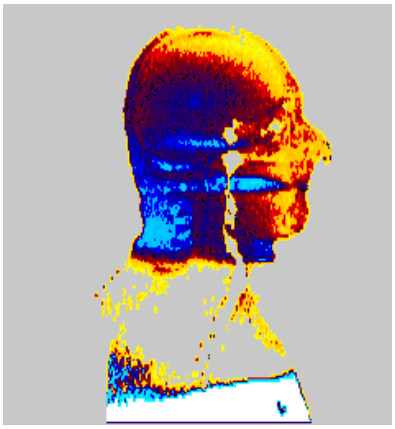

(h) *sag., Pat. C,* $\frac{D_{PB}-D_{MC}}{D_{MC}}$

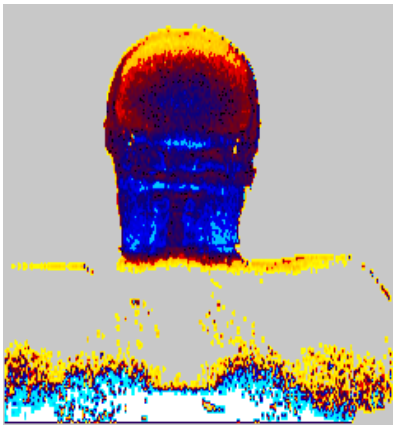

(i) *front., Pat. C,* $\frac{D_{PB}-D_{MC}}{D_{MC}}$

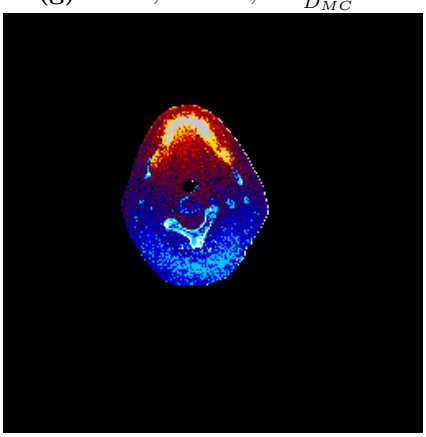

(j) *trans., Pat. C,* $D_{PB} - D_{MC}$

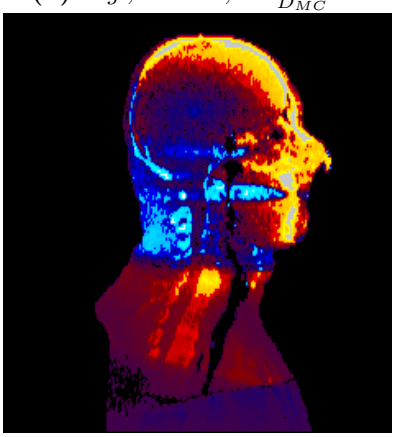

(k) *sag., Pat. C,* $D_{PB} - D_{MC}$

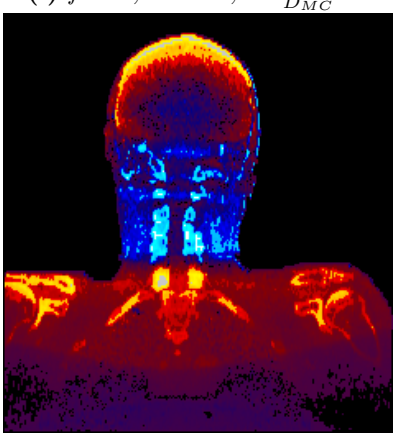

(l) *front., Pat. C,* $D_{PB} - D_{MC}$

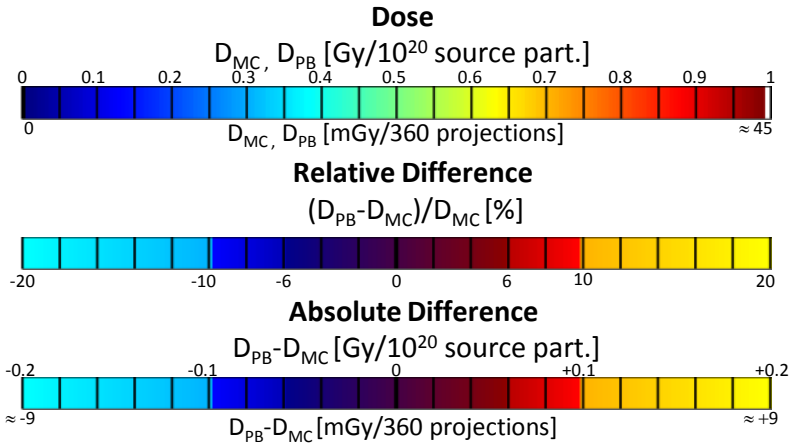

(m) *Colorscale for single projection image*

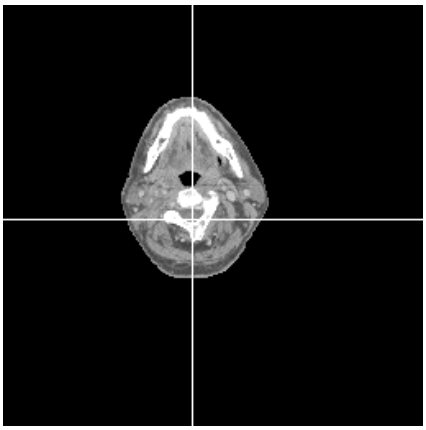

(n) *trans., Pat. C, CT*

(o) *sag., Pat. C, CT*

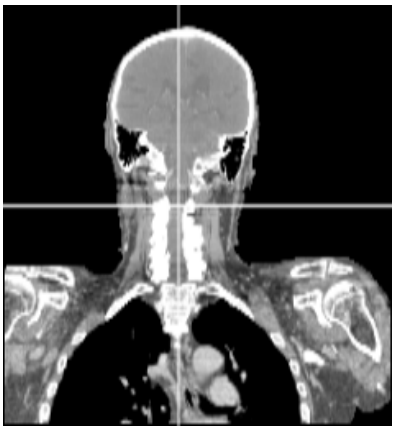

(p) *front., Pat. C, CT*

Figure B.12.: *Central slices for Pat. C for a cone beam CT acquisition (360° tube rotation). The slice positions are marked in the CT-slices shown in (n) - (p).*

B.3. Single beam - Pelvis

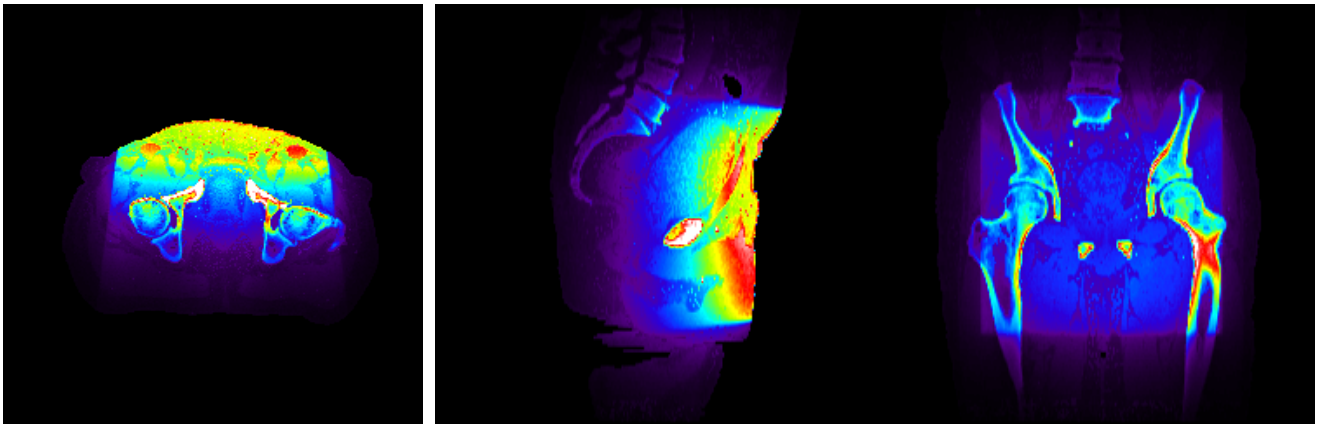

(a) *trans., Pat. D,* D_{MC} **(b)** *sag., Pat. D,* D_{MC} **(c)** *front., Pat. D,* D_{MC}

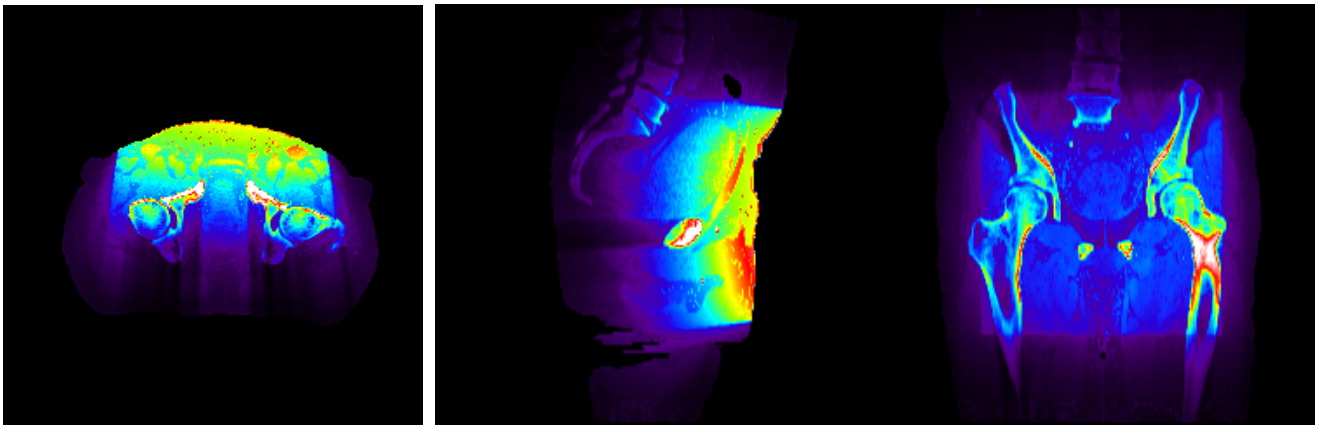

(d) *trans., Pat. D,* D_{PB} **(e)** *sag., Pat. D,* D_{PB} **(f)** *front., Pat. D,* D_{PB}

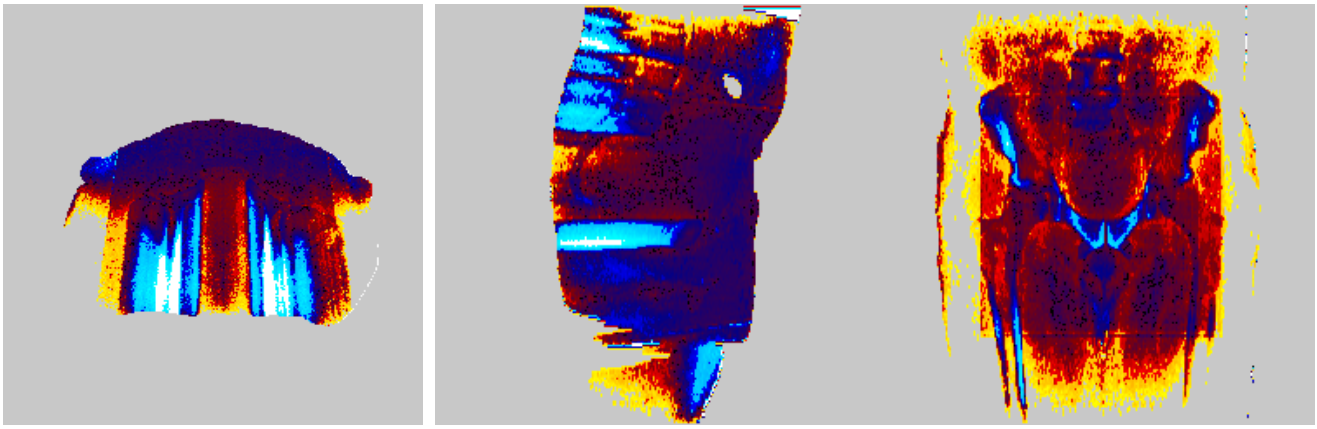

(g) *trans., Pat. D,* $\frac{D_{PB}-D_{MC}}{D_{MC}}$ **(h)** *sag., Pat. D,* $\frac{D_{PB}-D_{MC}}{D_{MC}}$ **(i)** *front., Pat. D,* $\frac{D_{PB}-D_{MC}}{D_{MC}}$

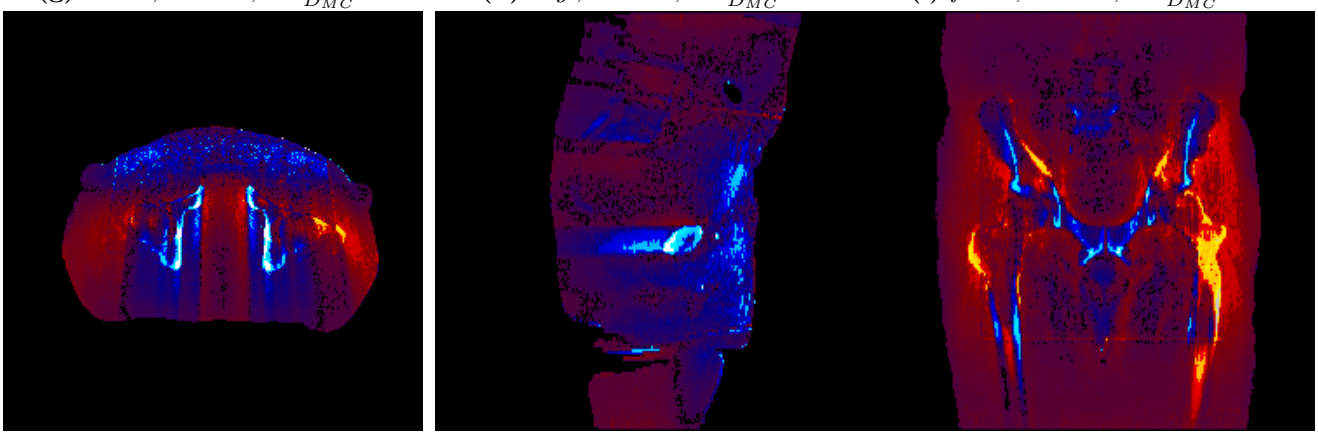

(j) *trans., Pat. D,* $D_{PB} - D_{MC}$ **(k)** *sag., Pat. D,* $D_{PB} - D_{MC}$ **(l)** *front., Pat. D,* $D_{PB} - D_{MC}$

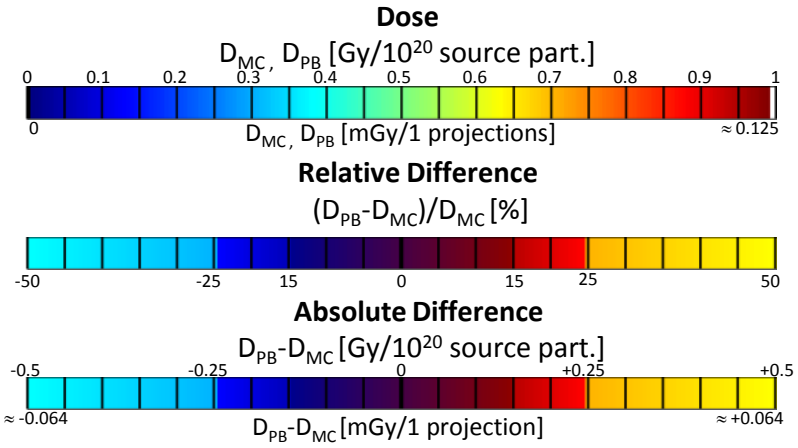

(m) *Colorscale for single projection image*

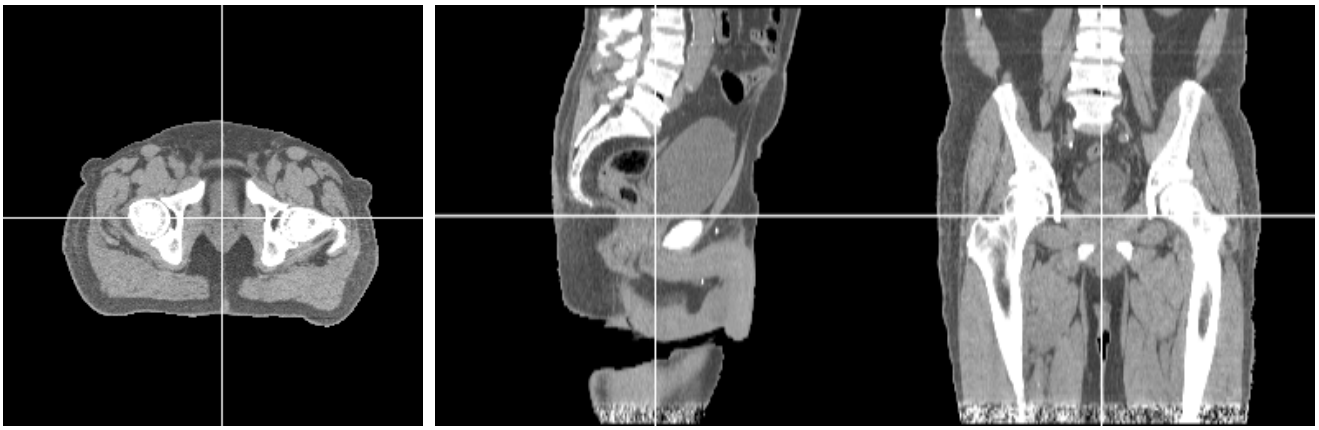

(n) *trans., Pat. D, CT* **(o)** *sag., Pat. D, CT* **(p)** *front., Pat. D, CT*

Figure B.13.: *Isocentric slices for Pat. D for a single beam at 0°. The slice positions are marked in the CT-slices shown in (n) - (p).*

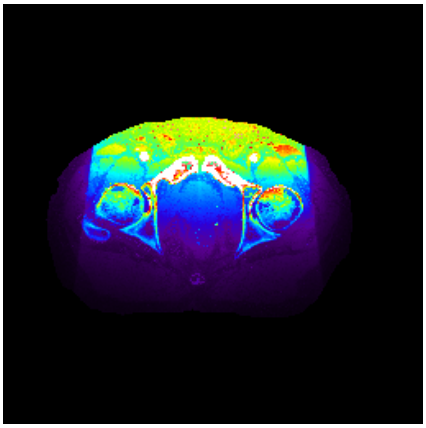

(a) *trans., Pat. E,* D_{MC}

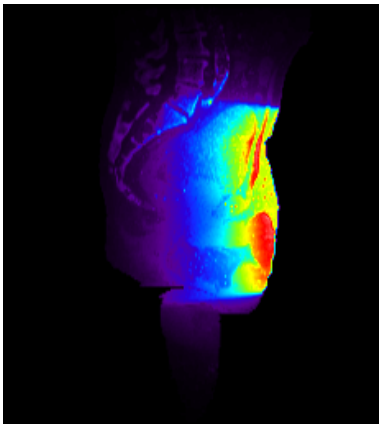

(b) *sag., Pat. E,* D_{MC}

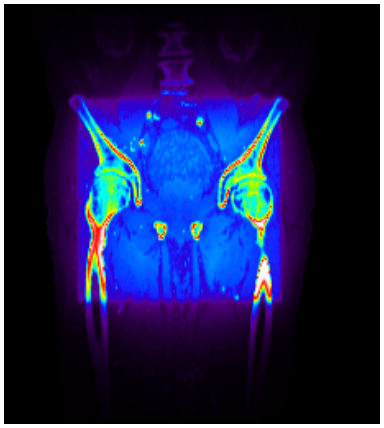

(c) *front., Pat. E,* D_{MC}

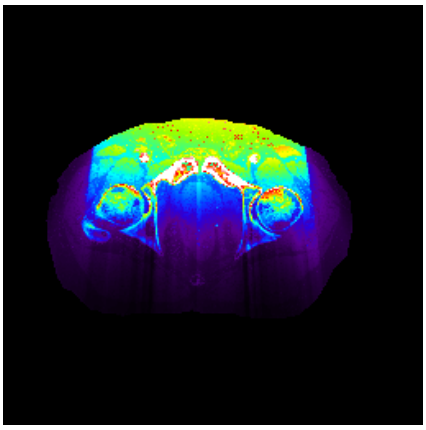

(d) *trans., Pat. E,* D_{PB}

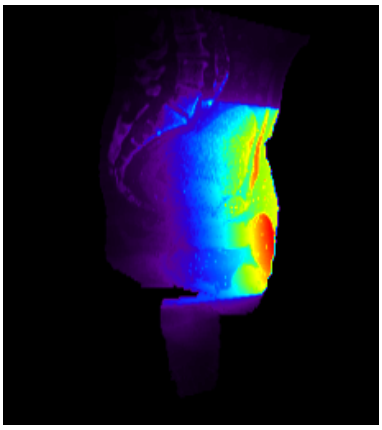

(e) *sag., Pat. E,* D_{PB}

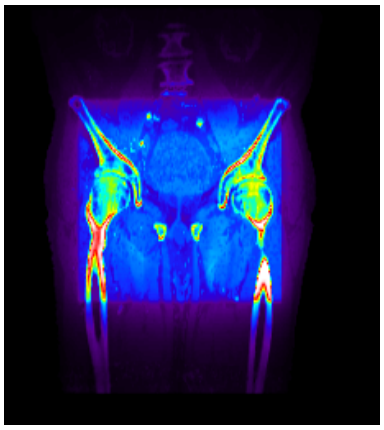

(f) *front., Pat. E,* D_{PB}

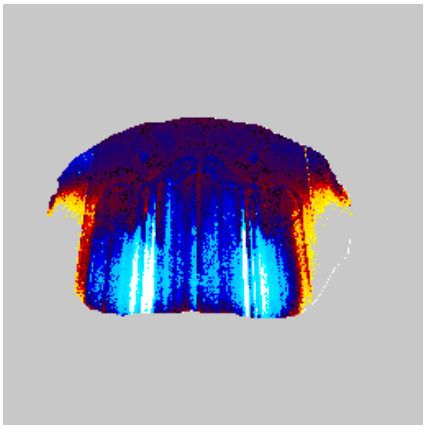

(g) *trans., Pat. E,* $\frac{D_{PB}-D_{MC}}{D_{MC}}$

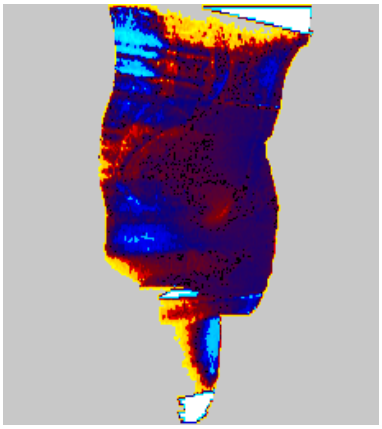

(h) *sag., Pat. E,* $\frac{D_{PB}-D_{MC}}{D_{MC}}$

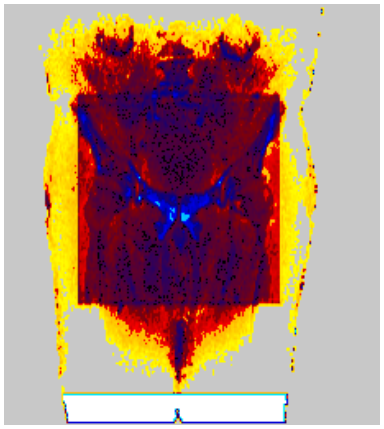

(i) *front., Pat. E,* $\frac{D_{PB}-D_{MC}}{D_{MC}}$

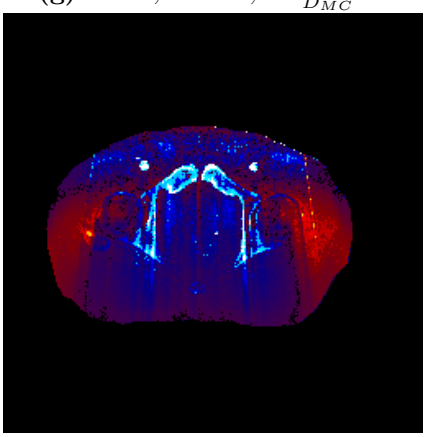

(j) *trans., Pat. E,* $D_{PB} - D_{MC}$

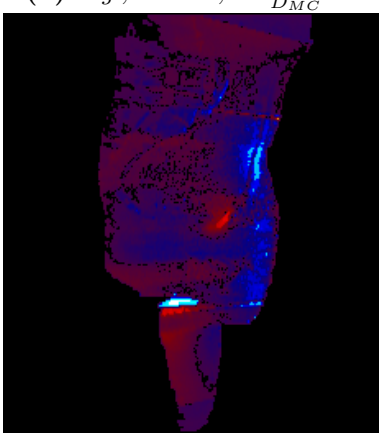

(k) *sag., Pat. E,* $D_{PB} - D_{MC}$

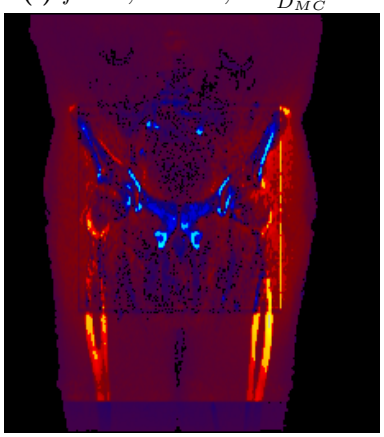

(l) *front., Pat. E,* $D_{PB} - D_{MC}$

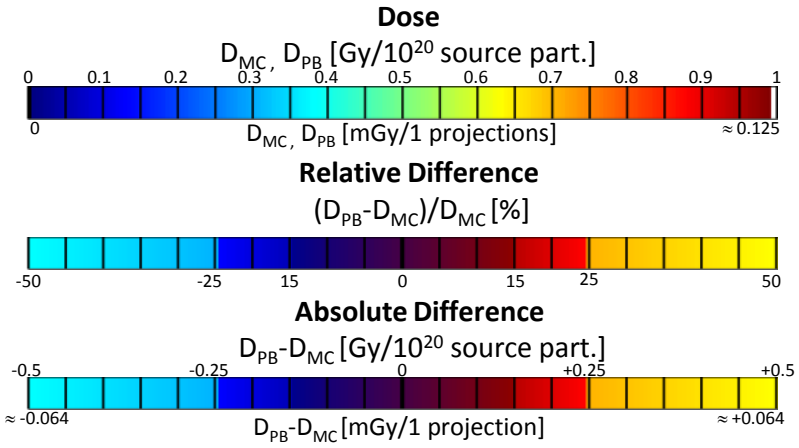

(m) *Colorscale for single projection image*

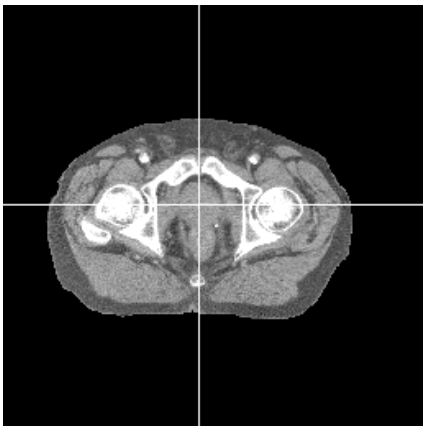

(n) *trans., Pat. E, CT*

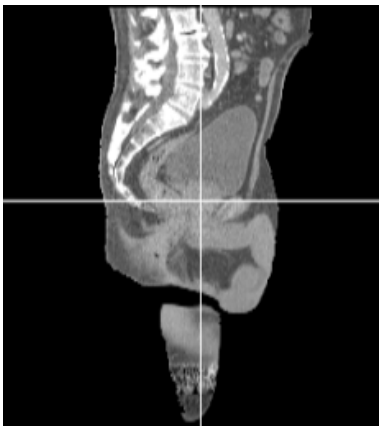

(o) *sag., Pat. E, CT*

(p) *front., Pat. E, CT*

Figure B.14.: *Isocentric slices for Pat. E for a single beam at 0°. The slice positions are marked in the CT-slices shown in (n) - (p).*

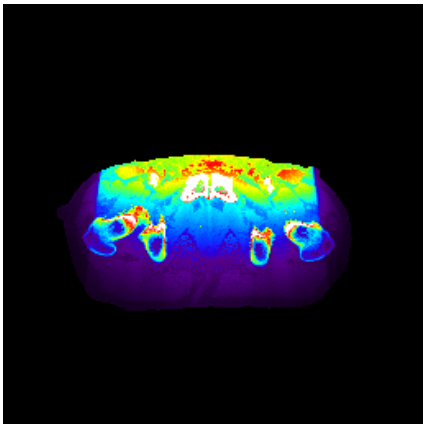

(a) *trans., Pat. F,* D_{MC}

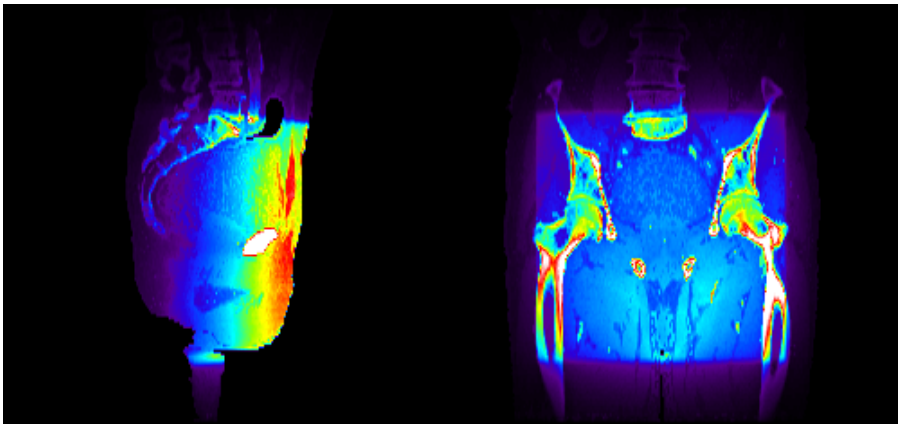

(b) *sag., Pat. F,* D_{MC} **(c)** *front., Pat. F,* D_{MC}

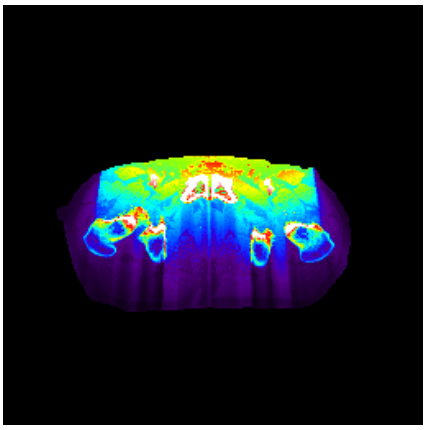

(d) *trans., Pat. F,* D_{PB}

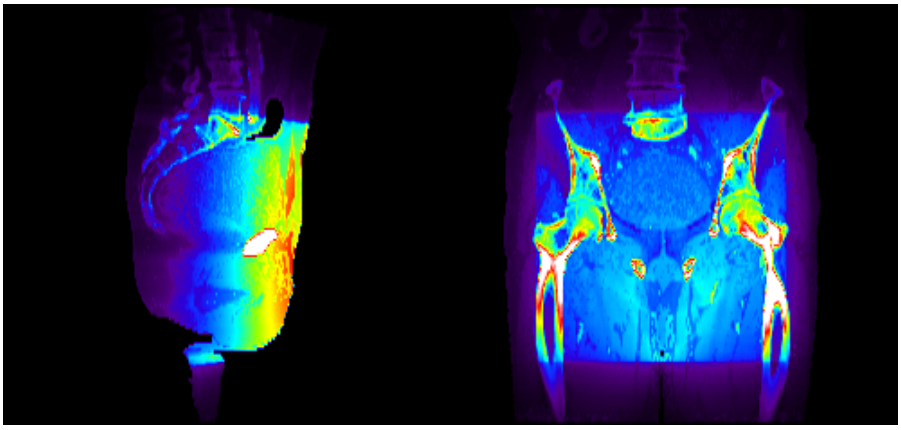

(e) *sag., Pat. F,* D_{PB} **(f)** *front., Pat. F,* D_{PB}

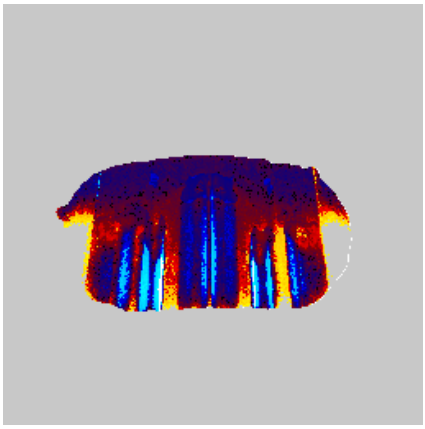

(g) *trans., Pat. F,* $\frac{D_{PB}-D_{MC}}{D_{MC}}$

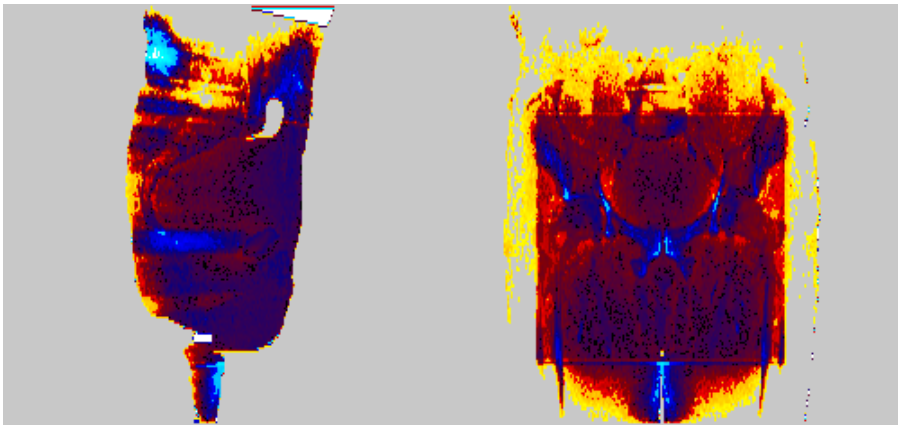

(h) *sag., Pat. F,* $\frac{D_{PB}-D_{MC}}{D_{MC}}$ **(i)** *front., Pat. F,* $\frac{D_{PB}-D_{MC}}{D_{MC}}$

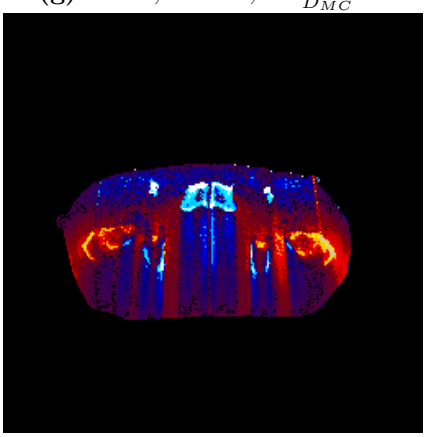

(j) *trans., Pat. F,* $D_{PB} - D_{MC}$

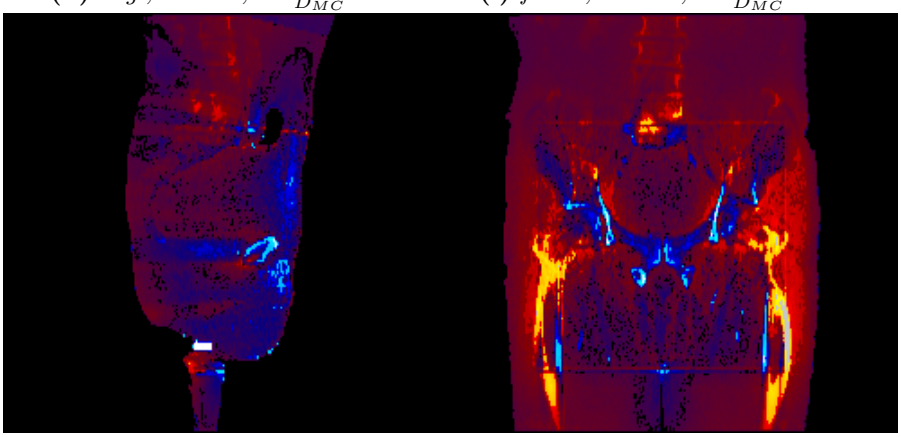

(k) *sag., Pat. F,* $D_{PB} - D_{MC}$ **(l)** *front., Pat. F,* $D_{PB} - D_{MC}$

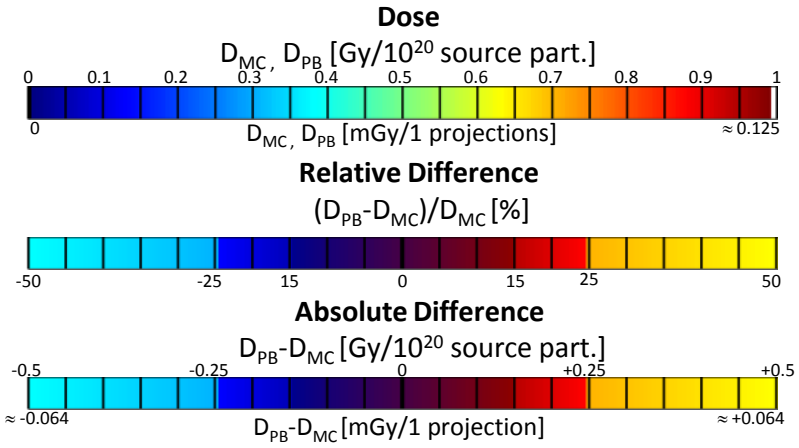

(m) *Colorscale for single projection image*

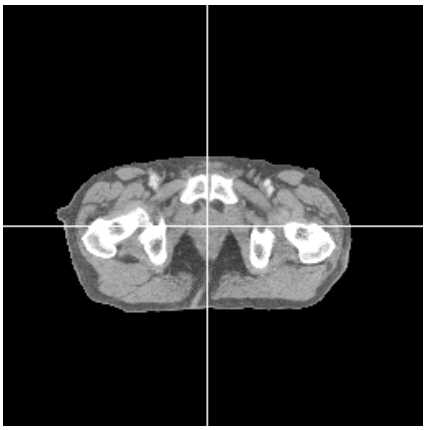

(n) *trans., Pat. F, CT*

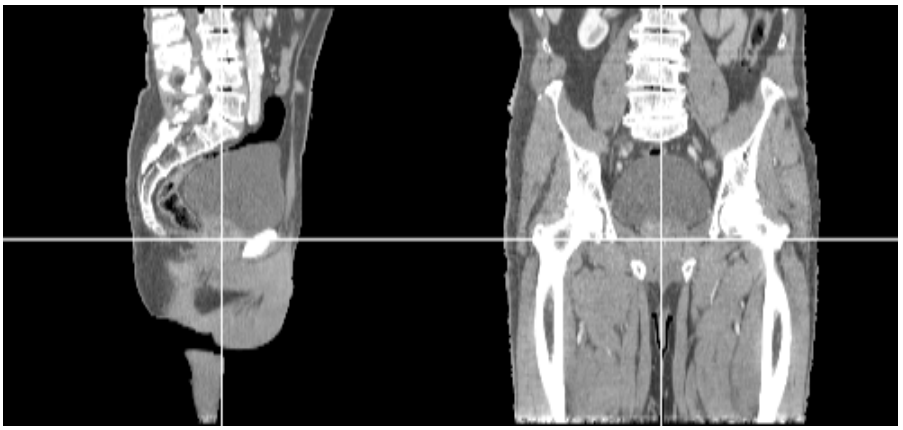

(o) *sag., Pat. F, CT* **(p)** *front., Pat. F, CT*

Figure B.15.: *Isocentric slices for Pat. F for a single beam at 0°. The slice positions are marked in the CT-slices shown in (n) - (p).*

B.4. Cone beam CT - Pelvis

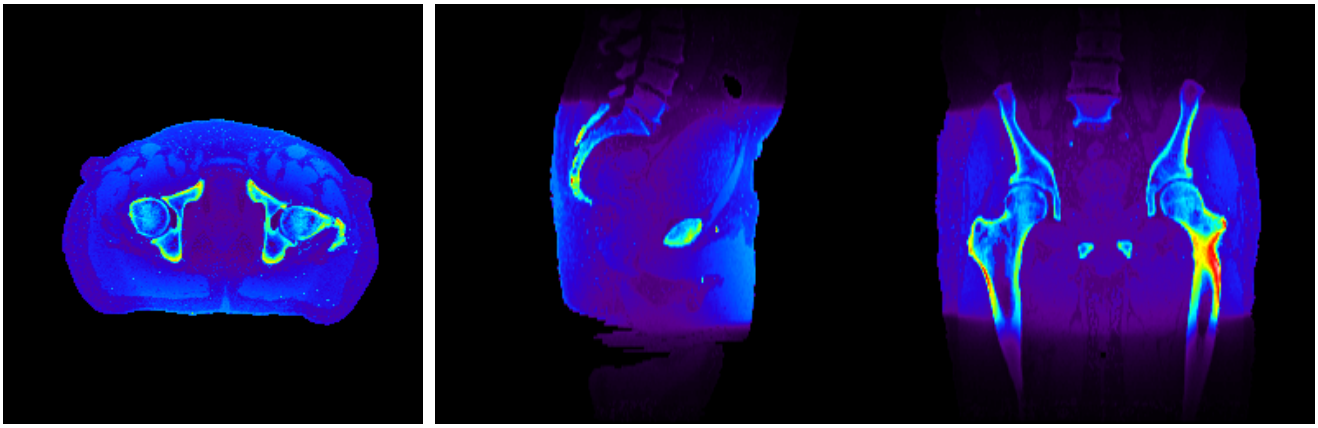

(a) *trans., Pat. D,* D_{MC} **(b)** *sag., Pat. D,* D_{MC} **(c)** *front., Pat. D,* D_{MC}

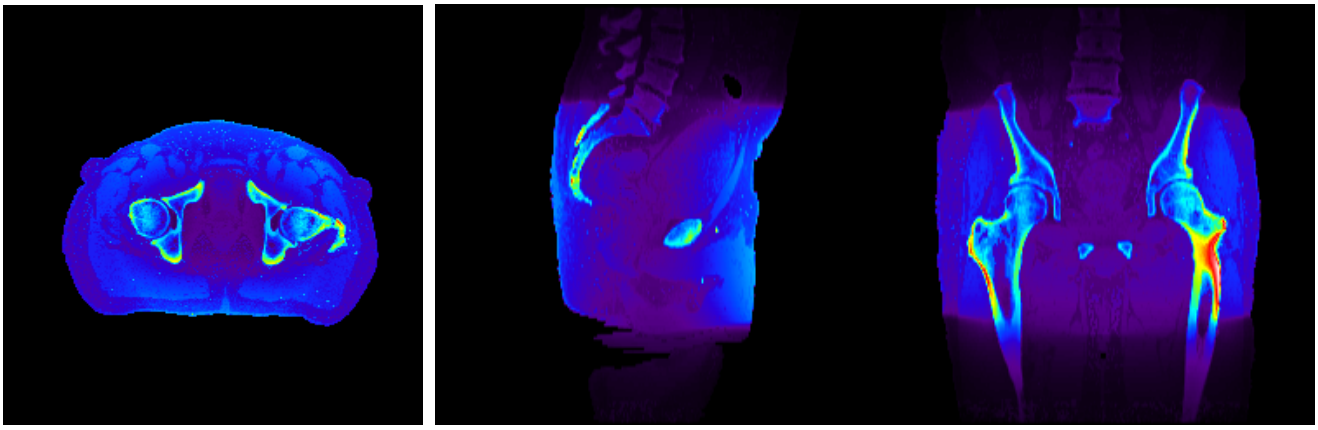

(d) *trans., Pat. D,* D_{PB} **(e)** *sag., Pat. D,* D_{PB} **(f)** *front., Pat. D,* D_{PB}

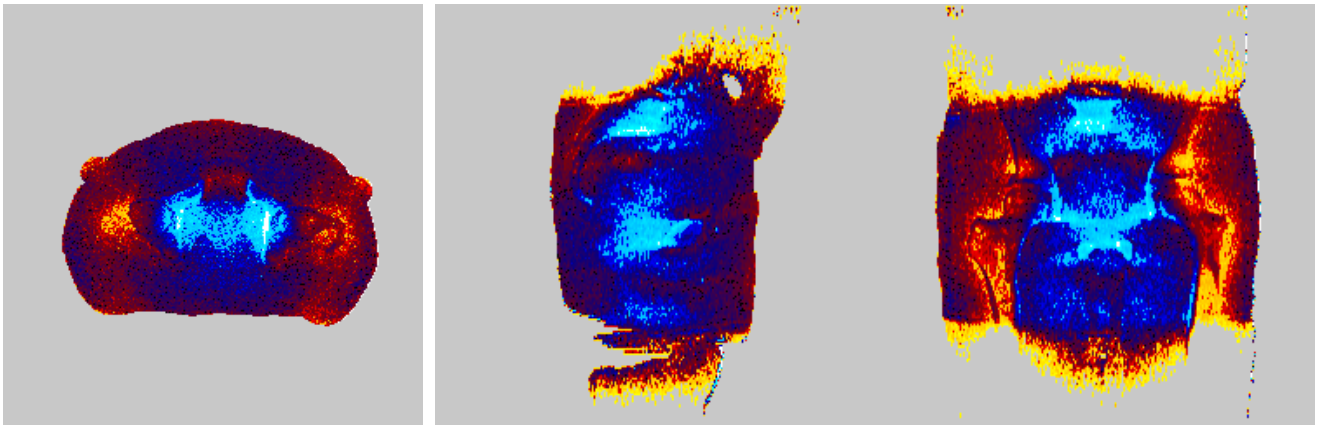

(g) *trans., Pat. D,* $\frac{D_{PB}-D_{MC}}{D_{MC}}$ **(h)** *sag., Pat. D,* $\frac{D_{PB}-D_{MC}}{D_{MC}}$ **(i)** *front., Pat. D,* $\frac{D_{PB}-D_{MC}}{D_{MC}}$

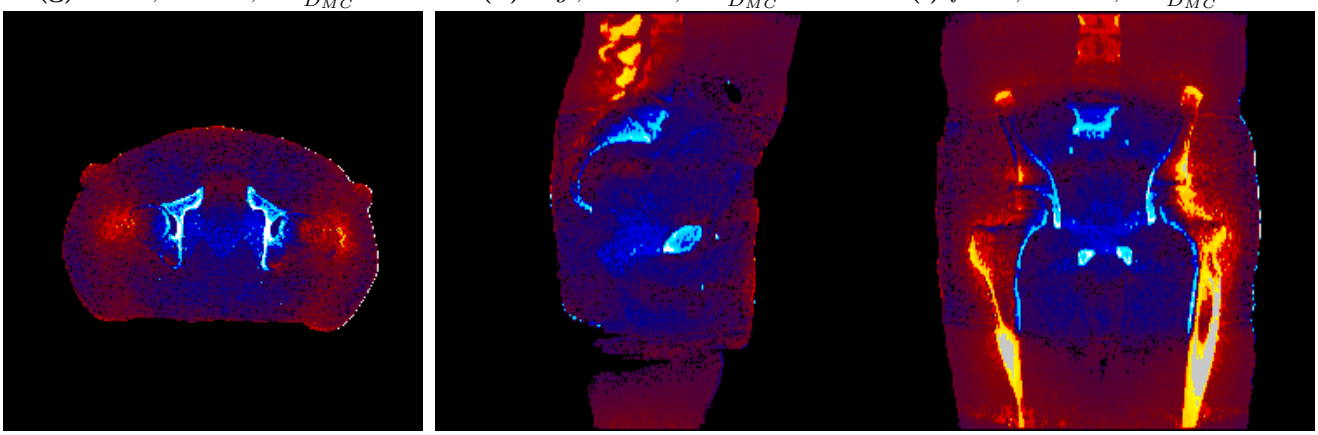

(j) *trans., Pat. D,* $D_{PB} - D_{MC}$ **(k)** *sag., Pat. D,* $D_{PB} - D_{MC}$ **(l)** *front., Pat. D,* $D_{PB} - D_{MC}$

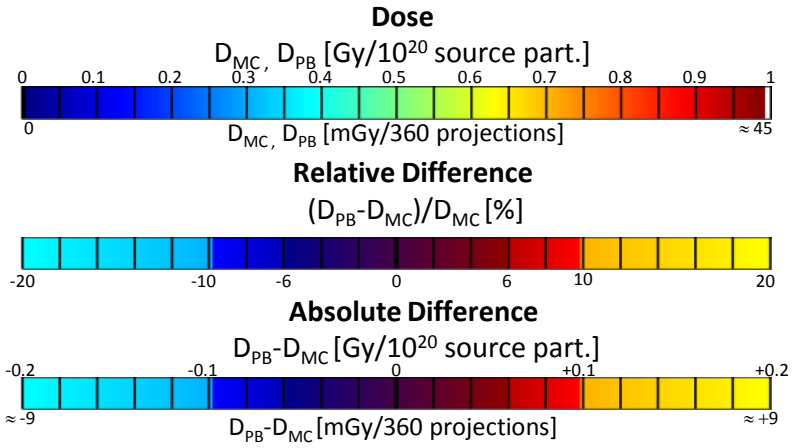

(m) *Colorscale for single projection image*

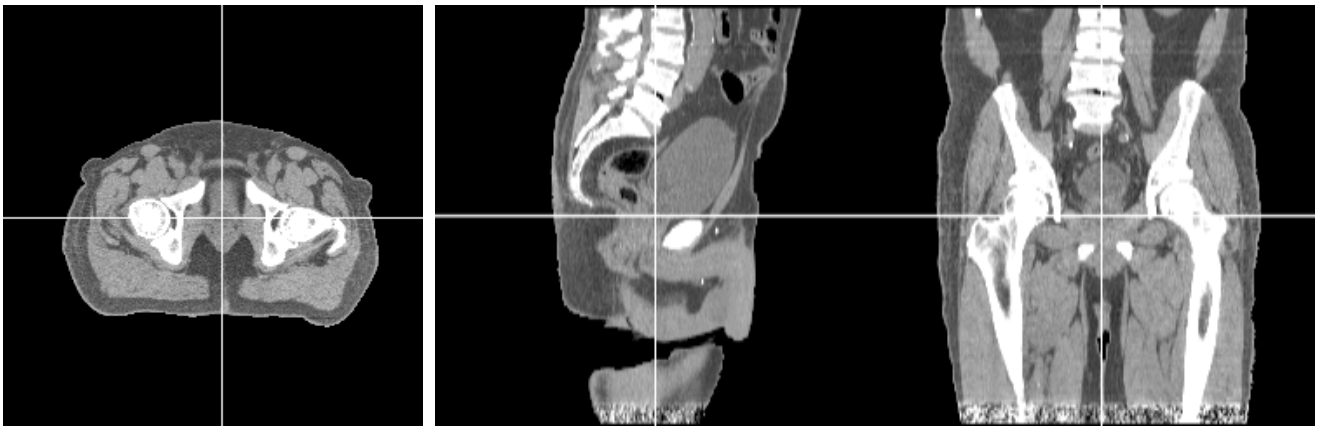

(n) *trans., Pat. D, CT* **(o)** *sag., Pat. D, CT* **(p)** *front., Pat. D, CT*

Figure B.16.: *Isocentric slices for Pat. D for a cone beam CT acquisition (360° tube rotation). The slice positions are marked in the CT-slices shown in (n) - (p).*

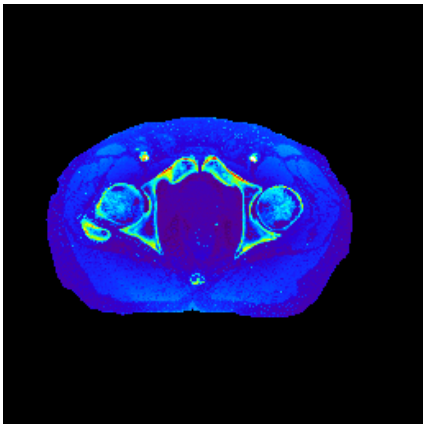

(a) *trans., Pat. E,* D_{MC}

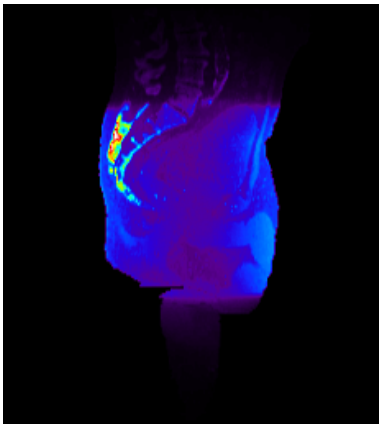

(b) *sag., Pat. E,* D_{MC}

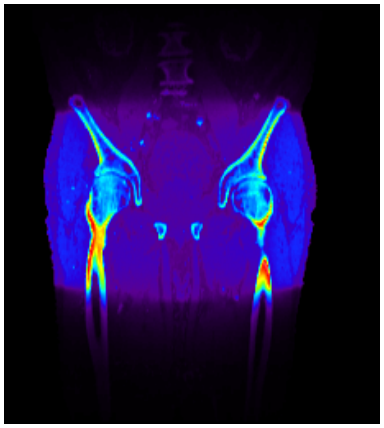

(c) *front., Pat. E,* D_{MC}

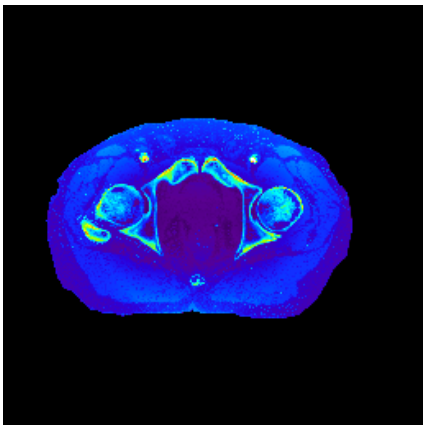

(d) *trans., Pat. E,* D_{PB}

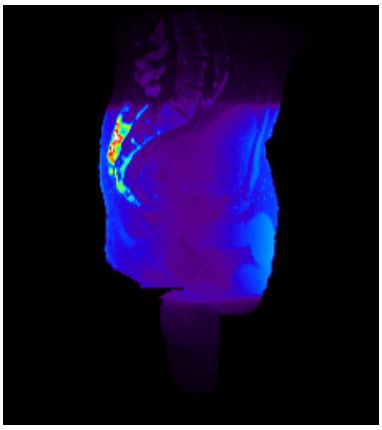

(e) *sag., Pat. E,* D_{PB}

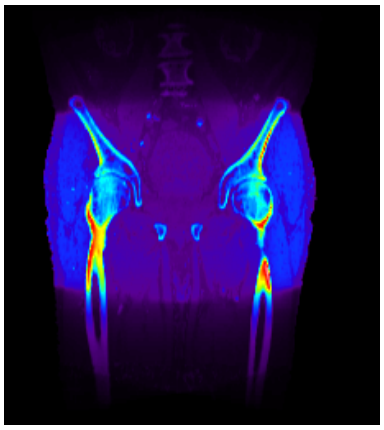

(f) *front., Pat. E,* D_{PB}

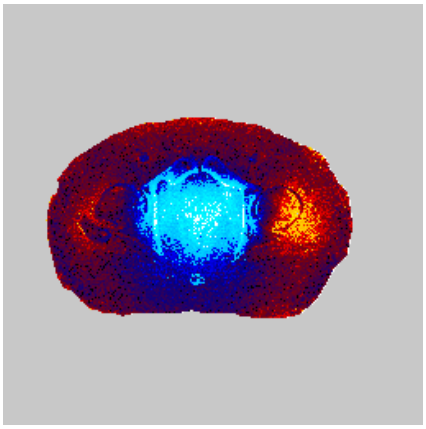

(g) *trans., Pat. E,* $\frac{D_{PB}-D_{MC}}{D_{MC}}$

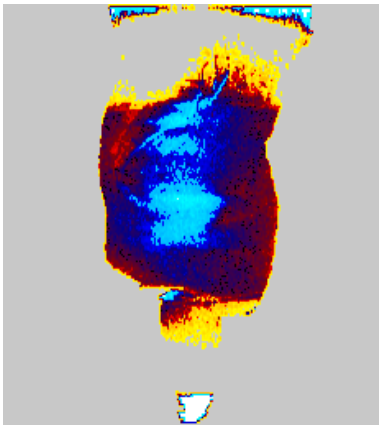

(h) *sag., Pat. E,* $\frac{D_{PB}-D_{MC}}{D_{MC}}$

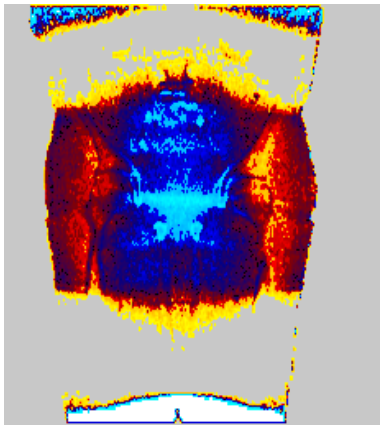

(i) *front., Pat. E,* $\frac{D_{PB}-D_{MC}}{D_{MC}}$

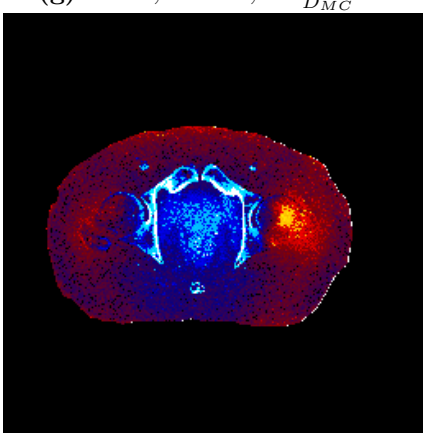

(j) *trans., Pat. E,* $D_{PB} - D_{MC}$

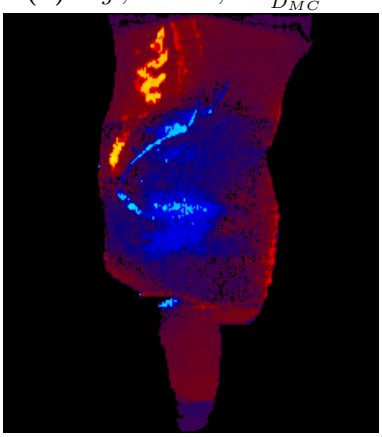

(k) *sag., Pat. E,* $D_{PB} - D_{MC}$

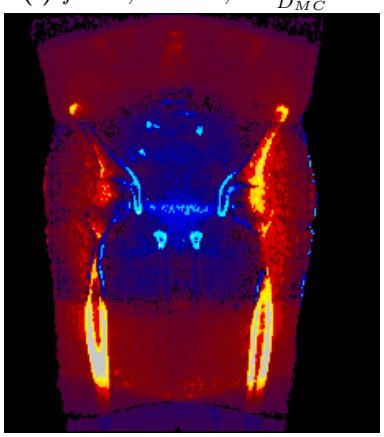

(l) *front., Pat. E,* $D_{PB} - D_{MC}$

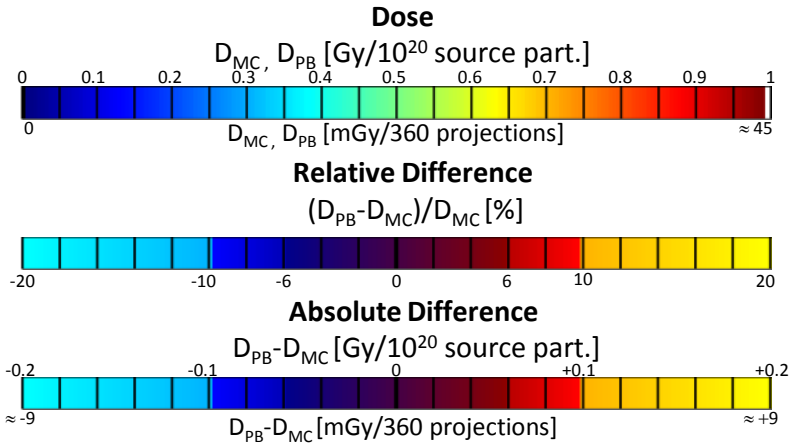

(m) *Colorscale for single projection image*

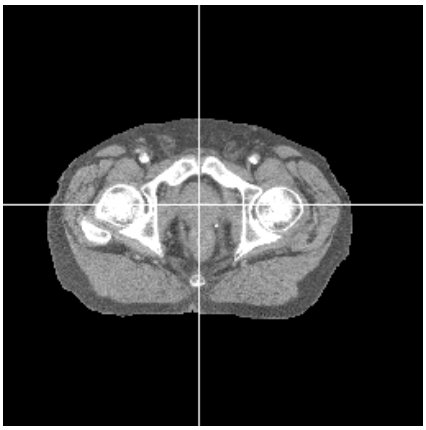

(n) *trans., Pat. E, CT*

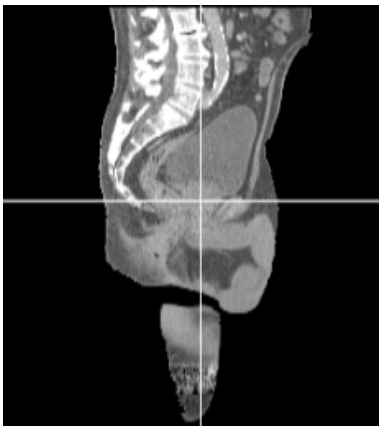

(o) *sag., Pat. E, CT*

(p) *front., Pat. E, CT*

Figure B.17.: *Isocentric slices for Pat. E for a cone beam CT acquisition (360° tube rotation). The slice positions are marked in the CT-slices shown in (n) - (p).*

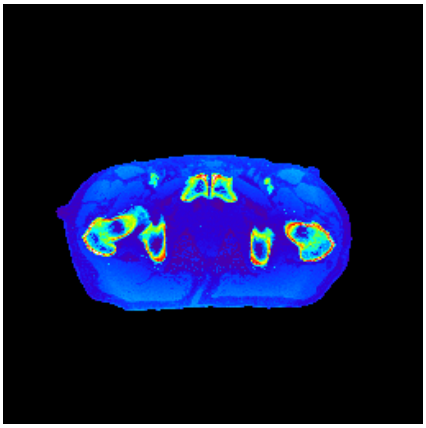

(a) *trans., Pat. F,* D_{MC}

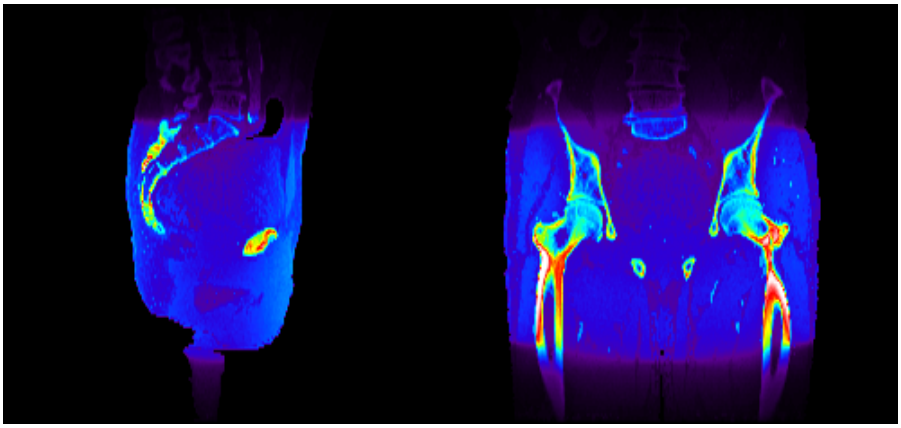

(b) *sag., Pat. F,* D_{MC} **(c)** *front., Pat. F,* D_{MC}

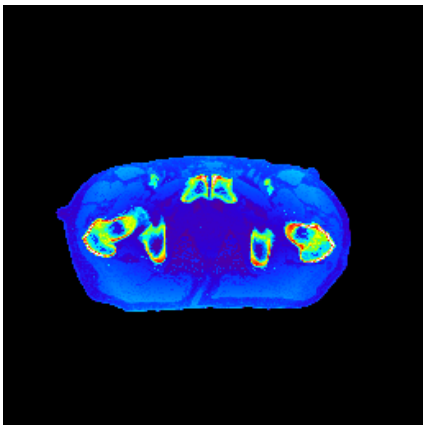

(d) *trans., Pat. F,* D_{PB}

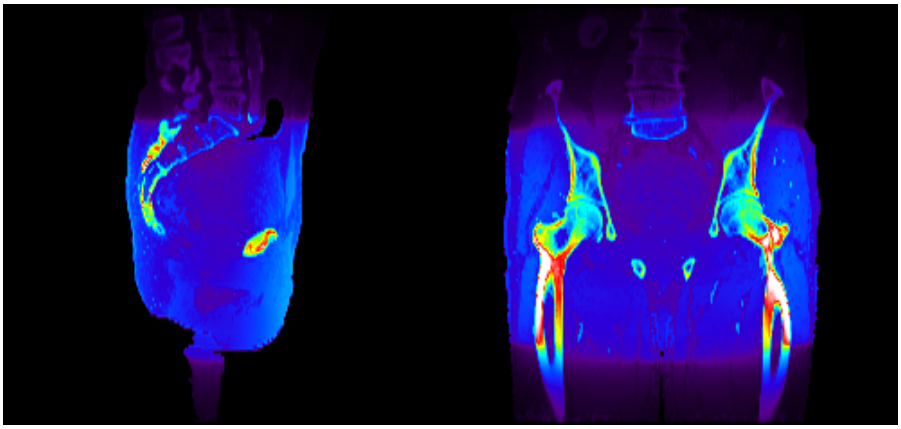

(e) *sag., Pat. F,* D_{PB} **(f)** *front., Pat. F,* D_{PB}

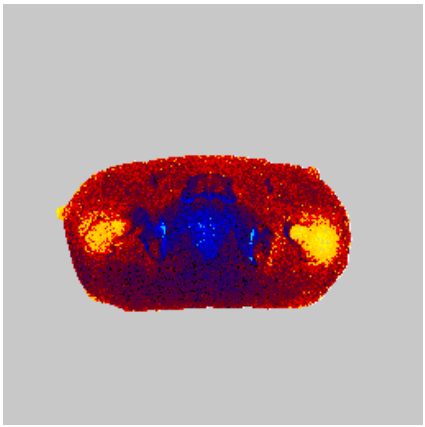

(g) *trans., Pat. F,* $\frac{D_{PB}-D_{MC}}{D_{MC}}$

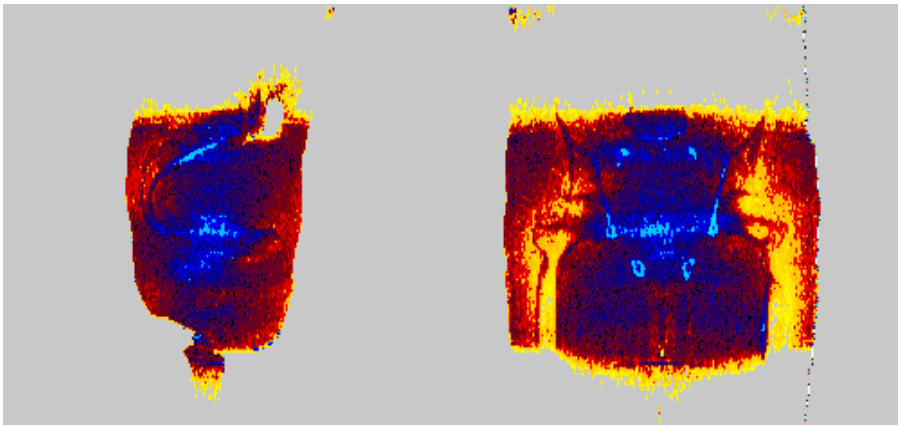

(h) *sag., Pat. F,* $\frac{D_{PB}-D_{MC}}{D_{MC}}$ **(i)** *front., Pat. F,* $\frac{D_{PB}-D_{MC}}{D_{MC}}$

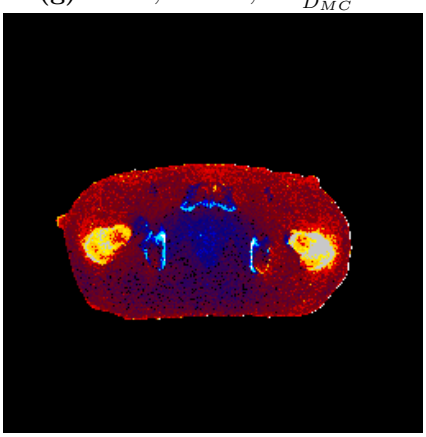

(j) *trans., Pat. F,* $D_{PB} - D_{MC}$

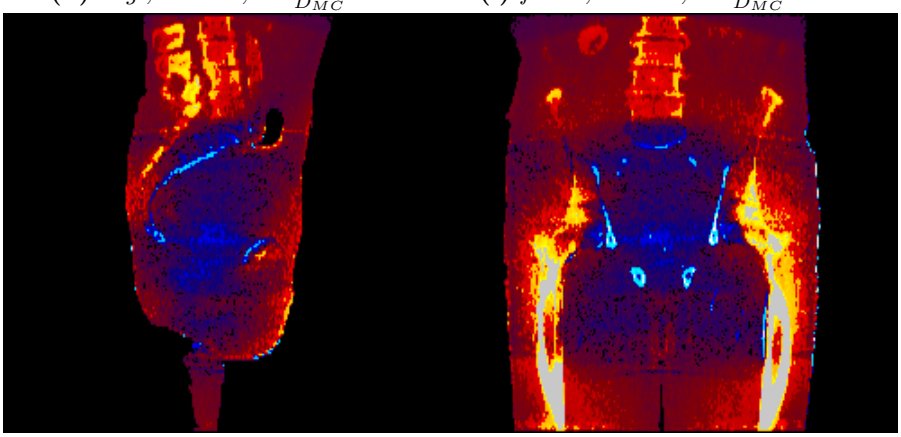

(k) *sag., Pat. F,* $D_{PB} - D_{MC}$ **(l)** *front., Pat. F,* $D_{PB} - D_{MC}$

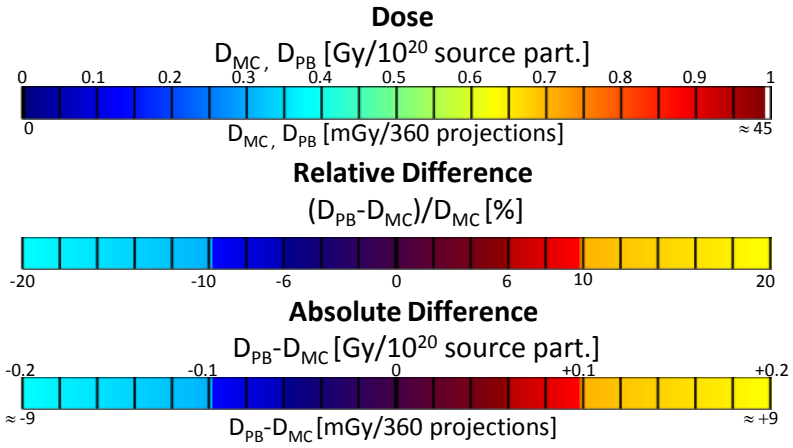

(m) *Colorscale for single projection image*

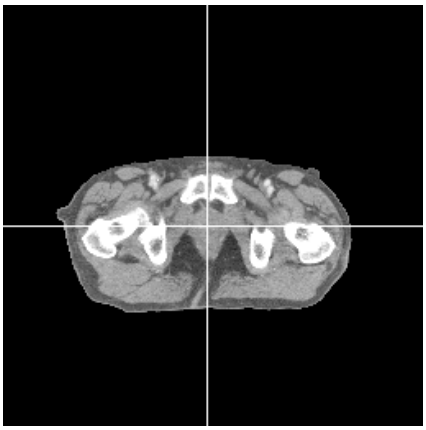

(n) *trans., Pat. F, CT*

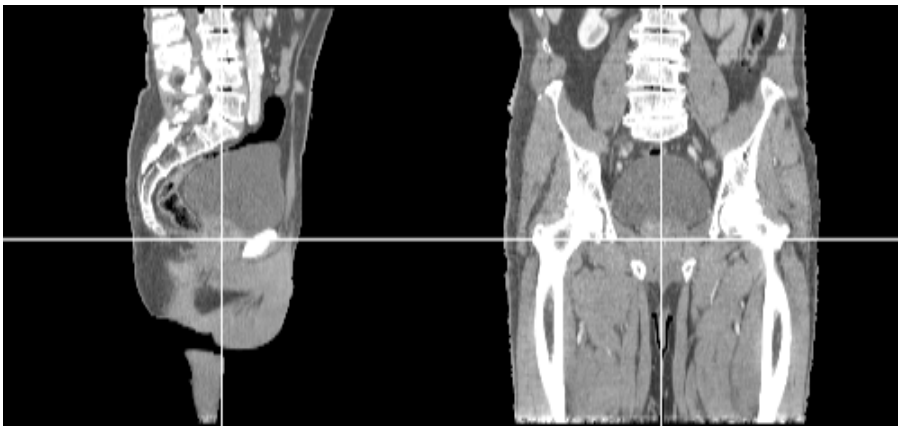

(o) *sag., Pat. F, CT* **(p)** *front., Pat. F, CT*

Figure B.18.: *Isocentric slices for Pat. F for a cone beam CT acquisition (360° tube rotation). The slice positions are marked in the CT-slices shown in (n) - (p).*

List of Figures

2.1. Elekta Synergy® and Varian Trilogy®: solutions for integrated IGRT. (Detail of Elekta press image [26] and detail of Varian press image [27]) . . . 3
2.2. Intrafractional tumor motion of a lung tumor . . . 4
2.3. Stereoscopic imaging in the Accuray Cyberknife Suite (Accuray press image [38]) . . . 6
2.4. Siemens ARTISTE^{TM}: solution for integrated IGRT (not yet commercially available) . . . 8

3.1. IEC coordinate system . . . 13
3.2. Phantom coordinate systems . . . 13
3.3. Patient coordinate systems . . . 14
3.4. Setup of a rotating anode X-ray tube and principle of the Heel effect . . . 15
3.5. Cross sections of an X-ray tube from a MV cone beam CT . . . 15
3.6. Photon Spectra for a 121kV X-ray tube and a 6MeV linear accelerator . . . 16
3.7. Photon production in a medical linear accelerator. (Figure shows a detail of a figure from [46]) . . . 16
3.8. Basic Principle of the Photoelectric and the Compton Effect . . . 17
3.9. Compton Effect. Differential cross section and energy fraction of the scattered photon. . . . 18
3.10. Mass Absorption Coefficient for Water: Photoeffect, Compton effect, Pair Production and Total Sum . . . 19
3.11. Stopping power and CSDA ranges for electrons in water . . . 20

4.1. Simulation geometry for the X-ray tube simulation . . . 24
4.2. Measurement setup for the verification of the tube model. . . . 26
4.3. Profiles from different measurement sets for the verification of the MC-tube model . . . 27
4.4. Comparison between measured and simulated profiles along the x-, y- and z-axis . . . 28

5.1. Summary of simulations to obtain the input data for the kernel calculation algorithm . . . 35
5.2. Nr. of particles in phase space files as a function of field area . . . 37
5.3. Input Data: PDDs for an SSD of 80cm. . . . 37
5.4. Input Data: output factors for all SSDs and normalized output factors . . . 38
5.5. Comparison of normalized profiles for an open field for different offaxis positions . . . 38
5.6. Primary fluence: Comparison dose plane vs. estimated fluence . . . 39
5.7. Data from different steps in the kernel decomposition algorithm . . . 40
5.8. Differences between square corrected PDD and fitted function for different field sizes . . . 41

6.1. Water phantom geometries . . . 43
6.2. Rectangular Water Phantom: Comparison between calculated and simulated depth dose curves and lateral profiles along the z-axis for 10cm x 10cm fields at different SSDs . . . 45
6.3. Rectangular Water Phantom: Comparison between calculated and simulated profiles along the z-axis . . . 46
6.4. Rectangular Water Phantom: Comparison between calculated and simulated profiles along the x-, y- and z-axis . . . 47
6.5. Rectangular Water Phantom: Difference maps for larger fields at an SSD of 90cm . . . 48

6.6. Rectangular Water Phantom: Summary of histograms of dose cube differences along the depth in water . . . 50
6.7. Cylindrical Phantom: Illustration of scatter situation and phantom and beam geometries 51
6.8. Cylindrical Phantom: Dose profiles and slices for normalization with dose conversion factor 52
6.9. Cylindrical Phantom: Absolute dose differences for both normalizations . . . 53
6.10. Cylindrical Phantom: Dose profiles and slices for normalization to isocenter dose . . . 53
6.11. Patient Outline: Sagittal slices and x- and y-profile from the Monte Carlo and pencil beam dose distributions for the water filled patient outline with water normalization factor . . . 55
6.12. Patient Outline: Sagittal Slices from the Monte Carlo and pencil beam dose distributions for the water filled patient outline normalized to isocenter . . . 56
6.13. Patient Outline: Profiles along the x-, y- and z-axis for the normalization to the isocenter dose . . . 56
6.14. Patient Outline: Difference maps for simulated and pencil beam dose distributions normalized to isocenter . . . 58

7.1. Water-to-medium mass collision stopping power ratios as a function of electron energy. . . 59
7.2. EGSnrc Conversion table: Density as a function of Hounsfield Unit and Material assignment 63
7.3. Schneider Density Conversion table. HU vs. mass density plot . . . 64
7.4. Linear fit of the logarithm of the simulated profiles . . . 66
7.5. Profiles as created by the different steps of the factor calculation. . . . 67
7.6. Dose profile comparison: Simulated profiles vs. scaled profiles in water (Schneider conversion table). . . . 69
7.7. Estimated depth scaling factors α as a function of the Hounsfield value . . . 71

8.1. Screenshot of a phantom slice in a .egsphant file . . . 74
8.2. Material and density map created with the graphical user interface using the Schneider conversion table. . . . 74
8.3. Sagittal slices of the material and density maps for both conversion tables . . . 76
8.4. Comparison of sagittal slices of the dose distributions for the Schneider and the EGSnrc conversion table . . . 77
8.5. Dose profile comparison for conversion tables according to Schneider and EGSnrc: profiles through the isocenter . . . 78
8.6. Dose profile comparison for conversion tables according to Schneider and EGSnrc: profiles through the brain . . . 79

9.1. β as the mean value of a gauss fit of the histogram . . . 83
9.2. Material map and targetpoints for the head and neck patients . . . 86
9.3. Summary of dose ratio histograms as a function of the Hounsfield Unit for Patient A for both beam geometries . . . 87
9.4. Dose scaling factors β as calculated for all head and neck patients for both beam configurations. . . . 87
9.5. Single photon beam at 0°: Dose profiles along the x-, y- and z-axis . . . 88
9.6. Transversal slices of the simulated and pencil beam dose distribution for Patient A for a single photon beam at 0° . . . 88
9.7. Transversal slices of the absolute difference between simulated and pencil beam dose distribution for all head & neck patients . . . 89
9.8. Single photon beam at 0°: Sagittal slices of the dose distributions and difference maps for all head and neck patients . . . 90
9.9. Histogram of differences for all patients for a beam at 0° . . . 91
9.10. Transversal slices of the simulated and pencil beam dose distribution for Patient A for a CBCT acquisition . . . 93
9.11. Colorscale for all plots in the section head and neck - CBCT Acquisition . . . 93
9.12. Transversal slices of relative differences for a CBCT acquisition for all head & neck patients 93

9.13. CBCT acquisition: Sagittal slices of the dose distributions and difference maps for all head and neck patients . . . 94
9.14. Histogram of differences for all patients for a beam at 360° . . . 95
9.15. DVHs for the spinal cord and the right optic nerve for a CBCT acquisition . . . 96
9.16. Material and density map for the pelvis patients . . . 97
9.17. Dose scaling factors β as calculated for all pelvis patients. For comparison, the scaling factors for the head & neck reference patient are also plotted. . . . 98
9.18. Profiles along the x- and y- axis of the patient coordinate system for the reference Patient D for a single beam at 0° . . . 99
9.19. Transversal slices of the simulated and pencil beam dose distribution for Patient D for a single photon beam at 0° . . . 99
9.20. Transversal slices of the relative difference between simulated and pencil beam dose distribution for all pelvis patients . . . 100
9.21. Histograms for the absolute and relative differences of the dose distributions for Patient D for a single beam at 0° . . . 100
9.22. Organs at risk for the pelvic area. . . . 101
9.23. DVHs for the intestine and the right femoral head for a single photon beam at 0° . . . 102
9.24. Transversal slices of the simulated and pencil beam dose distribution for Patient D for a CBCT acquisition . . . 103
9.25. Transversal slices of the relative difference for all pelvis patients for a CBCT acquisition . 103
9.26. Histogram of differences for the reference patients . . . 104
9.27. DVHs for the spinal cord and the right optic nerve for a CBCT acquisition . . . 104

B.1. Isocentric slices for Pat. A for a single beam at 0°. . . . 125
B.2. Central slices for Pat. A for a single beam at 0°. . . . 127
B.3. Isocentric slices for Pat. B for a single beam at 0°. . . . 129
B.4. Central slices for Pat. B for a single beam at 0°. . . . 131
B.5. Isocentric slices for Pat. C for a single beam at 0°. . . . 133
B.6. Central slices for Pat. C for a single beam at 0°. . . . 135
B.7. Isocentric slices for Pat. A for a cone beam CT acquisition (360° tube rotation). . . . 139
B.8. Central slices for Pat. A for a cone beam CT acquisition (360° tube rotation). . . . 141
B.9. Isocentric slices for Pat. B for a cone beam CT acquisition (360° tube rotation). . . . 143
B.10. Central slices for Pat. B for a cone beam CT acquisition (360° tube rotation). . . . 145
B.11. Isocentric slices for Pat. C for a cone beam CT acquisition (360° tube rotation). . . . 147
B.12. Central slices for Pat. C for a cone beam CT acquisition (360° tube rotation). . . . 149
B.13. Isocentric slices for Pat. D for a single beam at 0°. . . . 153
B.14. Isocentric slices for Pat. E for a single beam at 0°. . . . 155
B.15. Isocentric slices for Pat. F for a single beam at 0°. . . . 157
B.16. Isocentric slices for Pat. D for a cone beam CT acquisition (360° tube rotation). . . . 161
B.17. Isocentric slices for Pat. E for a cone beam CT acquisition (360° tube rotation). . . . 163
B.18. Isocentric slices for Pat. F for a cone beam CT acquisition (360° tube rotation). . . . 165

List of Tables

2.1. Organ absorbed doses and effective doses from CBCT 9
2.2. Threshold skin entrance doses for different skin injuries 10

5.1. Number of particles in the phase space files 37

7.1. EGSnrc Density and material conversion table 63
7.2. EGSnrc Conversion table. Elemental Composition of Materials 64
7.3. Schneider density conversion table as specified in [74]. 64
7.4. Schneider Conversion table: Elemental composition of ICRU Materials and minimum and maximum Hounsfield Unit for each material as specified in [74] 65

9.1. Mean organ doses in mGy/projection image for head and neck patients for a single photon beam at 0° 91
9.2. Mean organ doses in mGy/projection image for head and neck patients for a 360° rotation of the X-ray tube 96
9.3. Mean organ doses in mGy/projection image for pelvis patients for a single photon beam at 0° 101
9.4. Mean organ doses in mGy/projection image for pelvis patients for a 360° rotation of the X-ray tube 104

Bibliography

[1] Thomas Bortfeld. Imrt: a review and preview. *Physics in Medicine and Biology*, 51(13):R363–R379, 2006.

[2] U. OELFKE. Inverse planning for photon and proton beams. *Medical Dosimetry*, 26(2):113–124, 2001.

[3] Karl Otto. Volumetric modulated arc therapy: Imrt in a single gantry arc. *Medical Physics*, 35(1):310, 2008.

[4] Silke Ulrich, Simeon Nill, and Uwe Oelfke. Development of an optimization concept for arc-modulated cone beam therapy. *Physics in medicine and biology*, 52(14):4099–4119, 2007.

[5] Laura A. Dawson and David A. Jaffray. Advances in image-guided radiation therapy. *Journal of clinical oncology : official journal of the American Society of Clinical Oncology*, 25(8):938–946, 2007.

[6] George T. Y. Chen, Gregory C. Sharp, and Shinichiro Mori. A review of image-guided radiotherapy. *Radiological physics and technology*, 2(1):1–12, 2009.

[7] Lei Xing, Brian Thorndyke, Eduard Schreibmann, Yong Yang, Tian-Fang Li, Gwe-Ya Kim, Gary Luxton, and Albert Koong. Overview of image-guided radiation therapy. *Medical dosimetry : official journal of the American Association of Medical Dosimetrists*, 31(2):91–112, 2006.

[8] B. G. Fallone, B. Murray, S. Rathee, T. Stanescu, S. Steciw, S. Vidakovic, E. Blosser, and D. Tymofichuk. First mr images obtained during megavoltage photon irradiation from a prototype integrated linac-mr system. *Medical physics*, 36(6):2084–2088, 2009.

[9] B. W. Raaymakers, J. J. W. Lagendijk, J. Overweg, J. G. M. Kok, A. J. E. Raaijmakers, E. M. Kerkhof, R. W. van der Put, I. Meijsing, S. P. M. Crijns, F. Benedosso, M. van Vulpen, C. H. W. de Graaff, J. Allen, and K. J. Brown. Integrating a 1.5 t mri scanner with a 6 mv accelerator: proof of concept. *Physics in medicine and biology*, 54(12):N229–37, 2009.

[10] Mohammad K. Islam, Thomas G. Purdie, Bernhard D. Norrlinger, Hamideh Alasti, Douglas J. Moseley, Michael B. Sharpe, Jeffrey H. Siewerdsen, and David A. Jaffray. Patient dose from kilovoltage cone beam computed tomography imaging in radiation therapy. *Medical physics*, 33(6):1573–1582, 2006.

[11] Monica W. K. Kan, Lucullus H. T. Leung, Wicger Wong, and Nelson Lam. Radiation dose from cone beam computed tomography for image-guided radiation therapy. *International journal of radiation oncology, biology, physics*, 70(1):272–279, 2008.

[12] William Y. Song, Srijit Kamath, Shuichi Ozawa, Shlomi Al Ani, Alexei Chvetsov, Niranjan Bhandare, Jatinder R. Palta, Chihray Liu, and Jonathan G. Li. A dose comparison study between xvi and obi cbct systems. *Medical physics*, 35(2):480–486, 2008.

[13] Nada Tomic, Slobodan Devic, François DeBlois, and Jan Seuntjens. Reference radiochromic film dosimetry in kilovoltage photon beams during cbct image acquisition. *Medical physics*, 37(3):1083–1092, 2010.

[14] Cornelia Walter, Judit Boda-Heggemann, Hansjörg Wertz, Iris Loeb, Angelika Rahn, Frank Lohr, and Frederik Wenz. Phantom and in-vivo measurements of dose exposure by image-guided radiotherapy (igrt): Mv portal images vs. kv portal images vs. cone-beam ct. *Radiotherapy and oncology : journal of the European Society for Therapeutic Radiology and Oncology*, 85(3):418–423, 2007.

[15] Ning Wen, Huaiqun Guan, Rabih Hammoud, Deepak Pradhan, T. Nurushev, Shidong Li, and Benjamin Movsas. Dose delivered from varian's cbct to patients receiving imrt for prostate cancer. *Physics in medicine and biology*, 52(8):2267–2276, 2007.

[16] James C. L. Chow, Michael K. K. Leung, Mohammad K. Islam, Bernhard D. Norrlinger, and David A. Jaffray. Evaluation of the effect of patient dose from cone beam computed tomography on prostate imrt using monte carlo simulation. *Medical physics*, 35(1):52–60, 2008.

[17] George X. Ding and Charles W. Coffey. Radiation dose from kilovoltage cone beam computed tomography in an image-guided radiotherapy procedure. *International journal of radiation oncology, biology, physics*, 73(2):610–617, 2009.

[18] George X. Ding, Dennis M. Duggan, and Charles W. Coffey. Accurate patient dosimetry of kilovoltage cone-beam ct in radiation therapy. *Medical physics*, 35(3):1135–1144, 2008.

[19] R. Mohan, C. Chui, and L. Lidofsky. Differential pencil beam dose computation model for photons. *Medical physics*, 13(1):64–73, 1986.

[20] Parham Alaei, B. J. Gerbi, and R. A. Geise. Generation and use of photon energy deposition kernels for diagnostic quality x rays. *Medical physics*, 26(8):1687–1697, 1999.

[21] Parham Alaei, B. J. Gerbi, and R. A. Geise. Evaluation of a model-based treatment planning system for dose computations in the kilovoltage energy range. *Medical physics*, 27(12):2821–2826, 2000.

[22] Parham Alaei, B. J. Gerbi, and R. A. Geise. Lung dose calculations at kilovoltage x-ray energies using a model-based treatment planning system. *Medical physics*, 28(2):194–198, 2001.

[23] George X. Ding, Jason M. Pawlowski, and Charles W. Coffey. A correction-based dose calculation algorithm for kilovoltage x rays. *Medical physics*, 35(12):5312–5316, 2008.

[24] Parham Alaei, George X. Ding, and Huaiqun Guan. Inclusion of the dose from kilovoltage cone beam ct in the radiation therapy treatment plans. *Medical physics*, 37(1):244–248, 2010.

[25] Jason M. Pawlowski and George X. Ding. A new approach to account for the medium-dependent effect in model-based dose calculations for kilovoltage x-rays. *Physics in Medicine and Biology*, 56(13):3919–3934, 2011.

[26] Elekta AB (publ). Elekta image gallery - galerie.

[27] Inc Varian Medical Systems. Varian medical systems newsroom - image gallery.

[28] Omar A. Zeidan, Katja M. Langen, Sanford L. Meeks, Rafael R. Manon, Thomas H. Wagner, Twyla R. Willoughby, D. Wayne Jenkins, and Patrick A. Kupelian. Evaluation of image-guidance protocols in the treatment of head and neck cancers. *International journal of radiation oncology, biology, physics*, 67(3):670–677, 2007.

[29] Patrick A. Kupelian, Choonik Lee, Katja M. Langen, Omar A. Zeidan, Rafael R. Mañon, Twyla R. Willoughby, and Sanford L. Meeks. Evaluation of image-guidance strategies in the treatment of localized prostate cancer. *International journal of radiation oncology, biology, physics*, 70(4):1151–1157, 2008.

[30] Yvette Seppenwoolde, Hiroki Shirato, Kei Kitamura, Shinichi Shimizu, Marcel van Herk, Joos V. Lebesque, and Kazuo Miyasaka. Precise and real-time measurement of 3d tumor motion in lung due to breathing and heartbeat, measured during radiotherapy. *International journal of radiation oncology, biology, physics*, 53(4):822–834, 2002.

[31] Gig S. Mageras, Alex Pevsner, Ellen D. Yorke, Kenneth E. Rosenzweig, Eric C. Ford, Agung Hertanto, Steven M. Larson, D. Michael Lovelock, Yusuf E. Erdi, Sadek A. Nehmeh, John L. Humm, and C. Clifton Ling. Measurement of lung tumor motion using respiration-correlated ct. *International journal of radiation oncology, biology, physics*, 60(3):933–941, 2004.

[32] Jeremy D. P. Hoisak, Katharina E. Sixel, Romeo Tirona, Patrick C. F. Cheung, and Jean-Philippe Pignol. Correlation of lung tumor motion with external surrogate indicators of respiration. *International journal of radiation oncology, biology, physics*, 60(4):1298–1306, 2004.

[33] Alexis N. T. J. Kotte, Pieter Hofman, Jan J. W. Lagendijk, Marco van Vulpen, and Uulke A. van der Heide. Intrafraction motion of the prostate during external-beam radiation therapy: analysis of 427 patients with implanted fiducial markers. *International journal of radiation oncology, biology, physics*, 69(2):419–425, 2007.

[34] Amish P. Shah, Patrick A. Kupelian, Twyla R. Willoughby, Katja M. Langen, and Sanford L. Meeks. An evaluation of intrafraction motion of the prostate in the prone and supine positions using electromagnetic tracking. *Radiotherapy and oncology : journal of the European Society for Therapeutic Radiology and Oncology*, 99(1):37–43, 2011.

[35] Twyla R. Willoughby, Patrick A. Kupelian, Jean Pouliot, Katsuto Shinohara, Michelle Aubin, Mack Roach, Lisa L. Skrumeda, James M. Balter, Dale W. Litzenberg, Scott W. Hadley, John T. Wei, and Howard M. Sandler. Target localization and real-time tracking using the calypso 4d localization system in patients with localized prostate cancer. *International journal of radiation oncology, biology, physics*, 65(2):528–534, 2006.

[36] Haisen S. Li, Indrin J. Chetty, Charles A. Enke, Ryan D. Foster, Twyla R. Willoughby, Patrick A. Kupellian, and Timothy D. Solberg. Dosimetric consequences of intrafraction prostate motion. *International journal of radiation oncology, biology, physics*, 71(3):801–812, 2008.

[37] T. Moser, J. Biederer, S. Nill, G. Remmert, and R. Bendl. Detection of respiratory motion in fluoroscopic images for adaptive radiotherapy. *Physics in medicine and biology*, 53(12):3129–3145, 2008.

[38] Accuray Incorporated. Accuray::virtual press kit.

[39] C. Thieke. Kilovoltage ct using a linac-ct scanner combination. *British Journal of Radiology*, 79(Special Issue 1):S79–S86, 2006.

[40] J. STUTZEL, U. OELFKE, and S. Nill. A quantitative image quality comparison of four different image guided radiotherapy devices. *Radiotherapy and Oncology*, 86(1):20–24, 2008.

[41] Simeon Nill, Jan Unkelbach, Lars Dietrich, and Uwe Oelfke. Online correction for respiratory motion: evaluation of two different imaging geometries. *Physics in Medicine and Biology*, 50(17):4087–4096, 2005.

[42] Siemens AG. Pressebilder - siemens global website.

[43] Charles L. Perkins, Tim Fox, Eric Elder, David A. Kooby, Charles A. Staley, and Jerome Landry. Image-guided radiation therapy (igrt) in gastrointestinal tumors. *JOP : Journal of the pancreas*, 7(4):372–381, 2006.

[44] John W. Hirshfeld, Stephen Balter, Jeffrey A. Brinker, Morton J. Kern, Lloyd W. Klein, Bruce D. Lindsay, Carl L. Tommaso, Cynthia M. Tracy, Louis K. Wagner, Mark A. Creager, Michael Elnicki, Beverly H. Lorell, George P. Rodgers, and Howard H. Weitz. Accf/aha/hrs/scai clinical competence statement on physician knowledge to optimize patient safety and image quality in fluoroscopically guided invasive cardiovascular procedures: a report of the american college of cardiology foundation/american heart association/american college of physicians task force on clinical competence and training. *Circulation*, 111(4):511–532, 2005.

[45] George X. Ding and Charles W. Coffey. Beam characteristics and radiation output of a kilovoltage cone-beam ct. *Physics in medicine and biology*, 55(17):5231–5248, 2010.

[46] Wolfgang Schlegel and Andreas Mahr. *3D conformal radiation therapy*. Springer Berlin, Berlin ;, Heidelberg, 2 edition, 2007.

[47] International Electrotechnical Commission. Radiotherapy equipment - coordinates, movements & scales, May 1995.

[48] Thomas Tücking. *Development and Realization of the IGRT Inline Concept*. PhD thesis, Ruperto-Carola University of Heidelberg, Heidelberg, 2007.

[49] Arnulf Oppelt. *Imaging systems for medical diagnostics: Fundamentals, technical solutions and applications for systems applying ionizing radiation, nuclear magnetic resonance and ultrasound*. Publicis, Erlangen, [2. ed.] edition, 2005.

[50] John Ball and Adrian D. Moore. *Essential physics for radiographers*. Blackwell Science, Malden, Ma, 3rd edition, 1997.

[51] H. K. Kim, S. J. Han, J. L. Kim, B. H. Kim, S. Y. Chang, and J. K. Lee. Monte carlo simulation of the photon beam characteristics from medical linear accelerators. *Radiation protection dosimetry*, 119(1-4):510–513, 2006.

[52] Gopal B. Saha. *Physics and radiobiology of nuclear medicine*. Springer, New York, 2nd edition, 2001.

[53] I. Reitz. *Development and evaluation of a method for scatter correction in kV Cone Beam Computer Tomography*. PhD thesis, Ruperto-Carola University of Heidelberg, Heidelberg, 2008.

[54] Hanno Krieger. *Grundlagen der Strahlungsphysik und des Strahlenschutzes*. Vieweg+Teubner Verlag / GWV Fachverlage GmbH, Wiesbaden, Wiesbaden, 3., überarbeitete und erweiterte auflage. edition, 2009.

[55] Josef Bille and Wolfgang Schlegel, editors. *Medizinische Physik 2: Medizinische Strahlenphysik*. Springer, Berlin [u.a.], 2002.

[56] M.J Berger, J.H Hubbell, S.M Seltzer, J. Chang, J.S Coursey, R. Sukumar, D.S Zucker, and K. Olsen. Xcom: Photon cross sections database (version 1.5), 2010.

[57] M.J Berger, J.S Coursey, M.A Zucker, and J. Chang. Stopping-power and range tables for electrons, protons, and helium ions (version 1.2.3), 2005.

[58] T. R. Mackie, J. W. Scrimger, and J. J. Battista. A convolution method of calculating dose for 15-mv x rays. *Medical physics*, 12(2):188–196, 1985.

[59] T. R. Mackie, A. F. Bielajew, D. W. O. Rogers, and J. J. Battista. Generation of photon energy deposition kernels using the egs monte carlo code. *Physics in Medicine and Biology*, 33(1):1–20, 1988.

[60] T. Bortfeld, W. Schlegel, and B. Rhein. Decomposition of pencil beam kernels for fast dose calculations in three-dimensional treatment planning. *Medical physics*, 20(2 Pt 1):311–318, 1993.

[61] James C. L. Chow. Cone-beam ct dosimetry for the positional variation in isocenter: a monte carlo study. *Medical physics*, 36(8):3512–3520, 2009.

[62] P. Downes, R. Jarvis, E. Radu, Iwan Kawrakow, and E. Spezi. Monte carlo simulation and patient dosimetry for a kilovoltage cone-beam ct unit. *Medical physics*, 36(9):4156–4167, 2009.

[63] P. Downes and E. Spezi. Simulating oblique incident irradiation using the beamnrc monte carlo code. *Physics in medicine and biology*, 54(7):N93–N100, 2009.

[64] G. Asuni, J. M. Jensen, and B. M. C. McCurdy. A monte carlo investigation of contaminant electrons due to a novel in vivo transmission detector. *Physics in medicine and biology*, 56(4):1207–1223, 2011.

[65] Komanduri M. Ayyangar, M. Dinesh Kumar, Pradush Narayan, Fenedit Jesuraj, and M. R. Raju. Monte carlo simulation of a multi-leaf collimator design for telecobalt machine using beamnrc code. *Journal of medical physics / Association of Medical Physicists of India*, 35(1):23–32, 2010.

[66] Jason Belec, Nicolas Ploquin, Daniel J. La Russa, and Brenda G. Clark. Position-probability-sampled monte carlo calculation of vmat, 3dcrt, step-shoot imrt, and helical tomotherapy dose distributions using beamnrc/dosxyznrc. *Medical physics*, 38(2):948–960, 2011.

[67] T. Kairn, J. Kenny, S. B. Crowe, A. L. Fielding, R. D. Franich, P. N. Johnston, R. T. Knight, C. M. Langton, D. Schlect, and J. V. Trapp. Modeling a complex micro-multileaf collimator using the standard beamnrc distribution. *Medical physics*, 37(4):1761–1767, 2010.

[68] J. R. Treurniet, B. R. Walters, I. Kawrakow, and D. W. O. Rogers. Beamnrc, dosxyznrc and beamdp gui user's manual. *NRCC Report PIRS-0623(rev C)*, 2004.

[69] Kawrakow I, Rogers DW, and Walters BR. Large efficiency improvements in beamnrc using directional bremsstrahlung splitting. *Medical physics*, 31(10):2883–2898, 2004.

[70] I. Kawrakow, Ernesto Mainegra-Hing, D. W. O. Rogers, F. Tessier, and B. R. B. Walters. The egsnrc code system: Monte carlo simulation of electron and photon transport. *Technical Report PIRS-701, National Research Council of Canada, Ottawa, Canada*, 2010.

[71] B. R. B. Walters, I. Kawrakow, and D. W. O. Rogers. Dosxyznrc users manual. *NRC Report PIRS 794 (rev B)*, 2005.

[72] J. V. Siebers, P. J. Keall, A. E. Nahum, and R. Mohan. Converting absorbed dose to medium to absorbed dose to water for monte carlo based photon beam dose calculations. *Physics in medicine and biology*, 45(4):983–995, 2000.

[73] J. E. O'CONNOR. The variation of scattered x-rays with density in an irradiated body. *Physics in medicine and biology*, 1(4):352–369, 1957.

[74] W. Schneider, T. Bortfeld, and W. Schlegel. Correlation between ct numbers and tissue parameters needed for monte carlo simulations of clinical dose distributions. *Physics in medicine and biology*, 45(2):459–478, 2000.

[75] H. Q. Woodard and D. R. White. Bone models for use in radiotherapy dosimetry. *British Journal of Radiology*, 55(652):277–282, 1982.

[76] H. Q. Woodard and D. R. White. The composition of body tissues. *British Journal of Radiology*, 59(708):1209–1218, 1986.

[77] Iwan Kawrakow. 3d electron dose calculation using a voxel based monte carlo algorithm (vmc). *Medical Physics*, 23(4):445, 1996.

[78] Oliver Koelbl, Thomas Krieger, Ulrich Haedinger, Otto Sauer, and Michael Flentje. Influence of calculation algorithm on dose distribution in irradiation of non-small cell lung cancer (nsclc). *Strahlentherapie und Onkologie*, 180(12):783–788, 2004.

[79] Barbara Vanderstraeten, Nick Reynaert, Leen Paelinck, Indira Madani, Carlos de Wagter, Werner de Gersem, Wilfried de Neve, and Hubert Thierens. Accuracy of patient dose calculation for lung imrt: A comparison of monte carlo, convolution/superposition, and pencil beam computations. *Medical Physics*, 33(9):3149, 2006.

[80] Huixiao Chen, Frank Lohr, Peter Fritz, Frederik Wenz, Barbara Dobler, Friedlieb Lorenz, and Werner Mühlnickel. Stereotactic, single-dose irradiation of lung tumors: A comparison of absolute dose and dose distribution between pencil beam and monte carlo algorithms based on actual patient ct scans. *International Journal of Radiation Oncology*Biology*Physics*, 78(3):955–963, 2010.

[81] Alexei Kouznetsov and Mauro Tambasco. A hybrid approach for rapid, accurate, and direct kilovoltage radiation dose calculations in ct voxel space. *Medical Physics*, 38(3):1378, 2011.

Acknowledgments

I would like to thank my supervisor Prof. Uwe Oelfke for the constant support and especially for giving me the opportunity to work here at the DKFZ. I have always enjoyed working in his group. I am also obliged to Prof. Schlegel for acting as the second referee for this thesis.

Thanks to all members of E0401 and especially those who also spent their time at DKFZ in the "U-boot". In particular I want to express my gratitude towards Simeon Nill and Asja Pfaffenberger for their support in the last few months.

Finally I want to thank Gregor for helping and supporting me.